NASA Contractor Report 4207

Application of Triggered Lightning Numerical Models to the F106B and Extension to Other Aircraft

Poh H. Ng, Roger A. Dalke,
Jim Horembala, Terence Rudolph,
and Rodney A. Perala
Electro Magnetic Applications, Inc.
Lakewood, Colorado

Prepared for
Langley Research Center
under Contract NAS1-17748

National Aeronautics
and Space Administration

Scientific and Technical
Information Division

1988

TABLE OF CONTENTS

LIST OF FIGURES

LIST OF FIGURES - continued

LIST OF FIGURES - continued

LIST OF FIGURES - continued

LIST OF FIGURES - continued

LIST OF FIGURES - continued

LIST OF FIGURES - continued

LIST OF FIGURES - continued

LIST OF TABLES

CHAPTER 1
INTRODUCTION

Previous reports in this series [1-5] have concentrated on the development of numerical models intended to increase the level of understanding of in-flight triggered lightning strikes. This involved the analysis of electromagnetic data collected by the NASA F106B Thunderstorm Research Aircraft to determine the electromagnetic environment for an aircraft flying in or near a thunderstorm. In this report, the emphasis has been shifted to an application of the numerical models developed in previous years, and an extension of the present understanding of the triggered lightning environment to aircraft other than the F106B.

In Chapter 2, an extensive application of linear triggered lightning models to data collected by the F106B is presented [6-11]. The data, both measured and calculated, are analyzed statistically for correlations which may be used to predict electromagnetic aircraft responses for strikes on which a full complement of sensors was not available. For example, a D-dot response that, in general, correlates well with an I-dot sensor was unavailable or nonfunctional.

Chapter 3 presents the application of electrostatic field mill models to predict ambient field and charge levels for cases in which the F106B triggered lightning strikes. The predicted fields, combined with known enhancement factors of the F106B, are shown to be sufficient to cause the observed lightning strikes.

The application of subgrid modeling is presented in Chapter 4. There a subgrid is placed around the nose of the F106B and combined with an electrostatic field solution to predict ambient field breakdown levels and subsequent nonlinear electromagnetic responses on the aircraft. As one would expect, the ambient field levels required for air breakdown are less than for non-subgrid models because of the subgrid's ability to model finer details and sharper points in the nose region. Calculated electromagnetic sensor responses are compared with measured values and with calculated response for non-subgrid models.

Chapter 5 represents an attempt to extend the triggered lightning environment to aircraft other than the F106B. The responses of four different aircraft are analyzed to determine scaling laws for triggering fields and sensor responses between aircraft of differing sizes and shapes. The analysis is extended to aircraft in general through the use of canonical shapes.

Chapter 6 models the response of the F106B to a leader-return stroke sequence of events. The return stroke is assumed to approach the aircraft along the previously ionized channel of a leader which had begun at the aircraft or passed through it. The physics associated with the return stroke is included using nonlinear modeling techniques.

CHAPTER 2

EXTENDED APPLICATION OF THE LINEAR LIGHTNING INTERACTION MODEL

2.1 Introduction

The lightning data collected by the F106B contains large quantities of electromagnetic waveforms. This data set in its raw form is difficult to use because of its size and complexity. A distillation of the data set down to a collection of descriptive parameters is desirable. This chapter reports on the development of a database containing the electromagnetic quantities measured by the F106B during direct lightning strikes to the aircraft. Also included in the database are results from lightning strike simulations.

The linear lightning interaction model [4] has been used in conjunction with the in-flight data in order to construct a database of response characteristics for lightning events recorded on the NASA F106B Research Aircraft during 1984. Characteristics derived from the measured transient responses and from the responses calculated through the use of the linear transfer function technique and the linear finite difference model appear in the database and can be accessed through the use of a computer program written to display the prominent elements.

This chapter also presents a comparison of measured and calculated response records for 53 separate 1984 lightning events. Simulated and measured transient responses appear as one microsecond records in the overlays produced to supplement the information contained in the characteristic database.

Finally, the results of a correlation study relating lightning current responses to external and internal measured responses are discussed. The steps used in determining the relationships presented are given and the predictive capabilities of the models are indicated.

2.2 The 1984 Measured and Calculated Strike Database

2.2.1 Database Organization and Development

The 1984 database was developed with the primary goal of organizing the available data into a consistent structure of characteristics that would allow easy access to both the calculated and measured entries. The elements of NASA84DATABASE (the database file) were generated and constructed to meet these particular demands.

The framework selected for this purpose treated all of the information obtained for each measured or calculated strike as a structured data item. The items were then organized in array format to produce the present database. This type of implementation permits the particular structured data item of interest to be located easily by simply searching the "array" of structured items for an entry containing the appropriate identification.

The characteristics were developed so that a comparison between measured and calculated elements would be meaningful. The creation of one microsecond response records from the measured transient responses was a necessary part of this development when both measured and calculated data could be obtained for the same event. These records assured the consistency of certain characteristics appearing in the database.

The database contains strike characteristics determined from the examination of the in-flight data for 110 events and from the linear modeling results for 53 events. Every strike represented in the database contains information concerning the following sensor response characteristics:

(i) Maximum Sensor Value

(ii) Minimum Sensor Value

(iii) Peak Sensor Value (calculated as - max { | Maximum Sensor Value | , | Minimum Sensor Value | } with appropriate sign)

(iv) Range of the Sensor Response (calculated as the difference of the maximum and minimum values).

In cases where both measured and calculated data is available for the same event, the following additional characteristics are generally found:

- (v) Sensor Peak Width at Half Maximum
- (vi) Maximum Time Derivative of the Sensor Response
- (vii) Minimum Time Derivative of the Sensor Response
- (viii) Peak Positive Difference in Charge for Current Sensors
- (ix) Peak Negative Difference in Charge for Current Sensors.

The appearance of these secondary characteristics in the database depended upon sensor availability, the successful production of one microsecond records from the measured transient responses and in the case of sensor peak width at half maximum, the nature of the response waveform.

The methods used to obtain some of the quantities in the preceding list require a brief explanation. A discussion of the individual techniques is given below.

1. Sensor Peak Width at Half Maximum

This time was calculated by locating the peak response value in time and then moving away from the major peak in both directions until half peak response values were found. The length of the time interval defined by the successful location of the half peak response values is the time characteristic appearing in the database. If examination of the one microsecond record failed to produce the required pair of half peak response values, this characteristic was not produced. This could occur, for instance, if the sensor response stayed high after the peak response was achieved.

2. The Maximum and Minimum Time Derivatives of the Sensor Response.

The maximum and minimum values were found by comparing the derivatives obtained at each time step in the one microsecond records. A simple difference approximation was used to generate the derivative data.

3. The Peak Difference in Charge for Current Sensors

Linear interpolation was used between discrete data points to represent the current as a continuous function of time. This function was then integrated over the sample interval to arrive at a difference in charge value. For the measured data, these values were then scaled by the length of the sample interval so that the results could be compared to the one nanosecond "sampling" time interval used to obtain the calculated values. The peak values were then obtained by examining similar calculations throughout the one microsecond current response record.

Additional items attached to each strike entry include the unique flight, run and strike numbers and the type of data (measured or calculated) appearing in that particular entry. The calculated data entries also include the attach-detach locations used to produce the linear modeling results. Spaces were allocated in the database for temperature, altitude and attachment-detachment elements during the stages of database development. Unfortunately, this information could not always be obtained from the 1984 tapes.

2.2.2 Database Access

The more important features of the 1984 database may be viewed through the use of the FORTRAN program NASA84DATABASE_READ. Characteristics of a unique strike may be accessed by providing the interactive program with the appropriate flight, run and strike numbers. The program will also ask whether calculated or measured data is required and will inform the user if the requested strike does not appear in the database.

NASA84DATABASE_READ was written primarily to insure the correct production of strike entries during the process of constructing the database. As a result, some of the characteristics stored in the database are not displayed when using this program. These include the maximum and minimum time derivatives and the ranges of the sensor responses. The remaining strike elements (those listed as i, ii, iii, v, viii, ix in Section 2.2.1) are available through interactive use.

2.2.3 Comparison of the 1984 Measured and Calculated Data

The one microsecond records generated by one of the programs written to form the measured portion of the database provided a convenient basis for comparing the in-flight data with the data obtained from the linear simulation model. The set of overlays produced for this comparison appear in Appendix A. Several aspects of this response comparison deserve consideration. It should be noted that nose current measurements, which were made, are not included in Appendix A. They are omitted because the current shunt was felt to have a frequency dependent response, and no reliable method was found to calibrate it.

In general, the calculated response data obtained by using the B-dot longitudinal sensor to derive a current source using transfer function techniques described elsewhere [4] compares favorably with the aircraft sensor data. The results from this particular sensor appear to more consistently match the in-flight data than those obtained from the D-dot forward sensor used for many of the later flights. The probable reasons for this difference were given in a previous report [4].

A closer examination of the records reveals an apparent discrepancy in the response data obtained for the B-dot sensors on the wings of the F106B. These results may in part be due to the differences in sampling between the modeled and measured data.

The records from Flight 84.025 Run 2 Strike 3 and Flight 84.036 Run 2 Strike 2 provide an interesting basis for comparison. A sensor by sensor examination of the measured B-dot and D-dot waveshapes and amplitudes would seem to indicate that these two strikes represent similar lightning events. A similar conclusion is not evident if the measured current responses are examined. The current response record from Flight 84.025 shows better agreement with the calculated data and appears to be consistent with the other sensor responses which are indicative of a strike with a current response peak amplitude on the order of a few hundred amperes. In the case of Flight 84.036, the large amplitude current response differs significantly from the derived current and appears to be inconsistent with the other sensor responses.

The results from this comparison would seem to suggest a problem with the measured current record from the strike on Flight 84.036. This is supported by examining both the one microsecond measured I-dot record produced for this strike and a one microsecond record produced by integrating this particular response. These records shown in Figures 2.1 and 2.2, demonstrate that the large rise in current amplitude seen at the end of the response comparison data is inconsistent with the measured I-dot data.

The I-dot comparisons are absent from the present set of overlays in Appendix A because the results of a brief filtering study indicated that a closer comparison of the measured and calculated response data for this particular sensor is possible if the derived current is filtered before differentiation. In Figures 2.3 through 2.11, the filtered current and the corresponding calculated I-dot response is shown for 9 strikes from the 1984 modeling results. In each case, the derived current source obtained from the linear transfer function technique was filtered using a fifth order Chebyshev low-pass filter with a digital cutoff frequency of 50 MHz. Although the derived current source was obtained from measured data prefiltered at 50 MHz, further filtering was required on this source before the I-dot response comparison was favorable. The reason for this apparent discrepancy stems from the use of the digital Fourier transform in conjunction with the operation of differentiation. The derived current source obtained from the digital transform contains high frequency components which do not appear in the measured data. If a time derivative is calculated for this unfiltered source, the differentiation process will in turn produce a waveform with very high frequency content. Because of this phenomenon, it is necessary to remove the high frequency components before the time derivative is calculated.

(text continues on page 20)

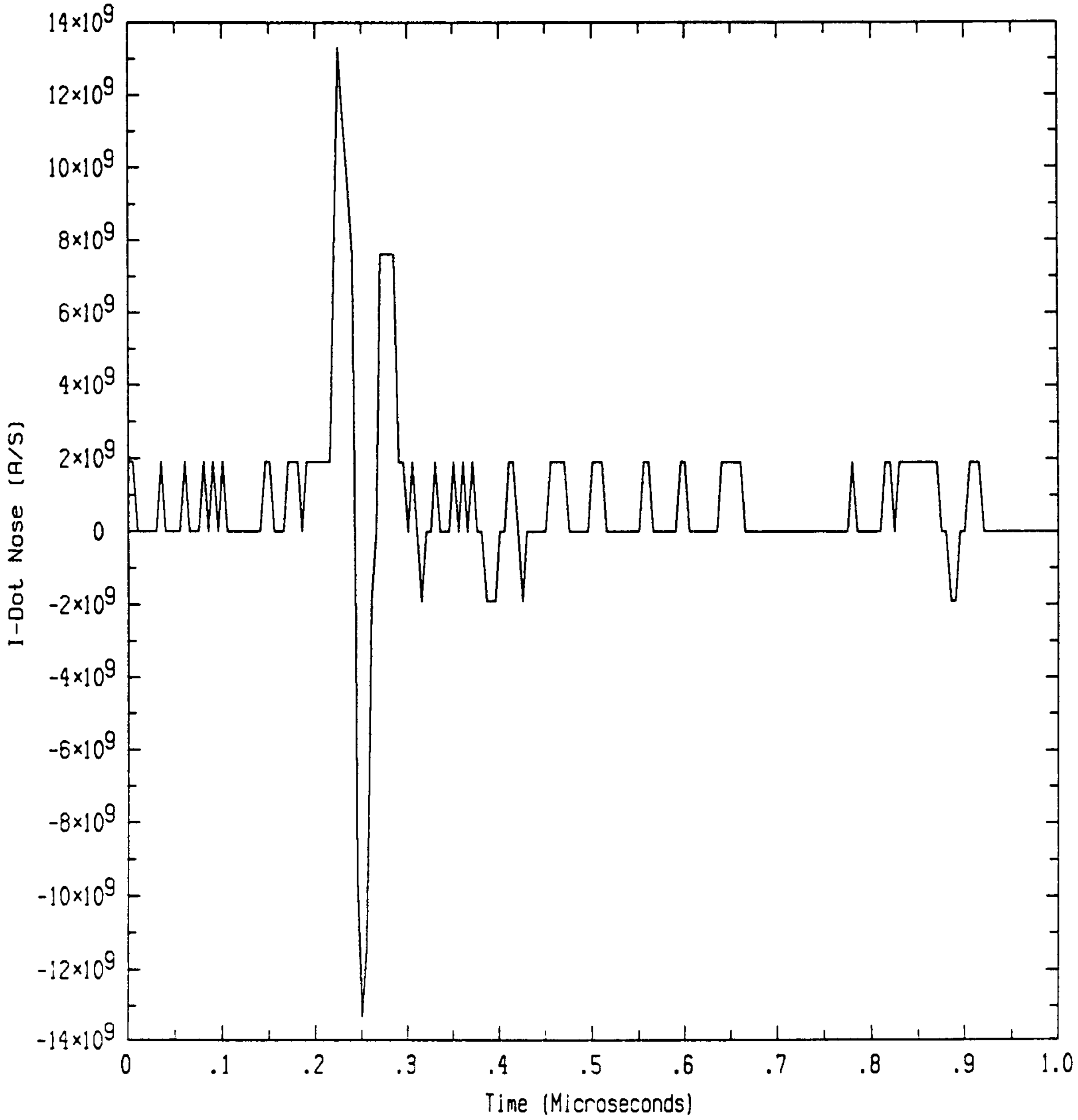

Figure 2.1 Measured I-dot Response from Flight 84-036 Run 002 Strike 002

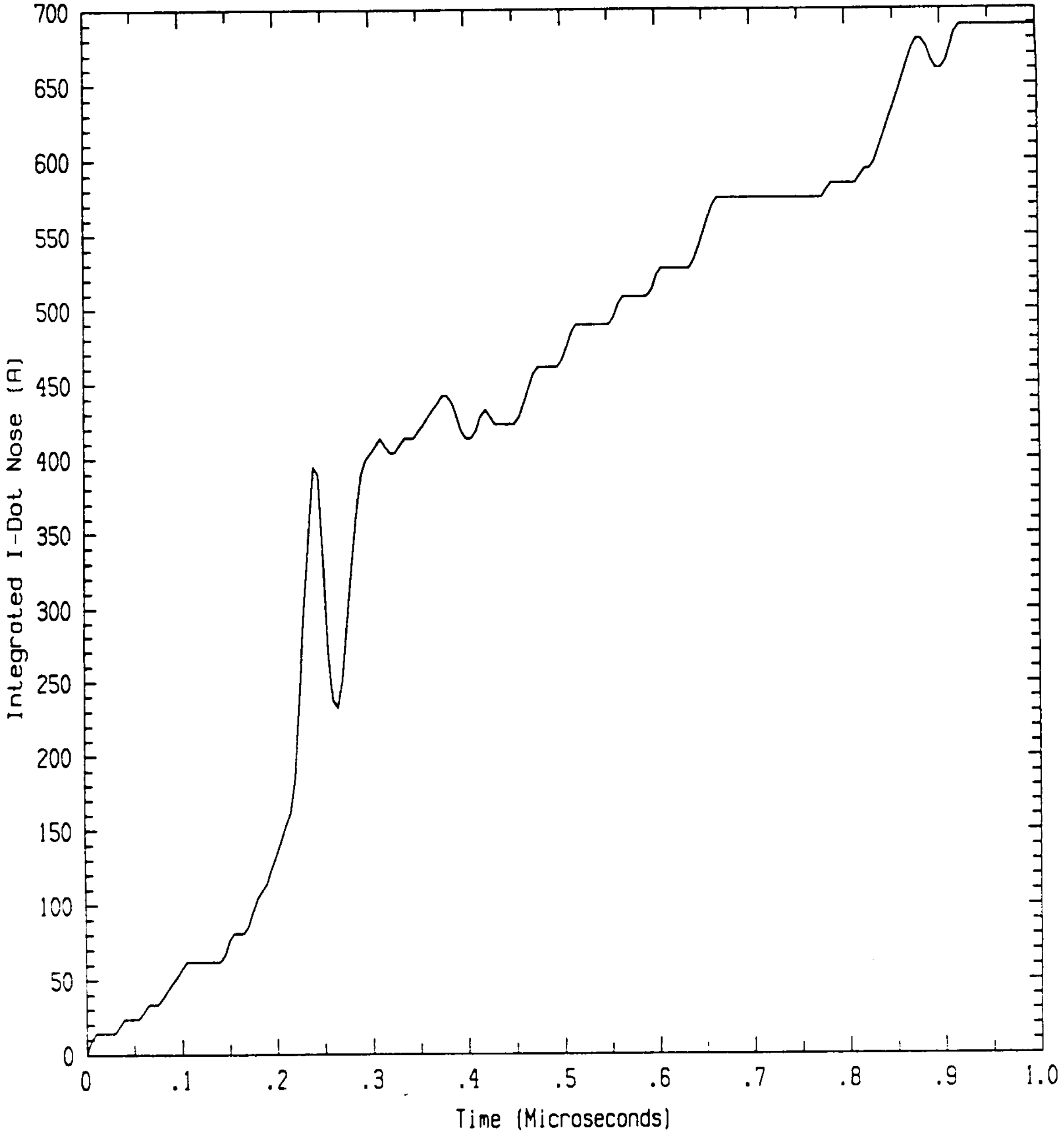

Figure 2.2 Integrated Measured I-dot Response from Flight 84-036 Run 002 Strike 002

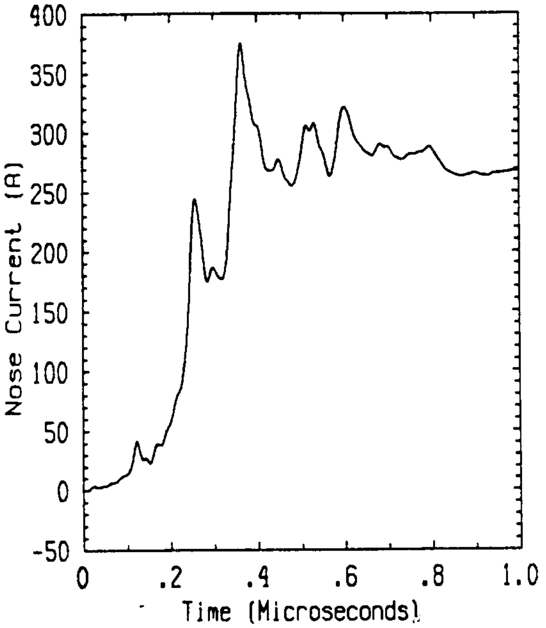

Figure 2.3(a) Calculated Nose Current After Filtering for Flight 84-021 Run 001 Strike 001

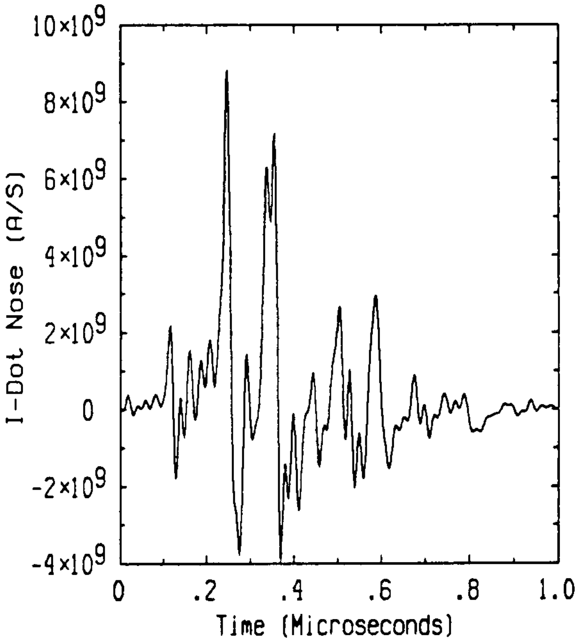

Figure 2.3(b) I-dot Response Obtained from Calculated Nose Current After Filtering for Flight 84-021 Run 001 Strike 001

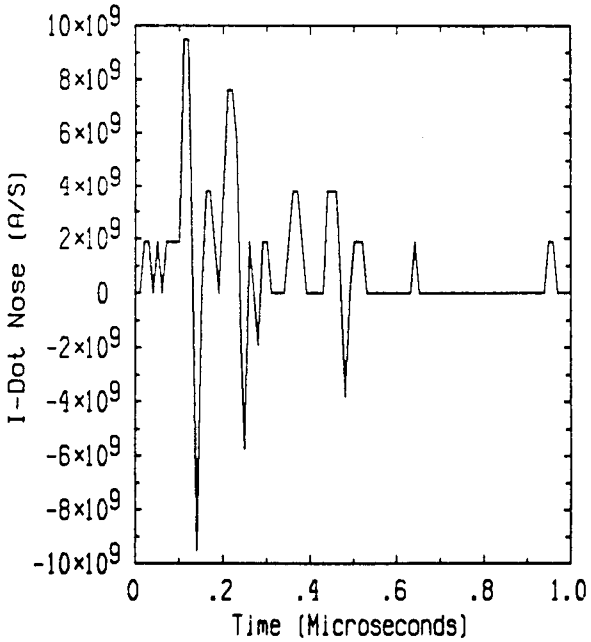

Figure 2.3(c) Measured I-dot Response for Flight 84-021 Run 001 Strike 001

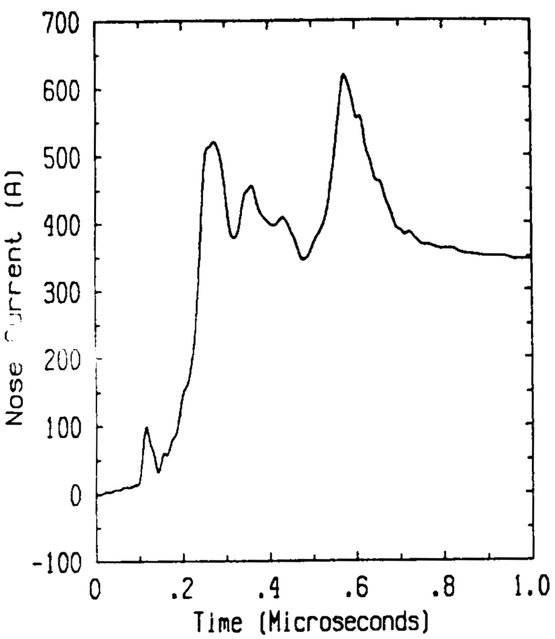

Figure 2.4(a) Calculated Nose Current After Filtering for Flight 84-023 Run 002 Strike 002

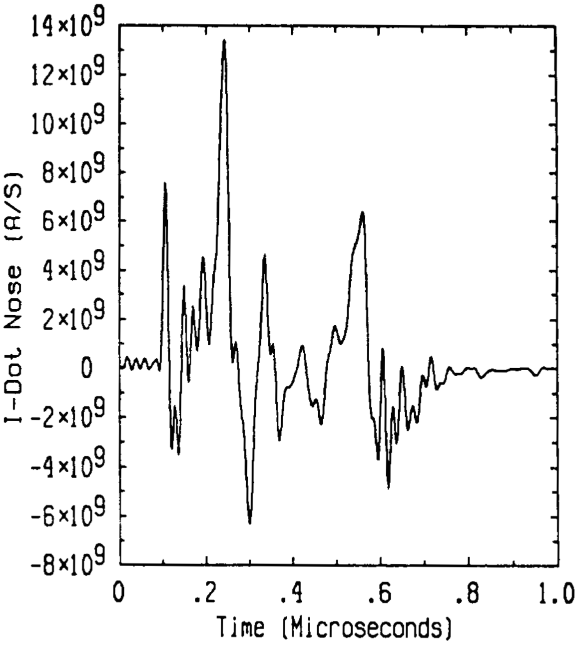

Figure 2.4(b) I-dot Response Obtained from Calculated Nose Current After Filtering for Flight 84-023 Run 002 Strike 002

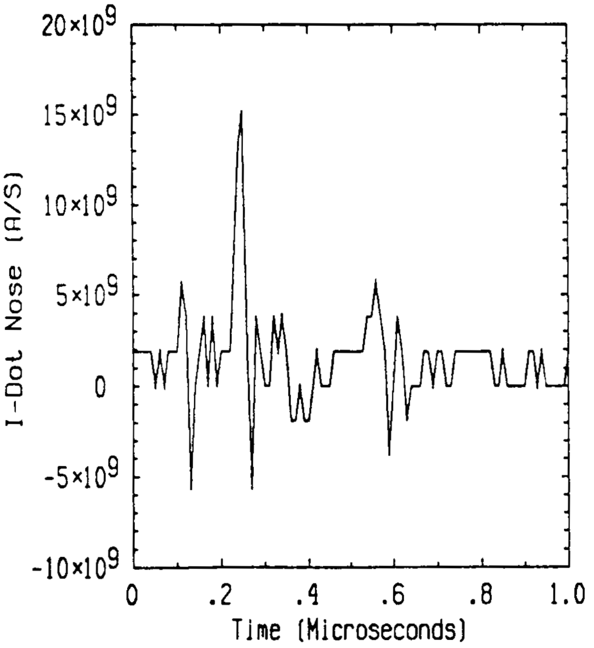

Figure 2.4(c) Measured I-dot Response for Flight 84-023 Run 002 Strike 002

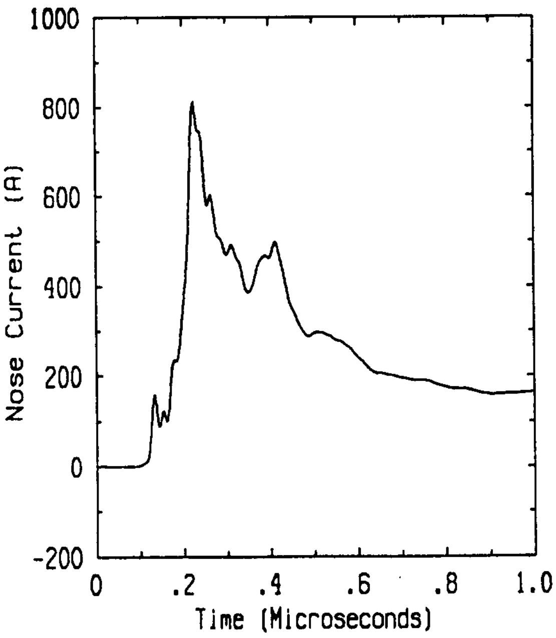

Figure 2.5(a) Calculated Nose Current After Filtering for Flight 84-017 Run 001 Strike 002

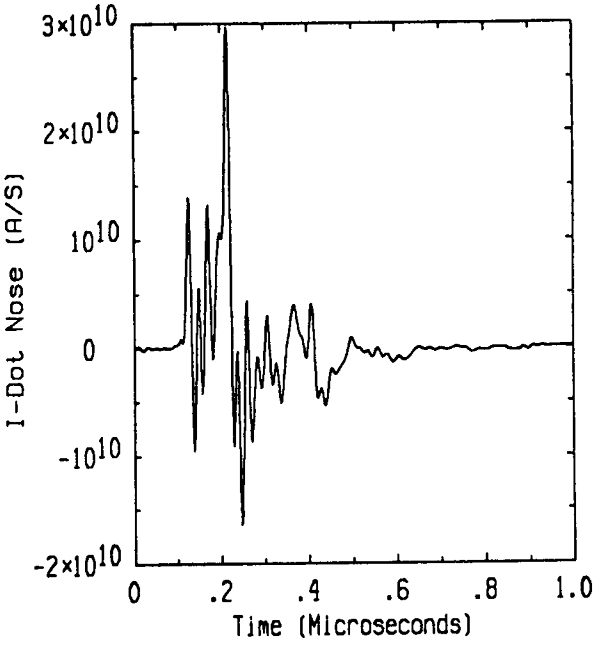

Figure 2.5(b) I-dot Response Obtained from Calculated Nose Current After Filtering for Flight 84-017 Run 001 Strike 002

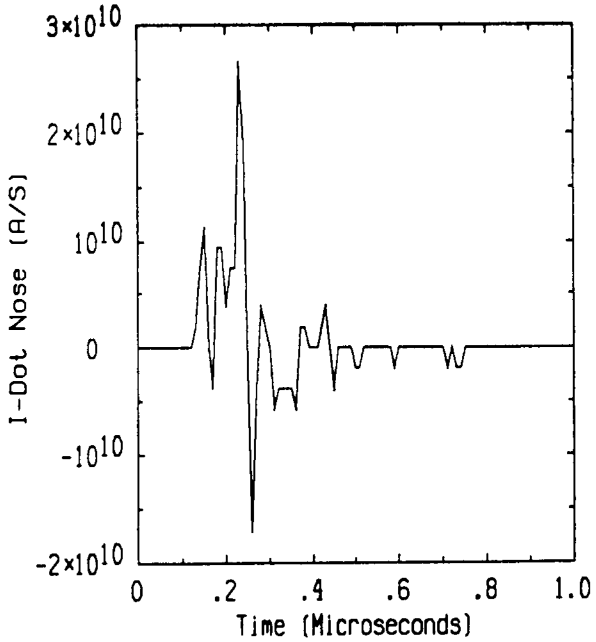

Figure 2.5(c) Measured I-dot Response for Flight 84-017 Run 001 Strike 002

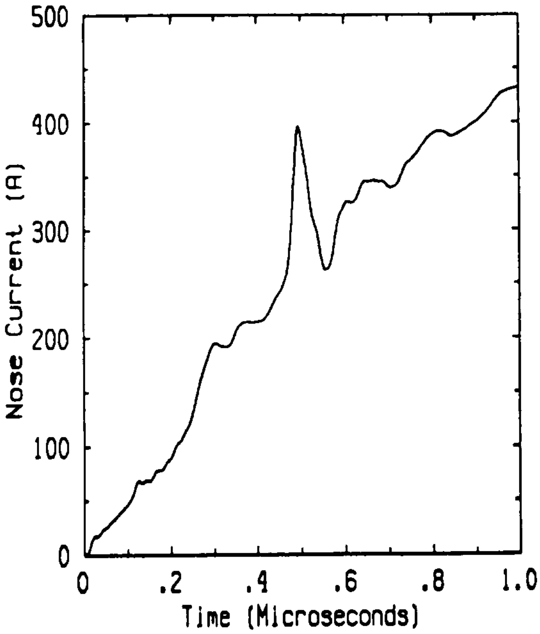

Figure 2.6(a) Calculated Nose Current After Filtering for Flight 84-025 Run 003 Strike 004

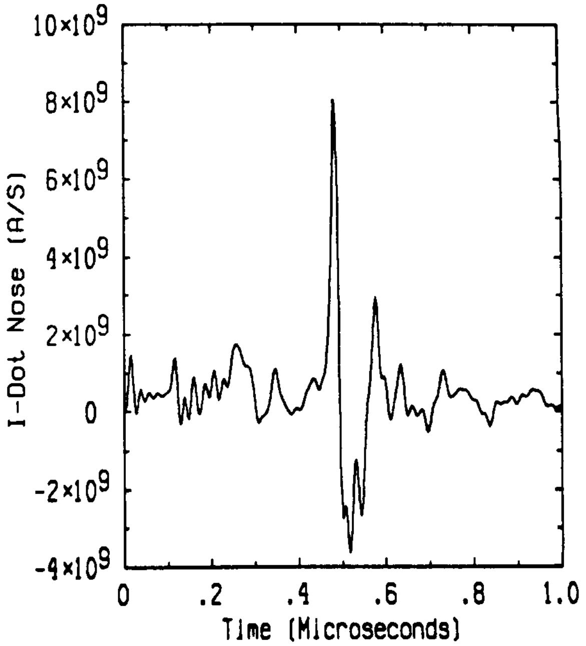

Figure 2.6(b) I-dot Response Obtained from Calculated Nose Current After Filtering for Flight 84-025 Run 003 Strike 004

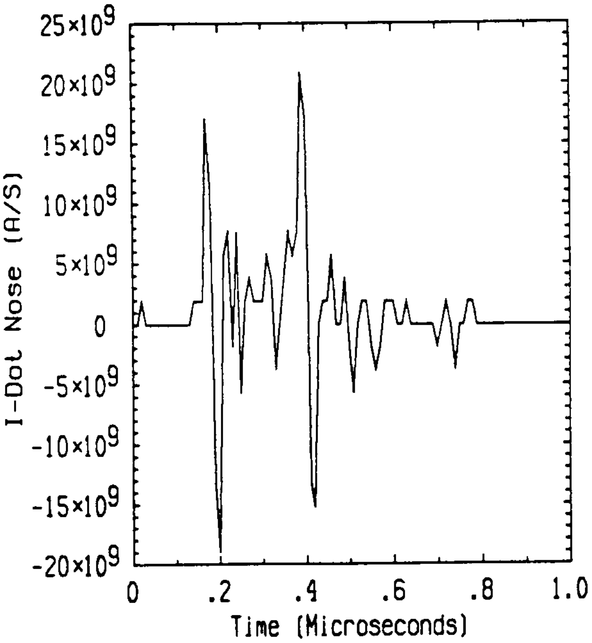

Figure 2.6(c) Measured I-dot Response for Flight 84-025 Run 003 Strike 004

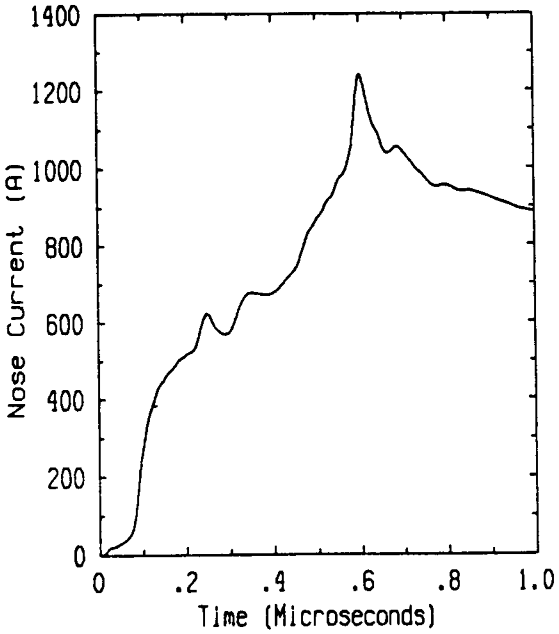

Figure 2.7(a) Calculated Nose Current After Filtering for Flight 84-025 Run 004 Strike 005

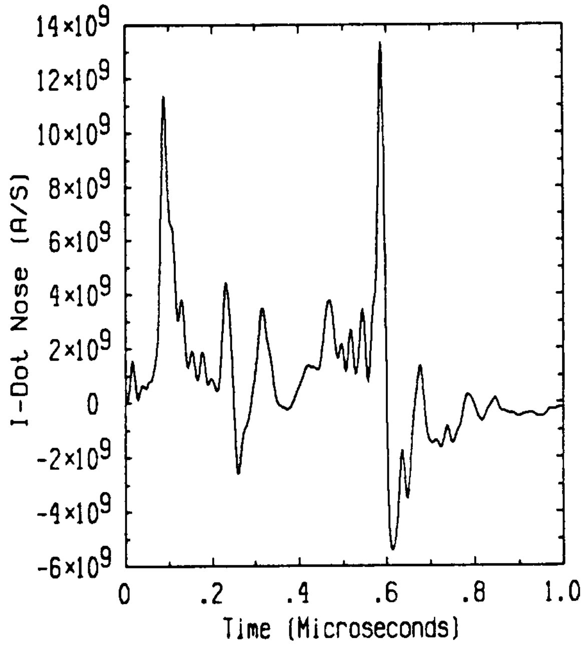

Figure 2.7(b) I-dot Response Obtained from Calculated Nose Current After Filtering for Flight 84-025 Run 004 Strike 005

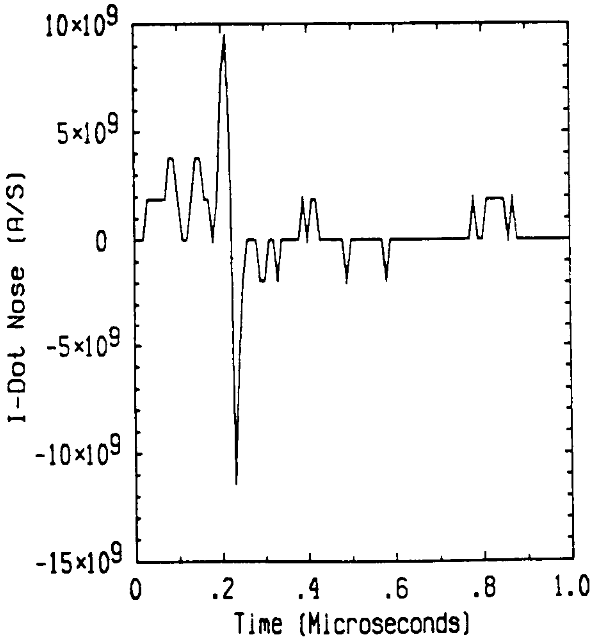

Figure 2.7(c) Measured I-dot Response for Flight 84-025 Run 004 Strike 005

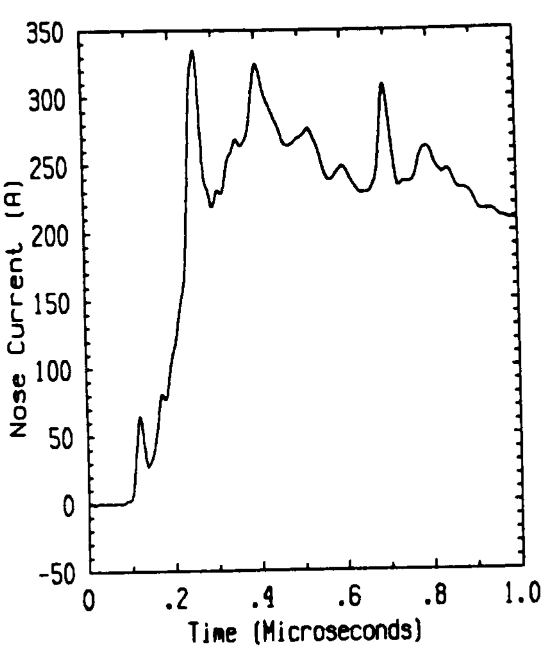

Figure 2.8(a) Calculated Nose Current After Filtering for Flight 84-025 Run 015 Strike 019

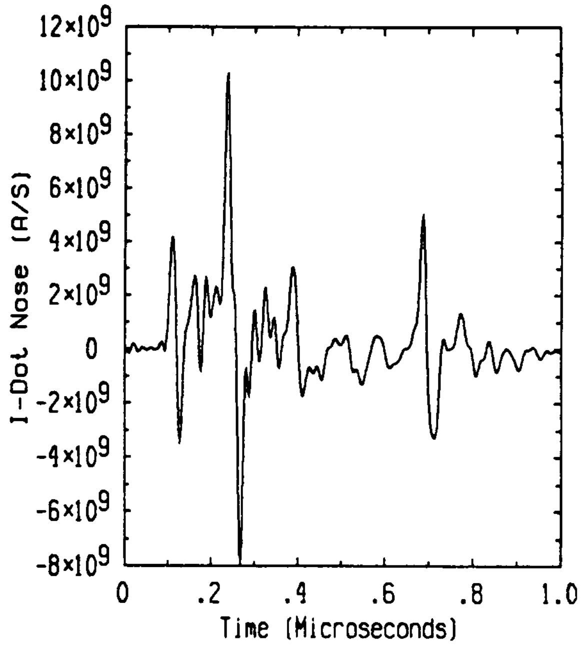

Figure 2.8(b) I-dot Response Obtained from Calculated Nose Current After Filtering for Flight 84-025 Run 015 Strike 019

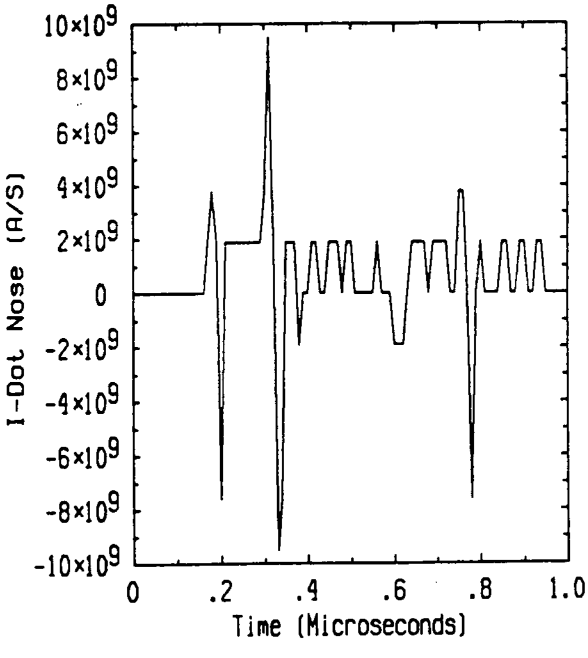

Figure 2.8(c) Measured I-dot Response for Flight 84-025 Run 015 Strike 019

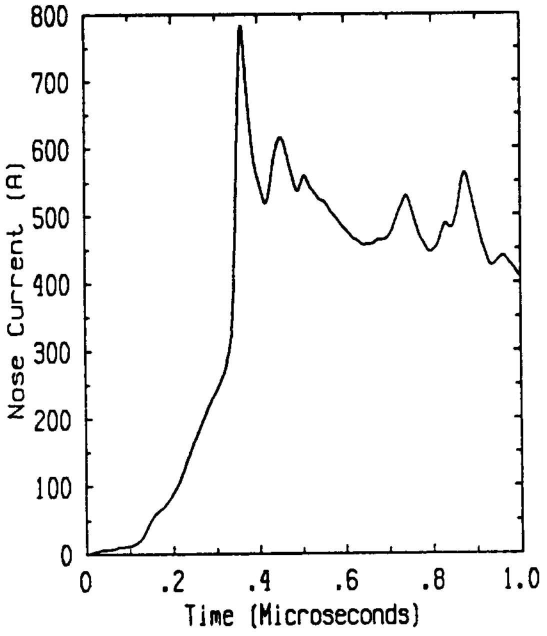

Figure 2.9(a) Calculated Nose Current After Filtering for Flight 84-024 Run 003 Strike 003

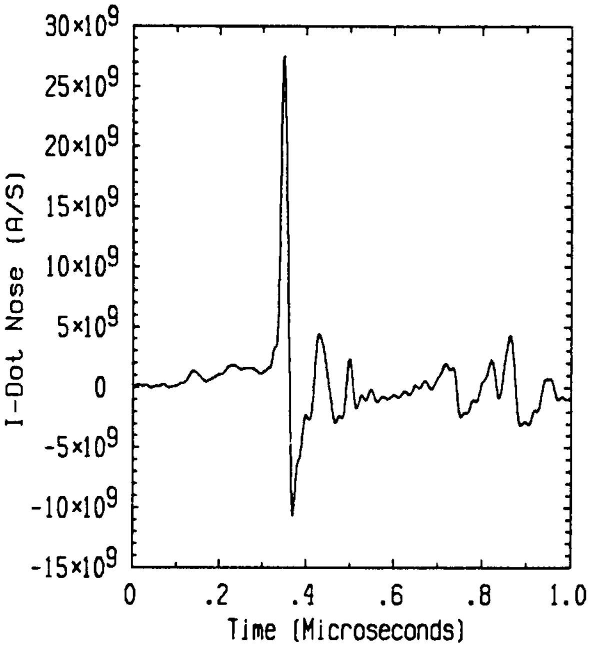

Figure 2.9(b) I-dot Response Obtained from Calculated Nose Current After Filtering for Flight 84-024 Run 003 Strike 003

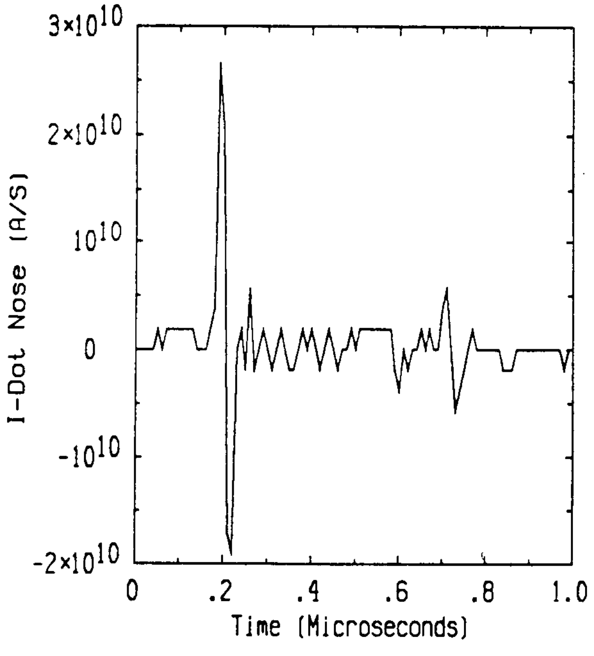

Figure 2.9(c) Measured I-dot Response for Flight 84-024 Run 003 Strike 003

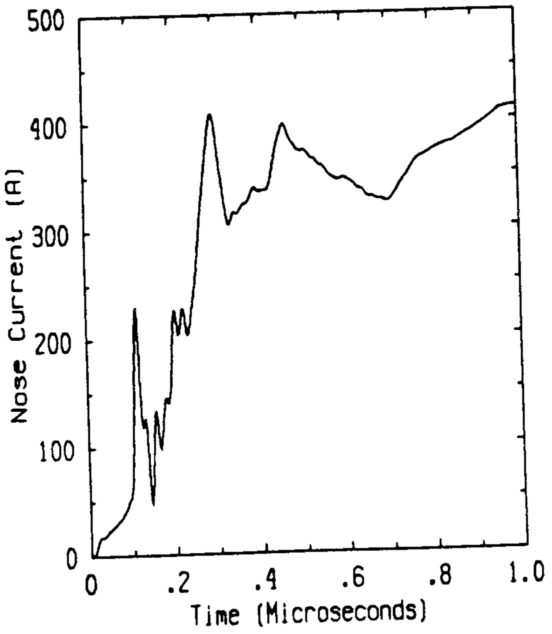

Figure 2.10(a) Calculated Nose Current After Filtering for Flight 84-027 Run 002 Strike 002

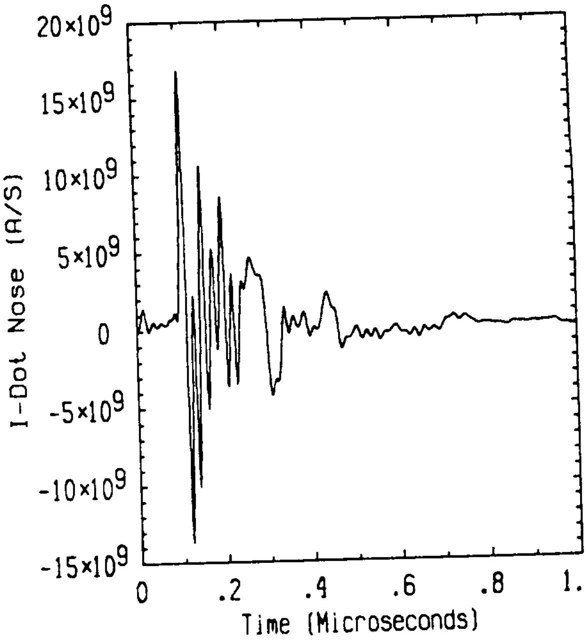

Figure 2.10(b) I-dot Response Obtained from Calculated Nose Current After Filtering for Flight 84-027 Run 002 Strike 002

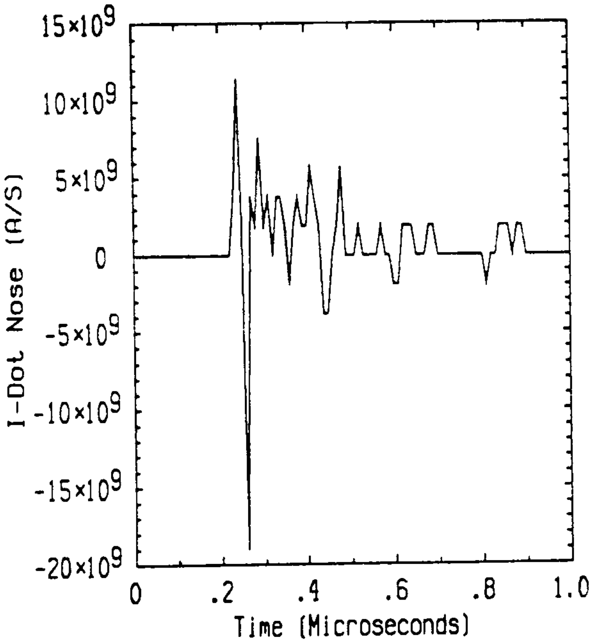

Figure 2.10(c) Measured I-dot Response for Flight 84-027 Run 002 Strike 002

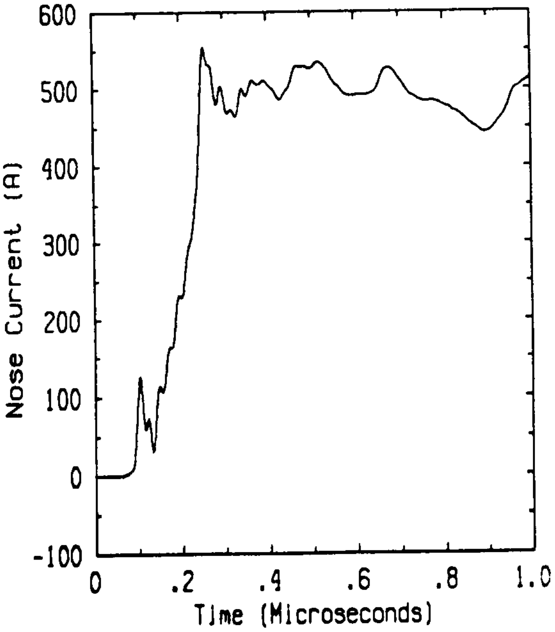

Figure 2.11(a) Calculated Nose Current After Filtering for Flight 84-028 Run 004 Strike 005

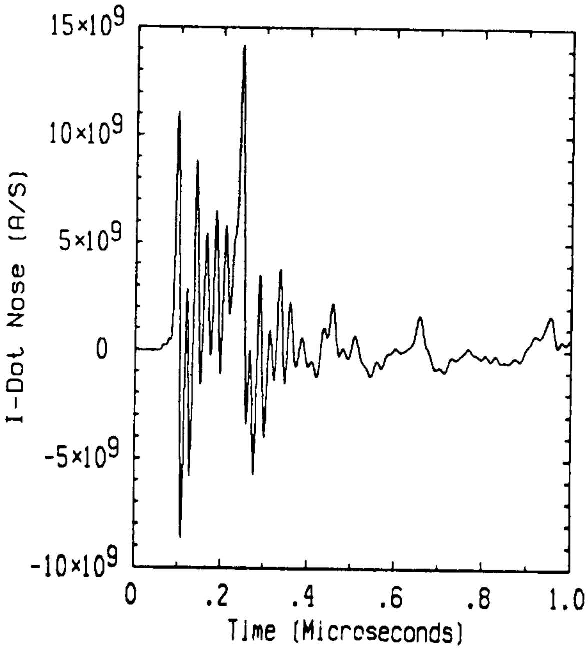

Figure 2.11(b) I-dot Response Obtained from Calculated Nose Current After Filtering for Flight 84-028 Run 004 Strike 005

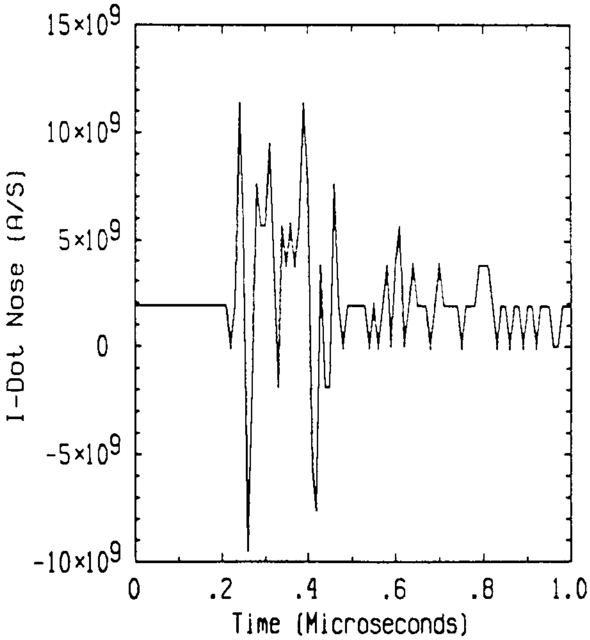

Figure 2.11(c) Measured I-dot Response for Flight 84-028 Run 004 Strike 005

2.3 Lightning Current Response Correlation Study

2.3.1 Method of Analysis

The strike characteristics developed from the 1984 data have been used to determine possible relationships between lightning current responses and the other sensor responses. The method of analysis used in this correlation study is detailed below.

The first step in the analysis of the 1984 characteristics was to produce scatter diagrams relating the characteristics of the lightning current and its time derivative to similar characteristics obtained from the external and internal responses. The diagrams, consisting of ordered pairs of sensor characteristics, allow a preliminary view of possible functional relationships existing between the two coordinates. The diagrams were produced from the available data and included an examination of the maximum, minimum, peak value and sensor peak width at half maximum characteristics. The plots were necessary to identify both the candidates and regions for possible correlation.

The next step involved the production of polynomial approximations for the most promising data sets. The least squares program designed for this purpose used a modified orthogonal decomposition algorithm using Householder Reflections [12] to obtain the polynomial approximations for degrees one through five that were used to study the behavior of the lightning data. In addition, the program contained the following statistical measures:

(i) A generalized correlation coefficient given by

$$\sqrt{\frac{\Sigma(y_{est}-y_m)^2}{\Sigma(y-y_m)^2}}$$

where y is a functional value obtained from the appropriate data set

y_{est} is the corresponding functional value obtained from the least squares curve

y_m is the mean functional value obtained from the appropriate data set.

(ii) A standard error of estimate given by

$$\sqrt{\frac{1}{m}\Sigma(y - y_{est})^2}$$

where m is the number of data points.

These values were used to help determine whether the data could be modeled by a lower order polynomial approximate (having the form $y = \sum_{J=0}^{N} a_J X^J$ for $N \leq 5$) and in evaluating the accuracy of the least squares curves as predictive tools.

In the final stage of analysis, plots were generated for the most useful correlations to determine the behavior of the least squares curves in the strongly correlated regions. The regions were the regions having the highest degree of correlation.

Also considered in the analysis was the fact that a higher order approximate might marginally improve the statistical characteristics of a system well served by a lower order curve. This was taken into consideration when the least squares results were examined.

2.3.2 Results of the Correlation Study

Using the method of analysis described in the previous section, several relationships were obtained based upon trends in the 1984 data. These relationships represent the strongest indications of possible connections between the aircraft response characteristics considered in this study.

The best correlations found between the lightning current response data and the remaining sensor response data resulted when the I-dot peak values were compared to the peak values from some of the external sensors. The restricted ranges of the response characteristics used to obtain these relationships are given in Table

2.1. The distribution of the data and the consideration of reasonable sensor responses were the primary factors used to determine these regions.

TABLE 2.1
Restricted Peak Value Ranges

Sensor	Peak Value Range
I-dot	5×10^9 A/S $\leq |\dot{I}| \leq 3 \times 10^{10}$ A/S
B-dot Longitudinal	1×10^2 T/S $\leq |\dot{B}_L| \leq 1.8 \times 10^3$ T/S
D-dot Forward	2 A/sq.m $\leq |\dot{D}_F| \leq 13$ A/sq.m
B-dot Right Wing	1×10^2 T/S $\leq |\dot{B}_{RW}| \leq 7 \times 10^2$ T/S
B-dot Left Wing	1×10^2 T/S $\leq |\dot{B}_{LW}| \leq 7 \times 10^2$ T/S

Restricing the ranges of the sensor response characteristics was a necessary part of the analysis because it was determined that many of the response pairs appeared to be inconsistent if they appeared outside these regions. For example, it was possible in certain instances to obtain an abnormally low $\dot{B}$ and $\dot{D}$ sensor peak value (in terms of absolute value) for a particular strike which was paired with a relatively high $\dot{I}$ peak value. This type of behavior played an important role in selecting these regions.

The scatter diagrams for the restricted data sets showing the highest degree of correlation appear in Figures 2.12 - 2.19. As these plots indicate, the data of interest was divided into two categories (producing two distinct scatter diagrams) based upon the signs of the appropriate sensor characteristics. This division was required so that a functional relationship could be developed between the peak value pairs. The plots also clearly indicate a spread in the data which will have the effect of limiting the use of the developed correlations.

Although many factors were considered in deciding which data sets represented the strongest trends, the correlation coefficient described above was used as a general guide in the selection process. All of the sets shown in Figures 2.12 - 2.19

(text continued on page 31)

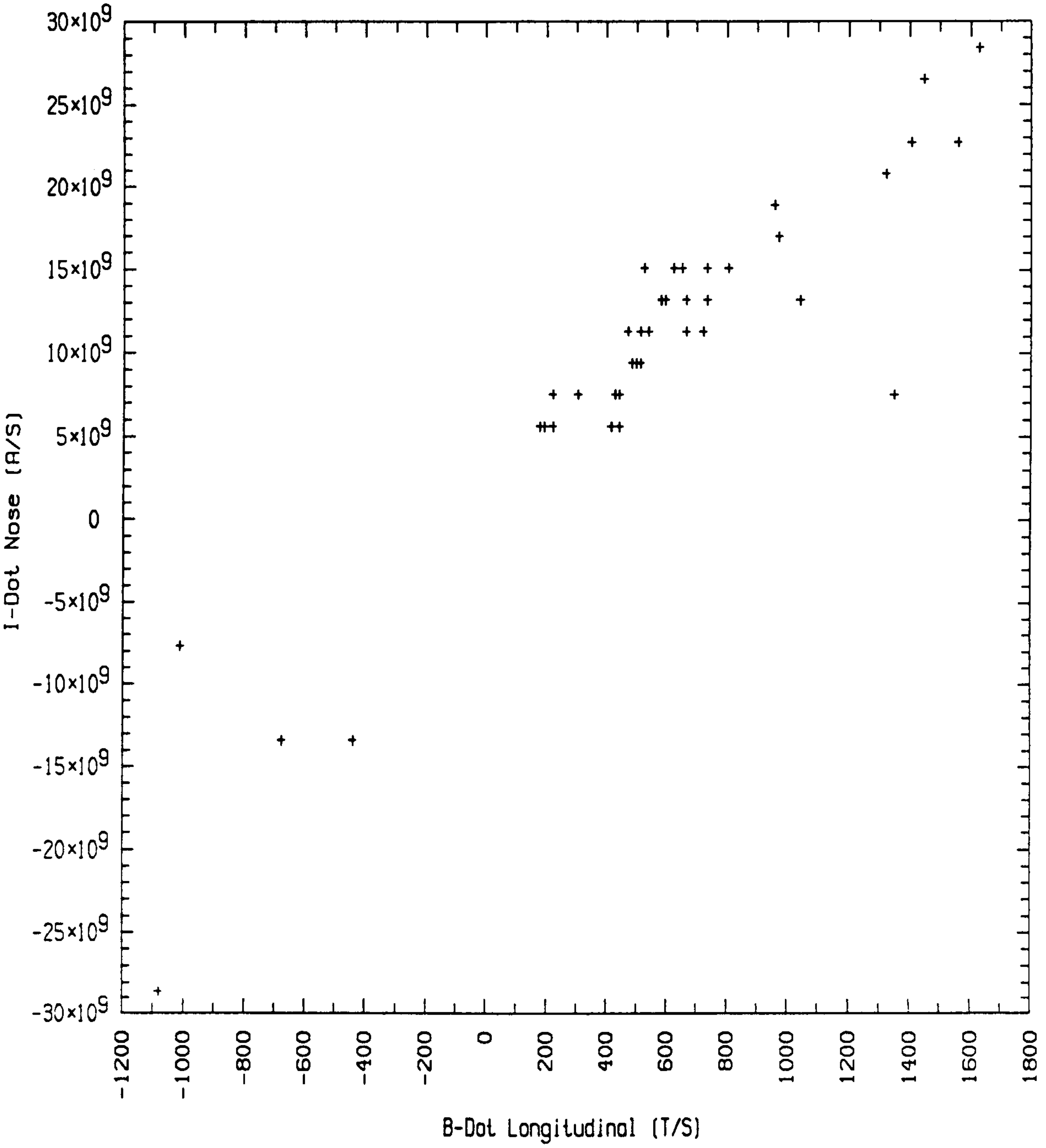

Figure 2.12 Restricted Peak Value Scatter Diagram 1 Derived from 1984 Measured I-dot and B-dot Longitudinal Response Data

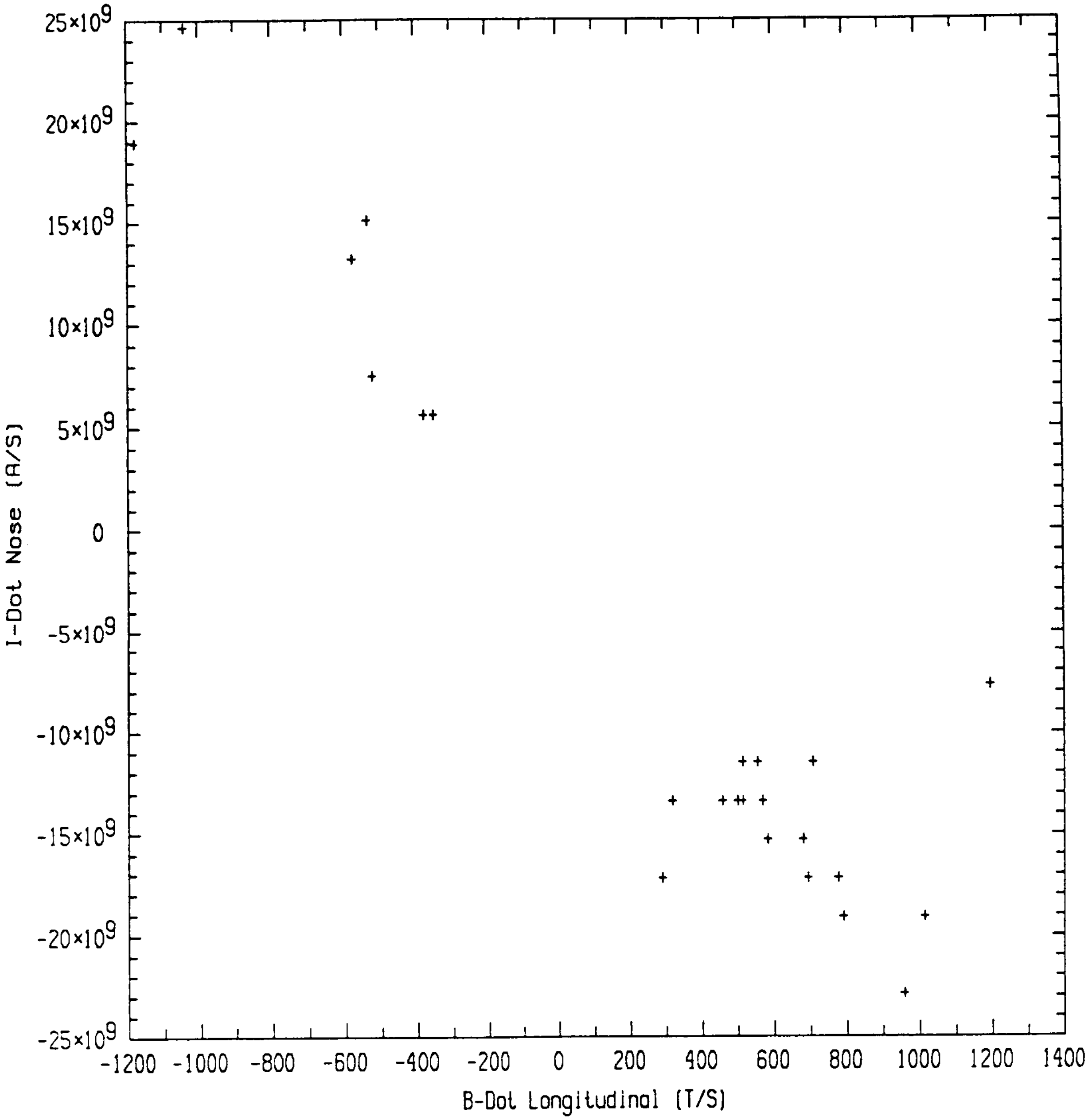

Figure 2.13 **Restricted Peak Value Scatter Diagram 2 Derived from 1984 Measured I-dot and B-dot Longitudinal Response Data**

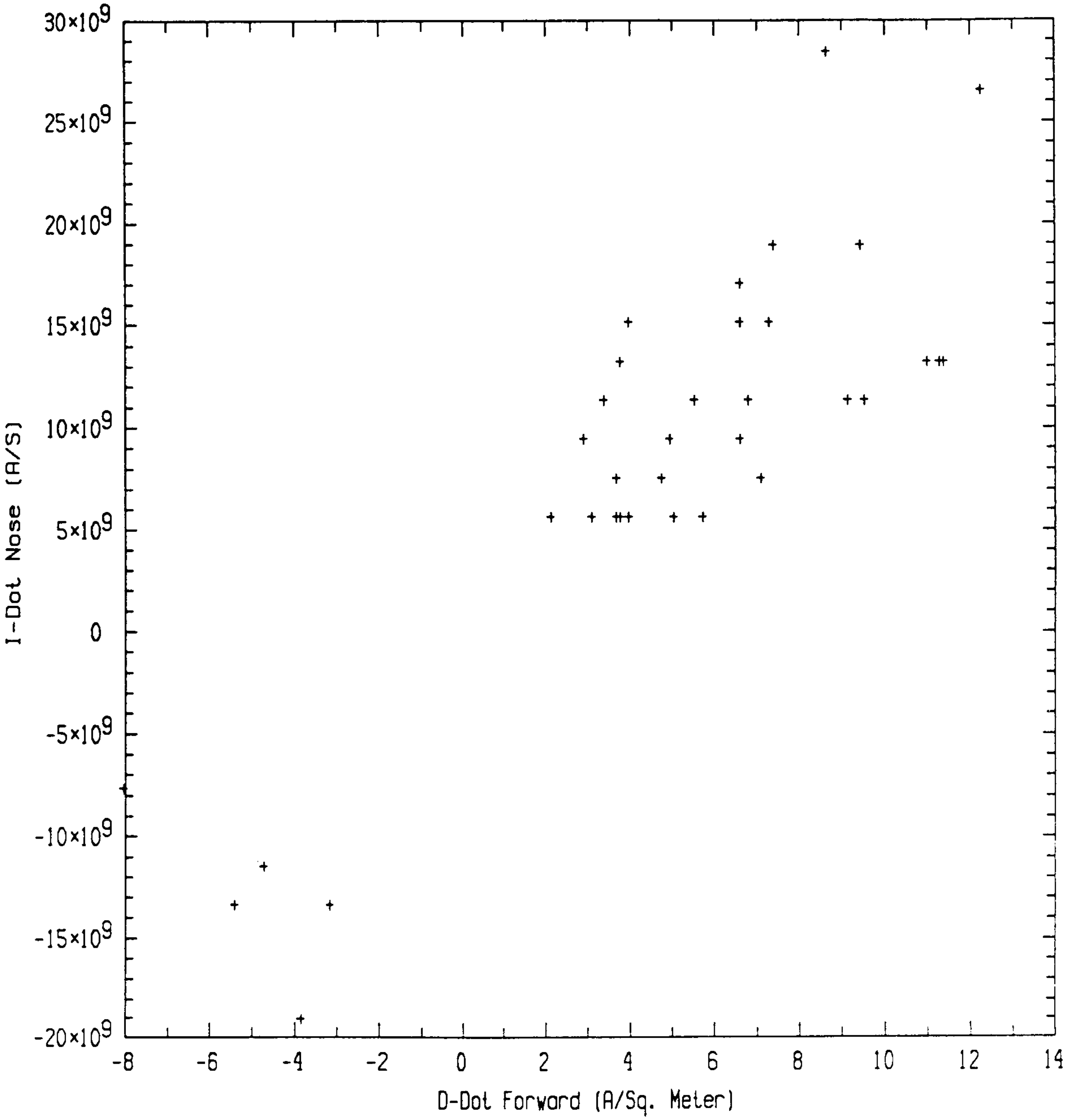

Figure 2.14 Restricted Peak Value Scatter Diagram 3 Derived from 1984 Measured I-dot and D-dot Forward Response Data

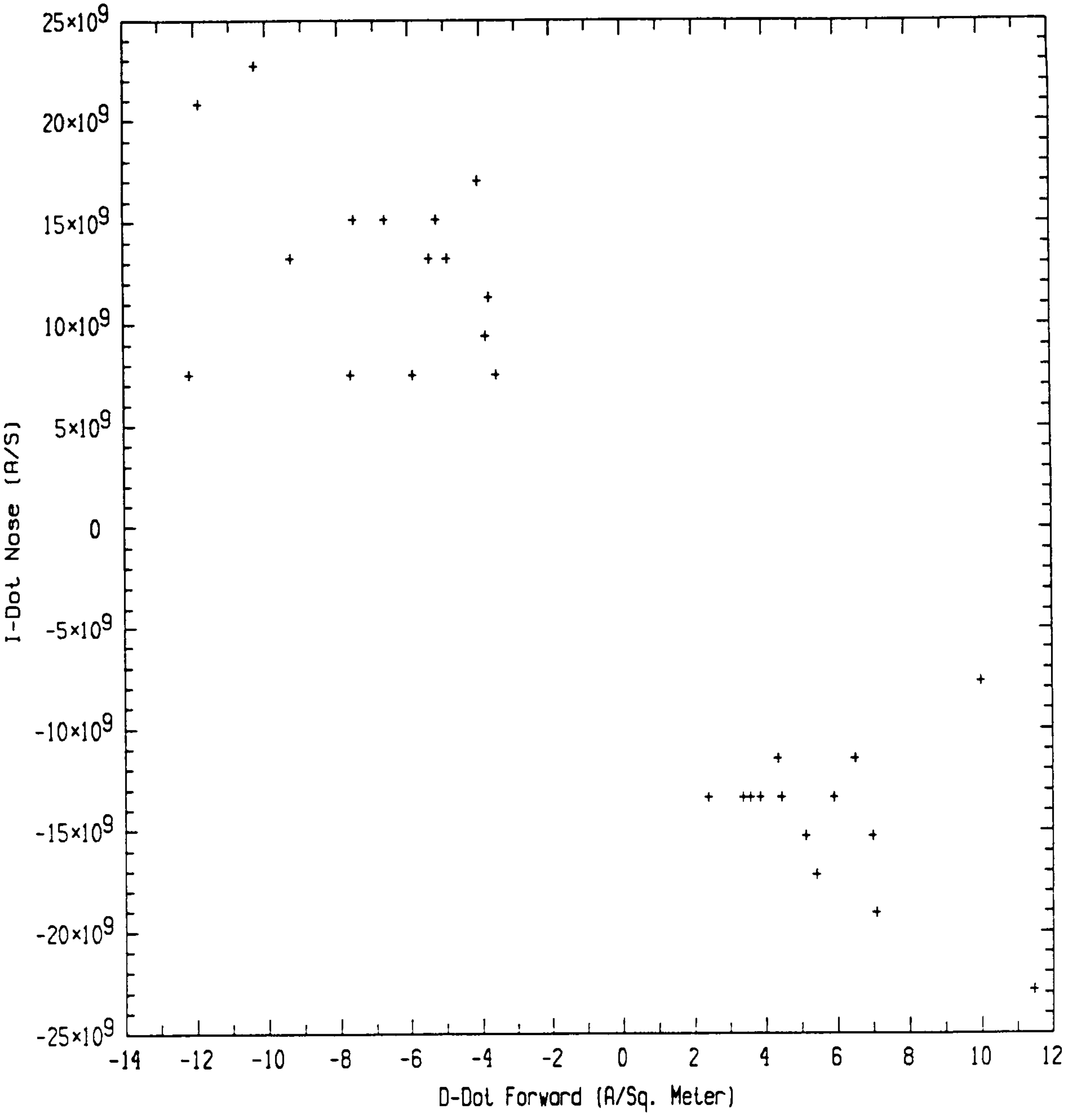

Figure 2.15 Restricted Peak Value Scatter Diagram 4 Derived from 1984 Measured I-dot and D-dot Forward Response Data

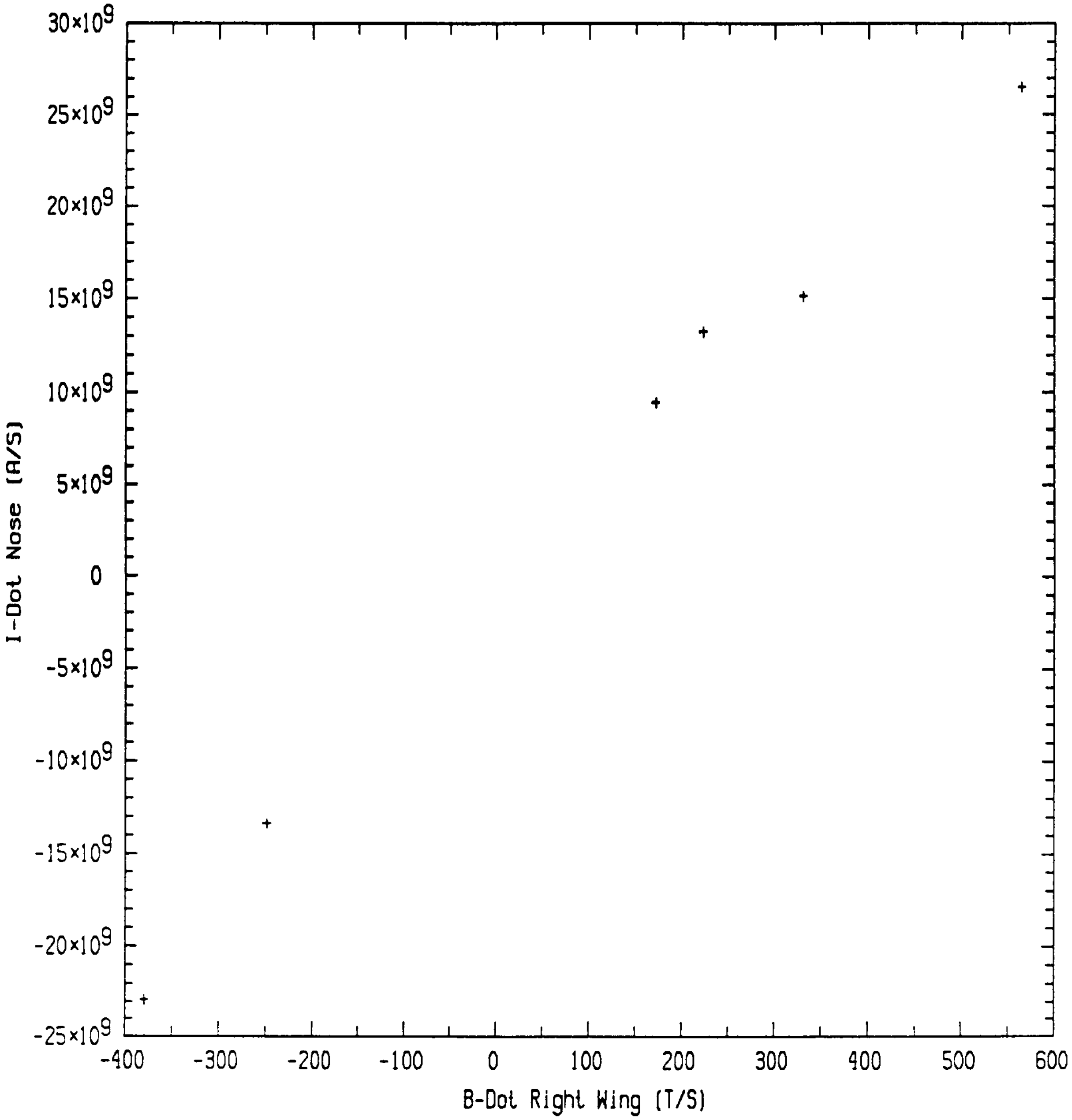

Figure 2.16 Restricted Peak Value Scatter Diagram 5 Derived from 1984 Measured I-dot and B-dot Right Wing Response Data

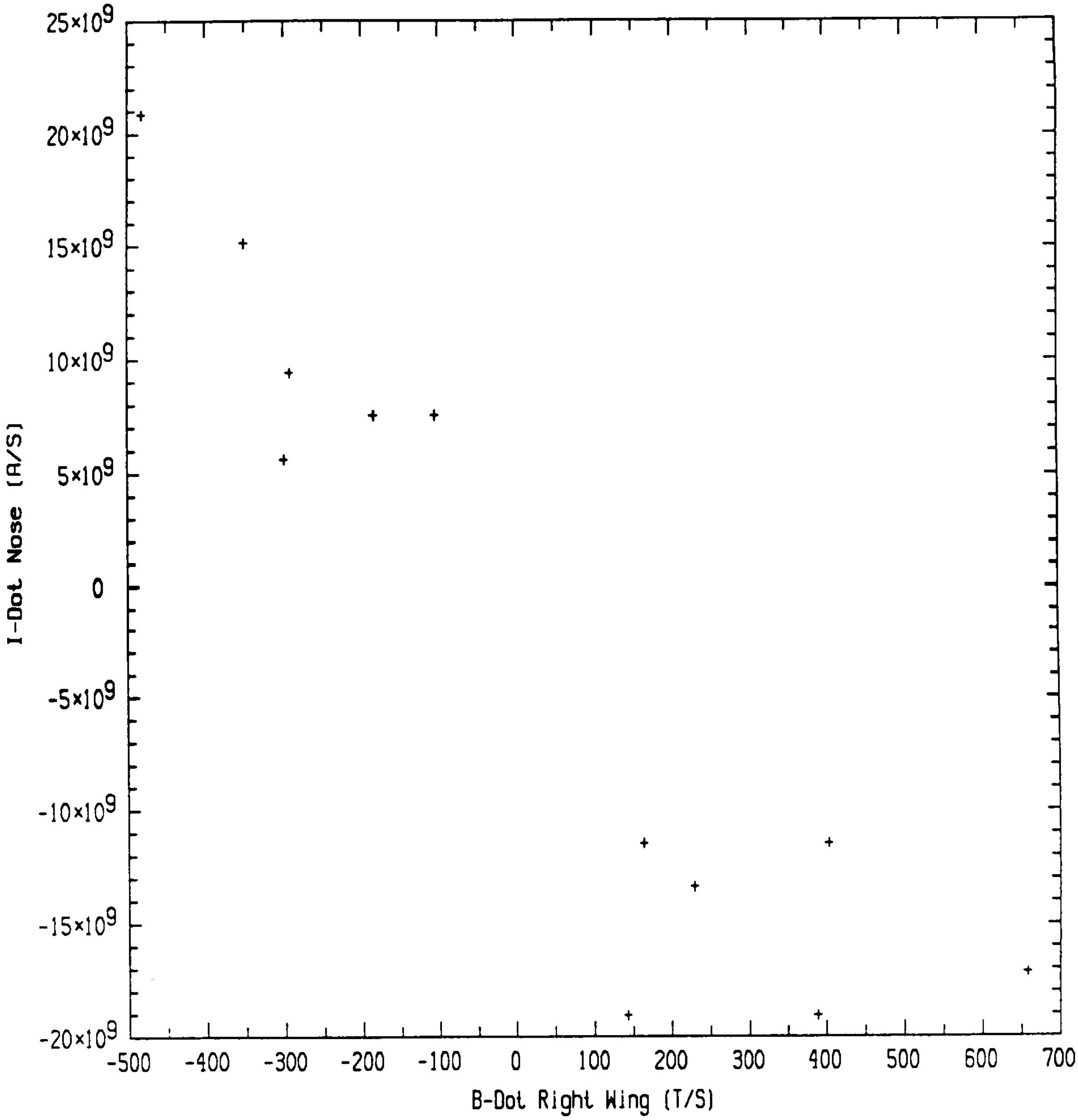

Figure 2.17 **Restricted Peak Value Scatter Diagram 6 Derived from 1984 Measured I-dot and B-dot Right Wing Response Data**

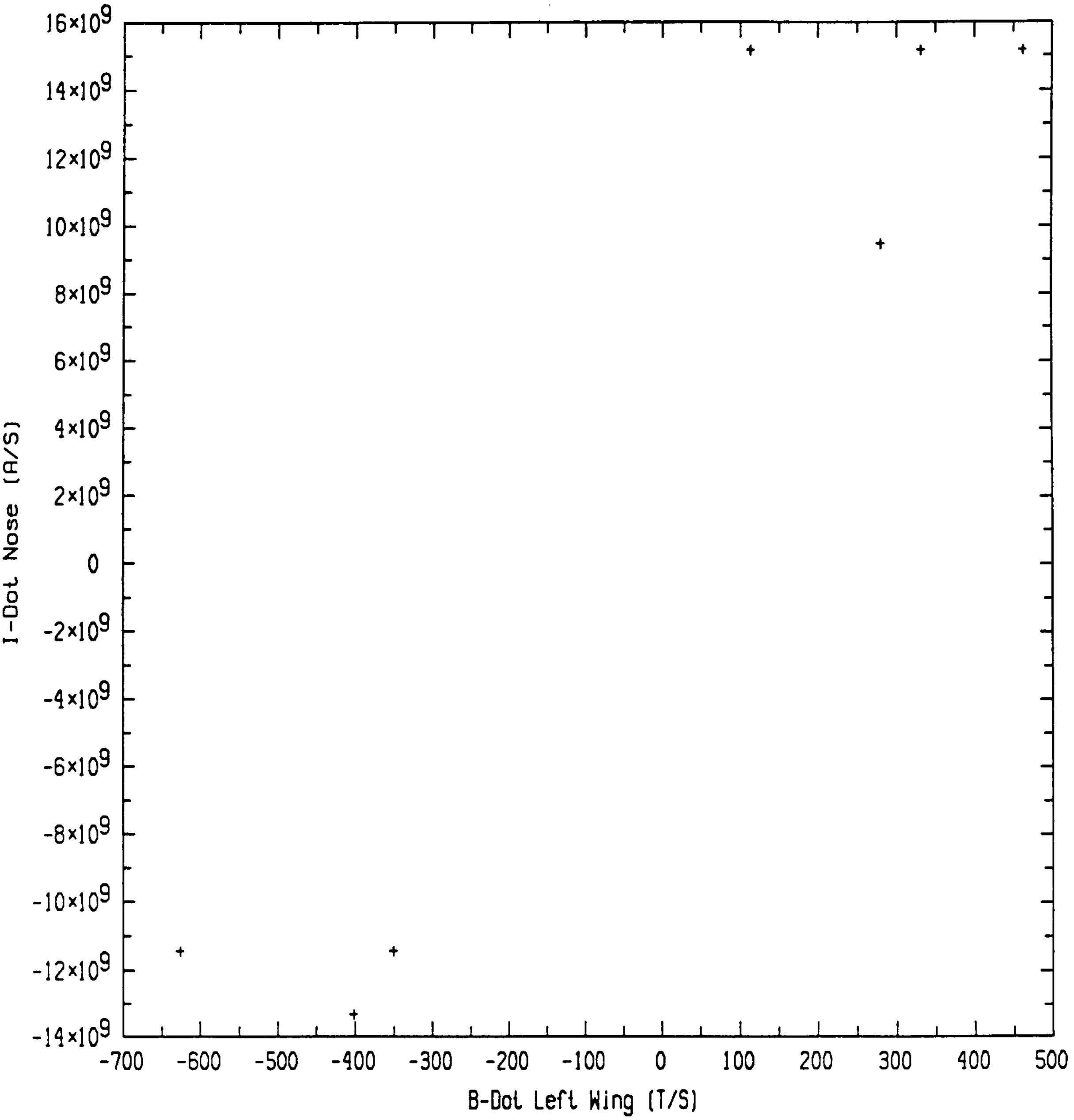

Figure 2.18 Restricted Peak Value Scatter Diagram 7 Derived from 1984 Measured I-dot and B-dot Left Wing Response Data

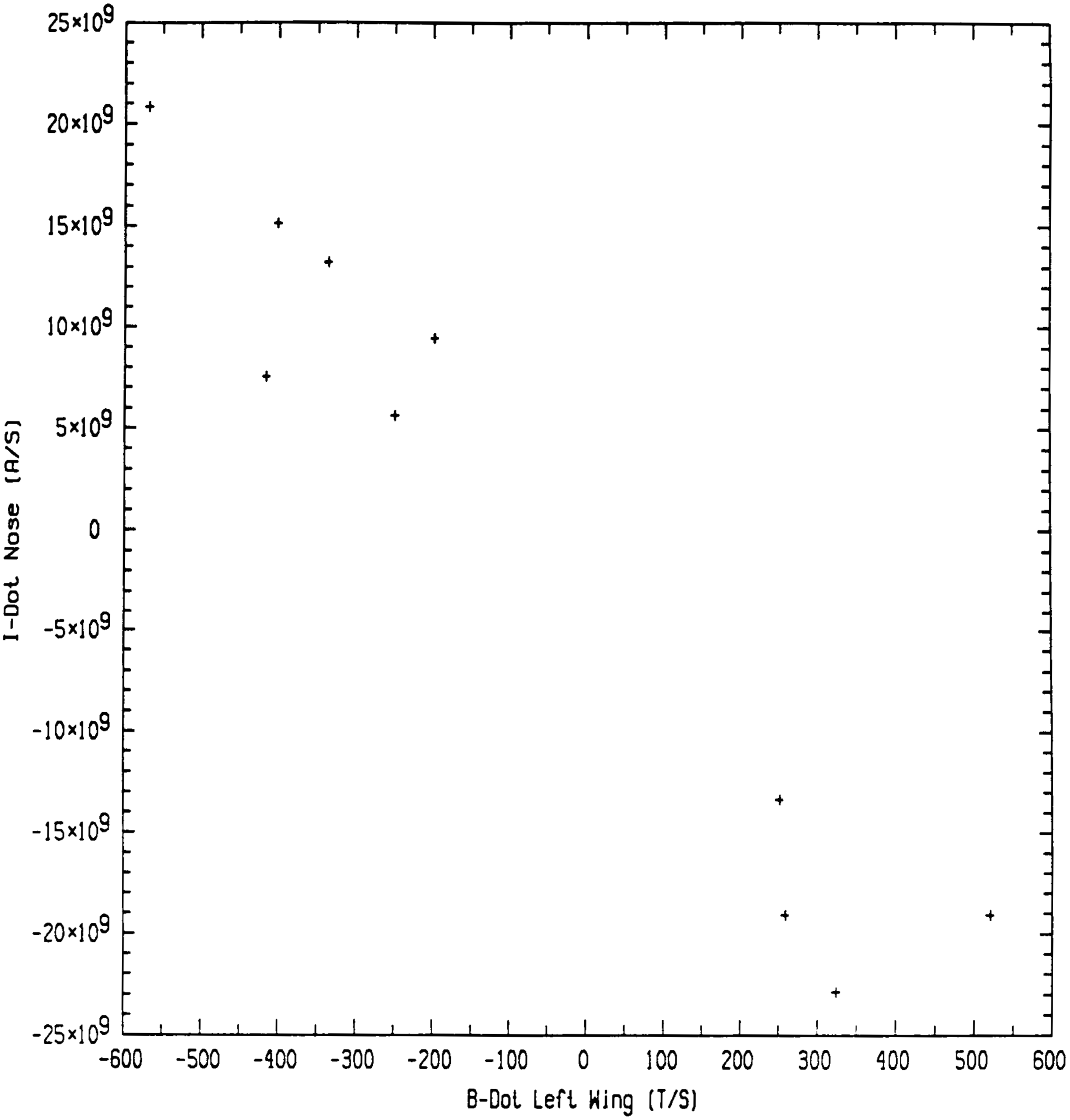

Figure 2.19 Restricted Peak Value Scatter Diagram 8 Derived from 1984 Measured I-dot and B-dot Left Wing Response Data

had correlation coefficients that reflected an explained variation percentage of roughly 75% or better (this percentage may be obtained easily by simply expressing the square of the correlation coefficient as a percentage.) This means that the majority of the total variation can be attributed to the least squares curves.

The corresponding polynomial approximates for these data sets appear in Figures 2.20 - 2.27. The differences in the approximates are in part due to the adjustment of the higher order approximates to data sets with an inherent spread. Differences showing up on the ends of the correlation region are in part due to the fact that data was not statistically removed during the correlation procedure. Features such as the departure from monotonic behavior and the more pronounced spreading of the curves often witnessed at the extremes of the correlation region are largely due to the inclusion of certain data points. The removal of these points would alter the correlations significantly in these regions. Finally, it should be noted that the smaller number of points available for the B-dot sensors on the wings of the F106B affected the higher order approximates in certain cases by turning the approximation problem into very nearly an interpolation problem. The affected curves for these cases would have a tendency to more closely follow the points rather than follow any general trend that may be indicated.

If these factors are taken into consideration, it appears that the plots indicate certain trends in the data. The most significant correlations in this set are the ones relating the I-dot peak values to the peak values of the B-dot longitudinal and D-dot forward sensors. More data was available for these sensors than for the remaining B-dot sensors in the set. These latter sensors were included in the figures because they correlated extremely well to the I-dot data. The fact that only a small number of data points were available did not greatly alter this view.

An examination of the data produced from this analysis indicates that the particular data sets under consideration can be adequately modeled using a first or second degree polynomial. Figures 2.28 - 2.35 show these least squares estimates. Although there were some higher order nonlinear data tendencies, the data residing in the restricted regions used for this analysis exhibited primarily lower order behavior. Much of the higher order behavior in this set is undoubtedly due to an effort on the part of the least squares curves to account for some of the data points mentioned above. In

(text continued on page 48)

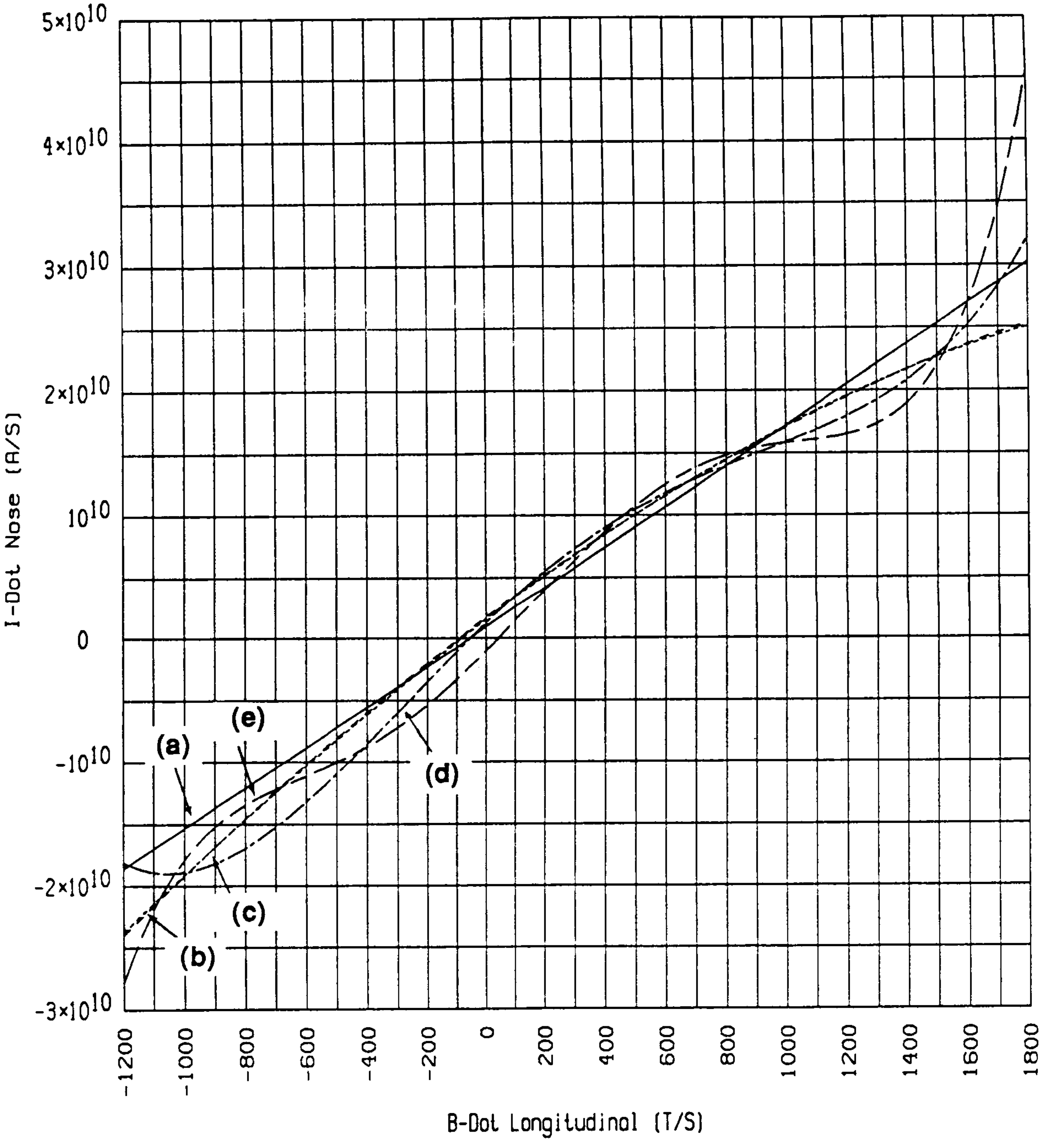

Figure 2.20 Polynomial Approximations Calculated from 1984 Measured I-dot and B-dot Longitudinal Peak Values

(a) ——— Linear
(b) - - - - - - - Quadratic
(c) ------------ Third Degree
(d) —·—·— Fourth Degree
(e) — — — — Fifth Degree

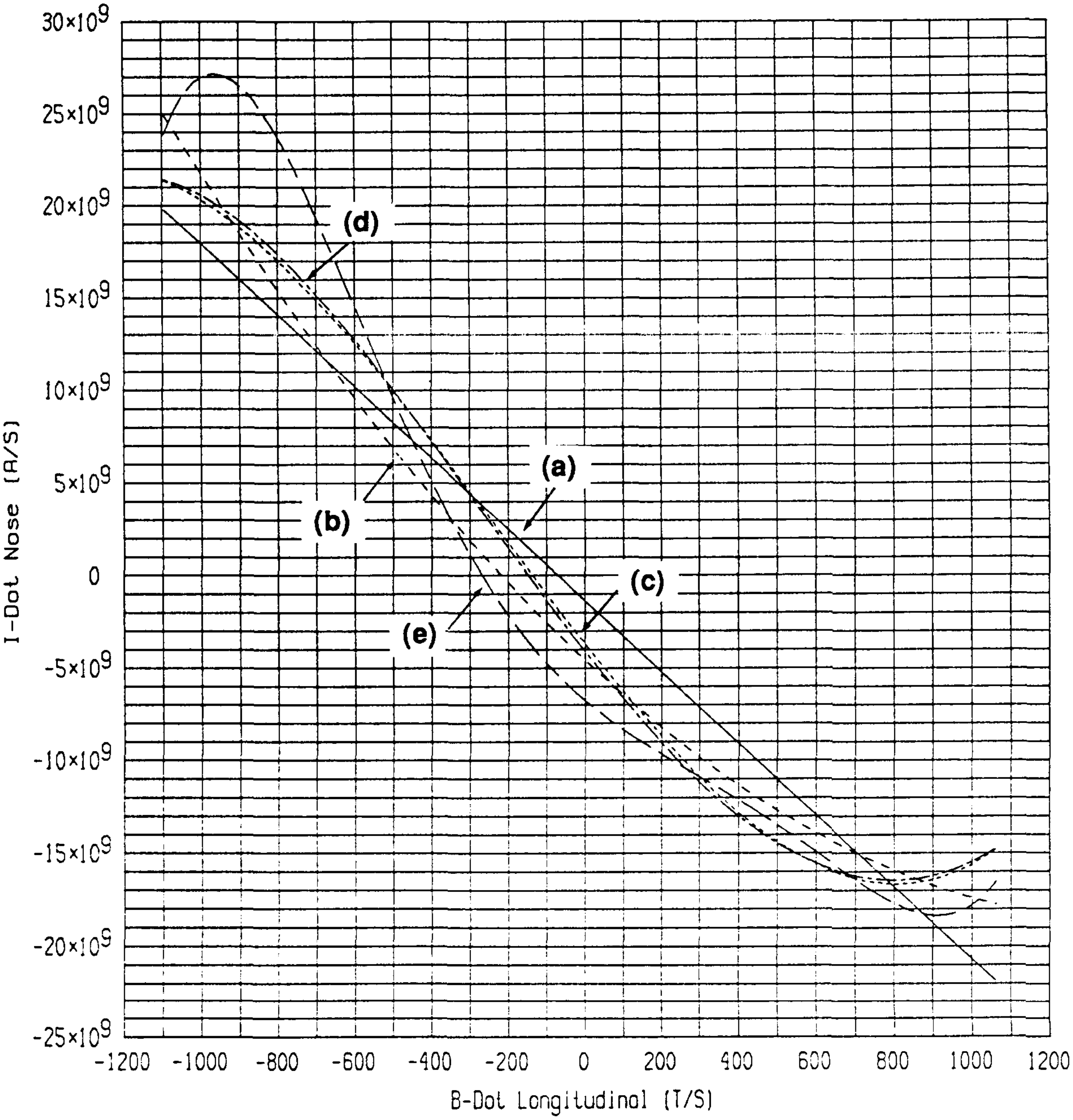

Polynomial Approximations for Restricted 1984 Measured Peak Values

Figure 2.21 **Polynomial Approximations Calculated from 1984 Measured I-dot and B-dot Longitudinal Peak Values**

(a) ——— Linear
(b) - - - - - - - Quadratic
(c) ------------ Third Degree
(d) —-—-— Fourth Degree
(e) — — — — Fifth Degree

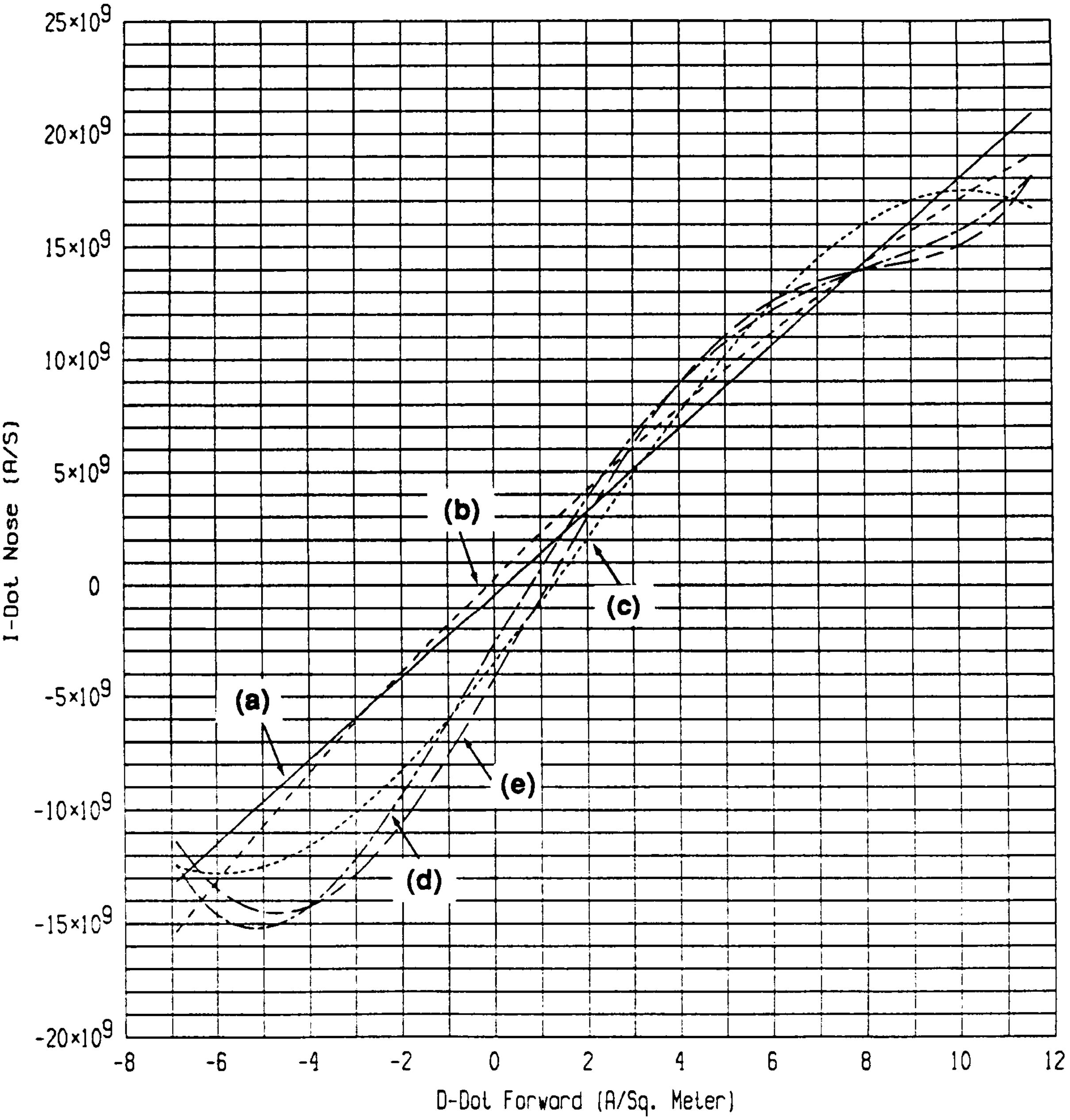

Figure 2.22 Polynomial Approximations Calculated from 1984 Measured I-dot and D-dot Forward Peak Values

(a)	———	Linear
(b)	- - - - - - -	Quadratic
(c)	------------	Third Degree
(d)	—·—·—	Fourth Degree
(e)	— — — —	Fifth Degree

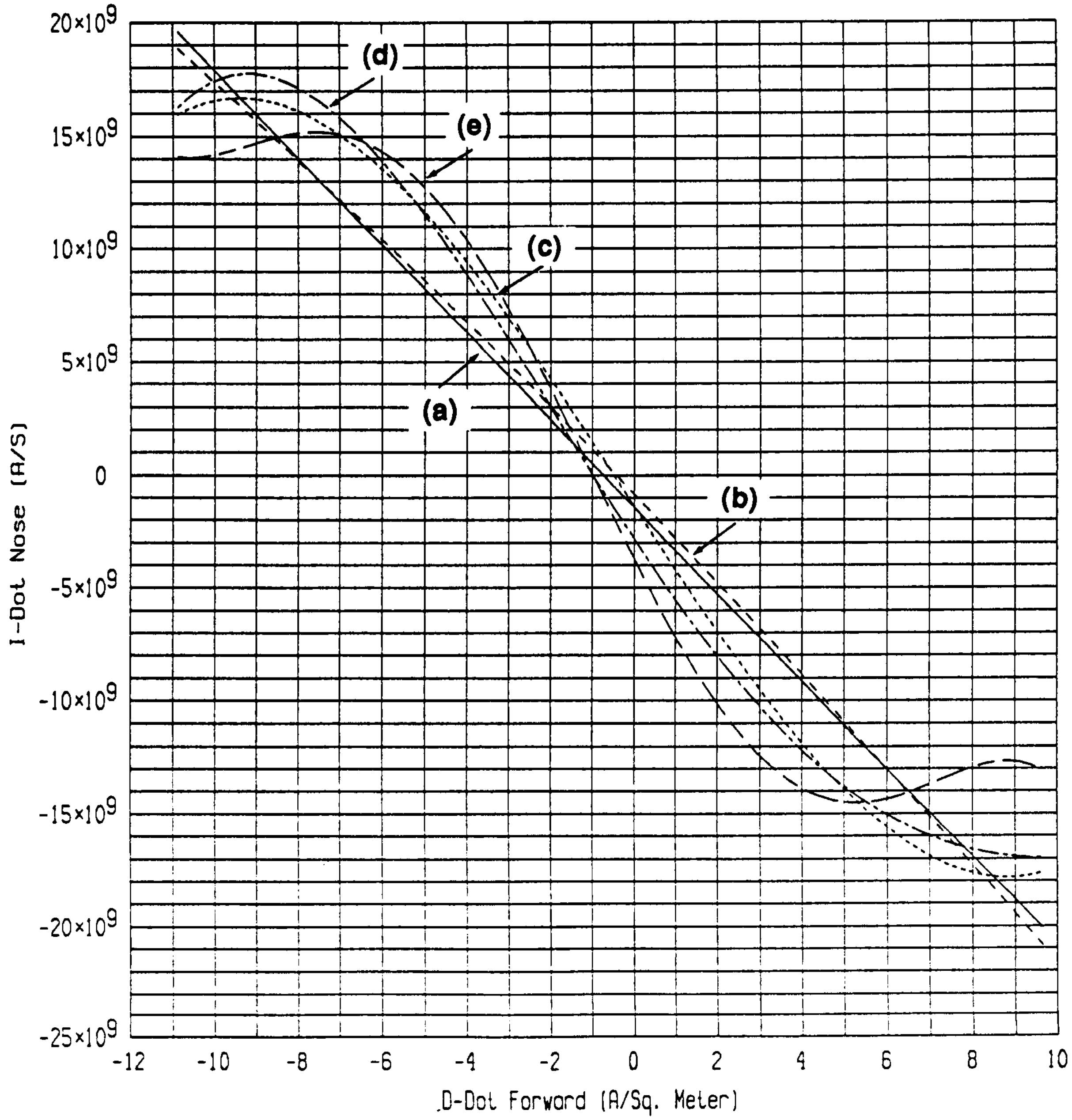

Figure 2.23 Polynomial Approximations Calculated from 1984 Measured I-dot and D-dot Forward Peak Values

(a) ——— Linear
(b) - - - - - - - Quadratic
(c) ------------ Third Degree
(d) —-—-— Fourth Degree
(e) — — — — Fifth Degree

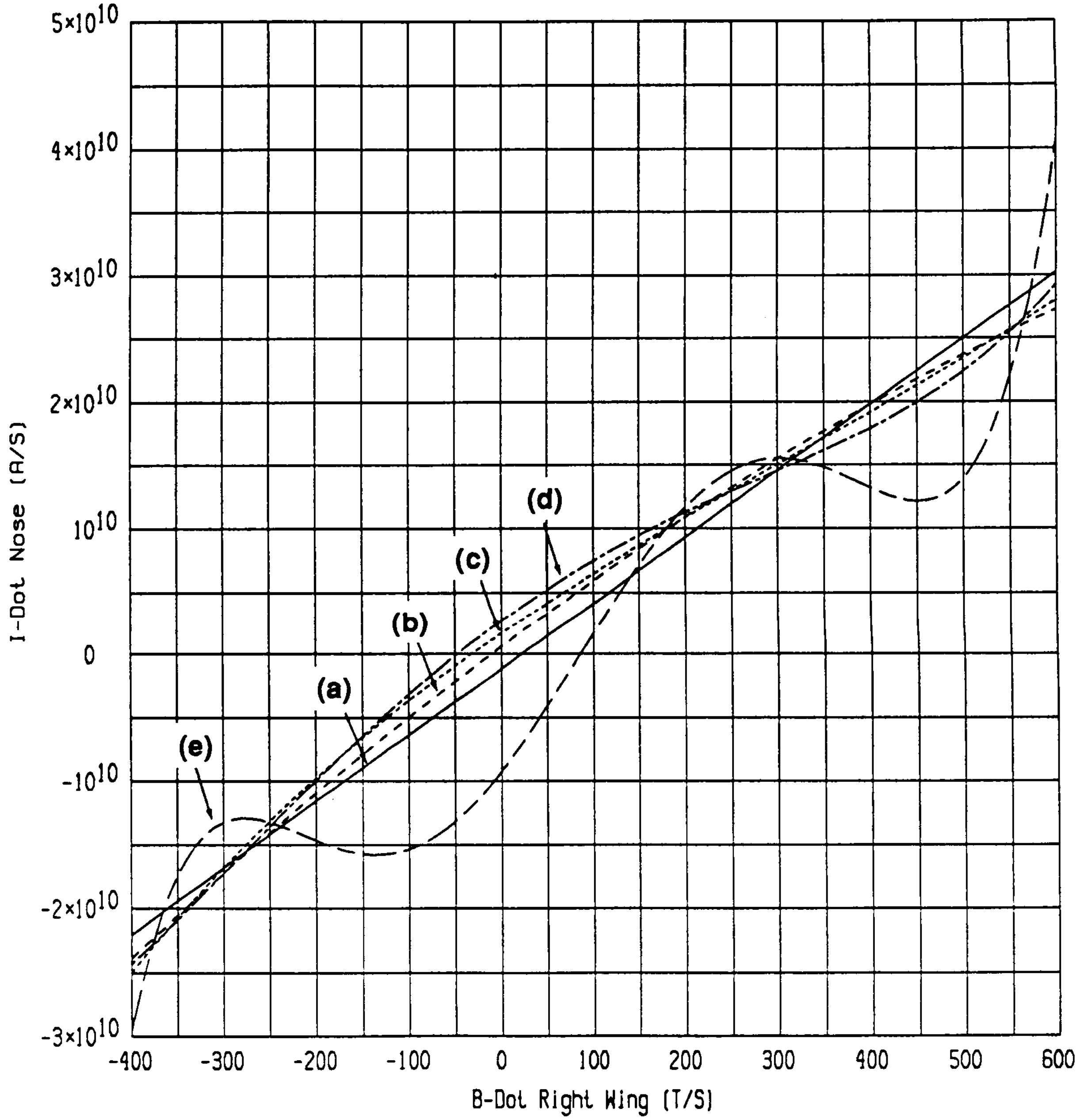

Figure 2.24 Polynomial Approximations Calculated from 1984 Measured I-dot and B-dot Right Wing Peak Values

(a) ———— Linear
(b) - - - - - - - Quadratic
(c) ------------- Third Degree
(d) —·—·— Fourth Degree
(e) — — — — Fifth Degree

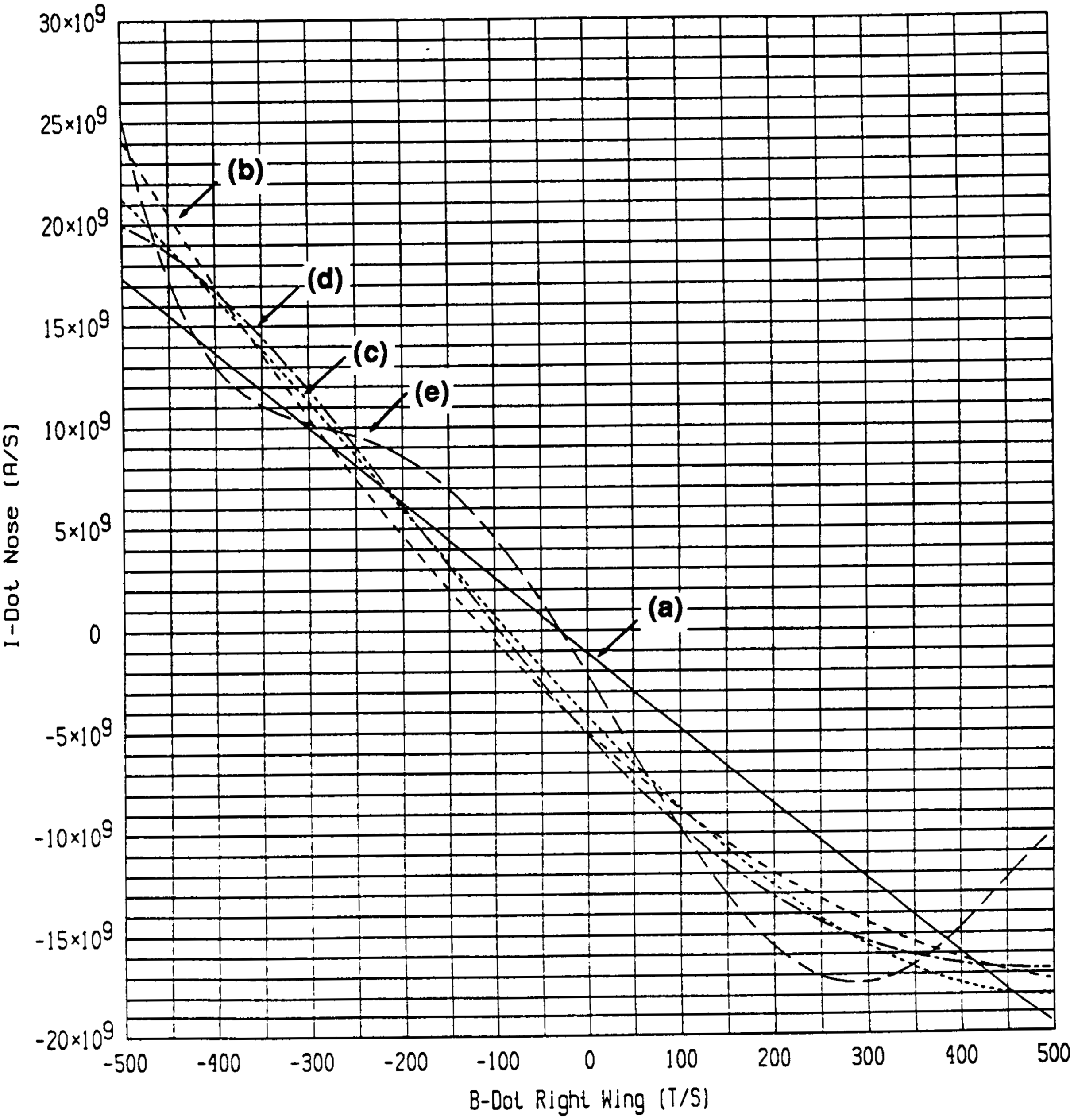

Figure 2.25 Polynomial Approximations Calculated from 1984 Measured I-dot and B-dot Right Wing Peak Values

(a) ——— Linear
(b) - - - - - - - Quadratic
(c) ------------ Third Degree
(d) —·—·— Fourth Degree
(e) — — — — Fifth Degree

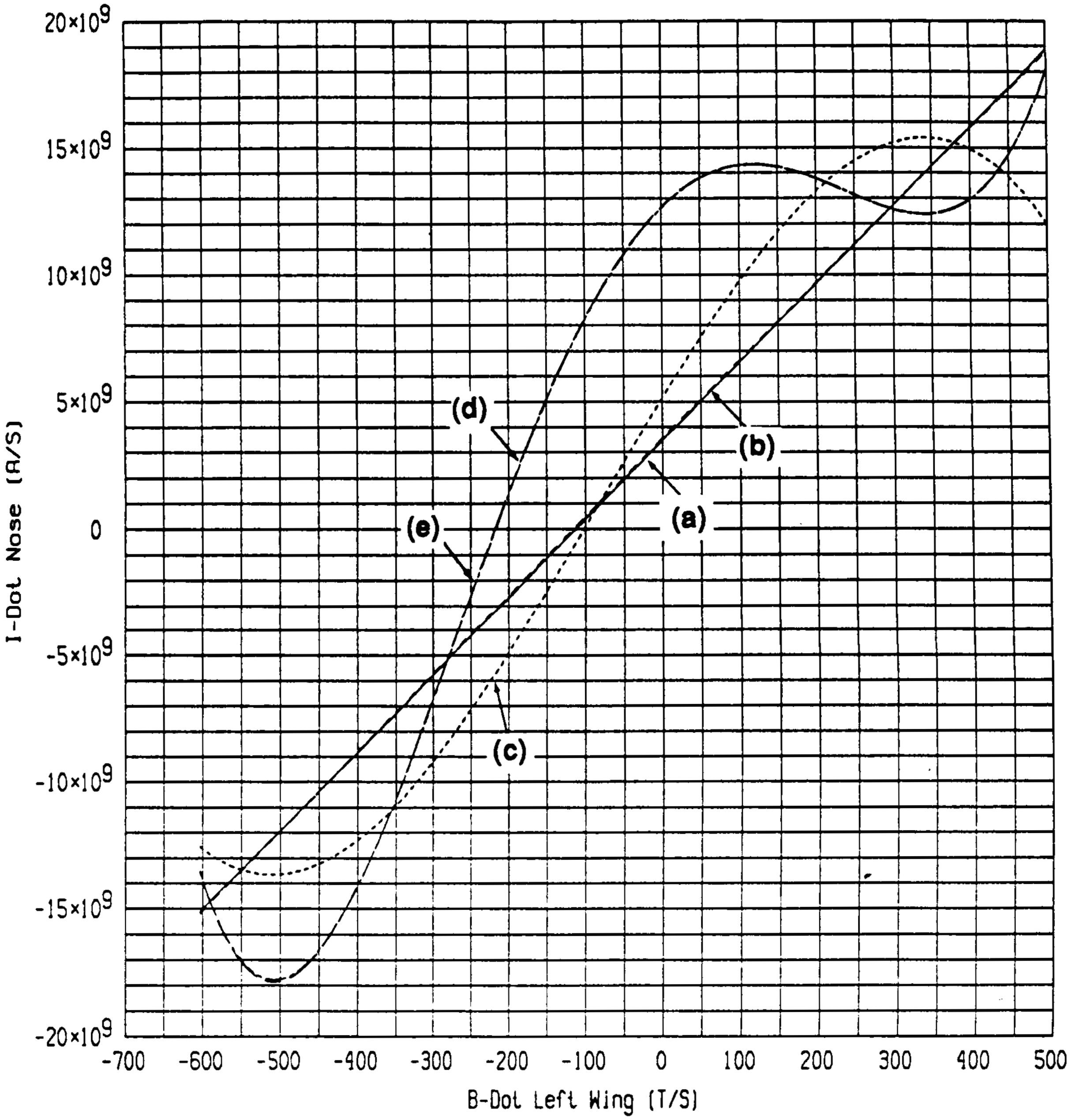

Figure 2.26 **Polynomial Approximations Calculated from 1984 Measured I-dot and B-dot Left Wing Peak Values**

(a) ——— Linear
(b) - - - - - - - Quadratic
(c) ------------- Third Degree
(d) —·—·— Fourth Degree
(e) — — — — Fifth Degree

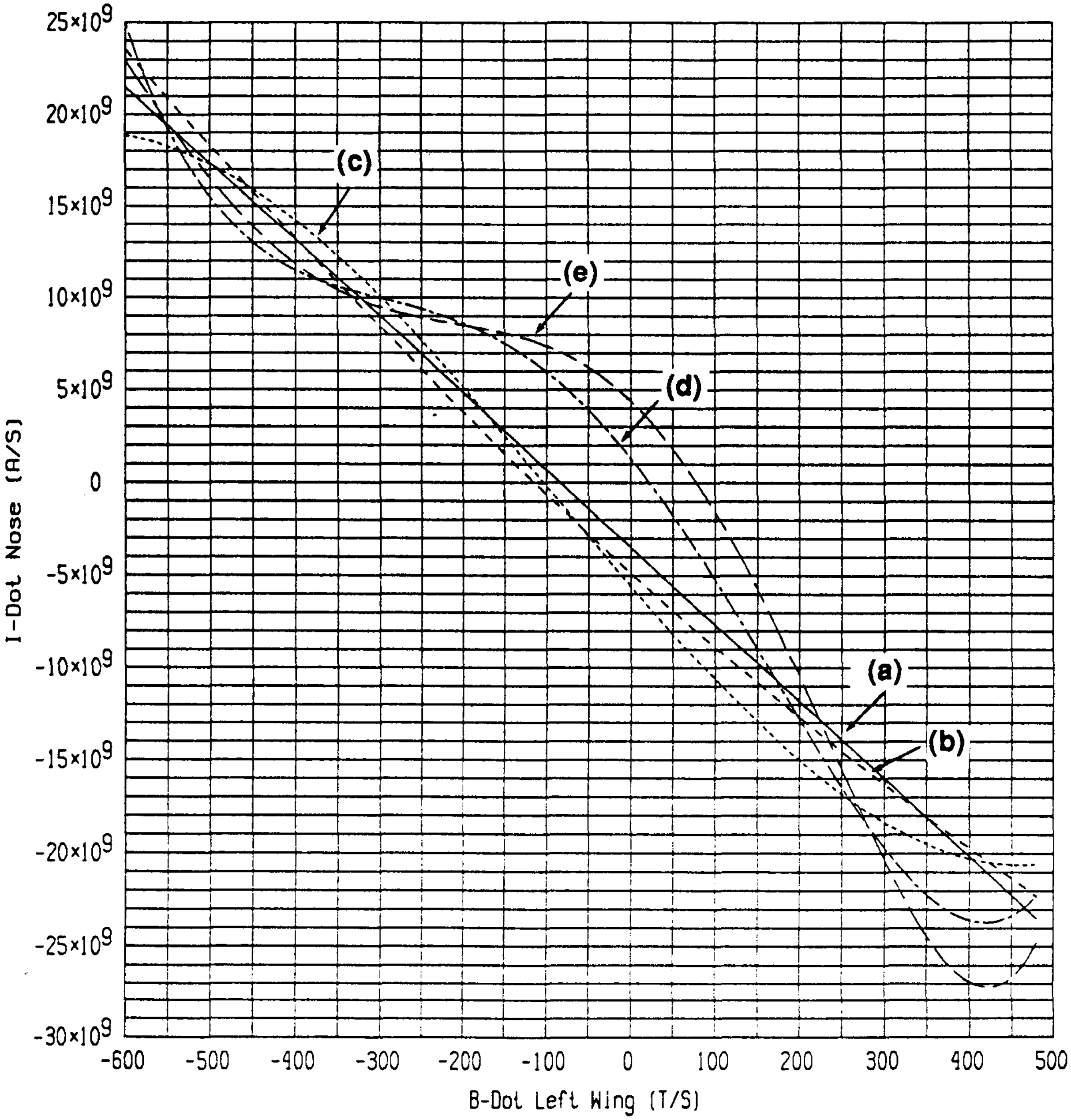

Figure 2.27 Polynomial Approximations Calculated from 1984 Measured I-dot and B-dot Left Wing Peak Values

(a) ———— Linear
(b) - - - - - - - Quadratic
(c) ------------ Third Degree
(d) —-—-— Fourth Degree
(e) — — — — Fifth Degree

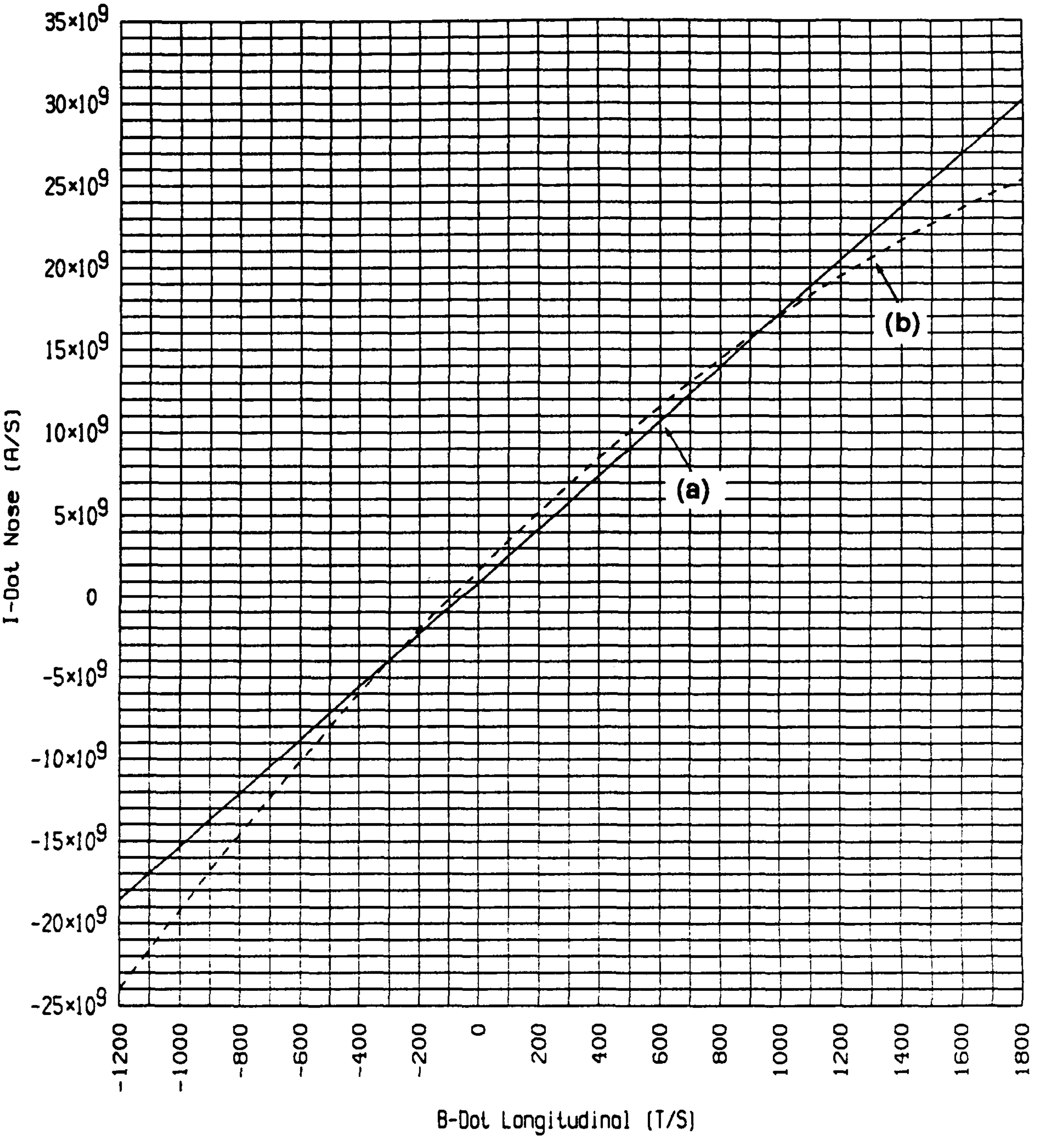

Figure 2.28 Linear and Quadratic Curves Obtained from 1984 Measured I-dot and B-dot Longitudinal Peak Values

(a) ——— Linear

(b) - - - - - - - Quadratic

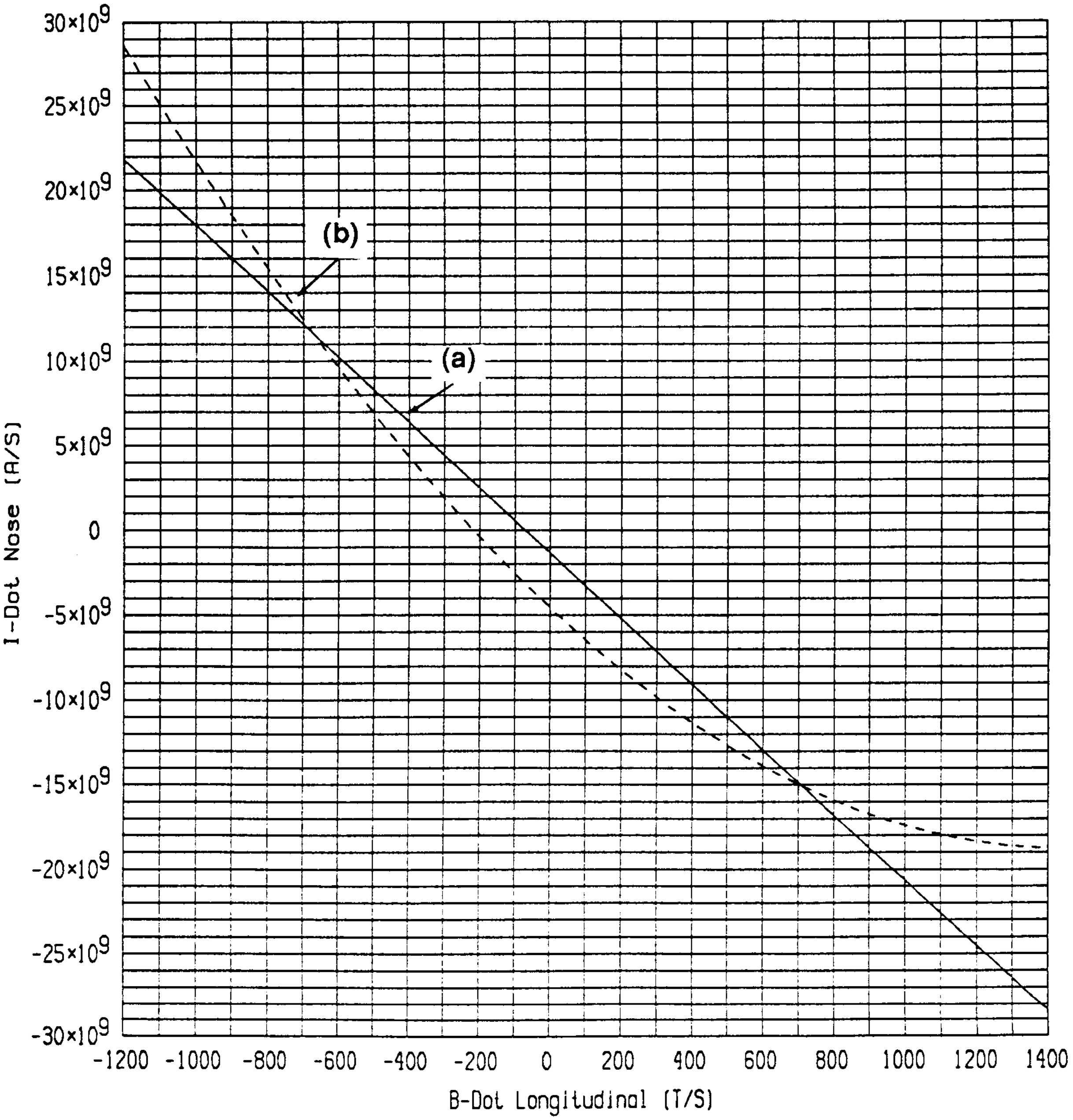

Figure 2.29 Linear and Quadratic Curves Obtained from 1984 Measured I-dot and B-dot Longitudinal Peak Values

(a) ———— Linear
(b) - - - - - - - Quadratic

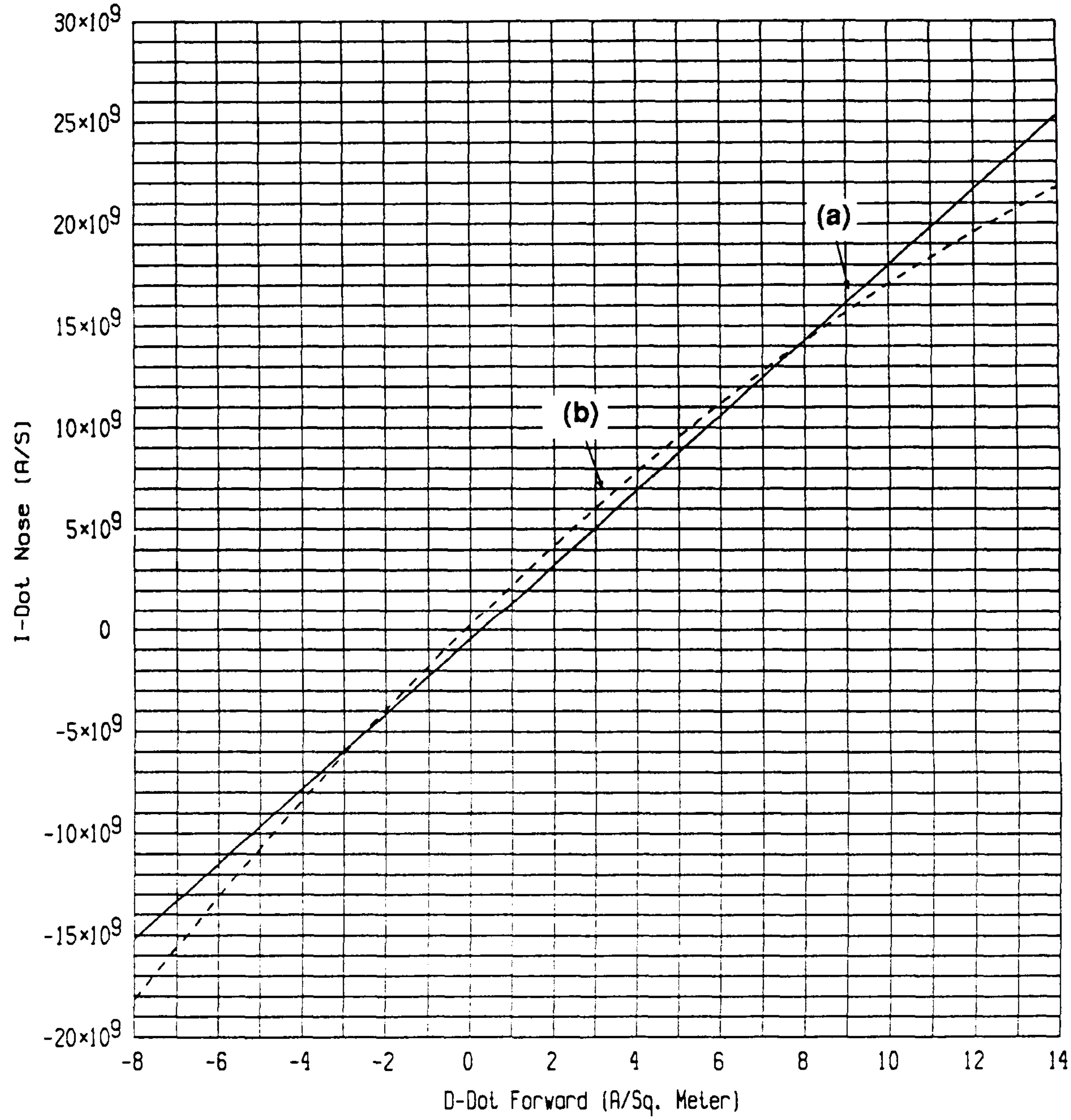

Figure 2.30 Linear and Quadratic Curves Obtained from 1984 Measured I-dot and D-dot Forward Peak Values

(a) ——— Linear

(b) - - - - - - - Quadratic

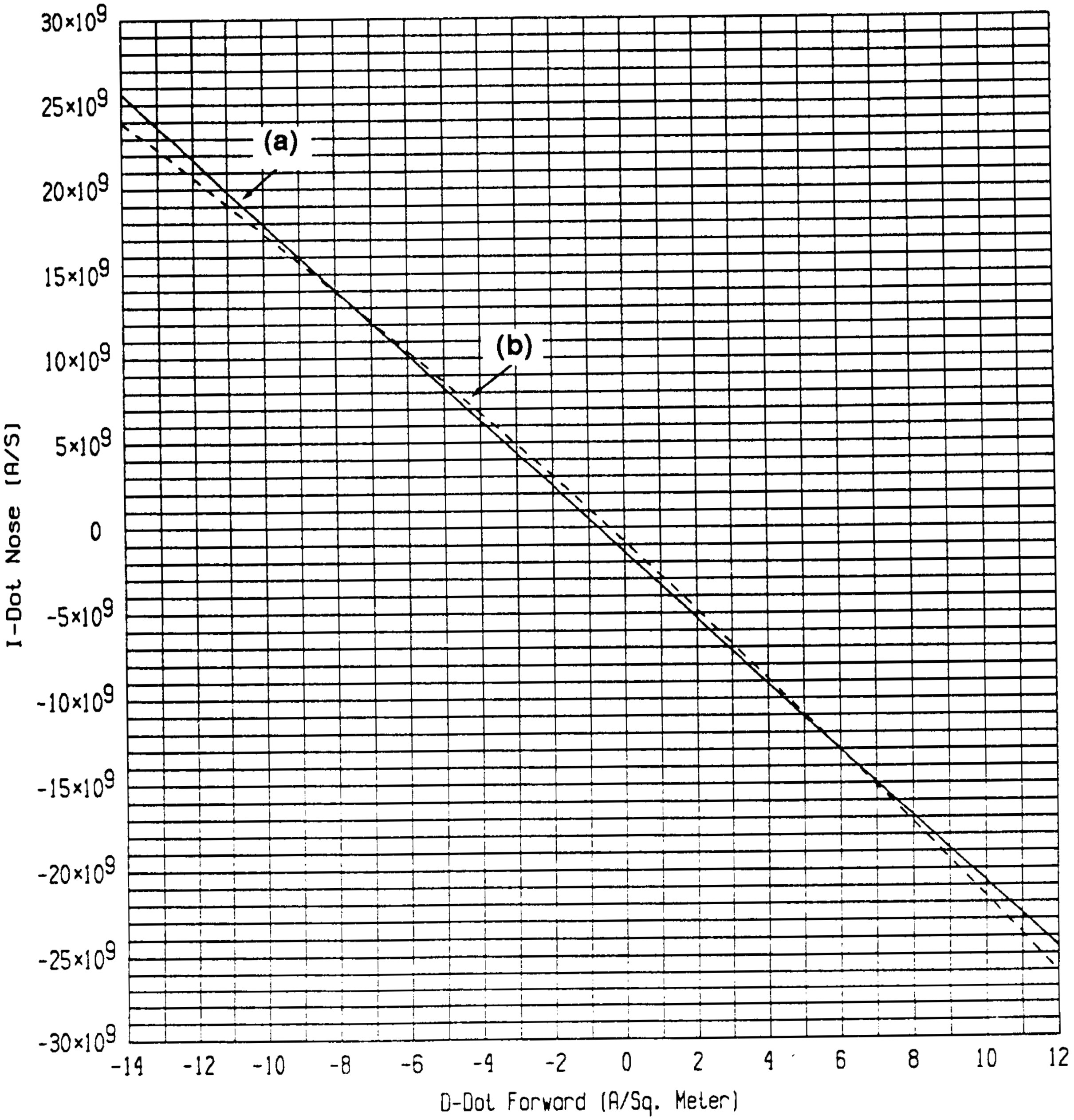

Figure 2.31 Linear and Quadratic Curves Obtained from 1984 Measured I-dot and D-dot Forward Peak Values

(a) ——— Linear
(b) - - - - - - - Quadratic

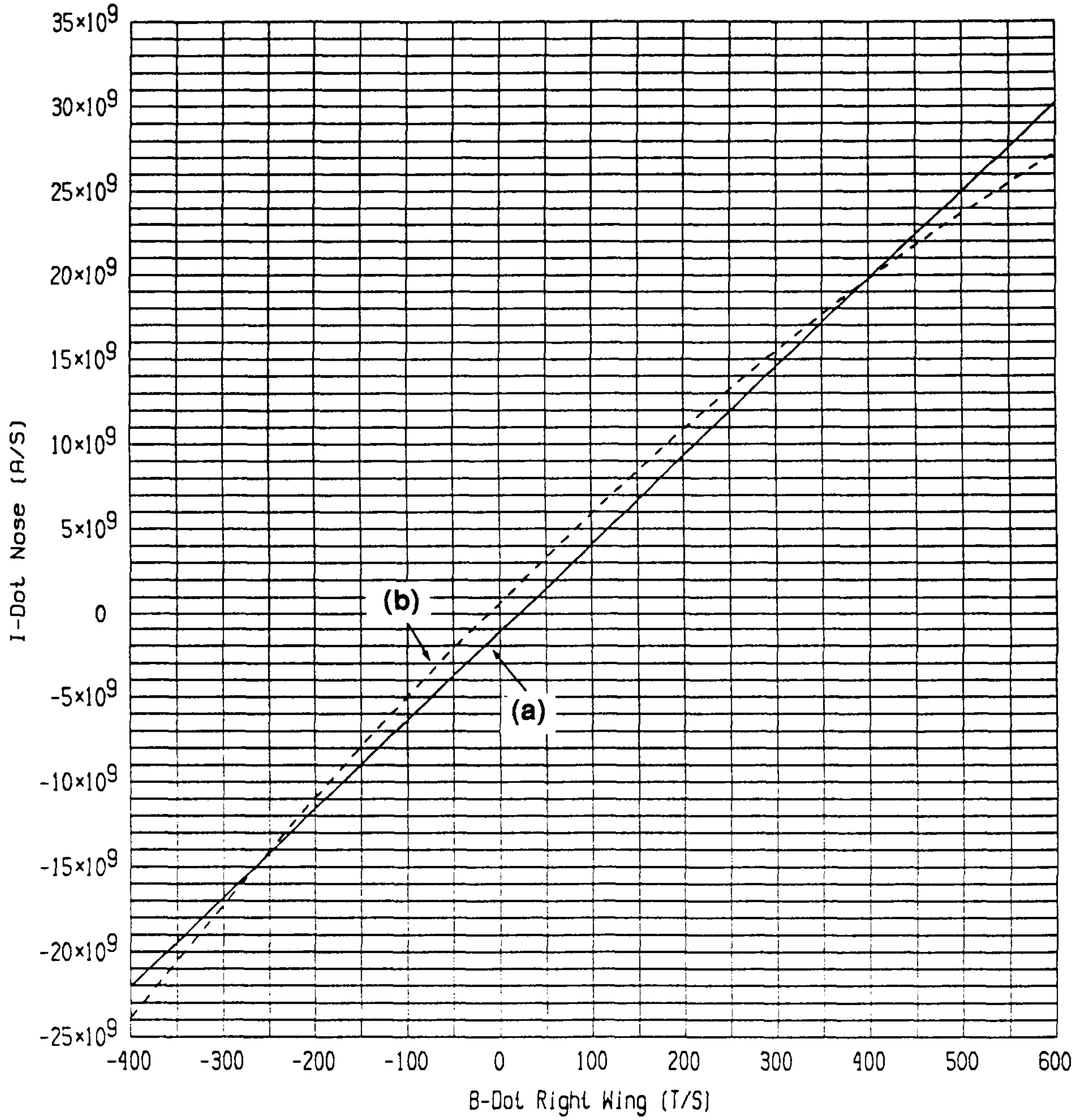

Figure 2.32 Linear and Quadratic Curves Obtained from 1984 Measured I-dot and B-dot Right Wing Peak Values

(a) ——— Linear
(b) - - - - - - - Quadratic

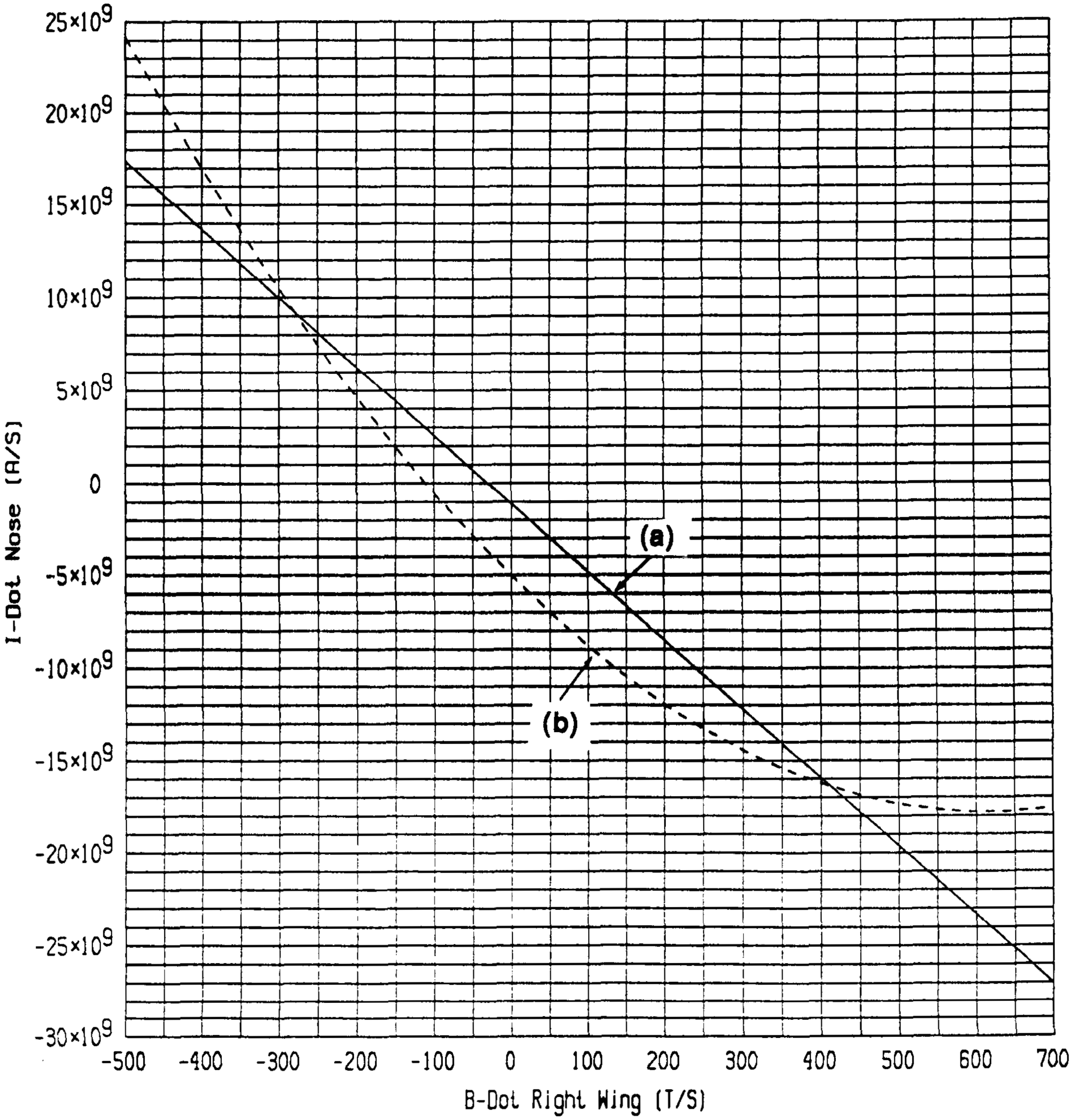

Figure 2.33 Linear and Quadratic Curves Obtained from 1984 Measured I-dot and B-dot Right Wing Peak Values

(a) ——— Linear
(b) - - - - - - - Quadratic

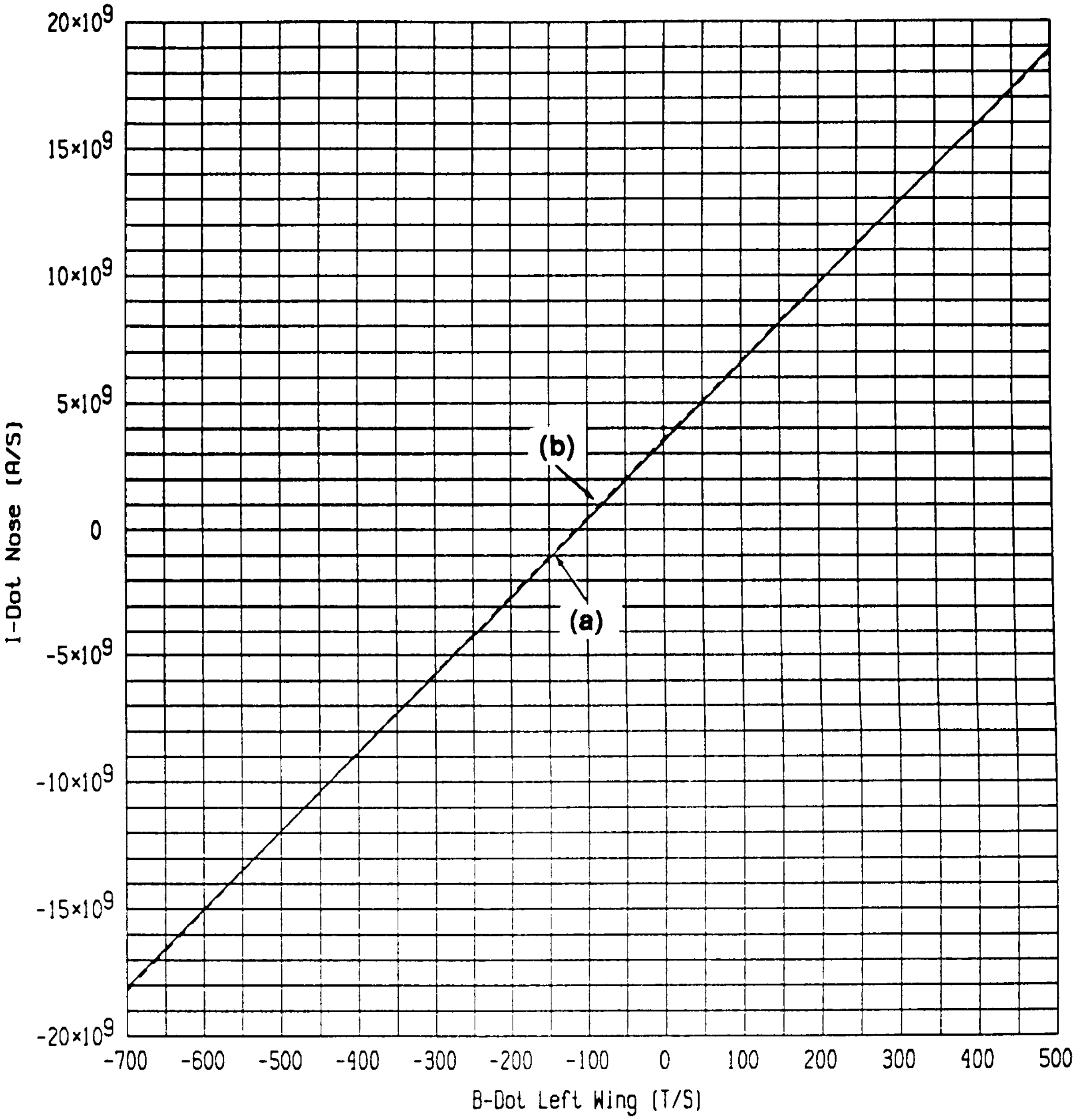

Figure 2.34 Linear and Quadratic Curves Obtained from 1984 Measured I-dot and B-dot Left Wing Peak Values

(a) ——— Linear
(b) - - - - - - - Quadratic

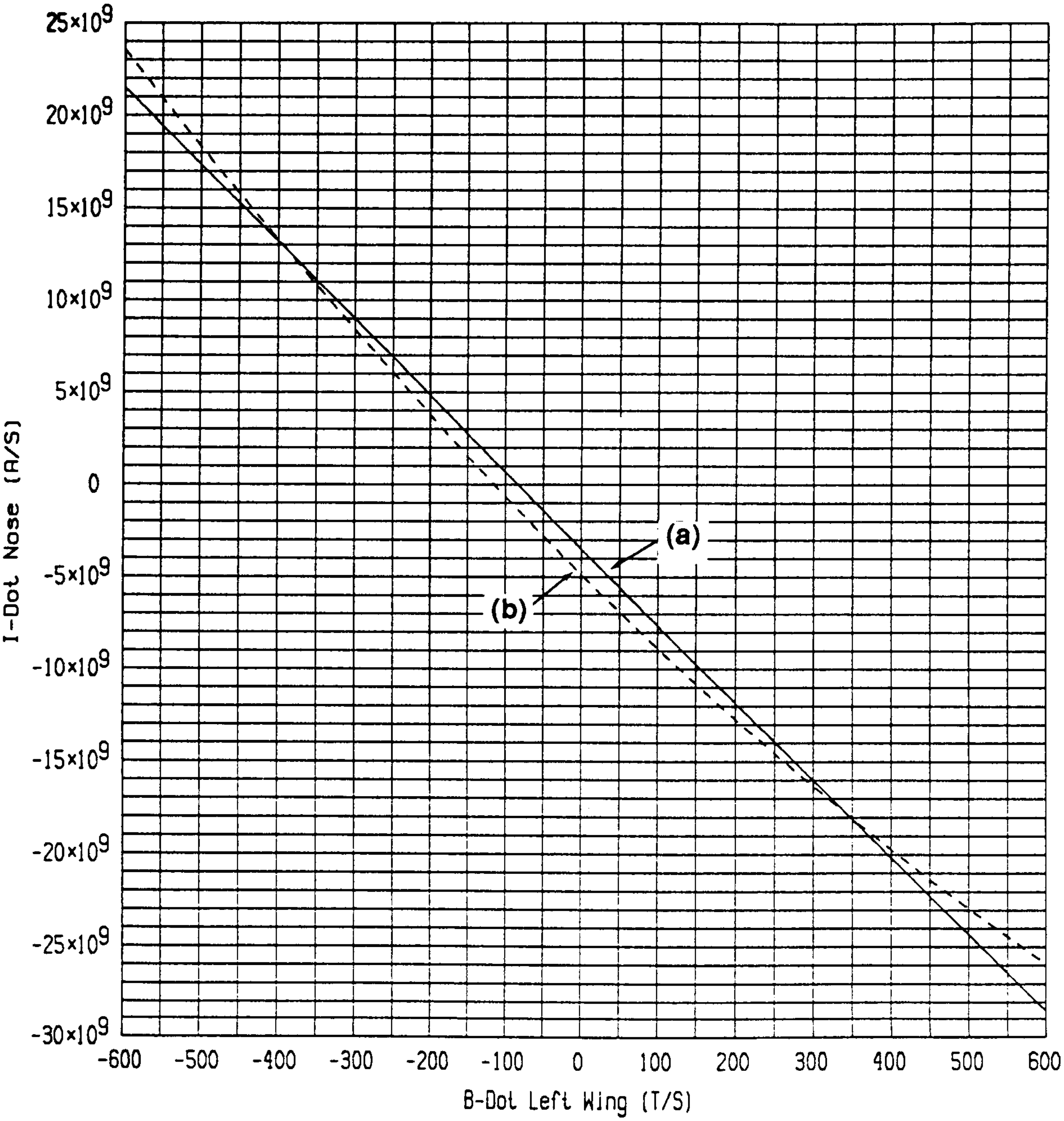

Figure 2.35 Linear and Quadratic Curves Obtained from 1984 Measured I-dot and B-dot Left Wing Peak Values

(a) ——— Linear
(b) - - - - - - - Quadratic

addition, the spread in the data allows some opportunity for the higher order curves to effectively reduce the standard error of estimate.

The standard errors of estimate for the linear and quadratic curves in Figures 2.28 - 2.35 are given in Table 2.2. In general, the errors indicate that only limited accuracy is obtained through the use of these curves. The curves presented in this analysis should therefore be used with care when attempting to extract information. Their primary role as indicators of trends in the lightning data should be recognized.

TABLE 2.2
Standard Errors of Estimate for Linear and Quadratic Correlation Curves

Sensor	Figure	Standard Error of Estimate Linear	 Quadratic
$\dot{B}_L$	29	4.1×10^9	3.8×10^9
$\dot{B}_L$	30	4.8×10^9	4.1×10^9
$\dot{D}_F$	31	5.3×10^9	5.2×10^9
$\dot{D}_F$	32	5.6×10^9	5.6×10^9
$\dot{B}_{RW}$	33	1.8×10^9	9.5×10^8
$\dot{B}_{RW}$	34	5.5×10^9	4.2×10^9
$\dot{B}_{LW}$	35	4.4×10^9	4.4×10^9
$\dot{B}_{LW}$	36	4.1×10^9	4.0×10^9

It is interesting to compare the correlations just presented to a similar set involving strictly D-dot sensor data. This set is found in Figures 2.36 - 2.47. The correlations in this set represent the most significant trends in the data sets which did not include one of the current sensors. Characteristics such as the spread in the data

(text continued on page 61)

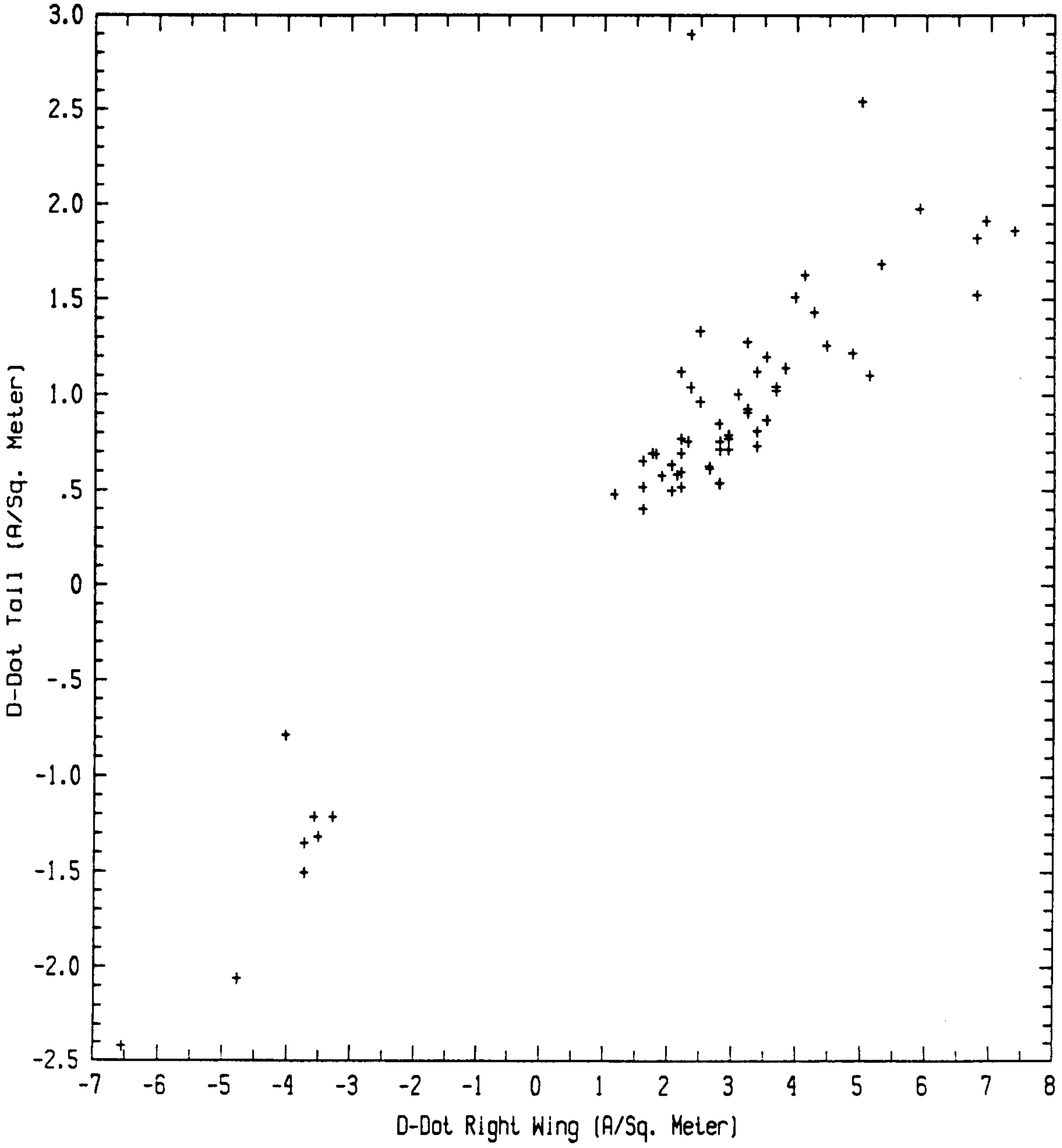

Figure 2.36 **Restricted Peak Value Scatter Diagram 9 Derived from 1984 Measured D-dot Tail and D-dot Right Wing Response Data (Restricted Peak Value)**

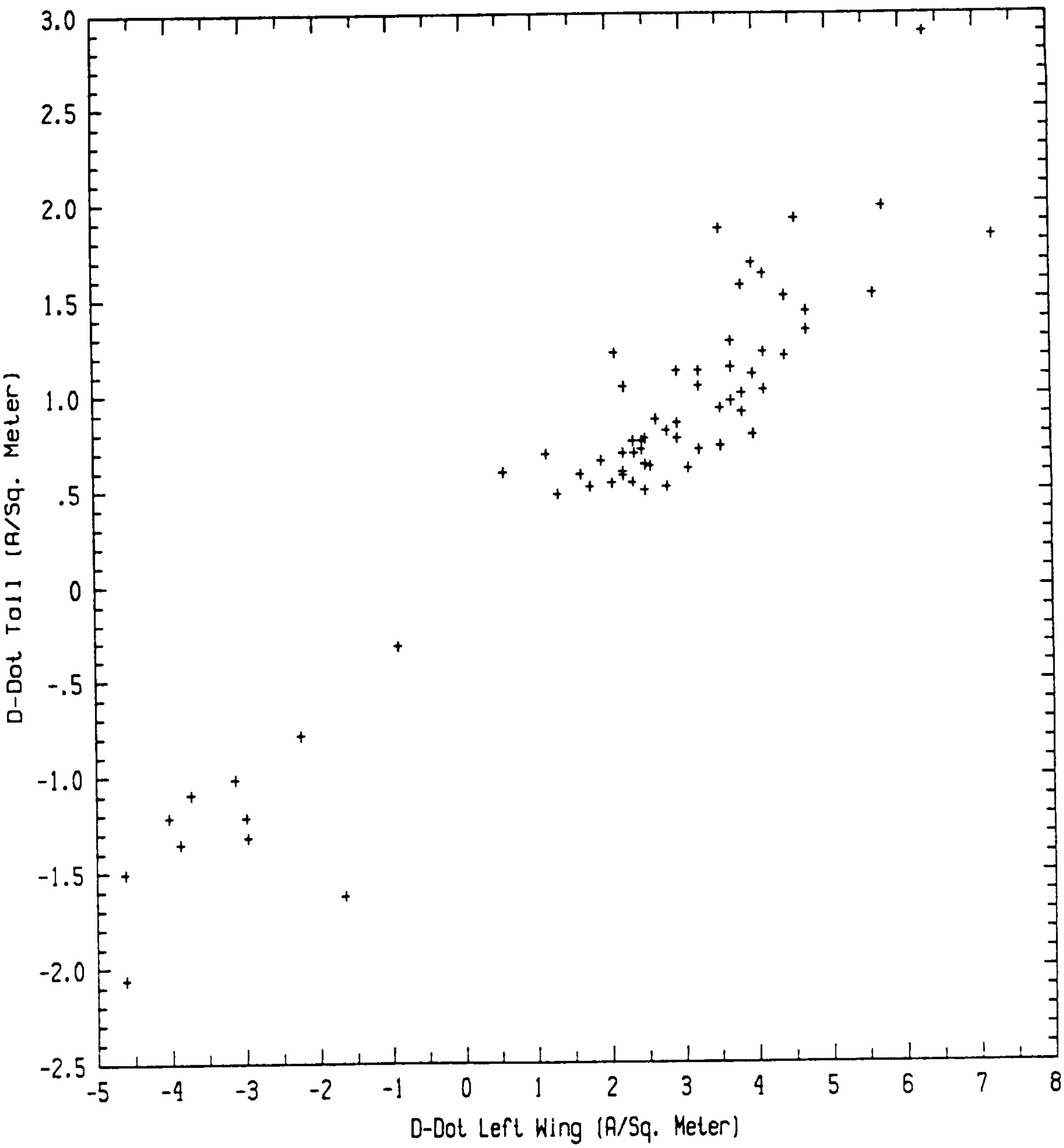

Figure 2.37 Restricted Peak Value Scatter Diagram 10 Derived from 1984 Measured D-dot Tail and D-dot Left Wing Response Data (Restricted Peak Value)

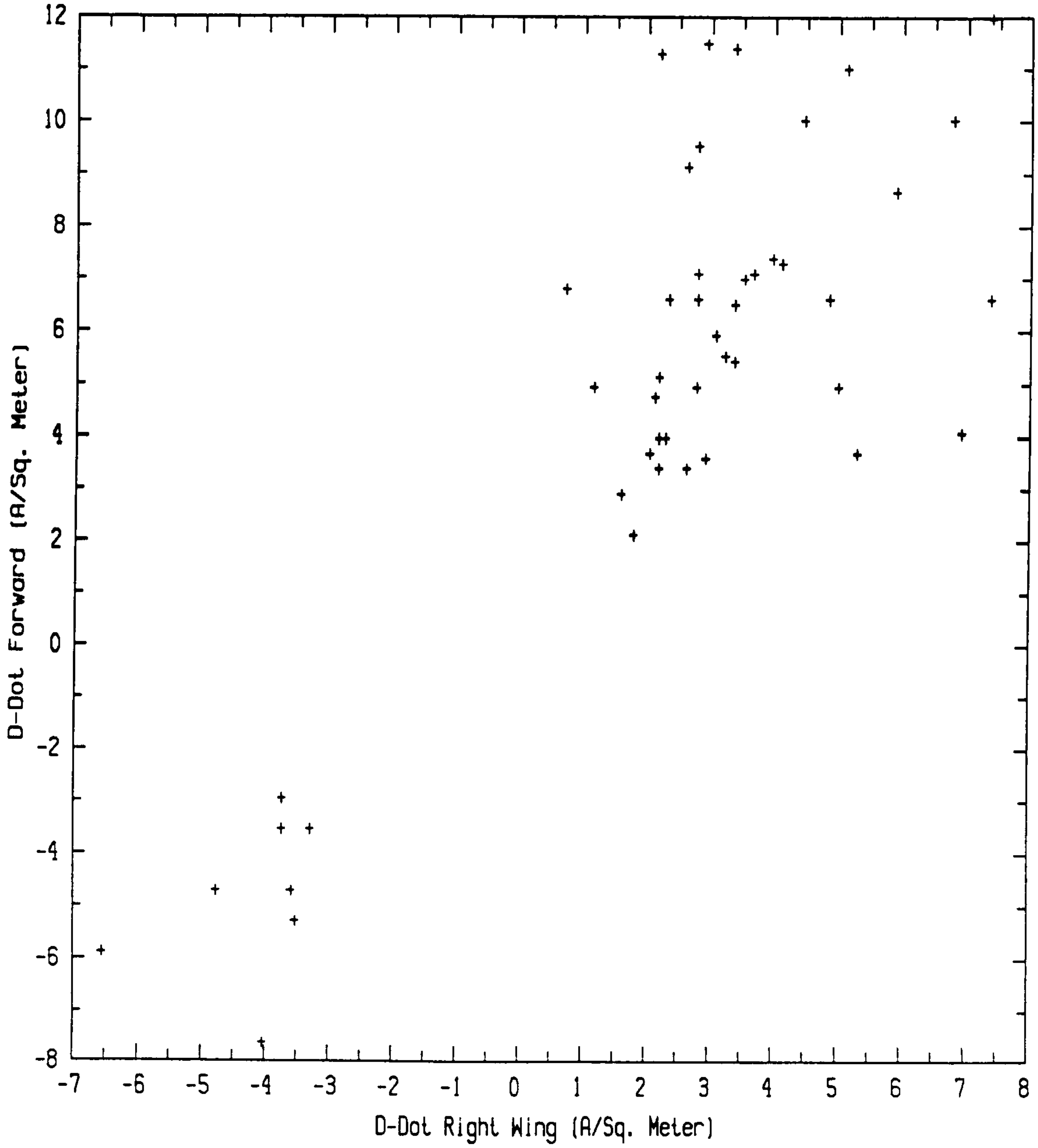

Figure 2.38 Restricted Peak Value Scatter Diagram 11 Derived from 1984 Measured D-dot Tail and D-dot Right Wing Response Data (Restricted Peak Value)

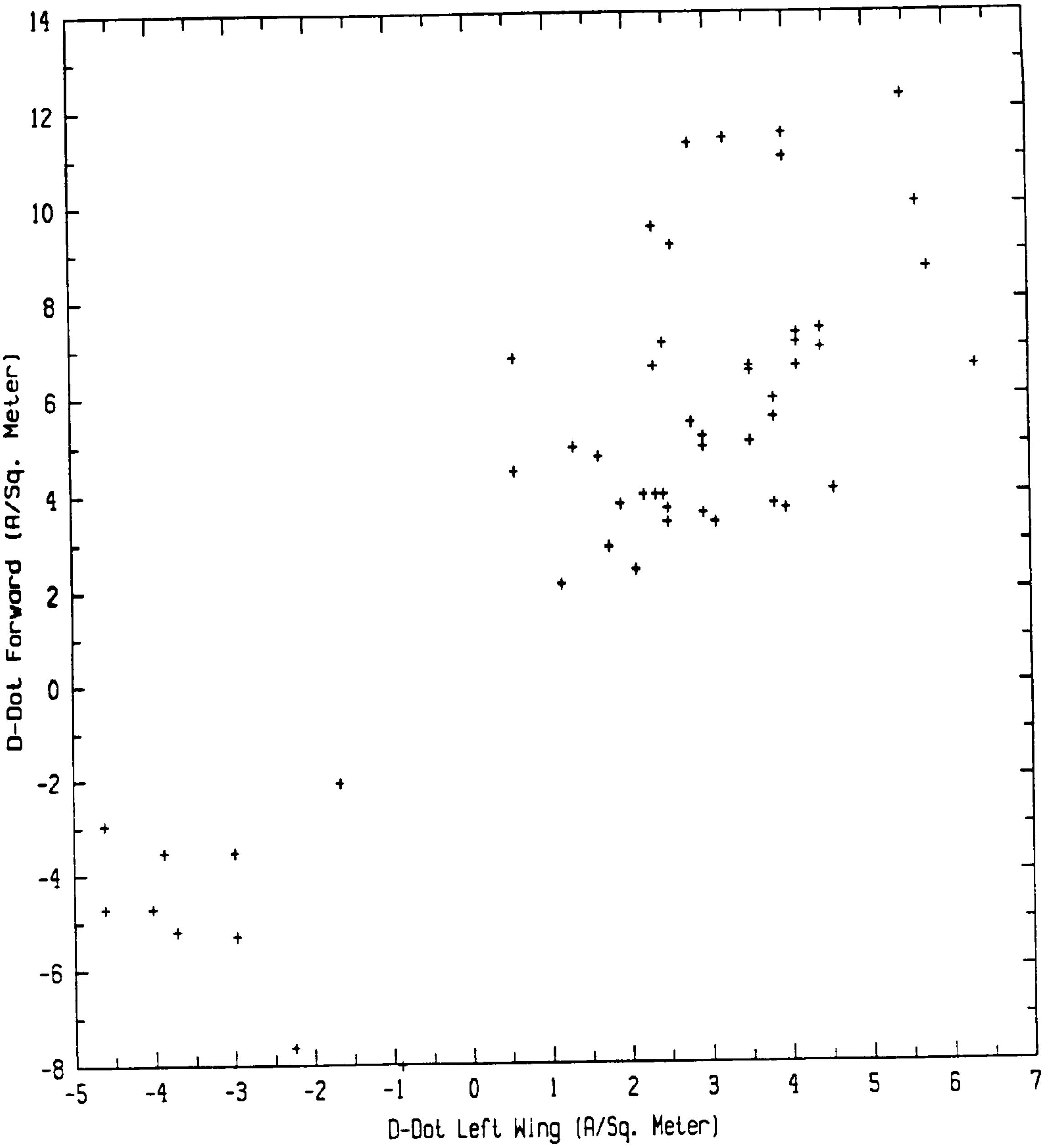

Figure 2.39 Restricted Peak Value Scatter Diagram 12 Derived from 1984 Measured D-dot Tail and D-dot Left Wing Response Data (Restricted Peak Value)

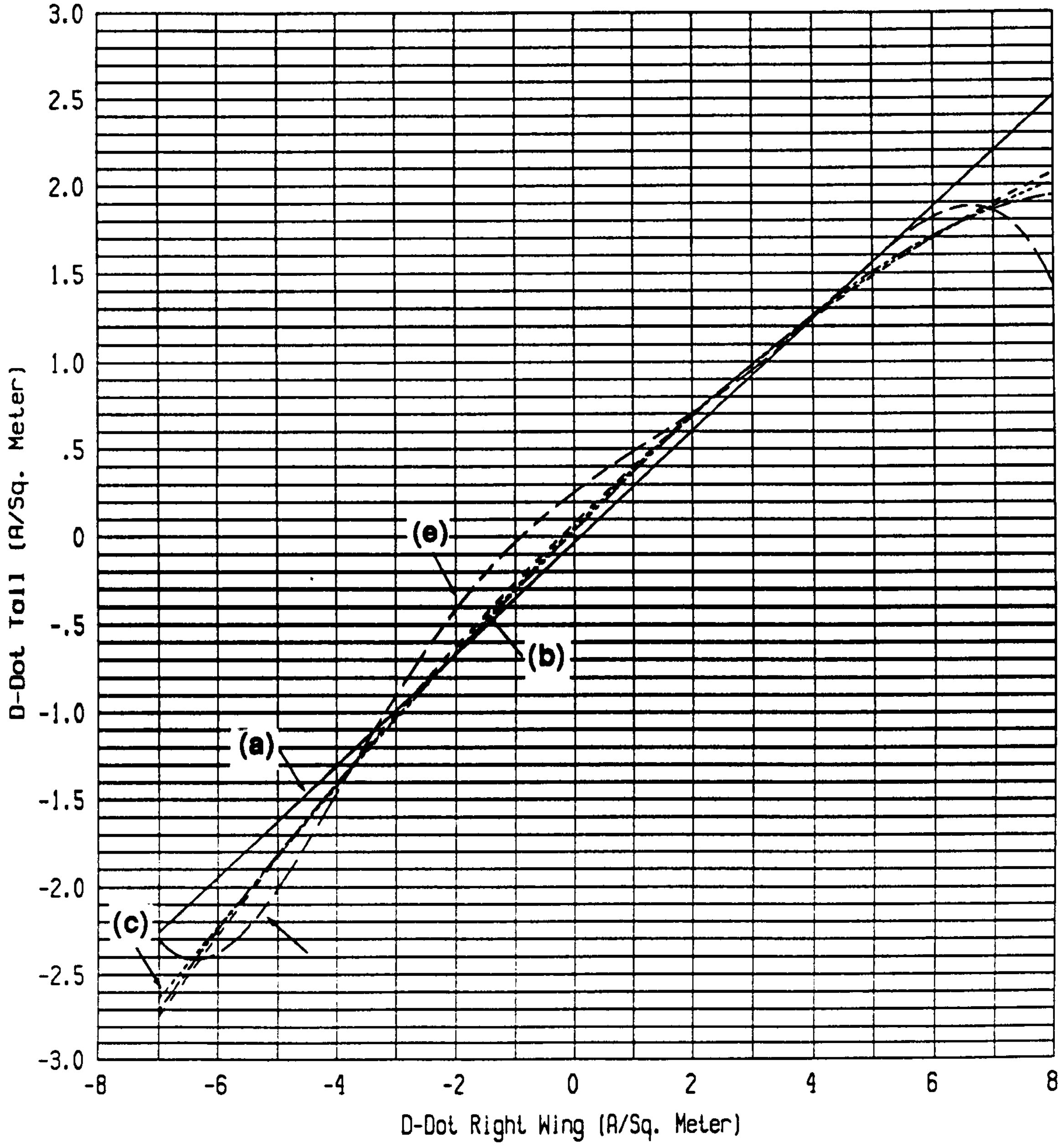

Figure 2.40 Polynomial Approximations Calculated from 1984 Measured D-dot Tail and D-dot Right Wing Peak Values

(a) ——— Linear
(b) - - - - - - - Quadratic
(c) ------------ Third Degree
(d) —·—·— Fourth Degree
(e) — — — — Fifth Degree

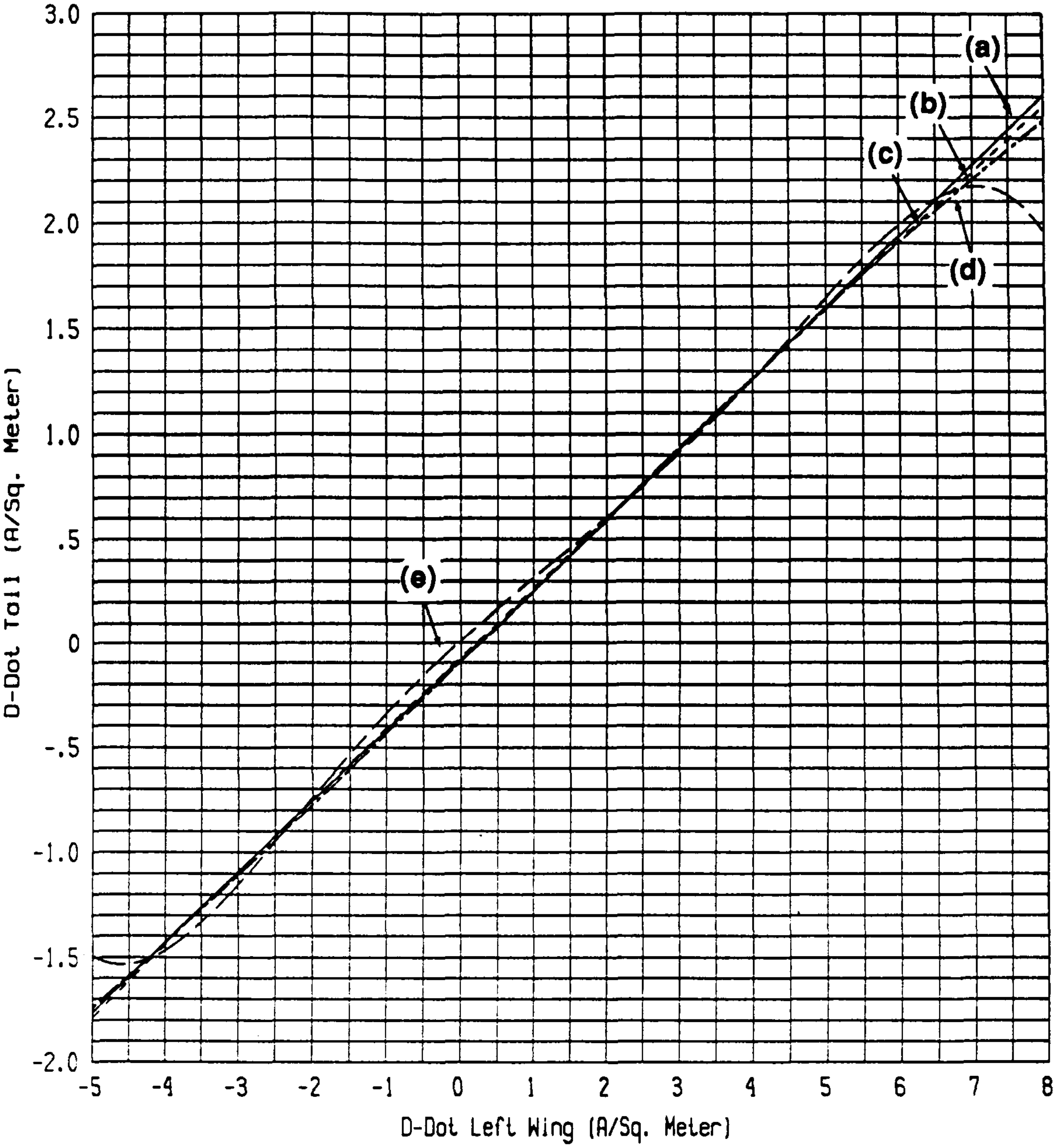

Figure 2.41 Polynomial Approximations Calculated from 1984 Measured D-dot Tail and D-dot Left Wing Peak Values

(a) ——— Linear
(b) - - - - - - - Quadratic
(c) ------------ Third Degree
(d) —·—·— Fourth Degree
(e) — — — — Fifth Degree

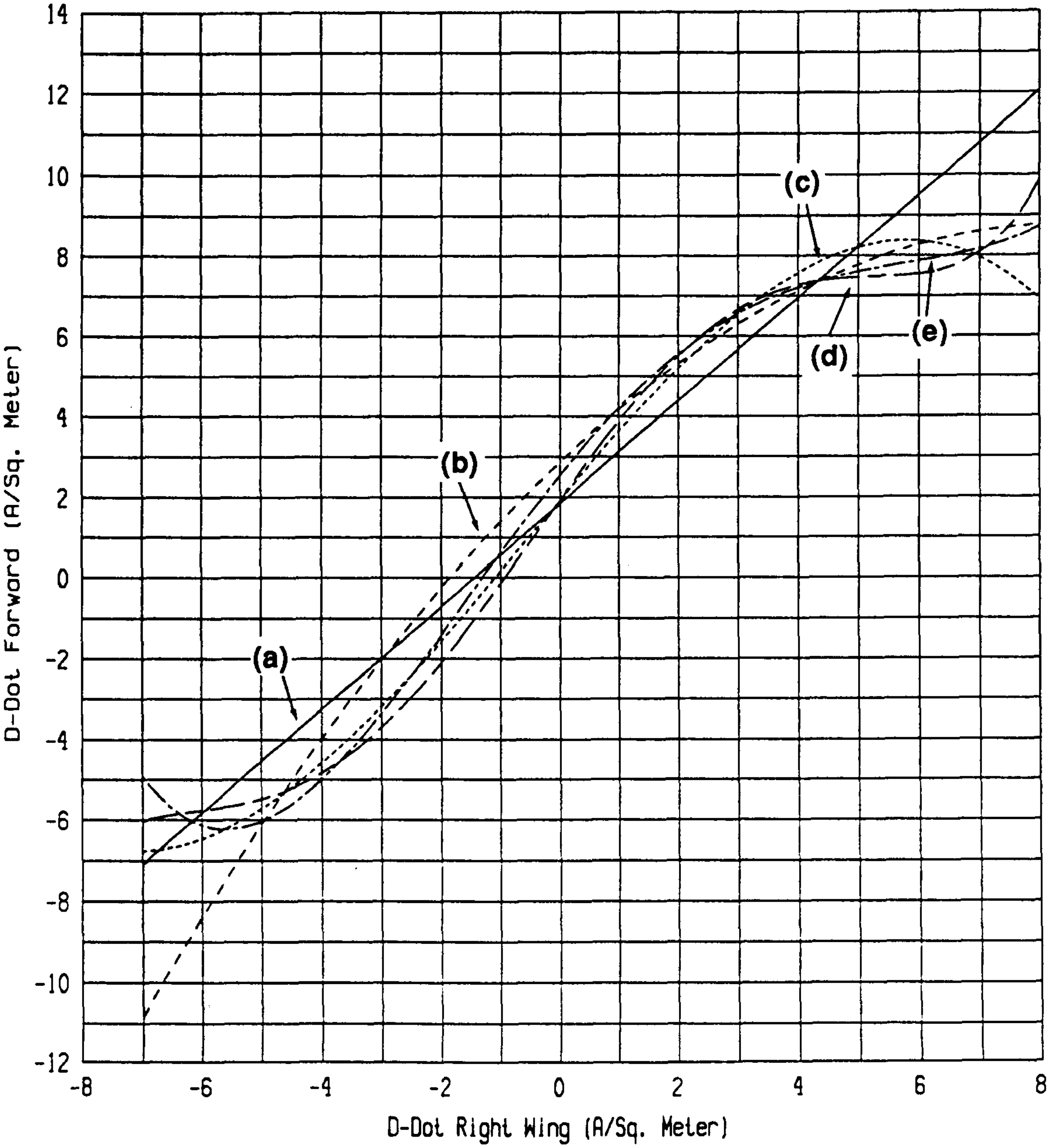

Figure 2.42 Polynomial Approximations Calculated from 1984 Measured D-dot Tail and D-dot Right Wing Peak Values

(a) ———— Linear
(b) - - - - - - - Quadratic
(c) ------------- Third Degree
(d) —·—·— Fourth Degree
(e) — — — — Fifth Degree

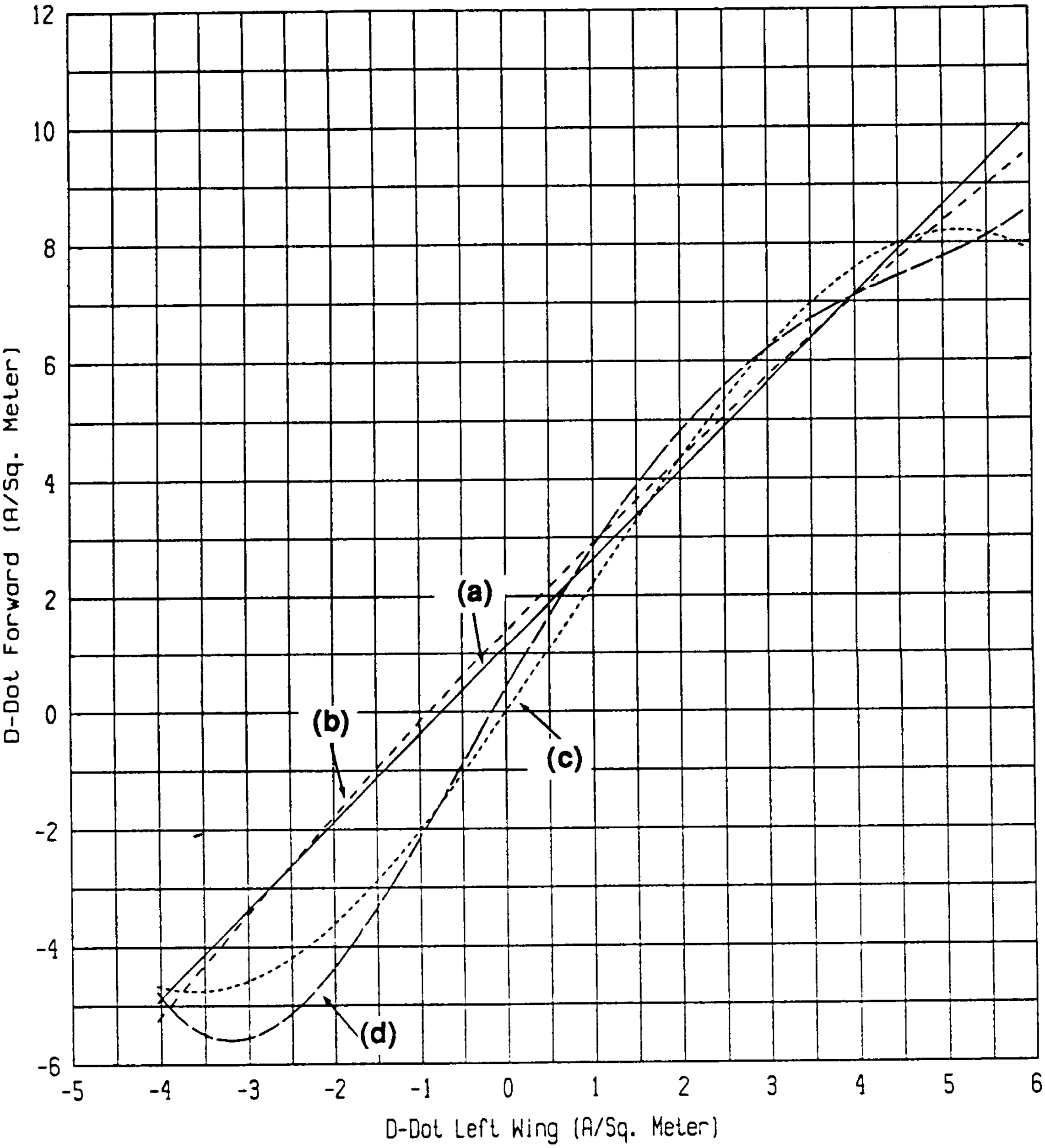

Figure 2.43 Polynomial Approximations Calculated from 1984 Measured D-dot Tail and D-dot Left Wing Peak Values

(a) ——— Linear
(b) - - - - - - - Quadratic
(c) ------------ Third Degree
(d) —-—-— Fourth Degree

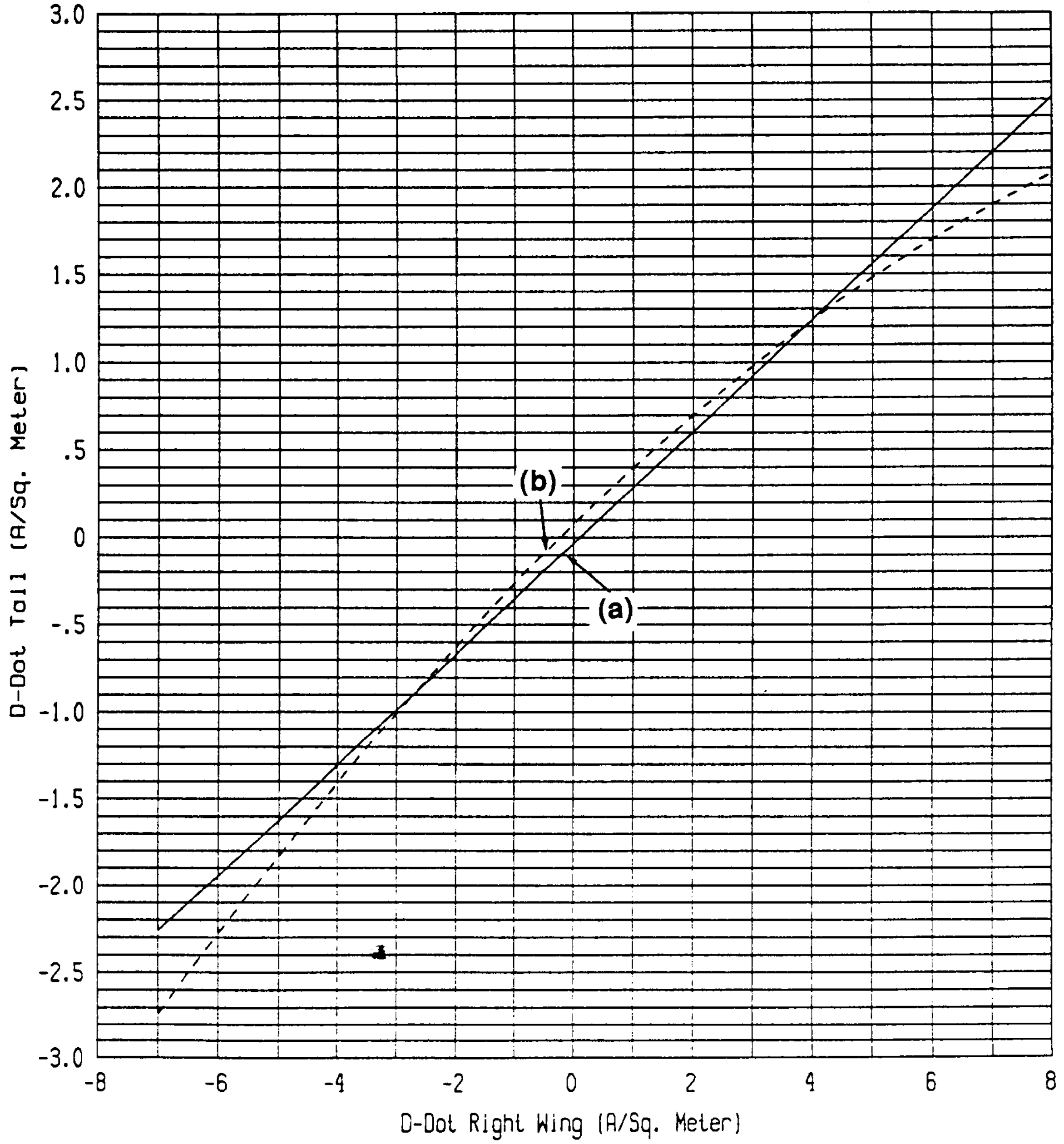

Figure 2.44 Linear and Quadratic Curves Obtained from 1984 Measured D-dot Tail and D-dot Right Wing Peak Values

(a) ——— Linear
(b) - - - - - - - Quadratic

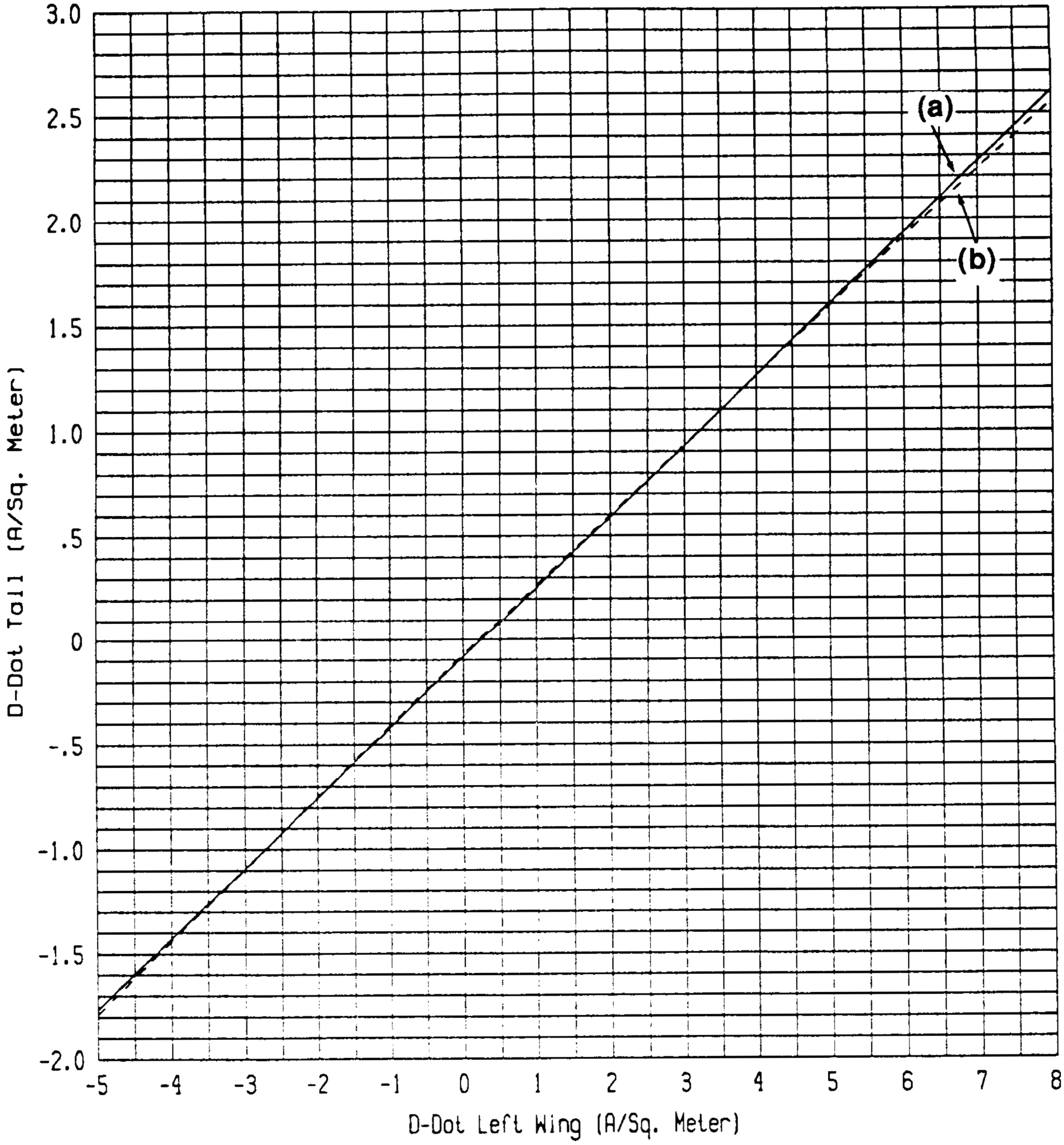

Figure 2.45 Linear and Quadratic Curves Obtained from 1984 Measured D-dot Tail and D-dot Left Wing Peak Values

(a) ——— Linear
(b) - - - - - - - Quadratic

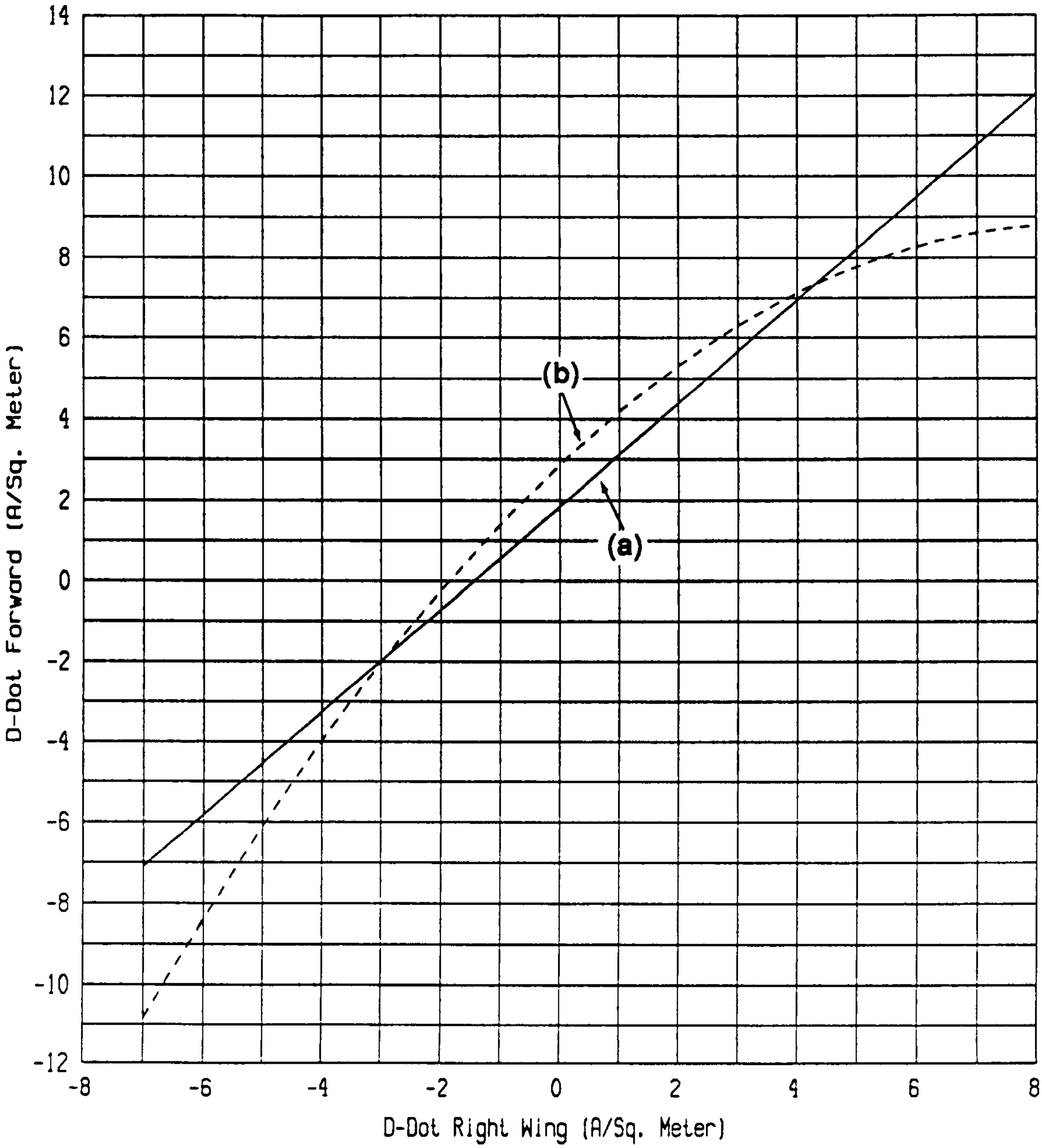

Figure 2.46 Linear and Quadratic Curves Obtained from 1984 Measured D-dot Tail and D-dot Right Wing Peak Values

(a) ——— Linear
(b) - - - - - - - Quadratic

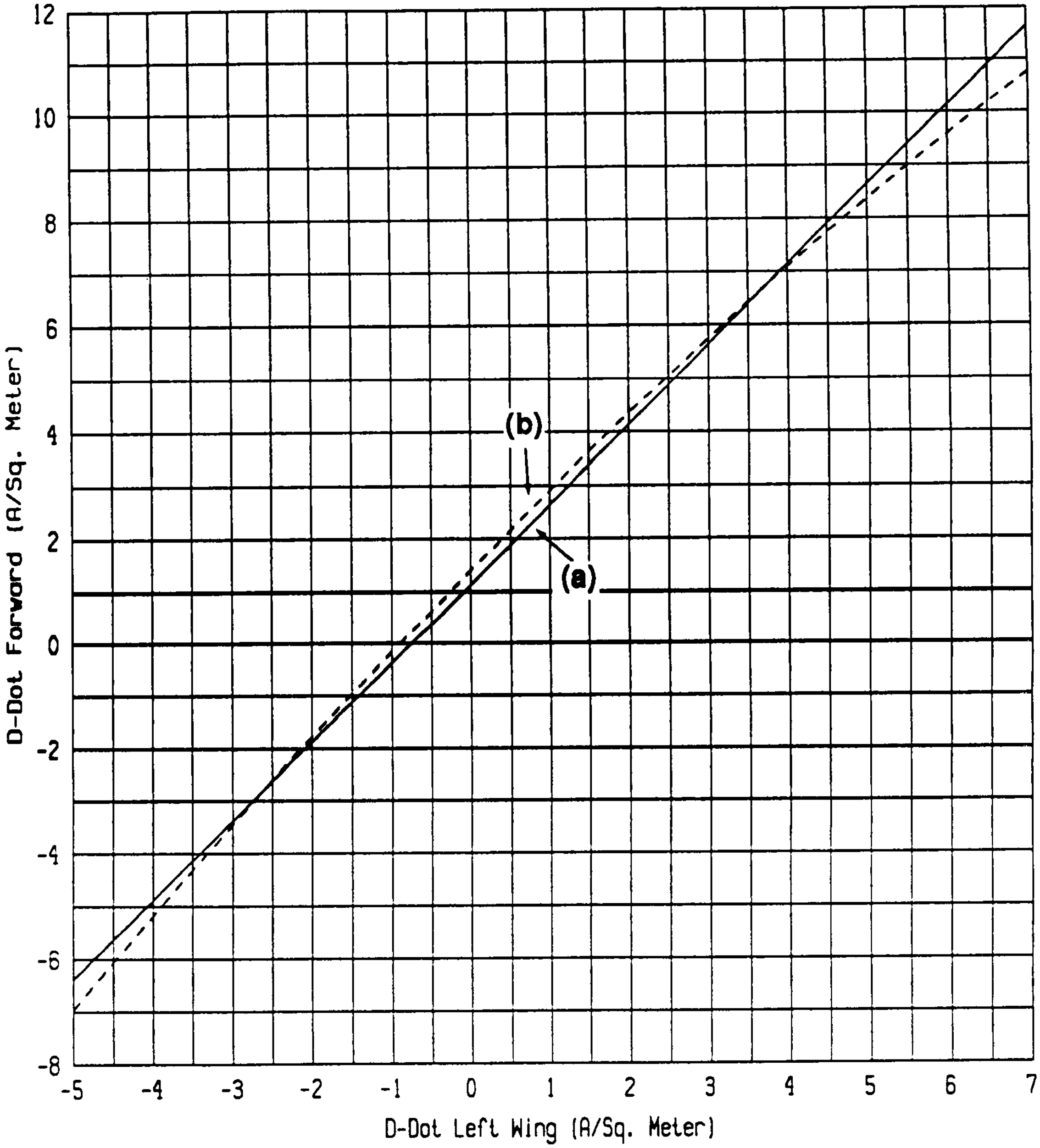

Figure 2.47 Linear and Quadratic Curves Obtained from 1984 Measured D-dot Tail and D-dot Left Wing Peak Values

(a) ——— Linear
(b) - - - - - - - Quadratic

and the predominantly lower order behavior are also apparent in this set. In particular, the standard errors of estimate for the approximations shown are similar to the previous set. The use of the approximation curves presented here may be demonstrated by considering a simple example. Table 2.3 lists the measured peak values obtained from several sensors during Flight 84-025 Run 003 Strike 004.

TABLE 2.3
Peak Values from Flight 84-025 Run 003 Strike 004

Sensor	Peak Value
I-dot Nose	2.09×10^{10} A/S
D-dot Forward	-11.8 A/sq.m
B-dot Longitudinal	1327 T/S

If one uses the peak values from this table for the D-dot forward and B-dot longitudinal sensor together with the linear correlation curves found in Figures 2.31 and 2.28 respectively, it is possible to obtain the approximate I-dot peak values found in Table 2.4

TABLE 2.4
Peak I-dot Values Obtained by Linear Approximation for Flight 84-025 Run 003 Strike 004

Sensor	Predicted I-dot Peak Values
D-dot Forward	2.15×10^{10} A/S
B-dot Longitudinal	2.23×10^{10} A/S

For this particular example, it is clear that the approximation curves have provided reasonable estimates for the peak I-dot values for the event under consideration. In general, approximations of this type are useful in cases where sensor transients are not available.

2.4 Summary and Conclusions

The in-flight data and the linear modeling results have been organized in a compact form that provides a basis of comparison for these data sets. In general, favorable comparisons were obtained for the lightning events when the linear model used a current source derived from the B-dot longitudinal sensor. This was supported by the transient response data presented.

The correlation study demonstrated that, under suitable restrictions, the peak values of the current time derivative are related to the peak value of the time derivatives of the magnetic and electric flux densities through lower order polynomial approximations. These results further justify the transient linear modeling of the F106B by exhibiting the approximately linear relationship that exists between these electromagnetic quantities in the response regions considered.

The correlation results further suggest that there may be geometric and sensor dependent factors associated with the measured data that require further attention before more accurate simple correlations are developed. Characteristics such as the attachment points (which are often unknown) may be critical to developing a class of correlations applicable to a particular strike geometry. In addition, the removal of questionable sensor data is a clear necessity in improving the utility of the apparent trends in the lightning data.

CHAPTER 3
ANALYSIS OF FIELD MILL DATA

3.1 Field Mill and Triggered Lightning Modeling

This chapter describes the analysis of field mill data for three F106B flights. The field mill data provides a means for determining the ambient fields and charge on the aircraft at the time of a lightning strike. The calculated ambient fields are used as input for the nonlinear numerical model. The transient response of the model can then be compared to the actual response for the F106B. The locations of the field mills on the F106B are shown in Figure 3.1. The frequency response of the field mill system was from DC to 250 Hz. Locations of transient sensors on the aircraft are shown in Figure 3.2.

Some introductory words of caution are necessary here with reference to the field mill system. These points should be kept in mind when evaluating the field mill system and analysis. They are summarized below.

1. The field mill system was considered to be developmental throughout the flight program.

2. Because of the developmental nature, the measurements were not primary, and often flights were made that did not record all field mill channels.

3. There were no satisfactory calibrations of the field mill system until 1986; nevertheless a number of events for three flights in 1985 were considered usable.

4. A special calibration of the field mill system was performed at the end of 1986 for the 1985 flights. That is the calibration used in the analysis documented here. The electronic configuration of the F106B was returned to the 1985 values to within component tolerances.

The numerical model assumes that the fields are quasistatic. The magnitudes of the fields (and charge) increase steadily until a strike occurs. The corresponding field mill data should show a steady change in magnitude until a strike

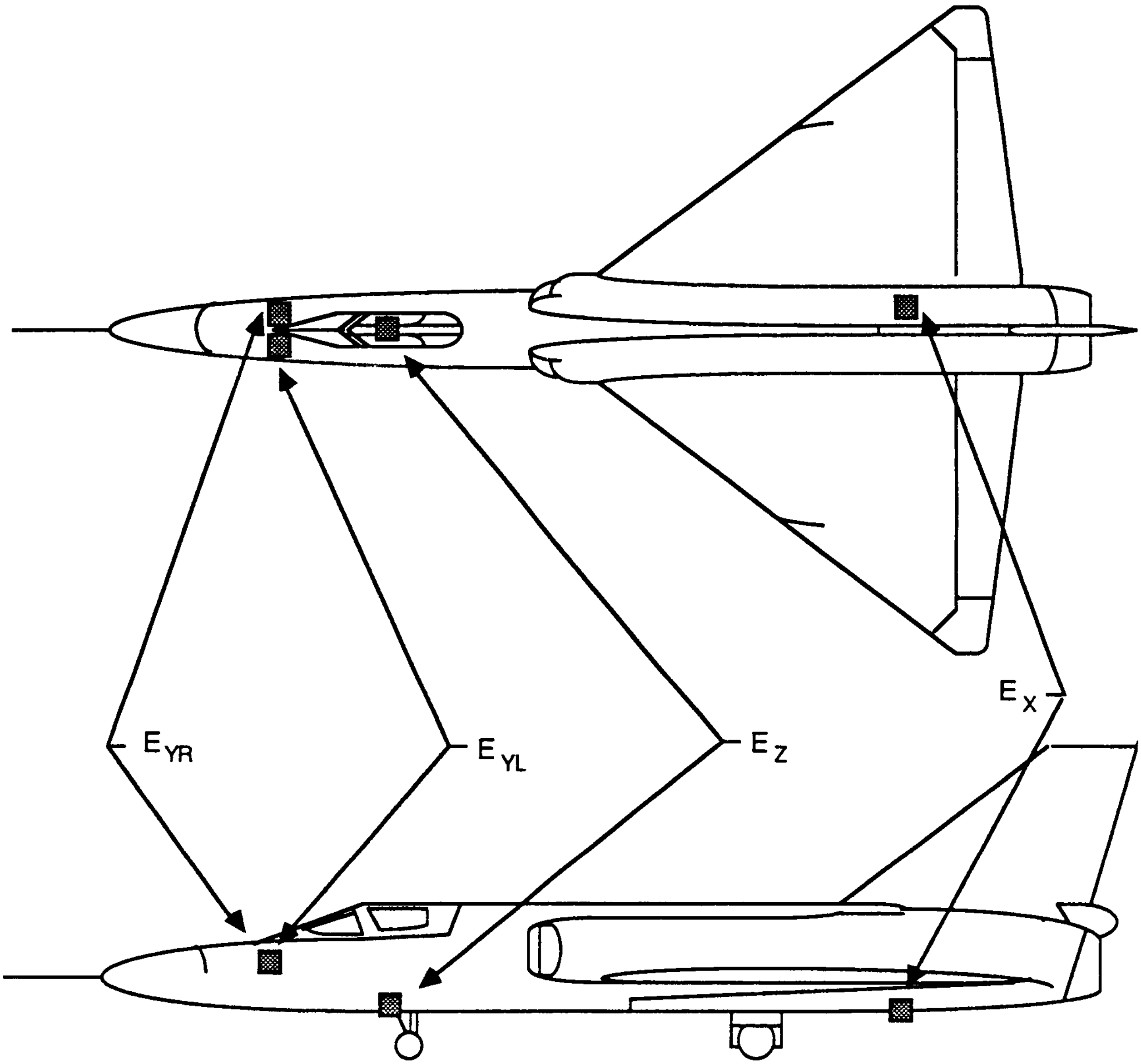

Figure 3.1 F106B Showing Field Mill Locations

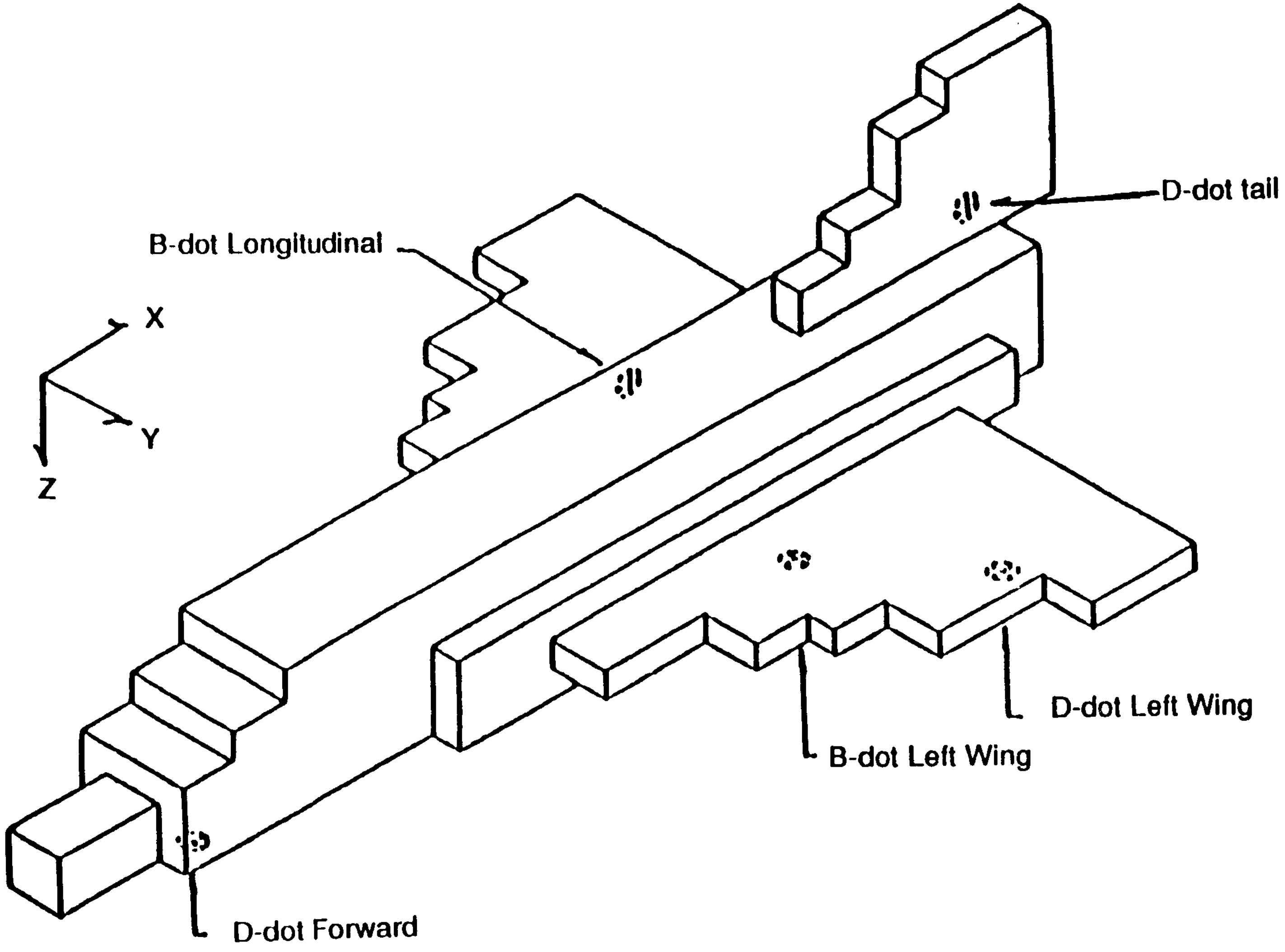

Figure 3.2 Model of F106B Used In Finite Difference Computer Code B-dot Right Wing and D-dot Right Wing Are Symmetrically Located

occurs. Many of the records do not have the desired behavior. In some cases the records show significant oscillations prior to the strike. This could indicate problems with the field mill, or variations in the fields due to nearby electrical activity. In other cases the records show relatively small changes just prior to the strike. Often these records are quite noisy.

There are three events which show the desired steady build up. The ambient fields for two of these events are used to obtain a transient response for the nonlinear model. In all cases the minimum field required to trigger a strike in the numerical model is higher than the measured data would indicate. This is likely because of restrictions on the resolution of sharp curves because of finite difference mesh size. The fields are enhanced by a compensating scaling factor to obtain the results in this chapter.

Digitization of the field mill data was done by hand. The calibration values used in this analysis are:

ER record: 227 kV/m
EA record: 216 kV/m
EL record: 232 kV/m
EF record: 248 kV/m,

where the number represents the full scale value.

Flight 85 - 026

The constant bandwidth frequency modulation recordings reveal four strikes. The strike corresponding to 19:31:34.8 (trigger time) shows a gradual buildup of the fields until the strike occurs. This record was digitized and multiplied by the F106B shape factors [13] to obtain the ambient field shown in Figure 3.3. The time scales on the plots are arbitrary and serve only to indicate the overall time span analyzed. The derived electric field components at the time of the strike are:

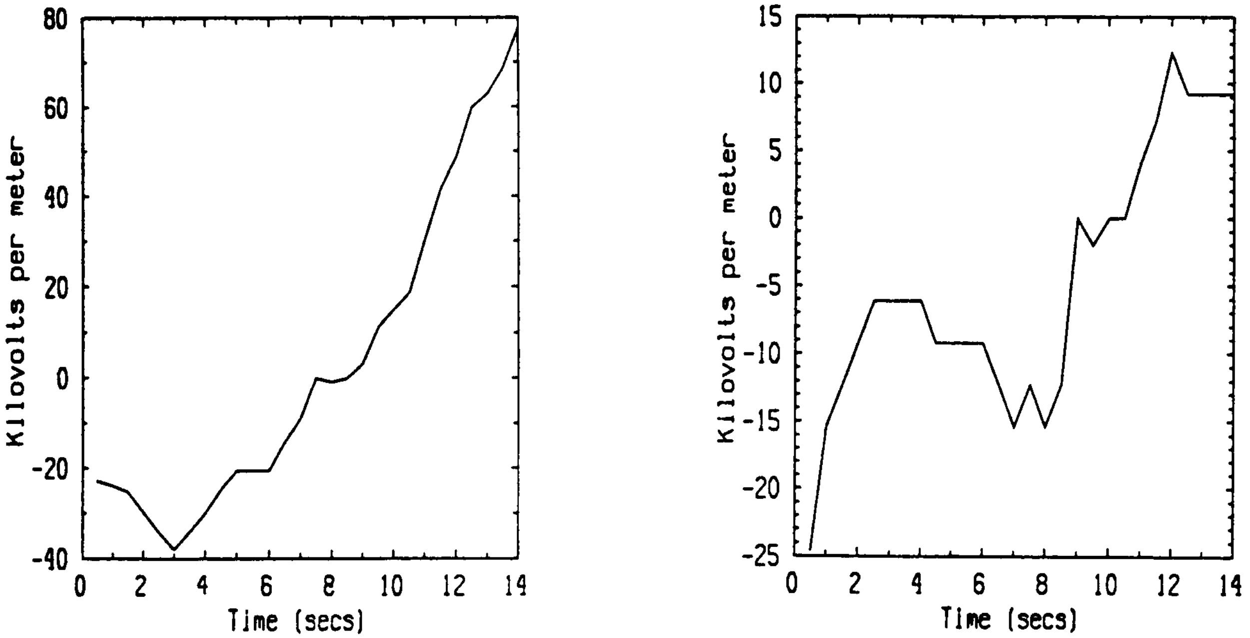

Ex Field
TRIGGER TIME = 19:31:34.8
Flight 85-26

Ey Field
TRIGGER TIME = 19:31:34.8
Flight 85-26

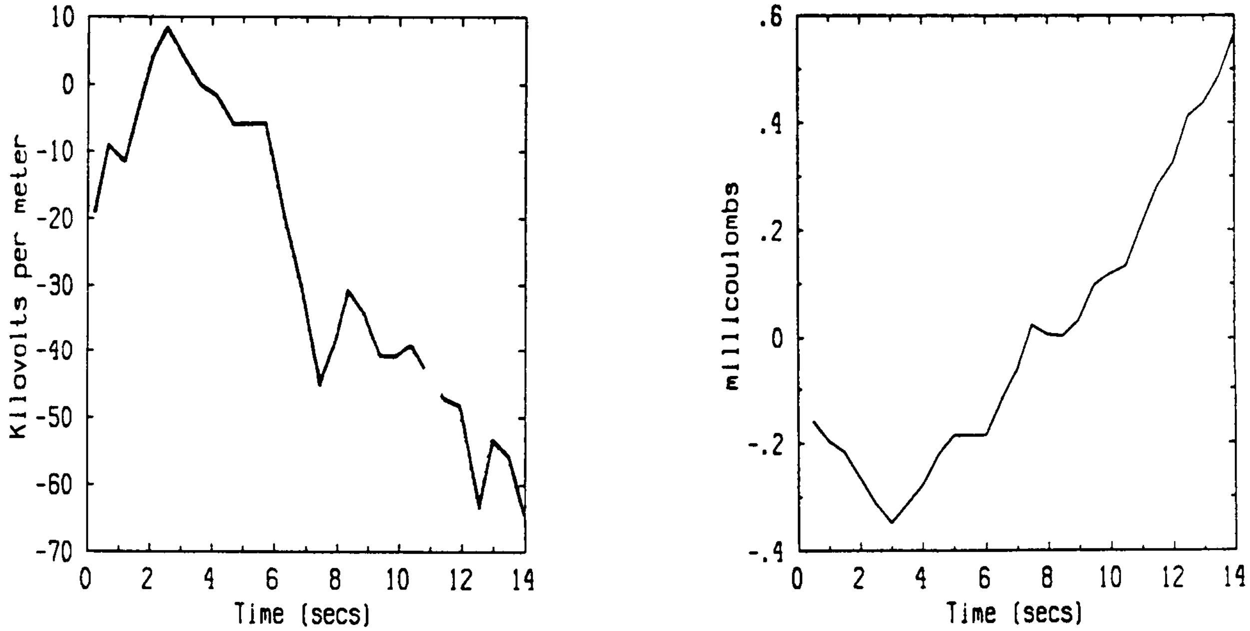

Ez Field
TRIGGER TIME = 19:31:34.8
Flight 85-26

Q
TRIGGER TIME = 19:31:34.8
Flight 85-26

Figure 3.3 Calculated Ambient Fields Just Prior to the Strike (Strike Time Is at 14 Seconds)

$E_x = 77{,}578$ V/m
$E_y = 9{,}234$ V/m
$E_z = -69{,}875$ V/m
Q = 566.8 microcoulombs.

The E_x field and the charge show a steady increase in time. This coupling of the field and charge is due to the character of the shape factor matrix. The maximum local field at trigger time due to the aircraft enhancement is roughly .96 MV/m. The value needed to trigger a strike for the nonlinear code is approximately 1.4 MV/m when the relative air density is .5. In order to obtain a transient response from the nonlinear model, the components of the recorded ambient field were boosted by the ratio of the minimum field required to trigger a strike and the measured field at the time of the strike. This amounts to preserving the orientation of the maximum electric field vector and increasing the magnitude by a factor of 1.46. The transient response of the nonlinear code is shown in Figures 3.4 - 3.8.

The ambient fields corresponding to the 20:13:15.2 strike were digitized starting at 50 seconds before the strike (Figure 3.9). The field mill records are quite oscillatory for much of this period. Prior to the strike there is a high frequency event which could not be adequately resolved. The resulting fields and charge are quite oscillatory and do not have the desired gradual increase until a strike occurs (as in the previous case). It would appear that the spatial variation of the fields is significant in this case.

The EF record corresponding to the 19:51:21.8 strike has a number of large events prior to the strike. Digitization of this record yields ambient fields which clearly show the presence of these events (Figure 3.10). These events are possibly due to nearby electrical activity.

Flight 85-028

This record contains one strike at 18:32:45.9. The fields gradually build up in the desired fashion. The ambient fields for this event are shown in Figure 3.11. As in the previous flight, the E_x field and charge gradually build up until the strike occurs. The ambient field components are :

(text continued on page 77)

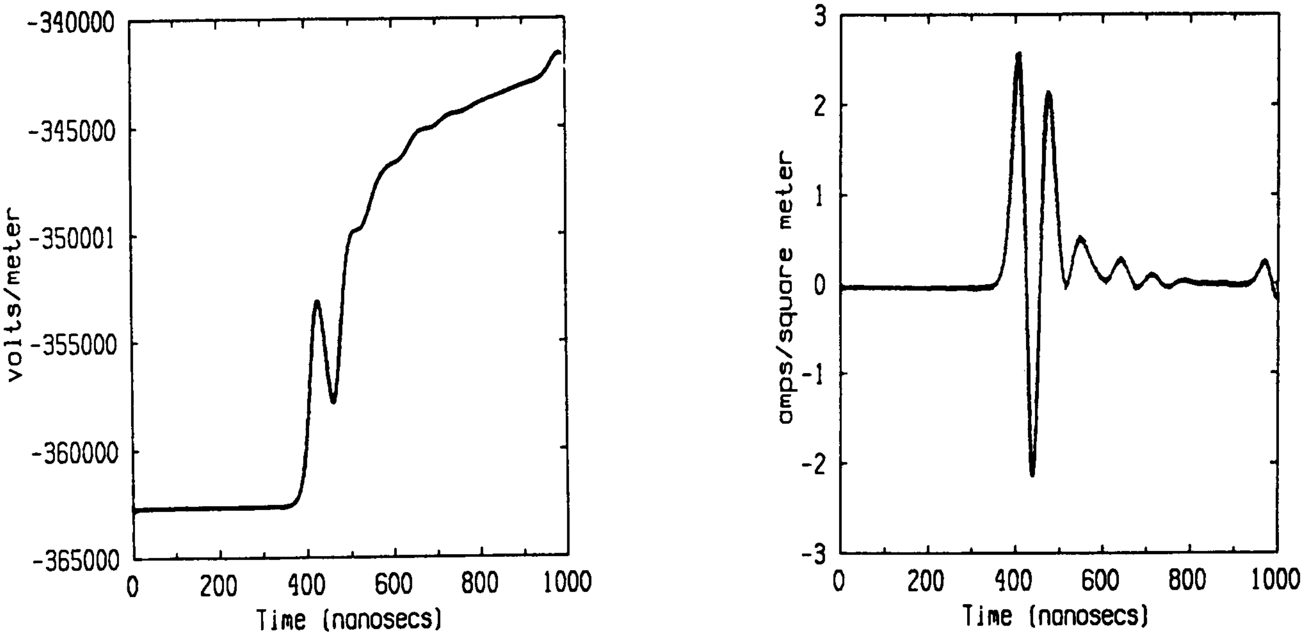

Ez Right Wing
Trigger time = 19:31:34.8
Flight 85-26

D-dot Right Wing
Trigger time = 19:31:34.8
Flight 85-26

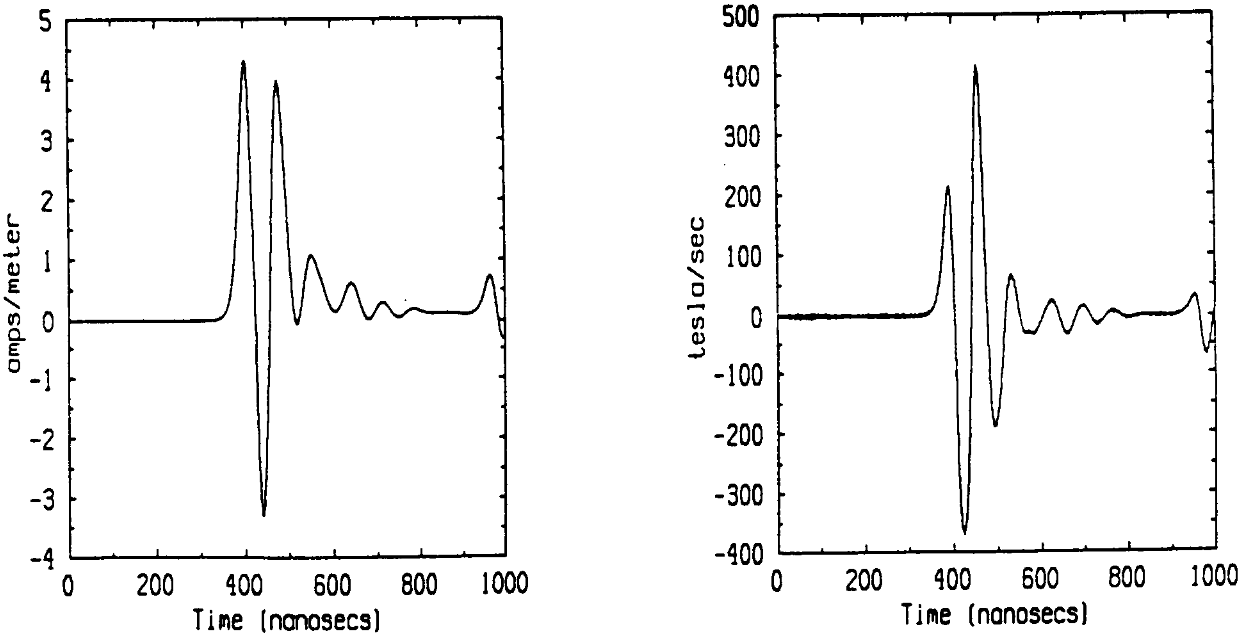

Hx Transverse
Trigger time = 19:31:34.8
Flight 85-26

B-dot Transverse
Trigger time = 19:31:34.8
Flight 85-26

Figure 3.4 Calculated Transient Response

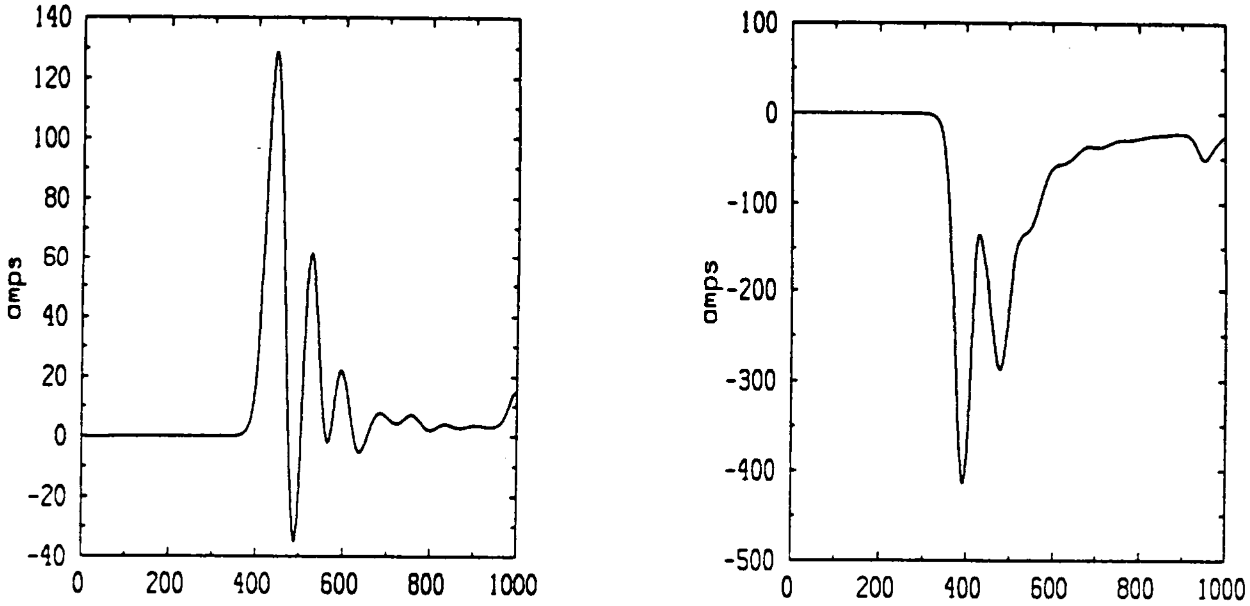

Current from Breakdown at Nose
Trigger time = 19:31:34.8
Flight 85-26

Current from Tail
Trigger time = 19:31:34.8
Flight 85-26

Figure 3.5 Calculated Transient Response

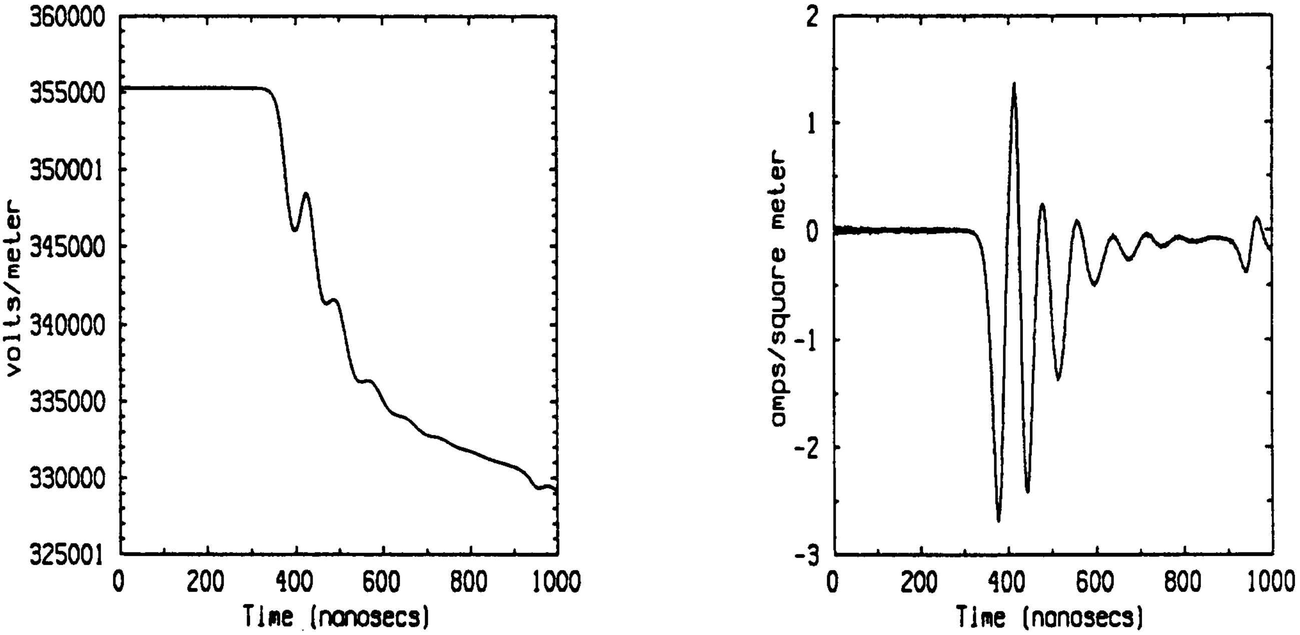

Ey Tail

Trigger time = 19:31:34.8
Flight 85-26

D-dot Tail

Trigger time = 19:31:34.8
Flight 85-26

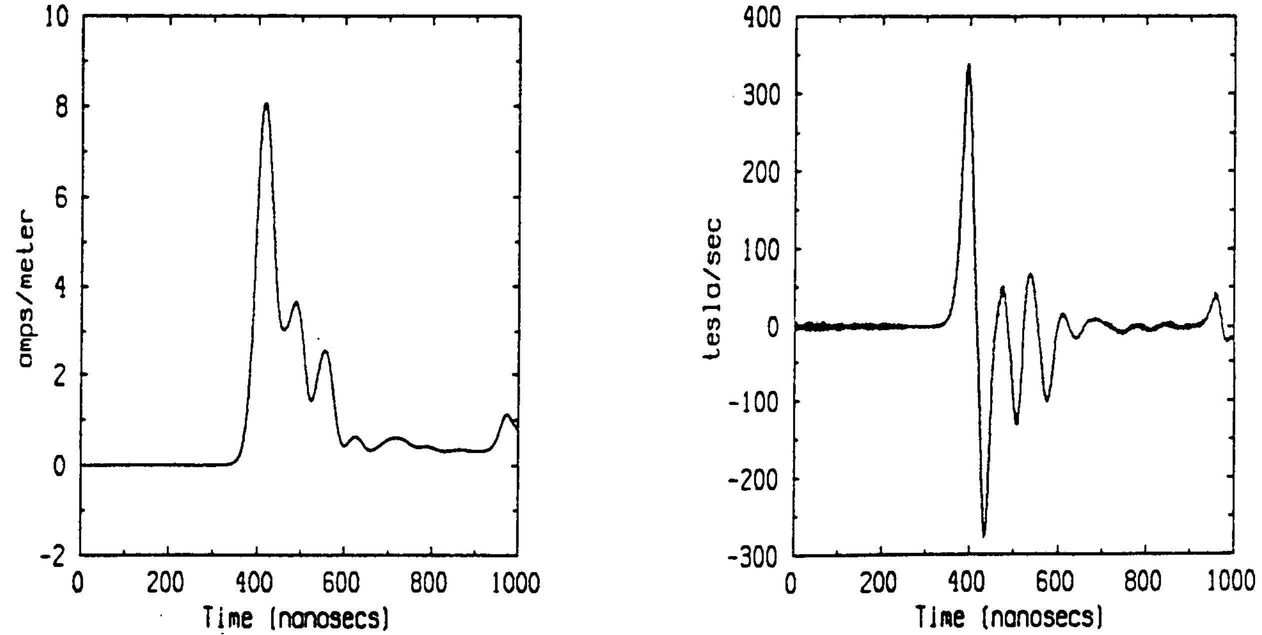

Hy Longitudinal

Trigger time = 19:31:34.8
Flight 85-26

B-dot Longitudinal

Trigger time = 19:31:34.8
Flight 85-26

Figure 3.6 Calculated Transient Response

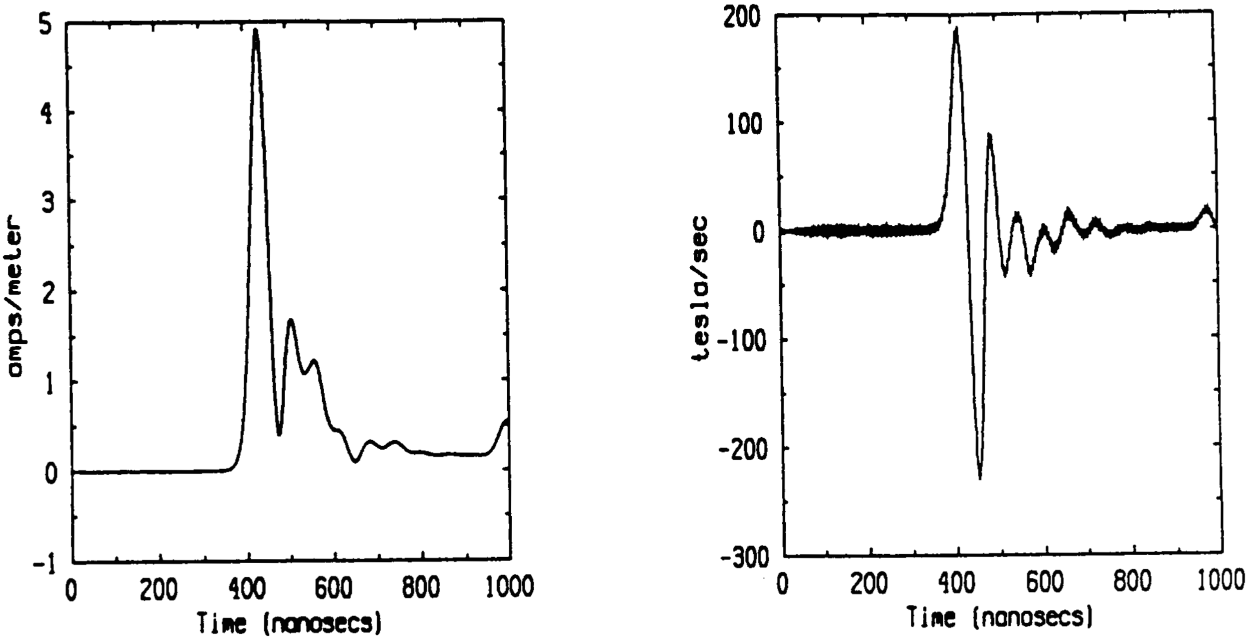

Hx Right Wing
Trigger time = 19:31:34.8
Flight 85-26

B-dot Right Wing
Trigger time = 19:31:34.8
Flight 85-26

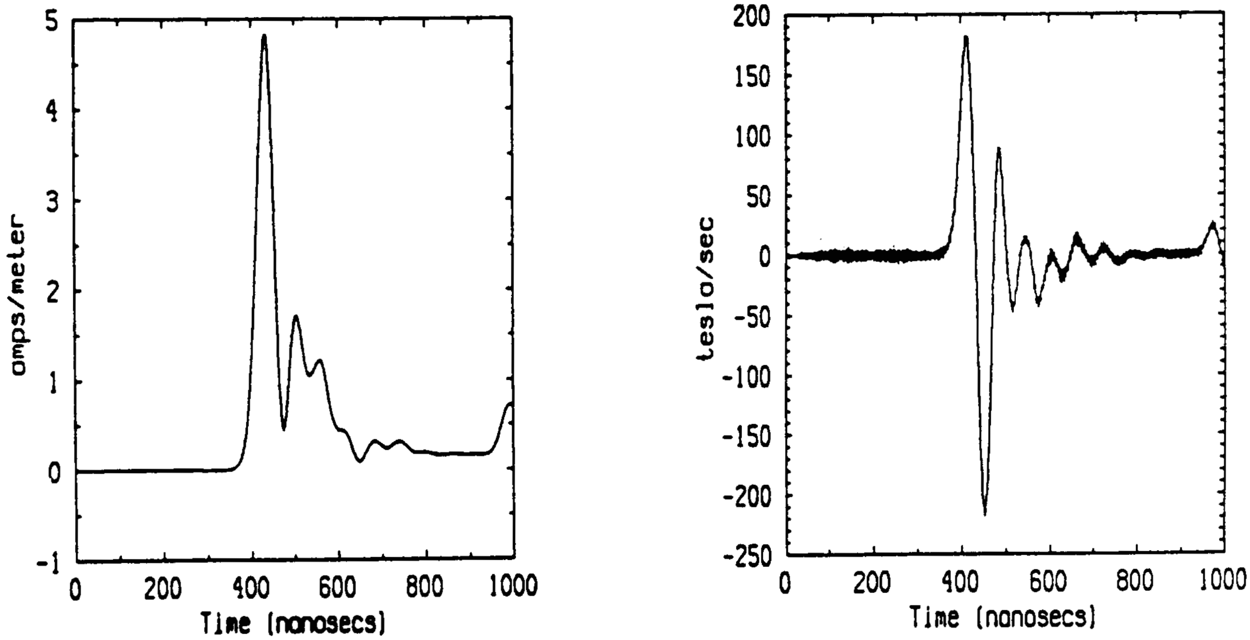

Hx Left Wing
Trigger time = 19:31:34.8
Flight 85-26

B-dot Left Wing
Trigger time = 19:31:34.8
Flight 85-26

Figure 3.7 Calculated Transient Response

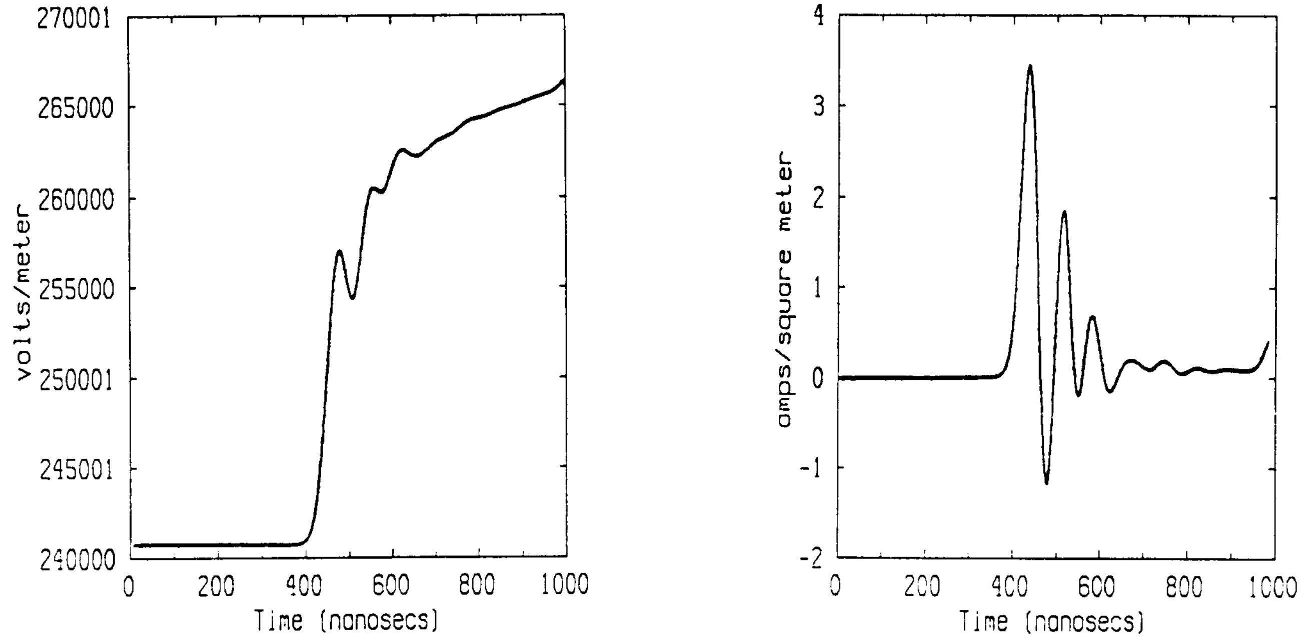

Ez Forward

Trigger time = 19:31:34.8
Flight 85-26

D-dot Forward

Trigger time = 19:31:34.8
Flight 85-26

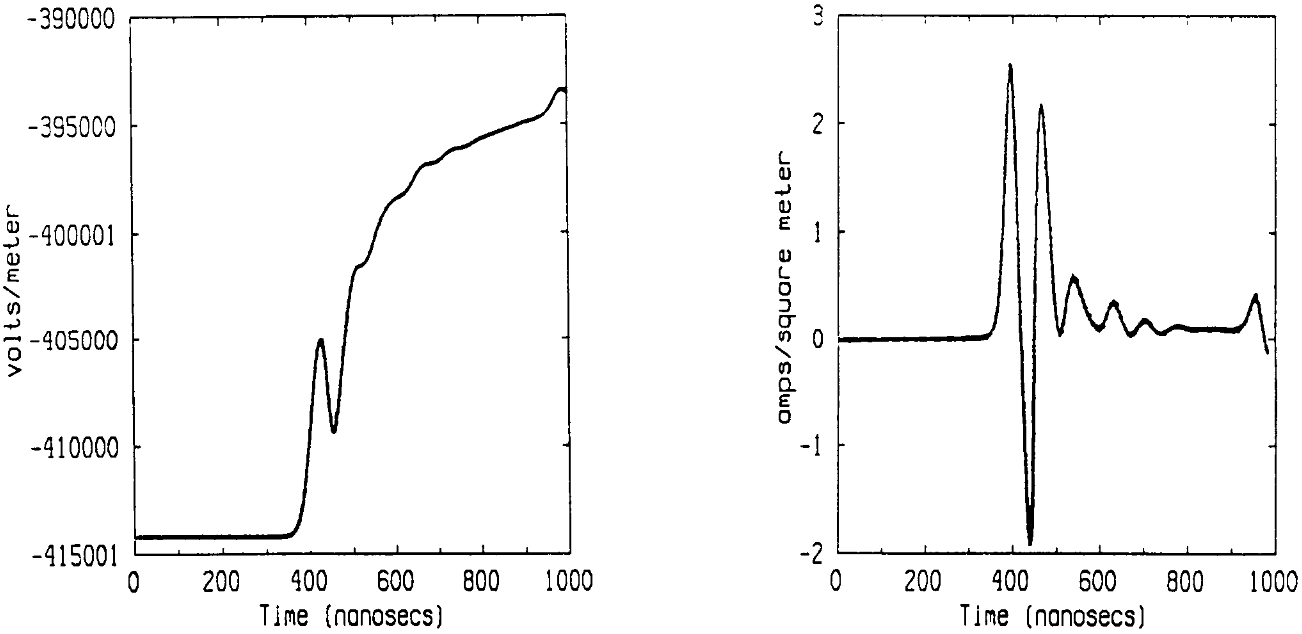

Ez Left Wing

Trigger time = 19:31:34.8
Flight 85-26

D-dot Left Wing

Trigger time = 19:31:34.8
Flight 85-26

Figure 3.8 Calculated Transient Response

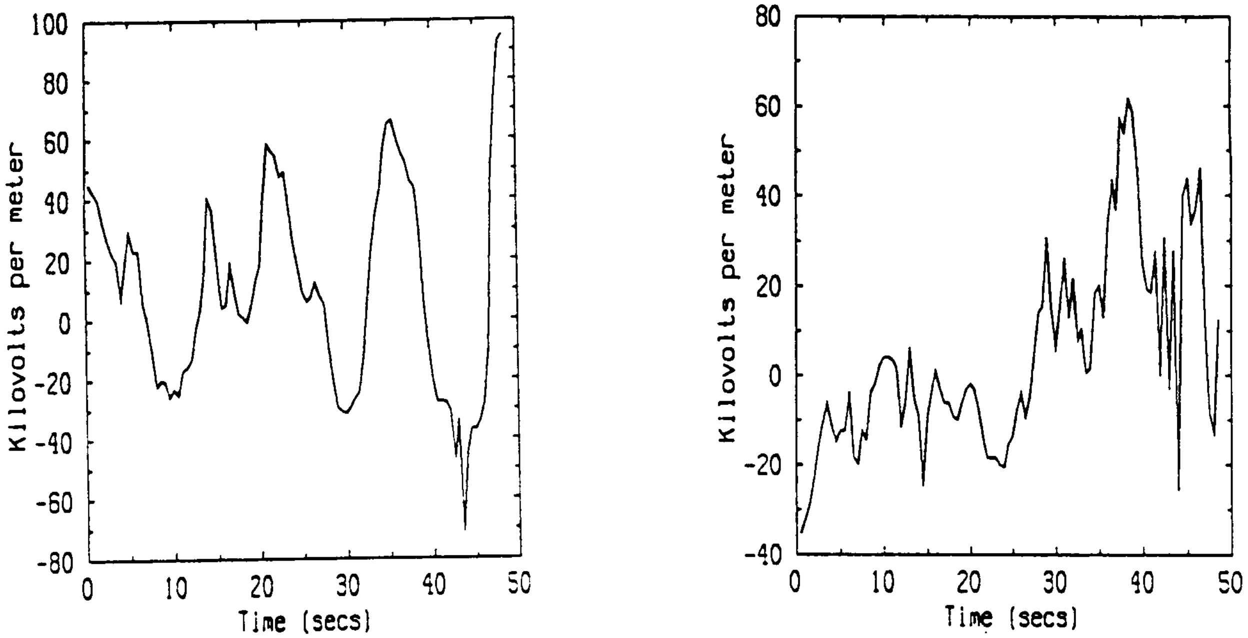

Ex Field

TRIGGER TIME = 20:13:15.2
Flight 85-26 CBW - FM

Ey Field

TRIGGER TIME = 20:13:15.2
Flight 85-26 CBW - FM

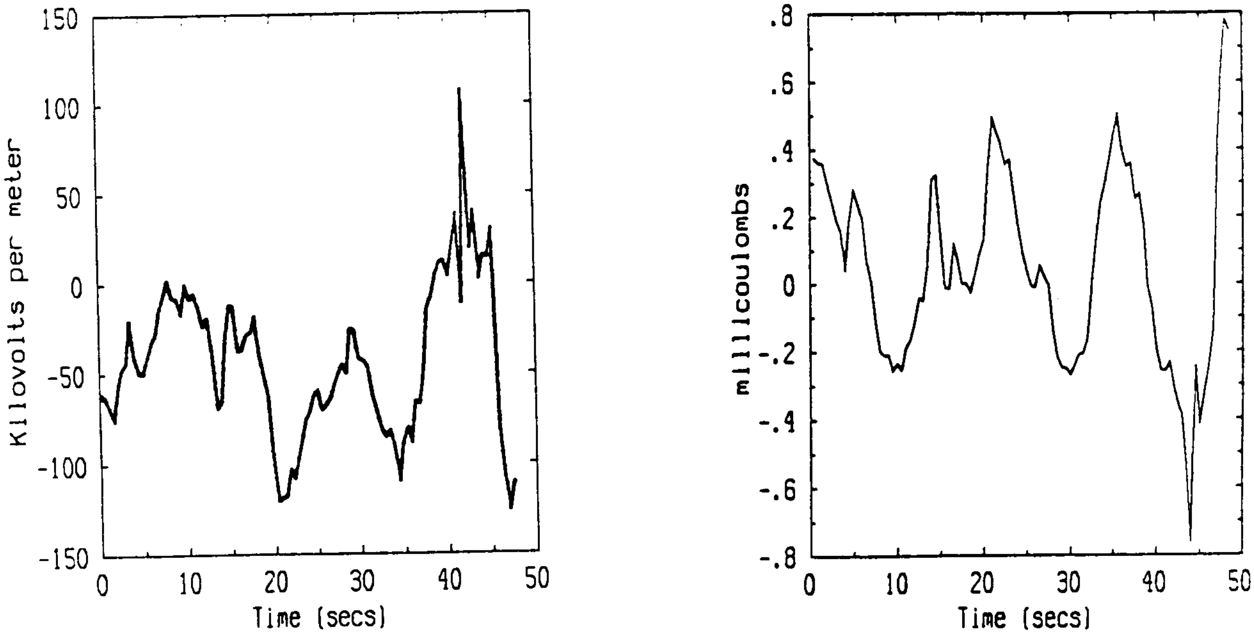

Ez Field

TRIGGER TIME = 20:13:15.2
Flight 85-26 CBW - FM

Q

TRIGGER TIME = 20:13:15.2
Flight 85-26 CBW - FM

Figure 3.9 Calculated Ambient Fields Just Prior to the Strike (Strike Time Is at 48 Seconds)

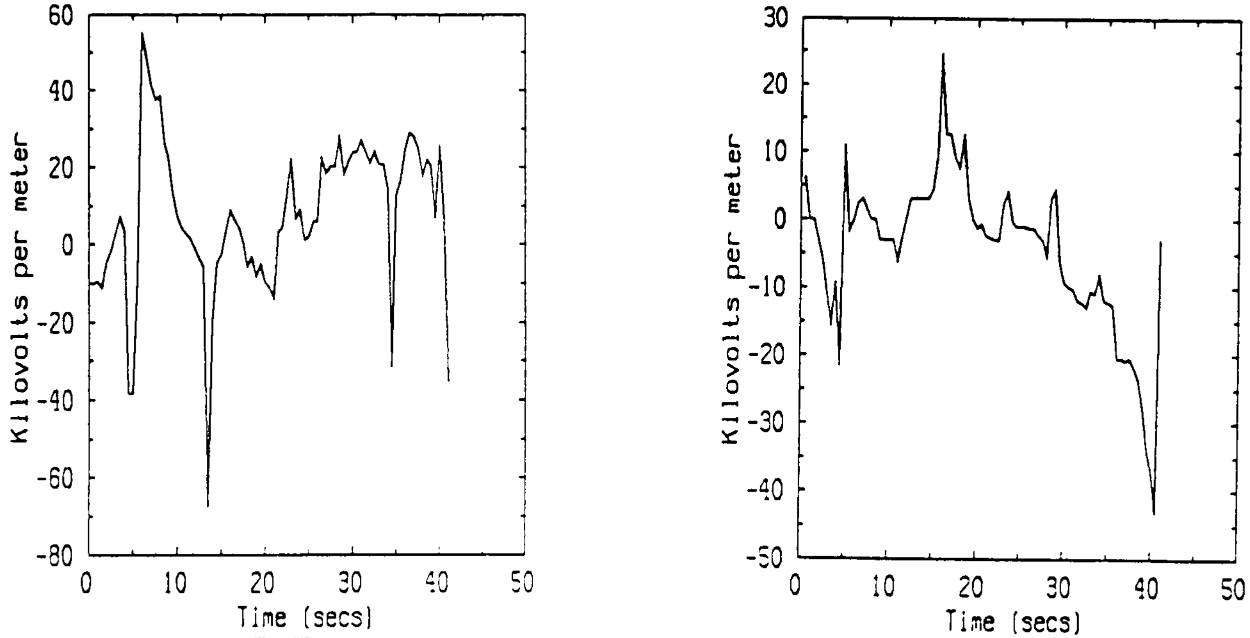

Ex Field

TRIGGER TIME = 19:51:21.8
Flight 85-26 CBW - FM

Ey Field

TRIGGER TIME = 19:51:21.8
Flight 85-26 CBW - FM

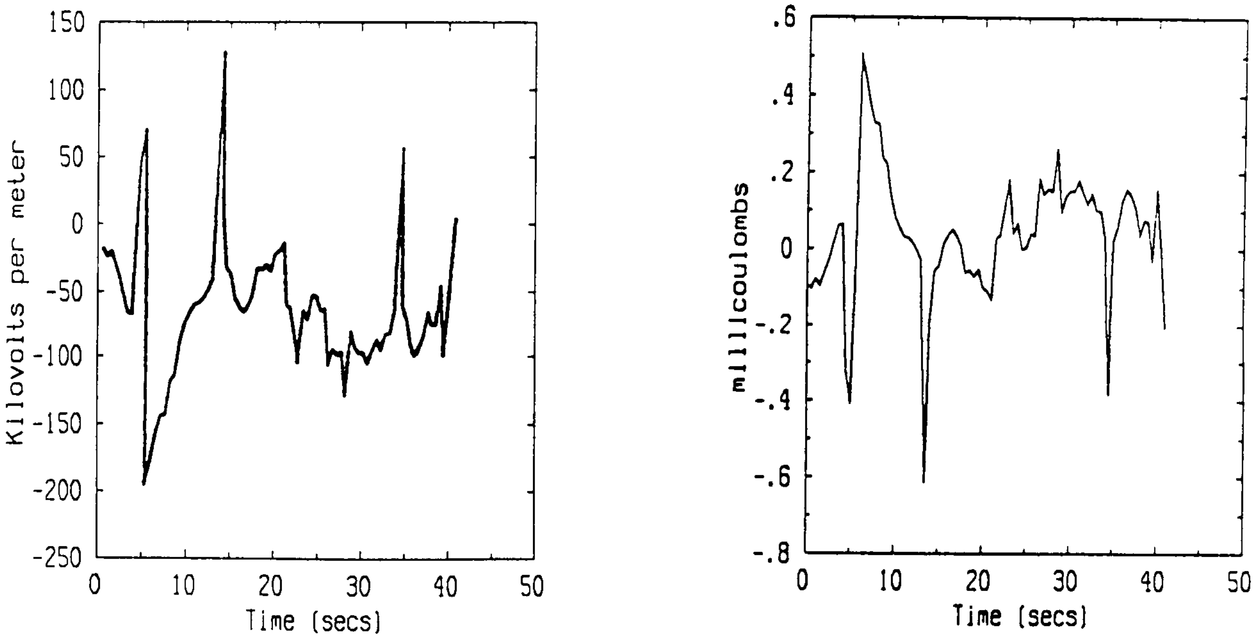

Ez Field

TRIGGER TIME = 19:51:21.8
Flight 85-26 CBW - FM

Q

TRIGGER TIME = 19:51:21.8
Flight 85-26 CBW - FM

Figure 3.10 Calculated Ambient Fields Just Prior to the Strike (Strike Time Is at 40 Seconds)

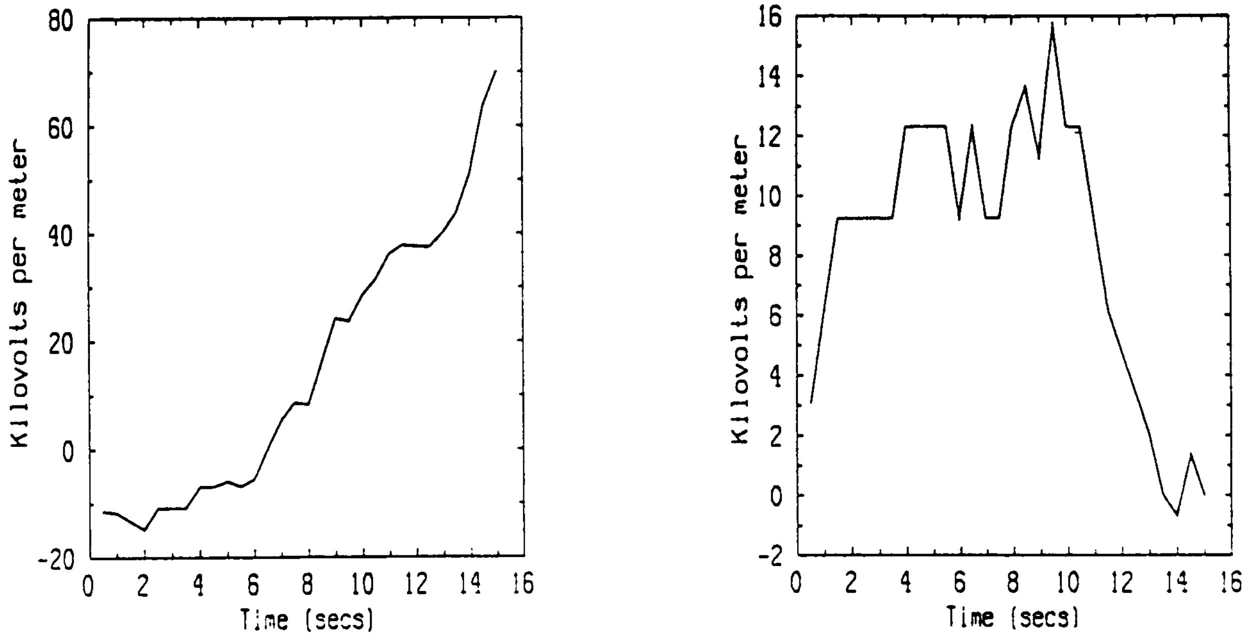

Ex Field
TRIGGER TIME = 18:32:45.9
Flight 85-28 CBW - FM

Ey Field
TRIGGER TIME = 18:32:45.9
Flight 85-28 CBW - FM

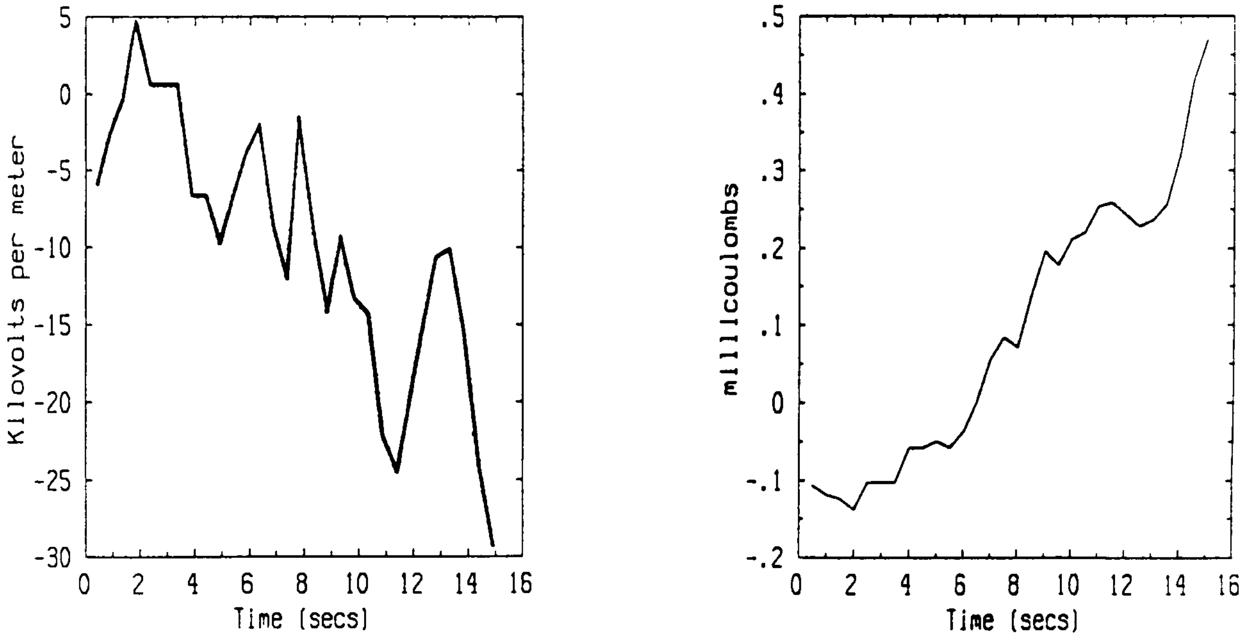

Ez Field
TRIGGER TIME = 18:32:45.9
Flight 85-28 CBW - FM

Q
TRIGGER TIME = 18:32:45.9
Flight 85-28 CBW - FM

Figure 3.11 Calculated Ambient Fields Just Prior to the Strike (Strike Time Is at 15 Seconds)

E_x = 70,145 V/m
E_y = 0 V/m
E_z = - 29,124 V/m
Q = 469 microcoulombs

The largest local field due to aircraft enhancement is .73 MV/m. In order to trigger the nonlinear code the fields must be boosted by approximately 90%.

Flight 85-029

The field mill data for this flight contains 12 strikes. Many of the events on the constant bandwidth frequency modulated (CBW - FM) records are quite 'noisy'. It does not appear that analysis of these events would yield reliable results (see for example Figure 3.12). In other cases the fields just prior to the strike show little change and do not appear to gradually build up in the desired fashion. This would indicate abrupt changes in the ambient fields or problems with the field mills. As an example, the ambient fields for the strike at 17:04:44.2 are shown in Figure 3.13. The pulses in the EF record are seen to be superimposed on ambient fields which do not vary greatly.

The strike occurring at 16:54:22.9 appears to have a relatively noise-free buildup. The ambient fields prior to the strike are shown in Figure 3.14. The field components at strike time are:

E_x = 29,133 V/m
E_y = 18,468 V/m
E_z = 67,830 V/m
Q = -755 microcoulombs

The largest field due to aircraft enhancement is .773 MV/m. The altitude of this flight is 39,000 feet. The minimum field required to trigger the nonlinear code is .943 MV/m or a boost of roughly 22%. Figures 3.15 - 3.19 show the transient response of the nonlinear model.

(text continued on page 86)

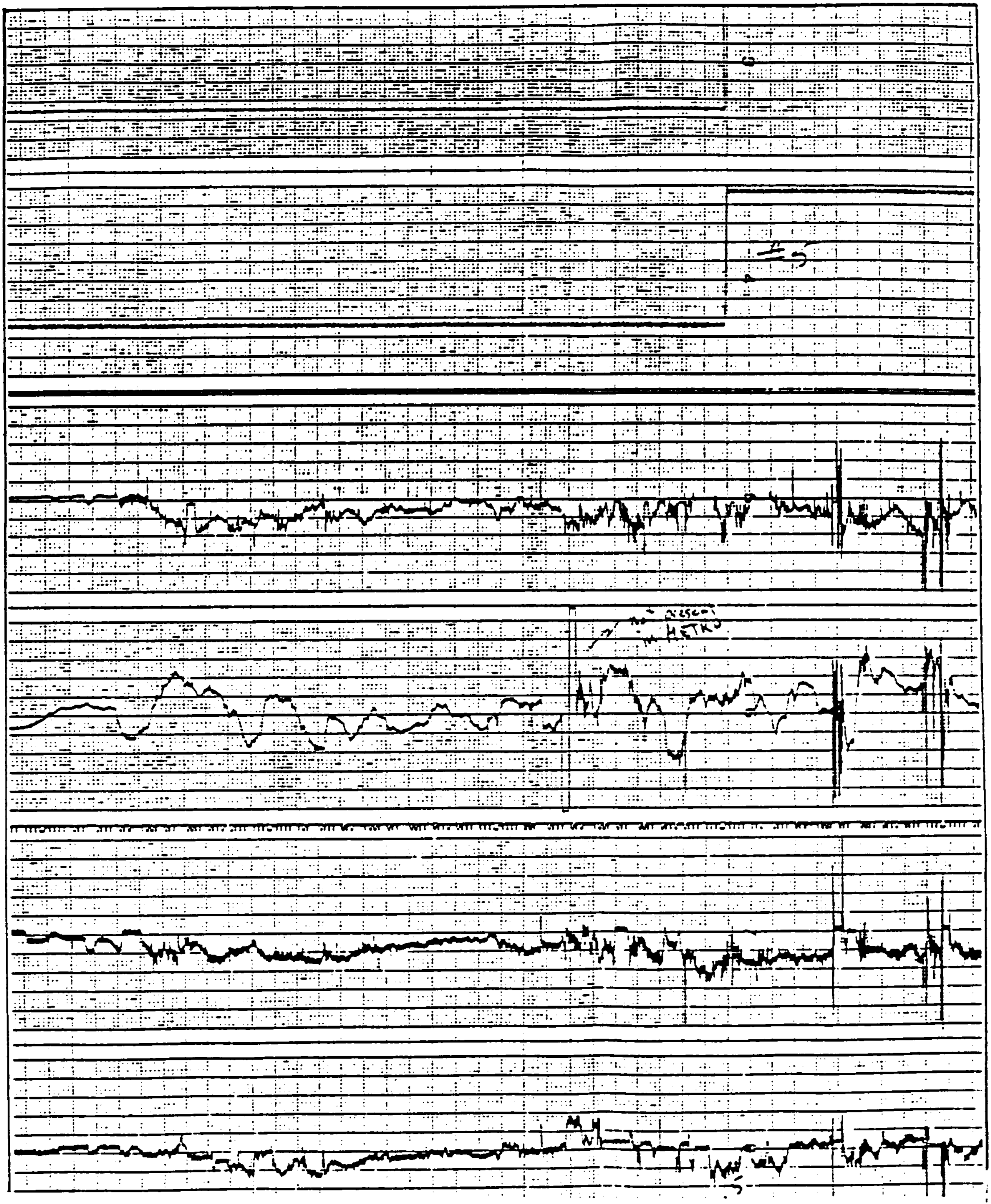

Figure 3.12 Example of Noisy Field Mill Data. The Step Response in the Top Two Traces Defines the Trigger Time

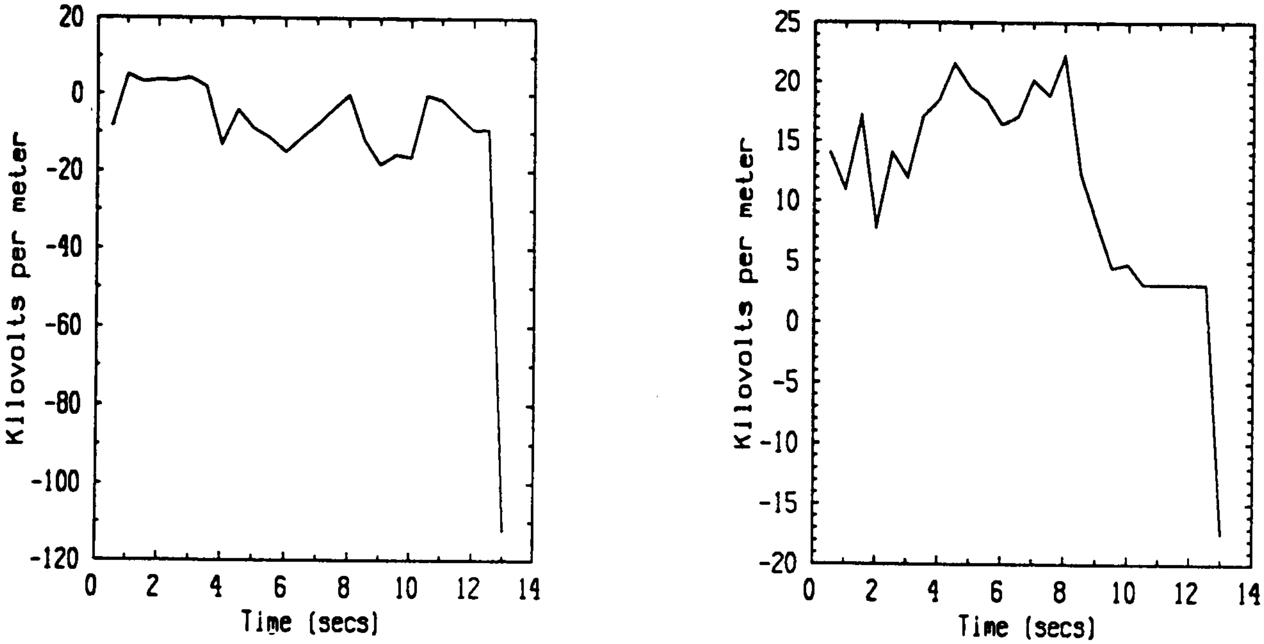

Ex Field

TRIGGER TIME = 17:04:44.2
Flight 85-29 CBW - FM

Ey Field

TRIGGER TIME = 17:04:44.2
Flight 85-29 CBW - FM

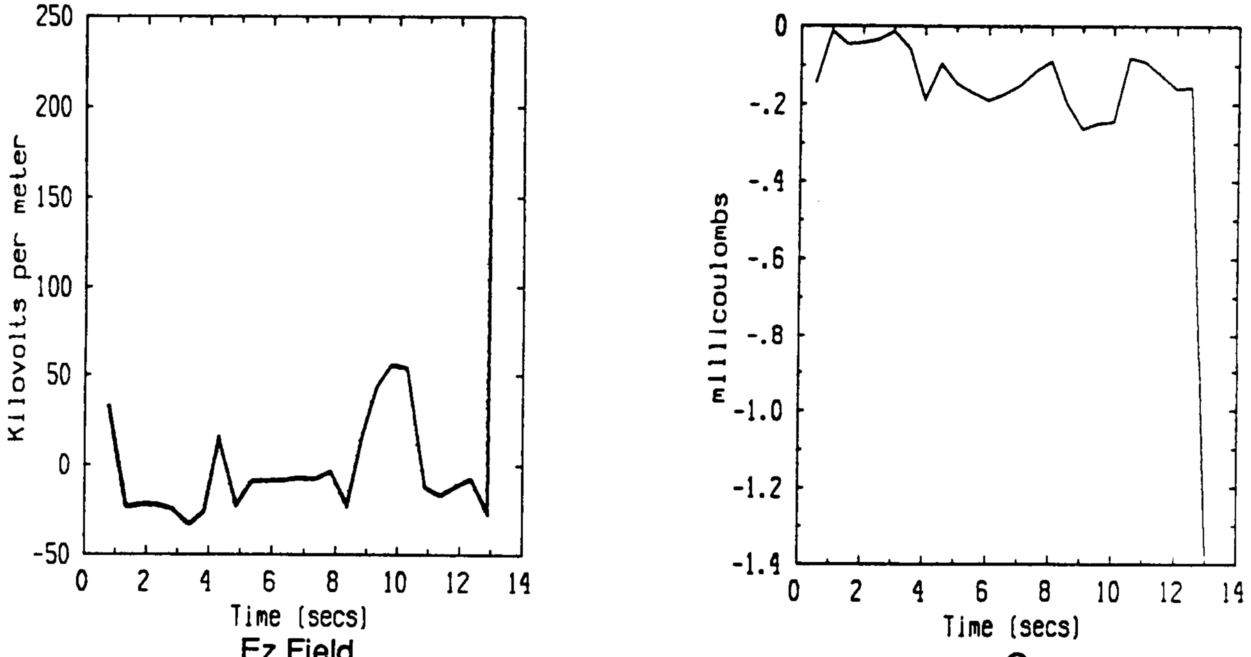

Ez Field

TRIGGER TIME = 17:04:44.2
Flight 85-29 CBW - FM

Q

TRIGGER TIME = 17:04:44.2
Flight 85-29 CBW - FM

Figure 3.13 Calculated Ambient Fields Just Prior to the Strike (Strike Time Is at 13 Seconds)

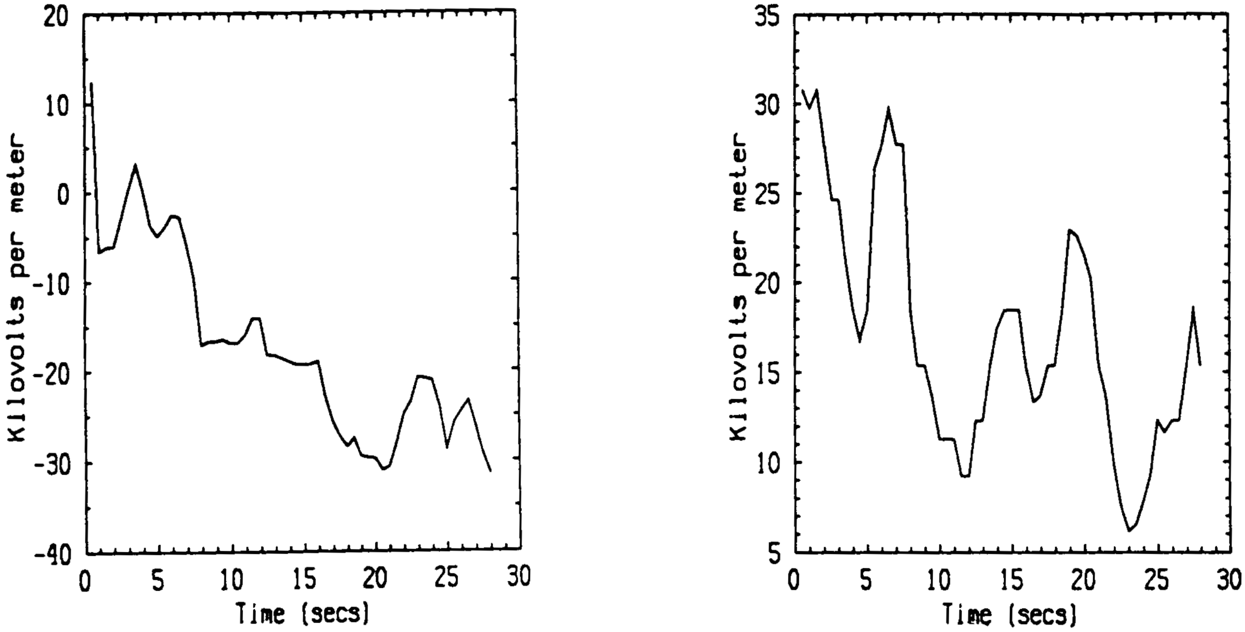

Ex Field

TRIGGER TIME = 16:54:22.9
Flight 85-29 CBW - FM

Ey Field

TRIGGER TIME = 16:54:22.9
Flight 85-29 CBW - FM

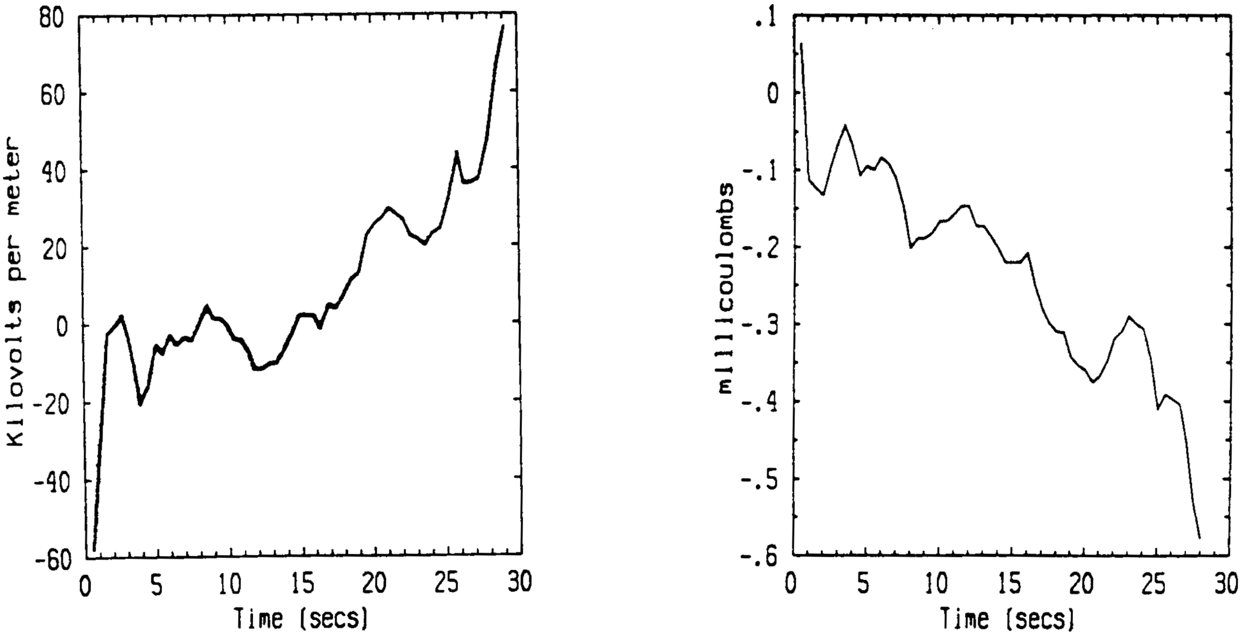

Ez Field

TRIGGER TIME = 16:54:22.9
Flight 85-29 CBW - FM

Q

TRIGGER TIME = 16:54:22.9
Flight 85-29 CBW - FM

Figure 3.14 Calculated Ambient Fields Just Prior to the Strike (Strike Time Is at 28 Seconds)

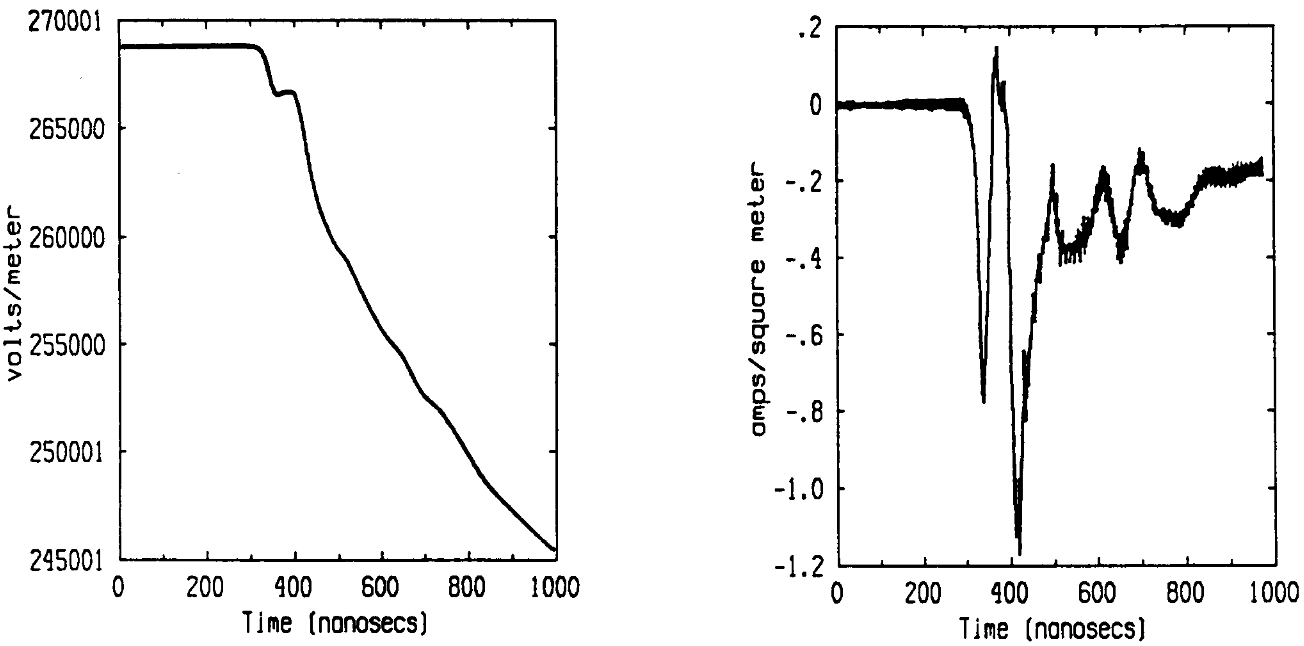

Ez Right Wing
Trigger time = 16:54:22.9
Flight 85-29

D-dot Right Wing
Trigger time = 16:54:22.9
Flight 85-29

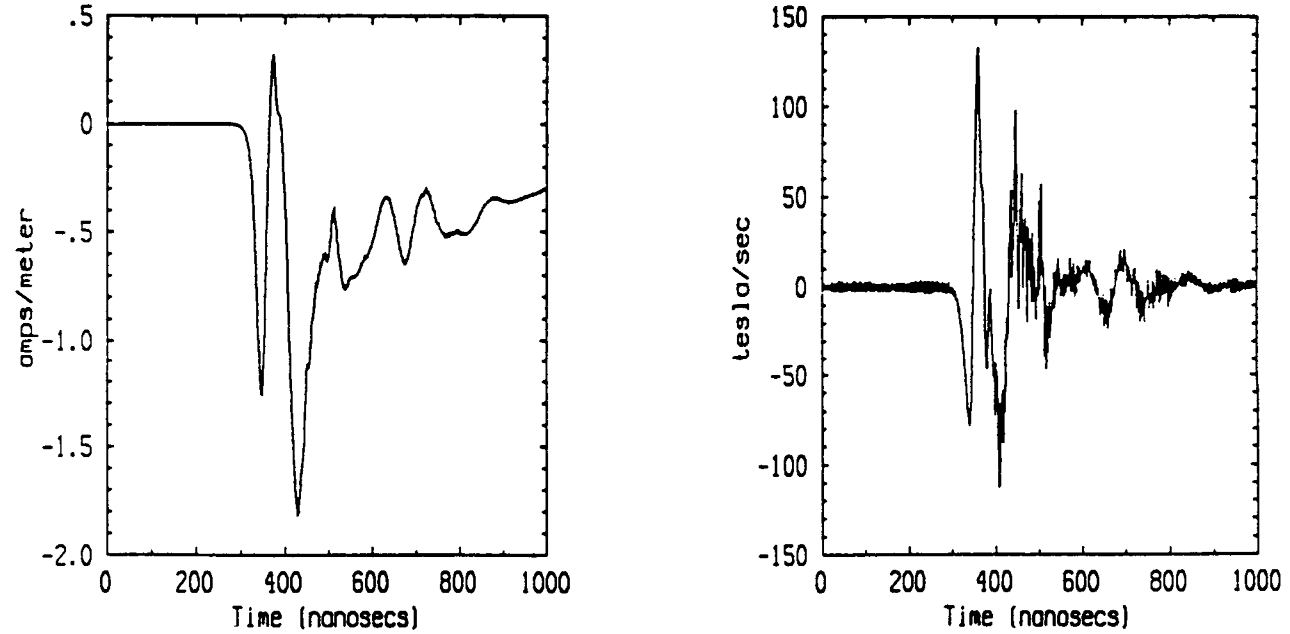

Hx Transverse
Trigger time = 16:54:22.9
Flight 85-29

B-dot Transverse
Trigger time = 16:54:22.9
Flight 85-29

Figure 3.15 Calculated Transient Response

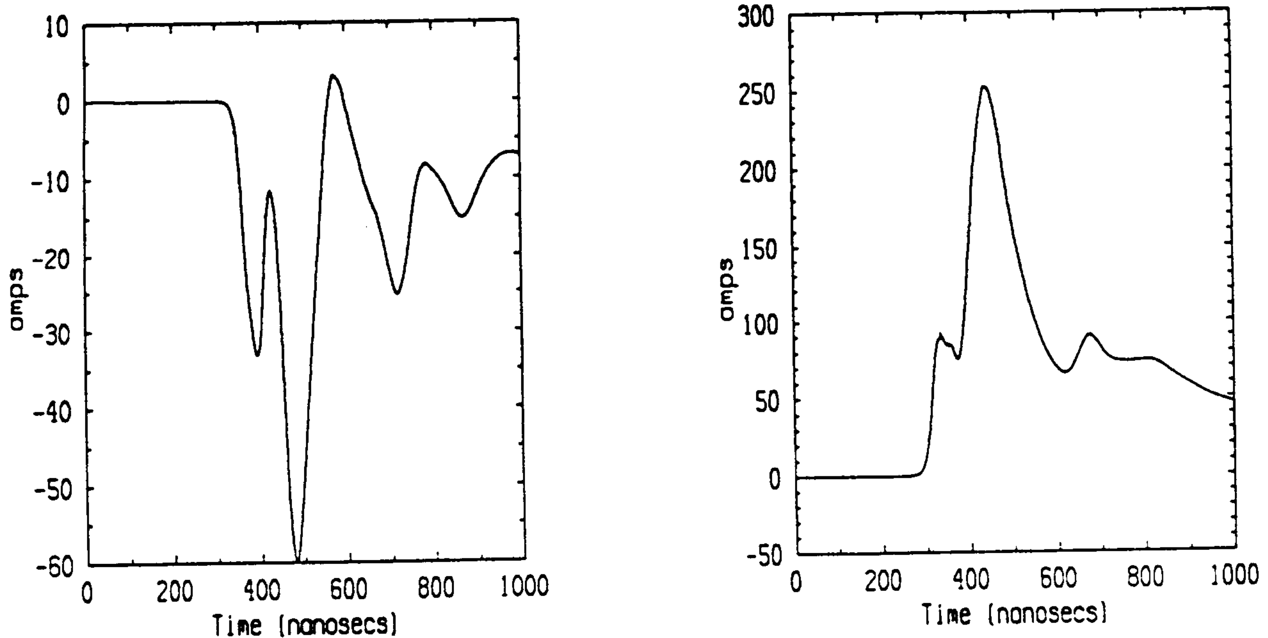

Current from Break Down at Nose

Trigger time = 16:54:22.9
Flight 85-29

Current from Tail

Trigger time = 16:54:22.9
Flight 85-29

Figure 3.16 Calculated Transient Response

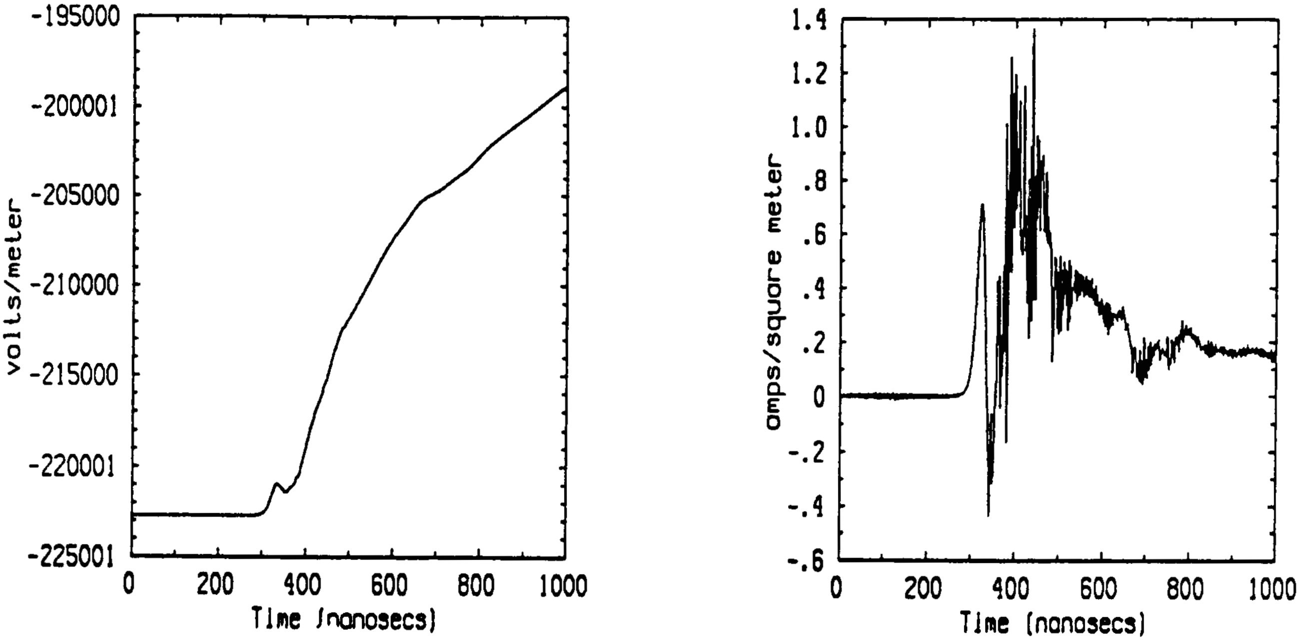

Ey tail
Trigger time = 16:54:22.9
Flight 85-29

D-dot tail
Trigger time = 16:54:22.9
Flight 85-29

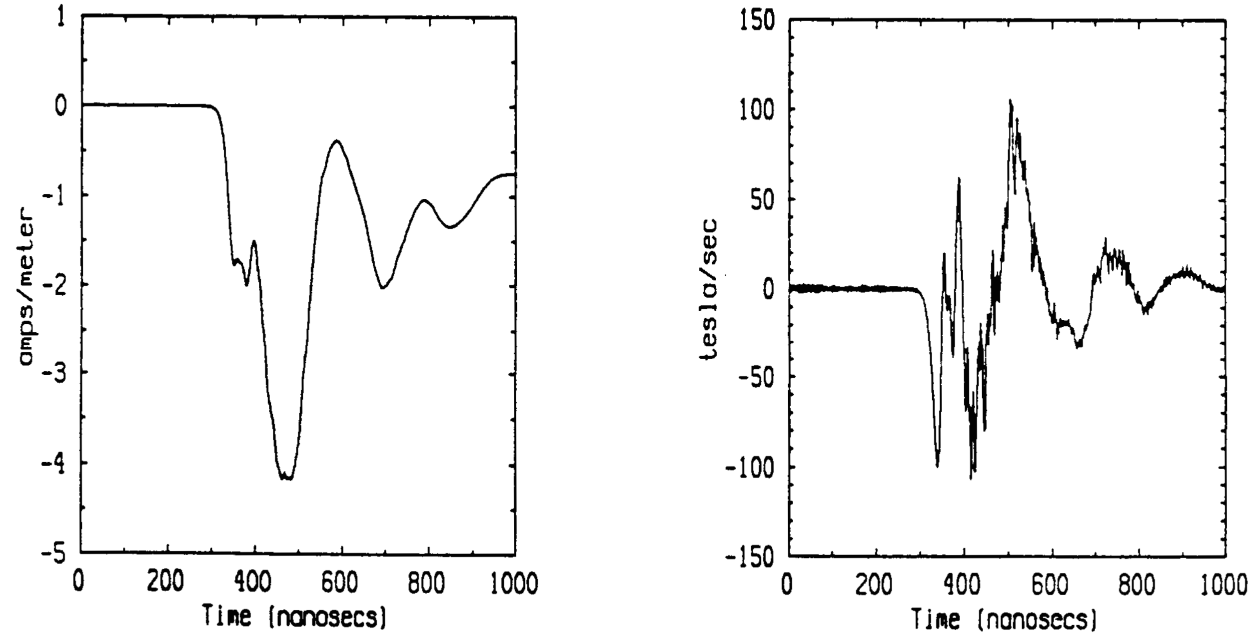

Hy Longitudinal
Trigger time = 16:54:22.9
Flight 85-29

B-dot Longitudinal
Trigger time = 16:54:22.9
Flight 85-29

Figure 3.17 Calculated Transient Response

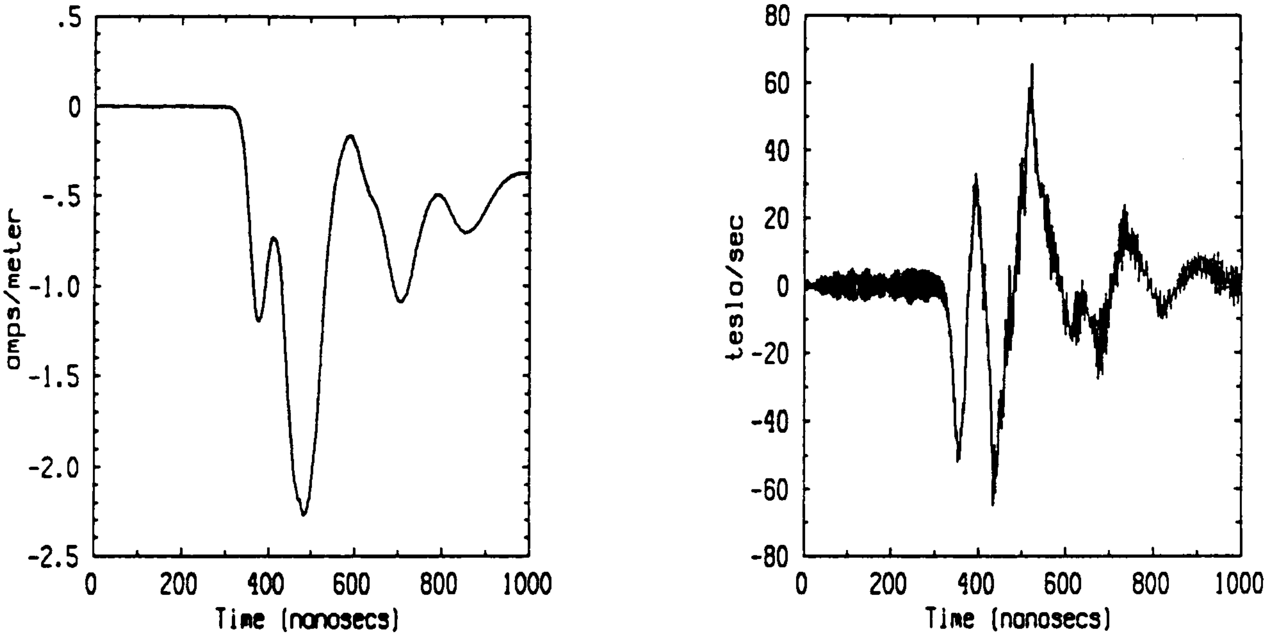

Hx Right Wing

Trigger time = 16:54:22.9
Flight 85-29

B-dot Right Wing

Trigger time = 16:54:22.9
Flight 85-29

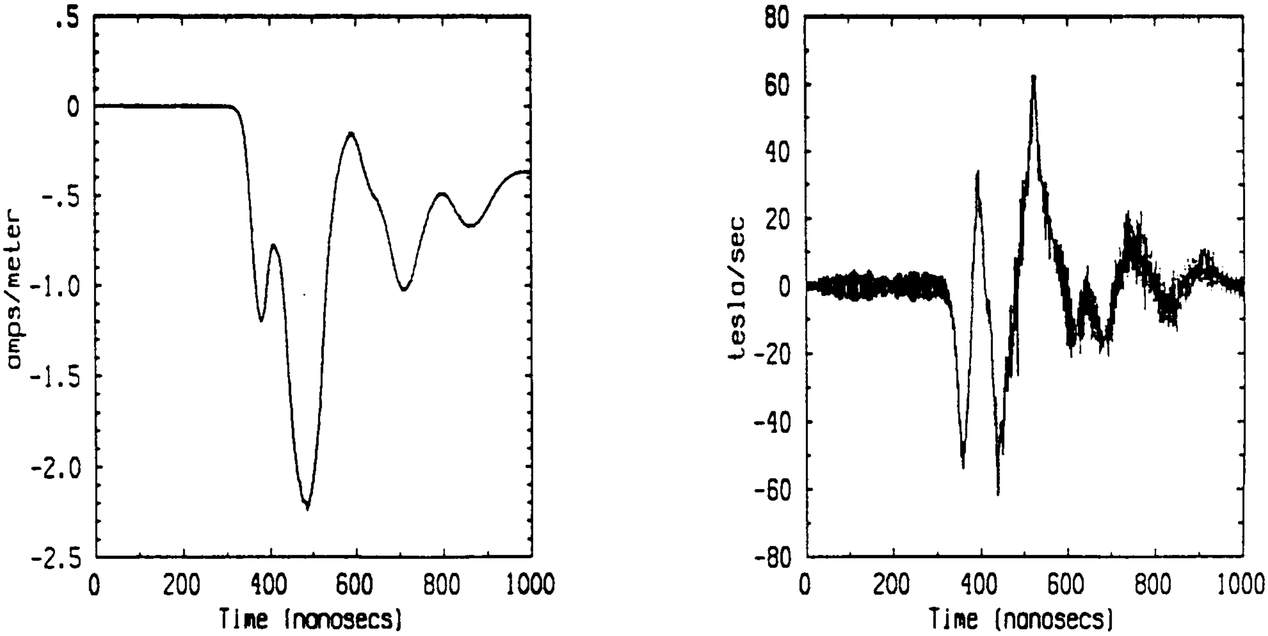

Hx Left Wing

Trigger time = 16:54:22.9
Flight 85-29

B-dot Left Wing

Trigger time = 16:54:22.9
Flight 85-29

Figure 3.18 Calculated Transient Response

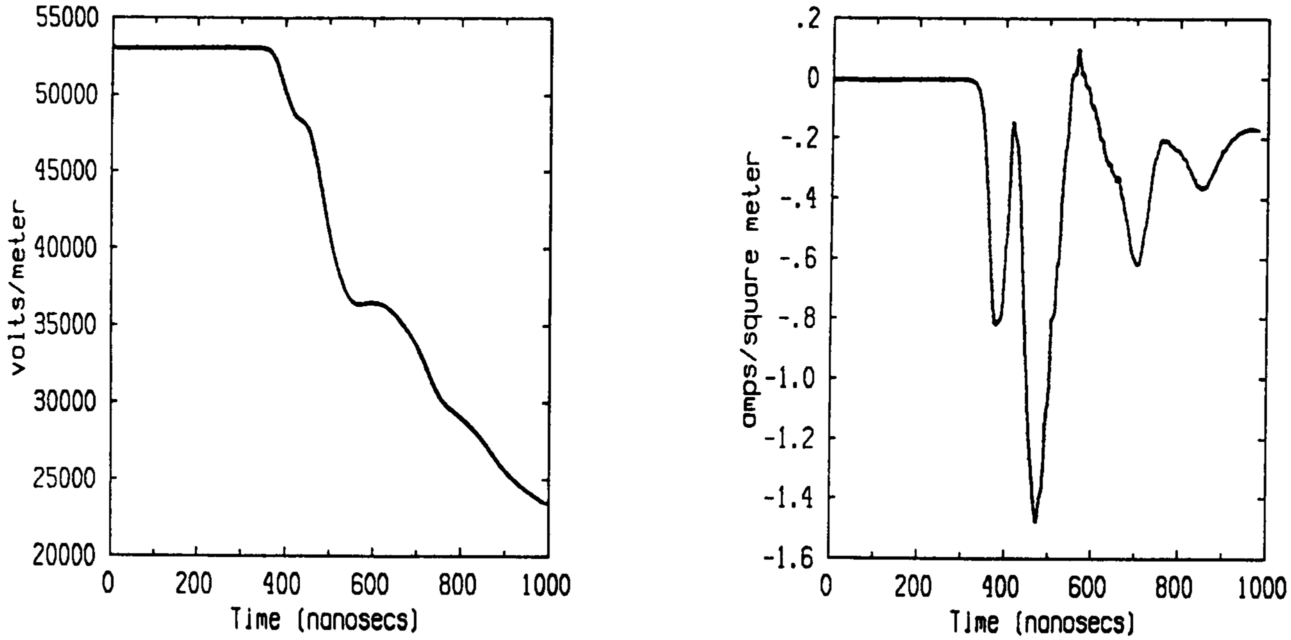

Ez Forward
Trigger time = 16:54:22.9
Flight 85-29

D-dot Forward
Trigger time = 16:54:22.9
Flight 85-29

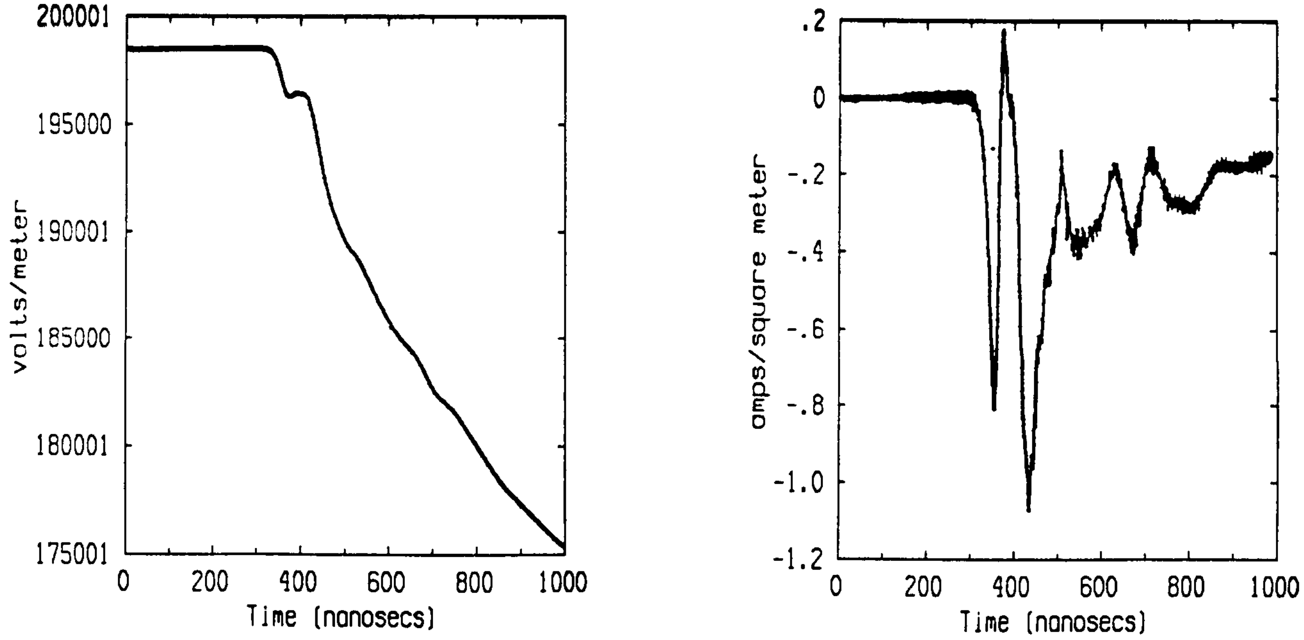

Ez Left Wing
Trigger time = 16:54:22.9
Flight 85-29

D-dot Left Wing
Trigger time = 16:54:22.9
Flight 85-29

Figure 3.19 Calculated Transient Response

3.2 Conclusions

The theoretical model assumes that the fields and charge gradually build up until a strike occurs. It is clear that many of the records analyzed do not show this ideal behavior. Possible reasons for this are: equipment failure, noise from adjacent activity, and abrupt spatial changes in the ambient fields. There are three events which are relatively noise free and show the desired trends. The ambient fields for two of these events were determined and used to calculate a transient response in the nonlinear model. Records of the actual response of the aircraft were not available for comparison at the time of this report.

There are a number of possible sources of error in this analysis. Likely sources are calibration errors and digitization errors. In many instances, the trace is one to two divisions thick, which would yield uncertainties of roughly 10 - 20 kV/m. Stability problems for the shape factor matrix have been reported [14]. It is shown there that relatively small errors can cause significant amplification and reorientation of the calculated fields.

CHAPTER 4
SUBGRID MODEL APPLICATION

4.1 Introduction

In the finite difference solution of Maxwell's equations the spatial resolution of objects in a problem space is restricted by the cell size used. Features that are smaller than the cell size can not be resolved. Thus in the current finite difference models of the F106B, the 1m x 1/2m x 1/2m cell size used does not allow accurate gridding near the nose of the airplane. To improve the resolution, the most straightforward method would be to use a cell size which is small enough to resolve the desired feature. The disadvantage of this method is the greatly increased demand on computer resources in terms of CPU time and memory. In one test, decreasing the cell size from 1m x 1m x 1m to .3m x .3m x .3m resulted in increasing the CPU time by a factor of 25. Worse still is the waste inherent in this method because regions where fine resolution is not needed are nevertheless gridded equally. To avoid these difficulties, the subgrid technique has been developed. The idea is to use a fine grid around the feature of interest only, such as the nose of the F106B, while a coarser grid is used for the rest of the problem space. A technique for such a local refinement of the grid size has been reported previously [4]. This section reports on a modification of the technique and its application to triggered lightning models.

In triggered lightning modeling, the most important parameter is the enhancement factor of the ambient field produced by the aircraft. There are two features which affect the calculation of the maximum enhanced field using the finite difference approximation. The first is the resolution of the extremities (points, edges) of the object. Since sharpness of an object increases the enhancement factor, it is important to model as closely as possible the actual shape for finite difference calculation. Better resolution of extremities is the motivation for the development of the subgrid method. The second feature is a direct consequence of finite difference approximation. For an object of a given shape, the largest local electric fields generally decrease as one moves farther from the metallic surface. Therefore for the same object, a finer grid would automatically show a higher enhancement factor simply because the mesh points are closer to the surface. A fine grid size of 1/6m x 1/3m x 1/6m is used in this study and the nose of the F106B is quite reasonably resolved except for details of the boom.

4.2 Review of the Subgrid Model

The objective of the subgrid technique is to obtain a finite difference solution of Maxwell's equations in a given volume of space which is divided into two regions characterized by different cell sizes. Specifically, the volume of space consists of an inner region of small cell size and an outer region of larger cell size. In the following the terms fine and coarse are used to characterize quantities associated with the fine grid region and the coarse grid region respectively. The boundary between the two regions is called the interface. In the finite difference solution of Maxwell's equations an explicit, centered difference procedure is used. The components of the electric and magnetic field vectors are assigned staggered grid locations. The reader is referred to Reference [14] for further detail. Within each region, the solution of Maxwell's equations proceeds as usual. At the interface a special method has been developed to handle the coupling of the two regions. In the present implementation, the interface is taken to be the surface defined by tangential electric field components. In a previous implementation the interface is defined by the tangential magnetic fields. On the interface the fine grid electric field and magnetic field components are calculated, using standard advance equations, while the coarse grid electric field components are derived from the calculated subgrid fields. When the coarse grid size is an odd multiple of the fine grid size, a coarse grid electric field is at the same location as one of the fine grid fields. Therefore after the fine grid electric fields have been calculated, it is an easy matter to pick up the fine grid fields at the locations of the coarse grid fields and assign their values to the corresponding coarse grid fields. When the coarse grid size is an even multiple of the fine grid size, a given coarse grid field is halfway between two fine grid fields. In this case the average of the two adjacent fine grid fields is assigned to the coarse grid field. With the coarse grid electric fields on the interface having been assigned, the coarse grid magnetic fields nearest to and parallel to the interface can be calculated. These coarse grid magnetic fields are half a coarse cell away from the interface. They are then used to calculate the fine grid electric fields on the interface. To do so, the values of the magnetic fields at the locations appropriate to the fine grid layout are obtained by interpolation of the coarse grid magnetic fields. A simple four point planar interpolation method is used. Thus it is seen that in the calculation of a fine grid electric field on the boundary, one of the magnetic fields used is half a coarse grid cell away inside the coarse grid region. The other three magnetic fields used are all fine grid fields at the usual half fine grid cell away, two of them on and normal to the interface, the other one inside the fine grid region. The procedure is then repeated to advance the solution in time. The procedure is summarized as follows:

(1) Calculate the coarse grid and fine grid magnetic fields.

(2) Interpolate the coarse grid magnetic fields which are nearest and parallel to the interface to obtain values at the locations needed by the fine grid layout. These magnetic field values are used to calculate the fine grid electric fields on the interface.

(3) Calculate the coarse grid and fine grid electric fields. The fine grid fields calculated include those on the interface.

(4) Obtain the coarse grid electric fields on the interface from the fine grid electric fields. These are either equal to the fine grid fields at the same locations or else are set equal to the average of the two nearest adjacent fine grid fields. These coarse grid electric fields are used to calculate the coarse grid magnetic fields nearest and parallel to the interface.

(5) Go to step (1).

A major difficulty arises in step two above if a metallic scatterer penetrates the interface, which is usually the case in the application of the subgrid technique. The difficulty arises from the use of the four point planar interpolation method in the immediate neighborhood of the metallic scatterer. Specifically, the values obtained from the bilinear interpolation are not correct for the magnetic field component parallel to the metallic surface. This is because the zero field inside the metal is used for the interpolation. As a result the interpolated field decreases toward the metallic surface whereas physically the parallel component should increase toward the metallic surface. In the present implementation the parallel component is assumed to remain constant as the metallic surface is approached. Further research to improve the approximation adopted is desirable.

4.3 Application of the Subgrid Model

The subgrid technique has been incorporated into the standard F106B finite difference model. The selection of a particular region in the standard model for the application of the subgrid is made simple by the fact that most of the lightning strikes that attached to the aircraft were initially at the nose of the aircraft. Moreover, most of the strikes are thought to be triggered strikes. It is of interest to study in more detail the initiation and extent of the corona discharge which is the precursor to a full fledged triggered lightning strike. Therefore a subgrid was placed in the region around the nose of the aircraft. The spatial resolution in the standard finite difference model of the F106B is one meter along the fuselage, and one-half meter in the other two coordinate directions. In this application the fine grid size around the nose is taken to be a third of the corresponding coarse grid size resulting in cell size of 1/3m x 1/6m x 1/6m. In volume the subgrid region is five coarse cells in the wing-wing direction, six coarse cells in the vertical direction and eight coarse cells in the fuselage direction. Along the fuselage the boundary of the fine grid region is approximately at the location of the pilot's seat.

The static solution for the field distribution around the F106B was achieved by imposing a field of one volt per meter along the fuselage direction in the whole problem space. This orientation of the static field is appropriate for the study of triggered strikes that attached to the nose of the aircraft. To minimize the excitation of resonances by the sudden imposition of a field on the problem space, the aircraft was initially modeled as a dielectric. Its conductivity was then gradually increased to that of the metal, i.e., infinity. The calculation was terminated once the static condition was reached. The standard finite difference model of the F106B gives a maximum enhancement of 8.9 for the vertical component under the nose of the aircraft. The maximum enhancement using the subgrid size 1/3m x 1/6m x 1/6m is 21.1, again under the nose of the aircraft. In comparison, the maximum enhancement calculated with a subgrid of grid size 1/4m x 1/4m x 1/4m is 19.2 in front of the nose [4]. The high enhancement of field extends for only a few cells from the nose of the aircraft. The fine grid fields more than a few of fine grid cells away from the nose become comparable or even slightly lower than those calculated without the subgrid. With an enhancement factor of 8.9 an ambient field of about 157 kV/m is needed to produce a triggered strike to the nose at 27,000 feet. The ambient field needed with an enhancement factor of 21.1 is reduced to only 67 kV/m. With the static field as an initial condition, the nonlinear electrical corona model can be used to study air breakdown around the nose of the aircraft.

In the standard application of the nonlinear model, air conductivities of finite difference cells are calculated throughout the problem space. This would naturally allow for corona formation wherever it is possible. With corona at different locations of the aircraft, charges can flow onto and off the aircraft. In the application of the subgrid to study corona discharge, only the conductivities of the fine grid cells are calculated, while those of the coarse grid cells are assumed to remain constant at a value of zero. The main reason for this procedure is because of the larger enhancement factor obtained with the subgrid, a lower ambient field is needed for air breakdown. The low ambient field makes corona formation in the coarse grid region quite unlikely. This is certainly true for a short time immediately following the initial breakdown near the nose, before the aircraft charges up to a sufficient level to cause corona formation near the other extremities. Indeed the extent of air breakdown in corona discharge is rather limited in volume. Air conductivity a few finite difference cells away from the breakdown region remains low and constant for all practical purposes.

The results of a triggered lightning study with the subgrid are shown in Figures 4.1 - 4.6. They consist of the usual D-dot, B-dot and boom current transient waveforms. The locations of the sensors was shown in Figure 3.2. For comparison the corresponding transient waveforms from a computer run without the subgrid and the measured waveforms from the strike 84-015, run 4, strike 2 are also shown. The ambient field used is oriented along the fuselage from the back to the nose of the aircraft. The magnitude of the ambient field is 70 kV/m for the run with the subgrid and 190 kV/m for the run without the subgrid. The relative air density is 0.5 which corresponds to an altitude of about 27,000 ft. Water vapor content is 0 %. There is no initial charge on the aircraft. For the subgrid implemented, only the D-dot forward sensor is within the subgrid region. The nose current is calculated by the line integral of the subgrid H fields around the nose within the subgrid region. All the other sensors are in the coarse grid region. From these figures, it is seen that generally the calculated responses with the subgrid at the nose are in better agreement with the measured responses. The responses from the subgrid contain higher frequency components than those from the normal grid. This is true for all sensors irrespective of whether they are located inside or outside the subgrid region. In particular, as shown

(text continued on page 98)

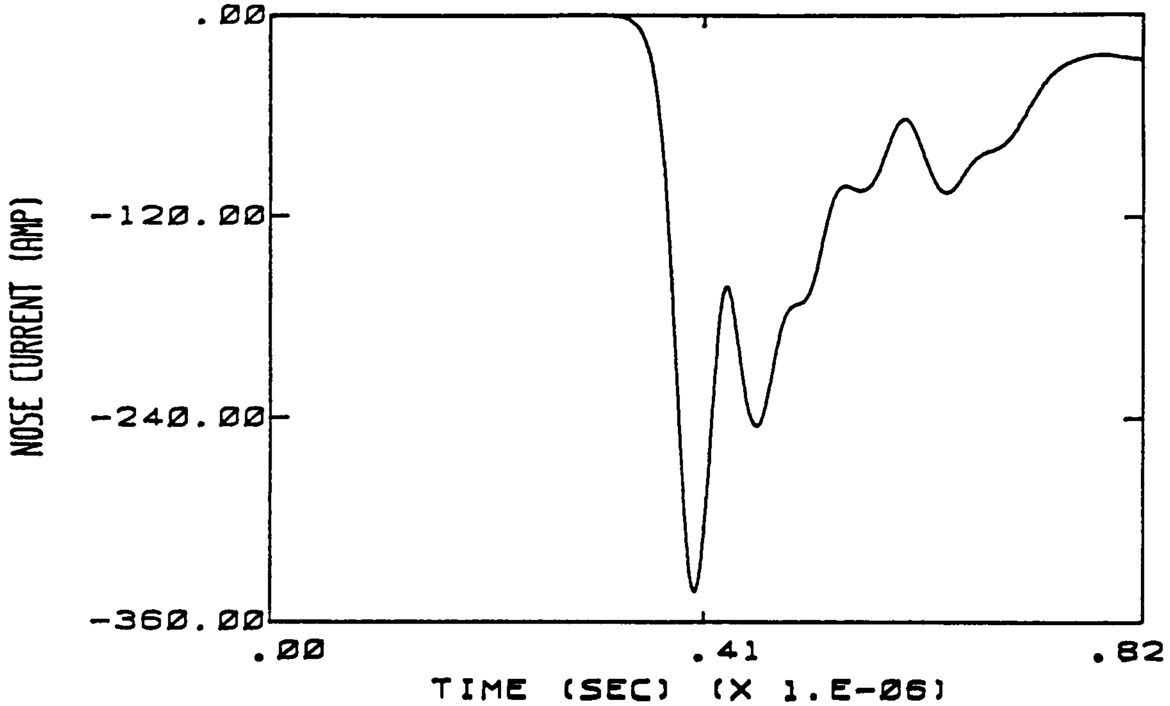

Normal Grid

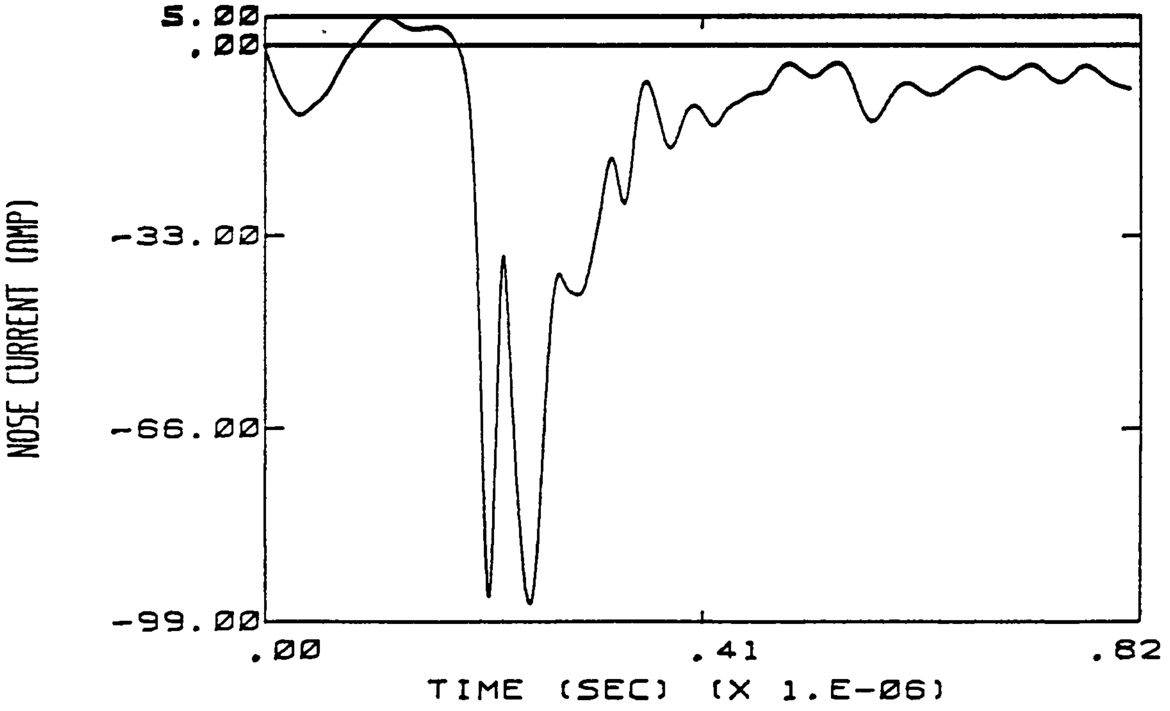

With Subgrid

Figure 4.1 Calculated Sensor Responses, Electric Field Oriented from Tail to Nose, Magnitude of 190 kV/m for Normal Grid, 70 kV/m with Subgrid In Place

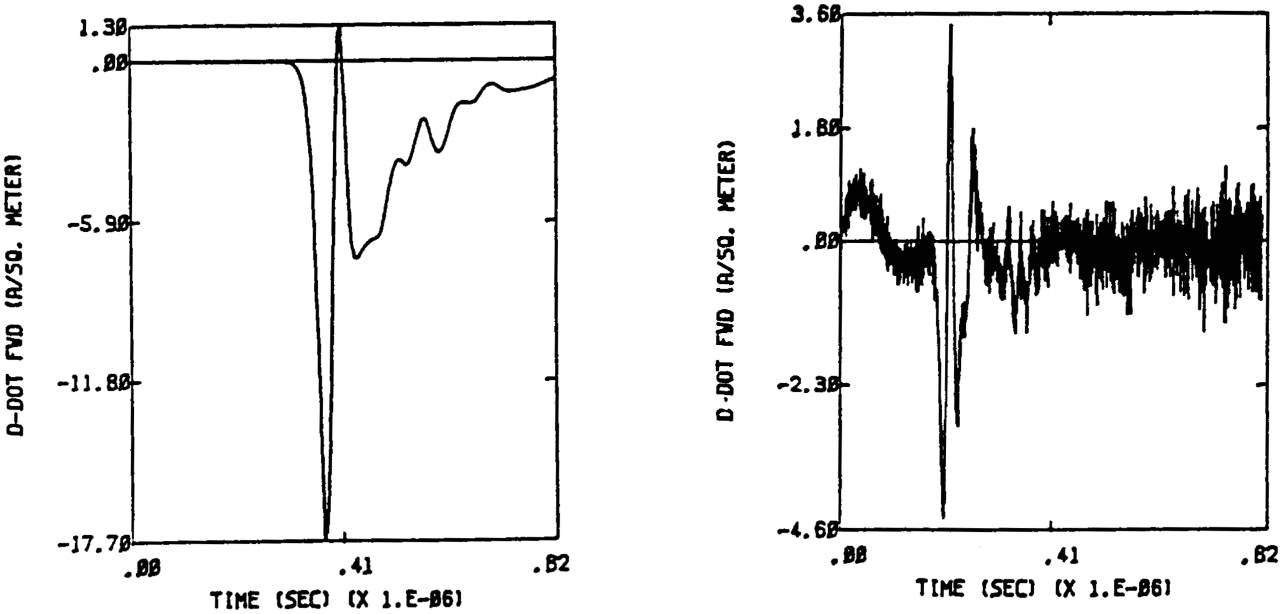

Normal Grid **With Subgrid**

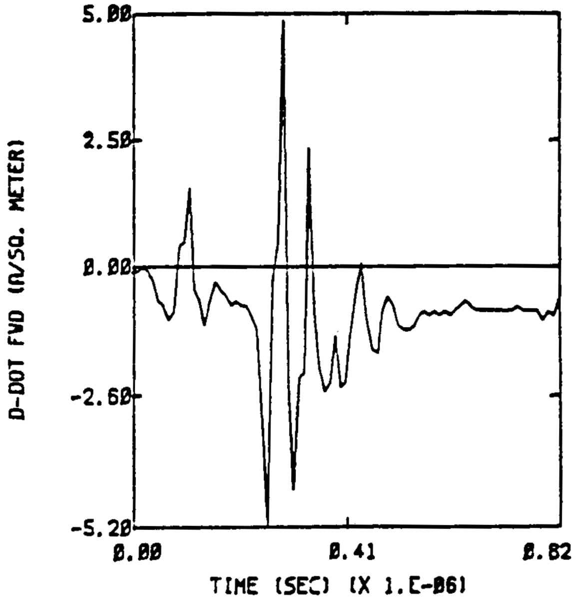

Flight 84-015 Run 4, Strike 2

Figure 4.2 Calculated and Measured Sensor Responses, Electric Field Oriented from Tail to Nose, Magnitude of 190 kV/m for Normal Grid, 70 kV/m with Subgrid in Place

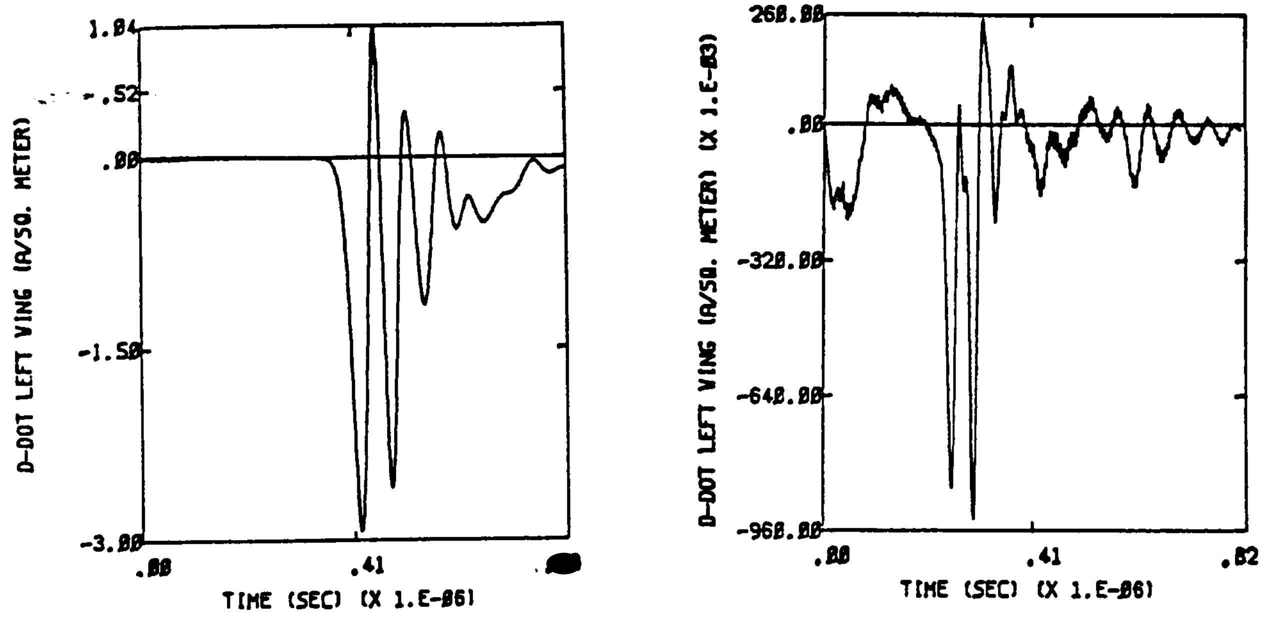

Normal Grid **With Subgrid**

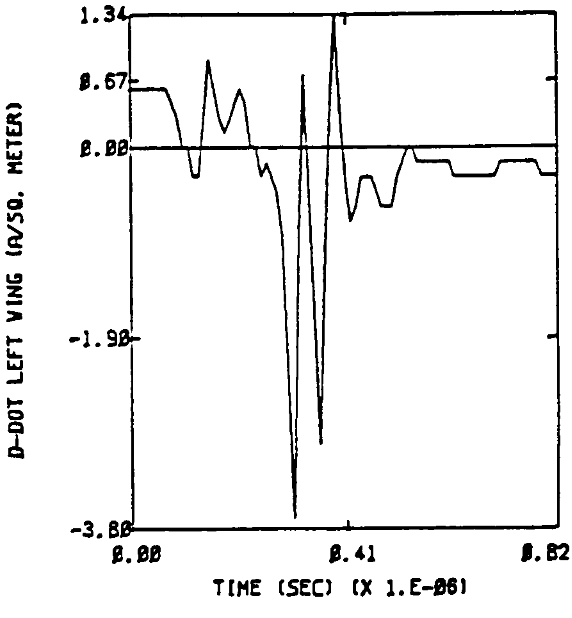

Flight 84-015 Run 4, Strike 2

Figure 4.3 Calculated and Measured Sensor Responses, Electric Field Oriented from Tail to Nose, Magnitude of 190 kV/m for Normal Grid, 70 kV/m with Subgrid in Place

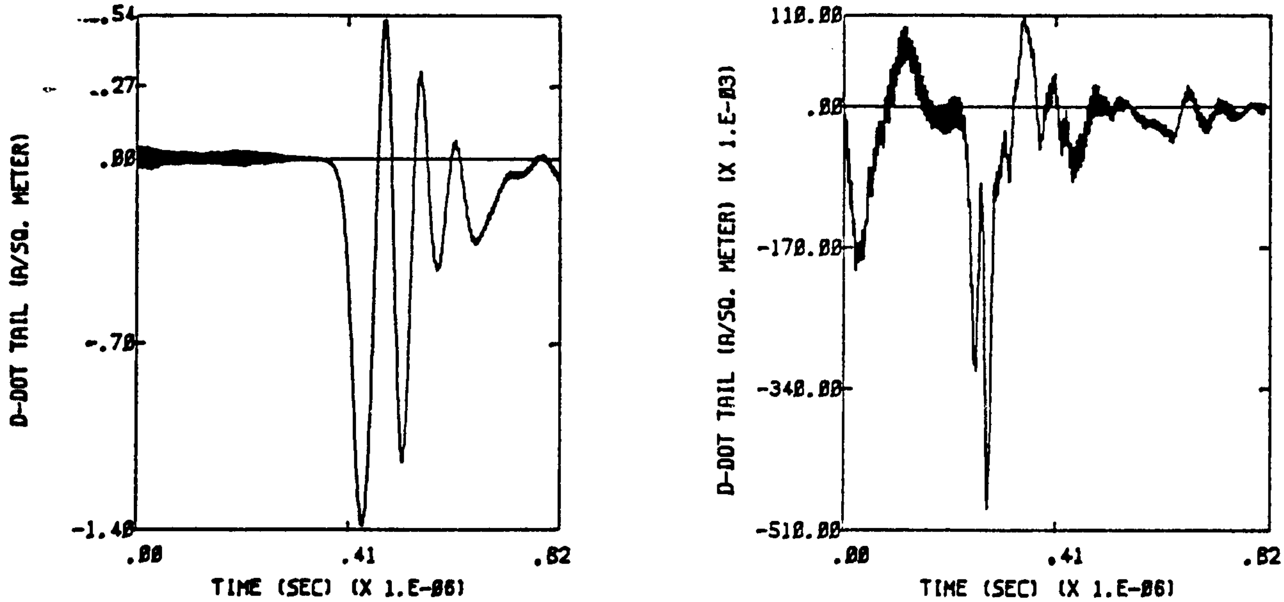

Normal Grid **With Subgrid**

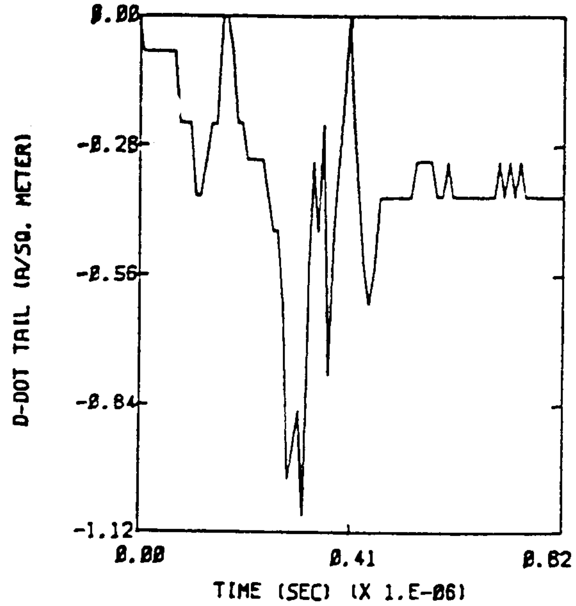

Flight 84-015 Run 4, Strike 2

Figure 4.4 Calculated and Measured Sensor Responses, Electric Field Oriented from Tail to Nose, Magnitude of 190 kV/m for Normal Grid, 70 kV/m with Subgrid in Place

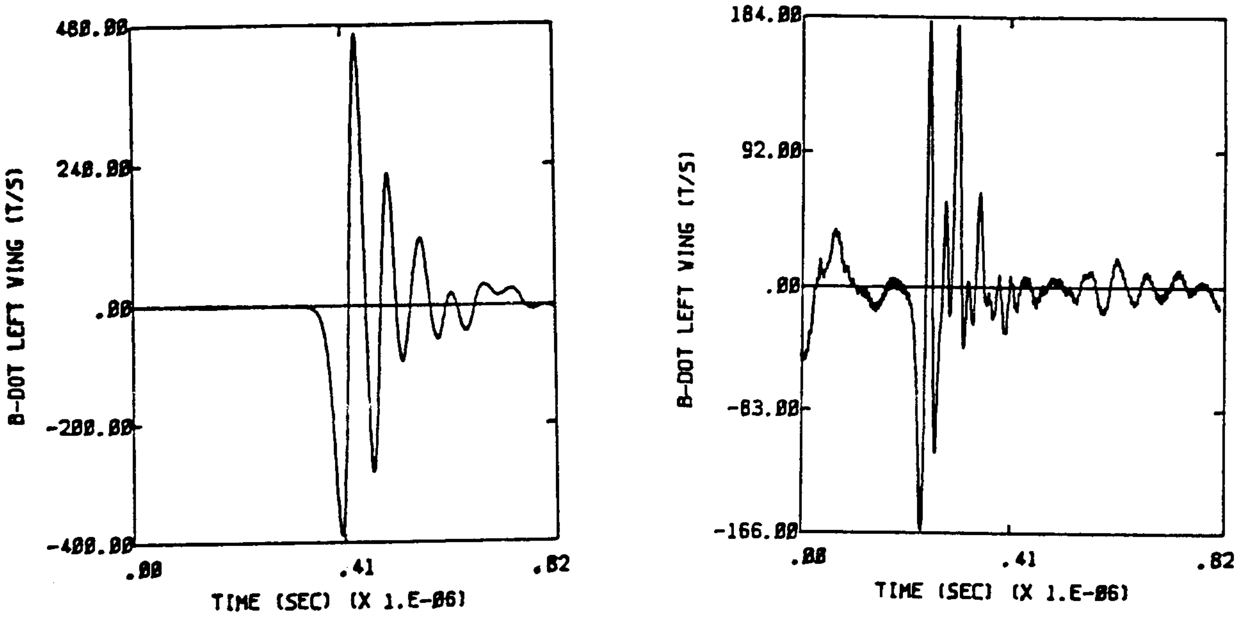

Normal Grid

With Subgrid

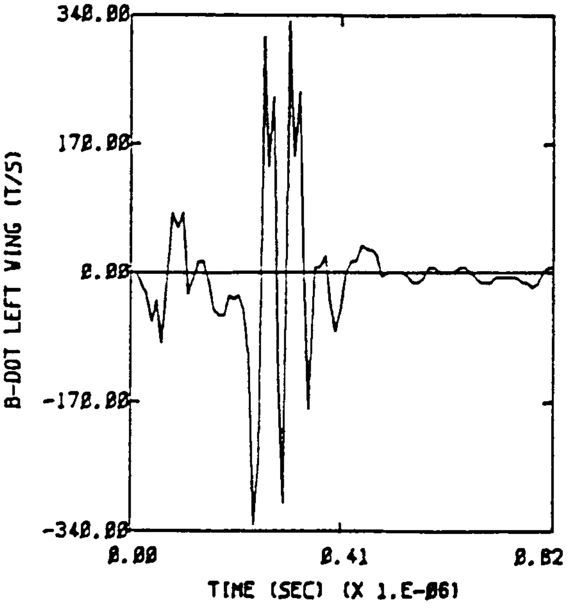

Flight 84-015 Run 4, Strike 2

Figure 4.5 Calculated and Measured Sensor Responses, Electric Field Oriented from Tail to Nose, Magnitude of 190 kV/m for Normal Grid, 70 kV/m with Subgrid in Place

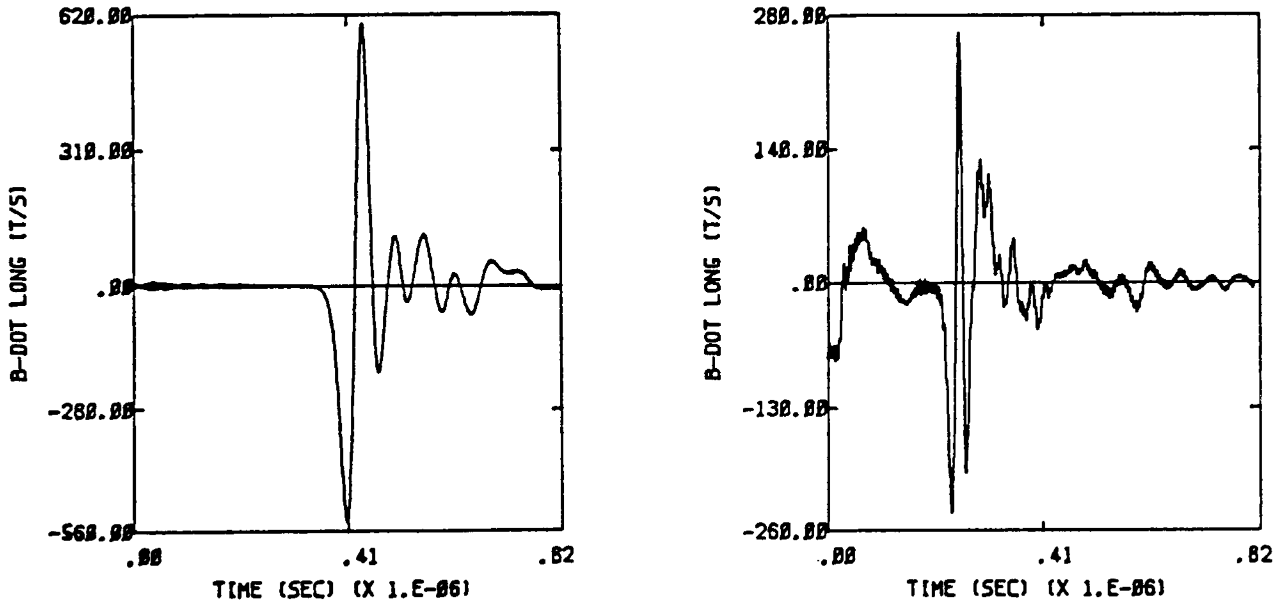

Normal Grid **With Subgrid**

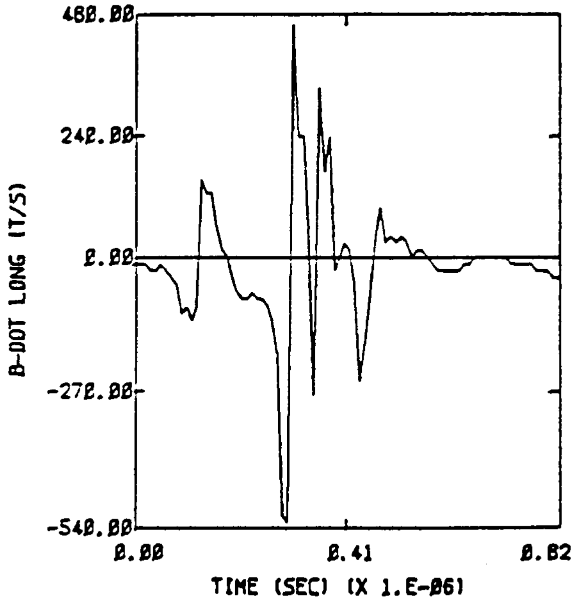

Flight 84-015 Run 4, Strike 2

Figure 4.6 Calculated and Measured Sensor Responses, Electric Field Oriented from Tail to Nose, Magnitude of 190 kV/m for Normal Grid, 70 kV/m with Subgrid in Place

in Figure 4.2, the shape and the amplitude of the main pulse of the D-dot forward sensor from the subgrid calculation are now in much better agreement with the measured response. Instead of three times the measured value, the calculated amplitude is now about 10% lower than the measured value. The amplitudes of the other transient waveforms are about 50% lower than the measured values.

It is not clear presently what causes the extremely high frequency oscillations in the waveforms, which are especially prominent after the main pulse in the D-dot sensor as shown in Figure 4.2. These oscillations might have resulted from the interpolation procedure adopted in the calculation of the field components on the interface of the coarse and fine grid regions.

A study was undertaken to determine why the calculated responses showed lower amplitudes than the measured responses. A calculated amplitude which was lower than the measured amplitude most probably resulted from the use of an ambient field which was too low. It seems intuitively reasonable to assume that by increasing the ambient field, the calculated amplitude should increase correspondingly. However when the initial ambient field in the study was increased from 70 kV/m to 90 kV/m, there were no significant changes in either the shapes or the amplitudes of the transient waveforms. On closer examination, it was found that the volumes of the corona discharges in both cases were the same. For comparison purposes, the corona is defined by cells with conductivities that reach at least 1×10^{-5} mho/m anytime in the course of the discharge. In the finite difference approximation, the conductivity is calculated at the locations of all the electric field components. By this definition the corona discharge was confined to only a couple of cells adjacent to the nose of the aircraft. This was also the case for the run without the fine grid region. However, though the number of cells that have air breakdown was about the same, the volume of the corona was much larger in the non-subgrid model simply because the cell size was twenty-seven times larger than that with the subgrid. Therefore it may be concluded that the amplitude of the transient is a function of air breakdown volume. In an actual physical strike, the volume of air breakdown and the ambient field are likely to be smoothly related. For a real strike, it is then intuitively reasonable to assume that the bigger the ambient field, the larger is the amplitude of the transient waveform. However, in the finite difference approximation, because of the discreteness of the field and conductivity calculations, the ambient field must be increased to cause breakdown in the surrounding cells before an increase in the amplitude of the transient waveform can be seen. This was verified by using ambient fields of various strengths as shown in Table 4.1:

TABLE 4.1
Statistics of High Conductivity Cells as a Function of Ambient Field Strength

Ambient Field (kV/M)	70	90	95	100
# of finite difference cells in corona	24	24	37	44

A finite difference cell is assumed to be in corona if the conductivity of that cell is greater than 1 x 10^{-5} mho/m. The volume of the corona region is then roughly given by the product of the number of cells and the volume of one cell. It was seen that increasing the ambient field from 70 to 90 kV/m did not increase the volume of the corona discharge, resulting in essentially similar transient waveforms. For ambient fields greater than 90 kV/m, the volume of the corona discharge started to increase. The transient waveforms for the ambient fields of 95 and 100 kV/m are shown in Figures 4.7 - 4.9 and can be compared to those for an ambient field of 70 kV/m shown in Figures 4.1 - 4.6. Increasing the ambient field from 90 to 100 kV/m caused the number of cells in corona to increase by about a factor of two while the amplitudes of the nose current and transient waveforms for the D-dot and B-dot sensors increased by a factor of three. Increasing the ambient field also increased the avalanche rate which is reflected in the faster rise time of the transient waveforms.

It should be noted that when the corona is beyond a couple of cells from the enhancement center the field increment required to enlarge the volume of the corona discharge becomes smaller. This is not surprising since the variation of the field is largest near the enhancement center and decreases rapidly away from the center.

(text continued on page 103)

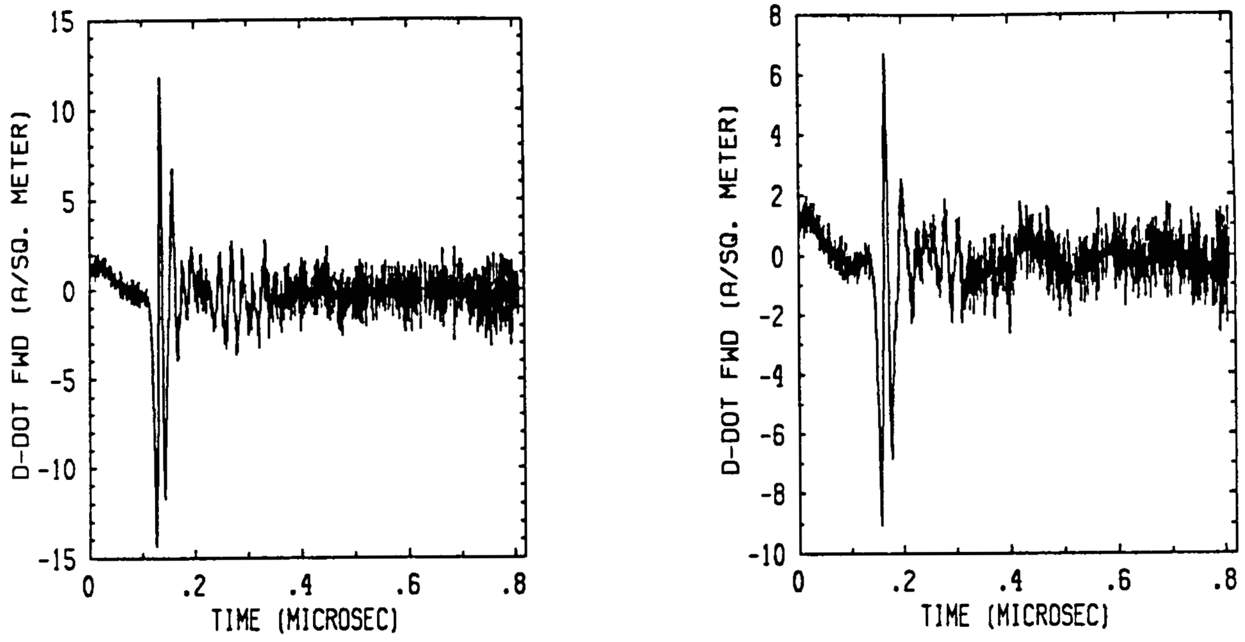

E = 100KV/M

E = 95KV/M

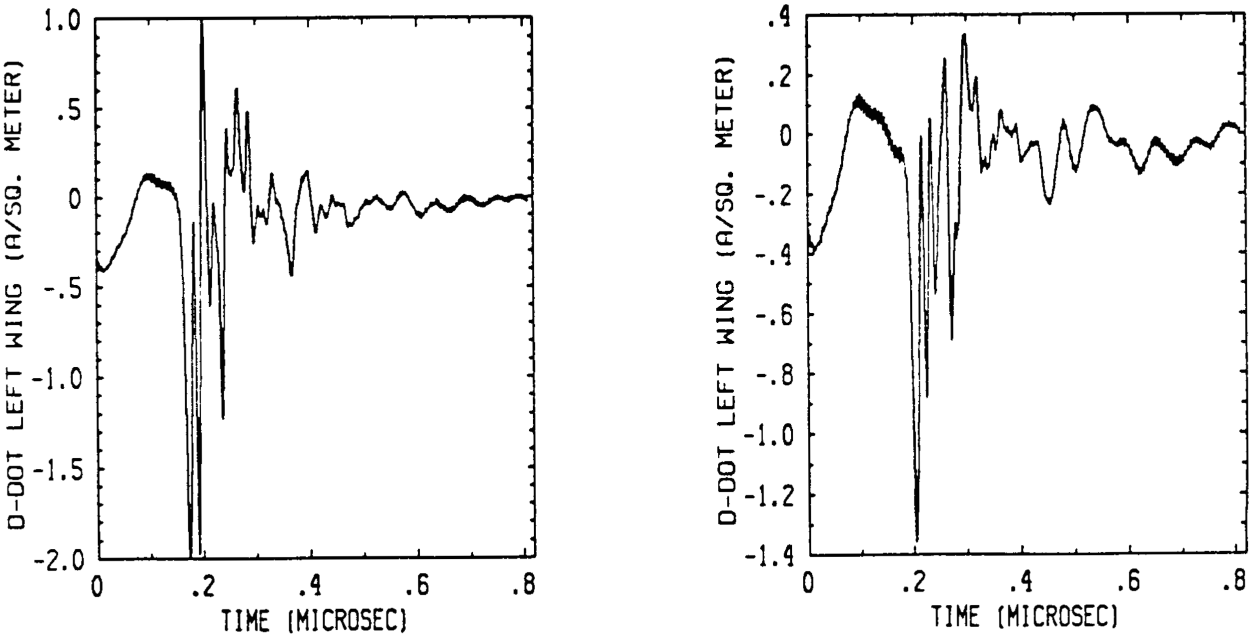

E = 100KV/M

E = 95KV/M

Figure 4.7 Calculated Sensor Responses for Two Values of Ambient Field

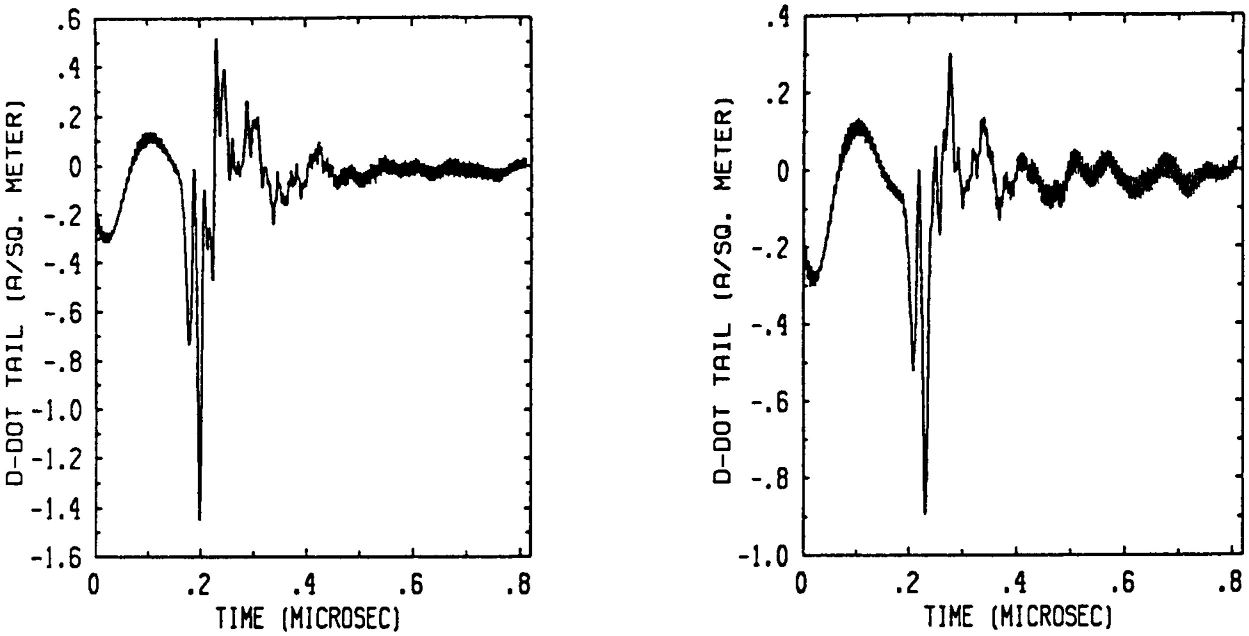

E = 100KV/M

E = 95KV/M

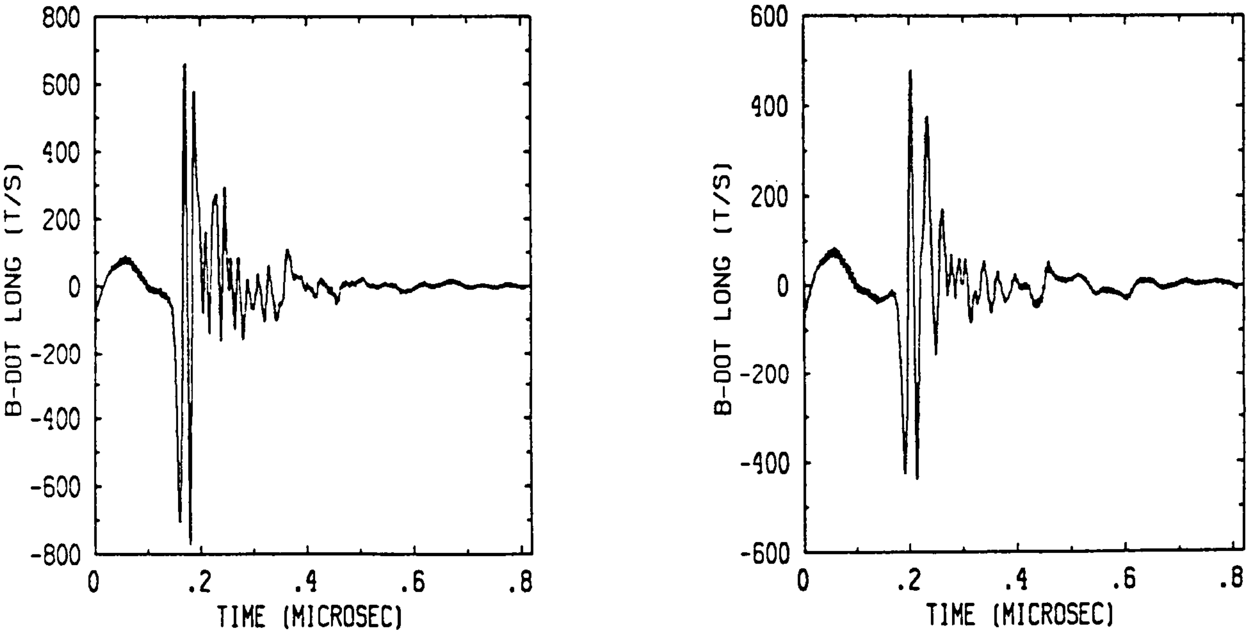

E = 100KV/M

E = 95KV/M

Figure 4.8 Calculated Sensor Responses for Two Values of Ambient Field

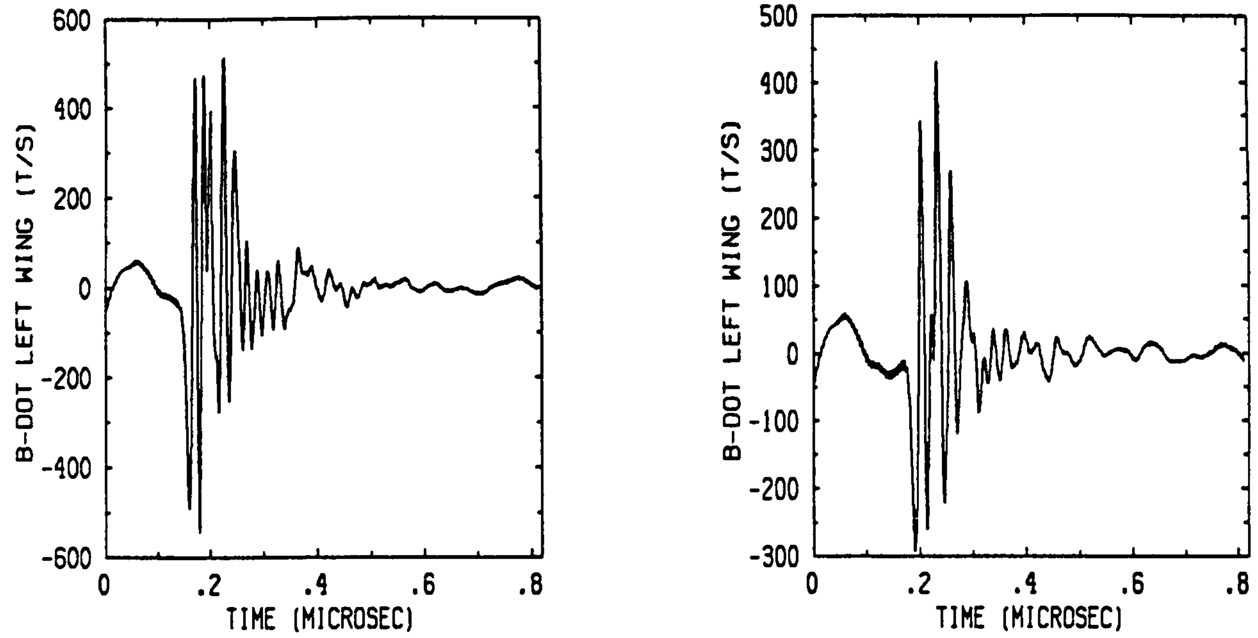

E = 100KV/M   E = 95KV/M

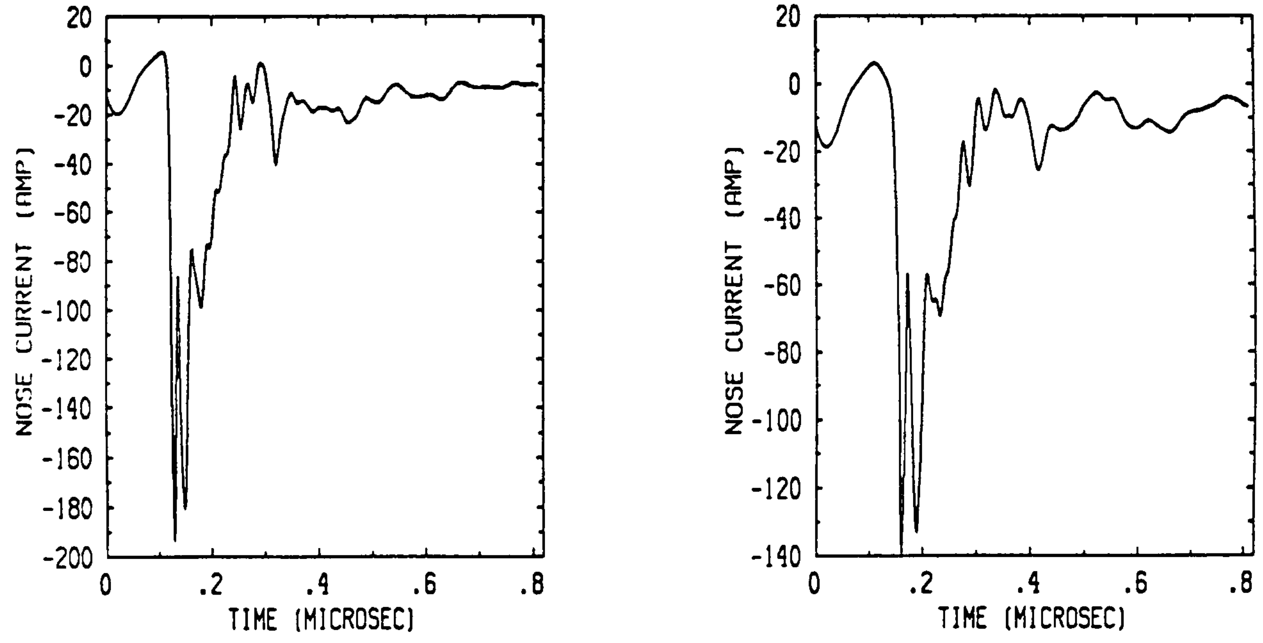

E = 100KV/M   E = 95KV/M

Figure 4.9 Calculated Sensor Responses for Two Values of Ambient Field

Thus a few cells away from the nose of the aircraft the difference of the fields in adjacent finite difference cells is small. Consequently, a small increase in the ambient field is sufficient to cause breakdown in the adjacent cells, i.e., a situation approaching that of a physical triggered strike.

4.4 Conclusions

The subgrid method has been applied to a region around the nose of the F106B aircraft. In the fine grid region the cell size was 1/3m x 1/6m x 1/6m. In the coarse grid region the cell size was 1m x 1/2m x 1/2m. The maximum enhancement factor of 21 under the nose was a factor of 2.5 over that without a subgrid region. Consequently the ambient field required for air breakdown decreased by the same factor, from 160 kV/m to 70 kV/m. It was found that with or without the subgrid region, the corona discharge typically occupied only a couple of cells adjacent to the enhancement center. The volume of the discharge thus decreased by a factor of twenty-seven over that of the standard model without the subgrid. The calculated response depended strongly on the volume of the corona discharge. In the finite difference approximation, the volume of the corona discharge was not a smooth function of the ambient field because of the discreteness in the field and conductivity calculations. The volume of corona discharge remained constant until the ambient field was increased enough to cause breakdown of the air in the cells adjacent to the existing discharge. However this was most probably a numerical effect and does not correspond to the real physical phenomenon in which a smoother dependency is to be expected. It was shown numerically that the calculated waveforms from an ambient field of 70 kV/m most resemble the measured waveforms. After multiplying by the enhancement factor of 20, the ambient field of 70 kV/m gave a local field at the nose which is sufficient to cause air breakdown at the nose of the F106B at an altitude of 27,000 feet. It is encouraging to note that field mill analyses often give a value of approximately 70 kV/m for the ambient field level immediately preceding a triggered strike. The analysis of this chapter indicates that the volume of corona discharge preceding the leader channel formation is rather small, about .2 cubic meters, and that the measured transients from strike 84-015 run 4, strike 2 were the responses of the sensors to corona discharge.

CHAPTER 5

AIRCRAFT SCALING LAWS FOR TRIGGERED LIGHTNING

5.1 Introduction

The relationship between the geometrical characteristics of an aircraft and lightning threat is an important consideration in the design and operation of a particular vehicle. Knowledge of this relationship is useful to design engineers and regulatory bodies. In general, there are significant geometrical differences between different types of aircraft. For example, the wing characteristics, engine type and location, horizontal and/or vertical stabilizers, and fuselage shape are different for different types of aircraft. As a consequence, it is necessary to create numerical models for each individual aircraft in order to obtain a detailed knowledge of the response to a given lightning threat.

Although particular models are necessary for a detailed analysis, it is useful to generate simplified scaling laws which relate the gross geometrical characteristics of various aircraft to the lightning threat. Such laws can be used for engineering estimates and to place bounds on the "worst case" threat. In this chapter, scaling laws based on simplified models of an aircraft are investigated. In particular, portions of an aircraft are approximated by ellipsoids. This allows for the use of closed form solutions which can be found in the literature.

5.2 Electric Field Enhancement and Triggered Lightning

Triggered lightning occurs when an aircraft enhances the local field enough to cause electrical breakdown of the air. In this case, the static electric field which the aircraft sees must be large enough and oriented properly so that the locally enhanced fields at extremes of the aircraft exceed the local air breakdown value. Knowledge of the field enhancement due to the presence of the aircraft allows for the prediction of the minimum field in which triggered lightning will occur and the most probable attachment point on the aircraft.

It is expected that the largest field enhancements will occur for objects having sharp points or edges, particularly if those points and edges are oriented in the direction of the ambient field. In general, the nose, wing tips, and the vertical stabilizer are likely candidates for a triggered strike. Taken individually, it appears that in many cases the geometrical characteristics of major portions of an airplane can be approximated by ellipsoids. For example, the fuselage of the CV580 closely resembles an ellipsoid of revolution, while the wings are better approximated by a "flat" ellipsoid.

The "worst case" field enhancement occurs when the ambient field is parallel to the major axis of the aircraft part (e.g., fuselage). In such cases, it is expected that the wings and horizontal stabilizer have only a small influence on the field near the nose. Conversely, it is expected that the fuselage has a small influence on the maximum field at the wing tip when the field is parallel to the wing. Using this logic, it is anticipated that the maximum field enhancement at the nose, wing tips, and vertical stabilizer can be predicted by using the expression for the potential due to an ellipsoid in a static field [15]. The principle of superposition allows for the estimation of maximum enhancement for a field of arbitrary orientation.

The expression for the potential at any point external to an ellipsoid in a static field is given by:

$$\phi = \phi_o \left[1 - \frac{\displaystyle\int_{\xi}^{\infty} \frac{d\xi}{(\xi + a^2)R_\xi}}{\displaystyle\int_{0}^{\infty} \frac{d\xi}{(\xi + a^2)R_\xi}} \right] \tag{5.1}$$

$$R_\xi \equiv \sqrt{(\xi + a^2)(\xi + b^2)(\xi + c^2)} \tag{5.2}$$

where a, b and c are the semi-axes of the ellipsoid and ϕ_o is the potential in the absence of the ellipsoid.

The equipotential surfaces are the ellipsoids ξ = constant ($\xi = 0$ is the surface of the ellipsoid.) The electric field is determined by taking the gradient of this expression. When using ellipsoidal coordinates, ξ, η, ζ, the appropriate metric tensor must be used to obtain the physical components of the electric field. The maximum field enhancement is obtained by evaluating the normal derivative at the tip of the ellipsoid:

$$E_n \equiv \frac{\partial\phi}{\partial n} = \frac{2\phi_o}{(\xi + a^2)\sqrt{(\xi - \eta)(\xi - \zeta)} \int_0^\infty \frac{d\xi}{R_\xi(\xi + a^2)}} \tag{5.3}$$

The definite integral given in the above expression can be decomposed into elliptic integrals of the first and third kind. These integrals are tabulated by various authors (see for example reference [16]). The integral is also readily calculated numerically. Calculations described below were made using Simpson's rule for integration. In cases where the ellipsoid has rotational symmetry, the potential may be expressed in terms of elementary functions:

$$\phi = \phi_o \left[1 - \frac{\ell n \left(\frac{\sqrt{1 + \xi/a^2 + e}}{\sqrt{1 + \xi/a^2} - e} \right) - \frac{2e}{\sqrt{1 + \frac{\xi}{a^2}}}}{\ell n \frac{1 + e}{1 - e} - 2e} \right]$$

where a and b are the semi-axes, and $e = \sqrt{1 - \frac{b^2}{a^2}}$ is the eccentricity of the ellipsoid [16]. Here, the semi-major axis and the ambient field are parallel to the x direction. In this case, the maximum field strength is given by:

$$E_{max} = E_o \frac{2e^3 \left(1 - e^2\right)^{-1}}{\ell n \frac{1 + e}{1 - e} - 2e} .$$

The electric fields resulting from an ellipsoid in a static field were compared with the maximum field enhancement obtained from the numerical models for the CV580, F106B and the Learjet. The dimensions of the principal axes of the ellipsoid are estimated from the finite difference models. When making this comparison, one must recognize that the numerical results yield the value of the fields averaged over a finite difference cell, while the calculation based on Equation (5.1) gives exact results everywhere in space. For example, if the CV580 is placed in an ambient field of 1 volt/meter, the maximum field is oriented parallel to the nose of the aircraft with a value of 7.4 volts/meter (finite difference result). The exact solution for the corresponding ellipsoid is 37.4 volts/meter. In this case, the maximum field is at the tip of the ellipsoid. In order to make a realistic comparison, the field on the axis of the ellipsoid is averaged over a cell length. The result is 8.3 volts/meter which is in good agreement with the finite difference model. A comparison between the averaged exact solution and various finite difference models are given in Table 5.1.

TABLE 5.1
Enhancement of an Ambient Electric Field of 1 Volt/Meter

Aircraft Type & Part	Predicted Field Enhancement Finite Difference	 Ellipsoid	Ellipsoid Dimensions (meters)		
CV580					
Fuselage	7.4	8.3	a=12.5	b=1.5	c=1.5
Wing	10.7	12.5	a=18	b=2	c=0.5
Tail	4	3.3	a=9	b =1.5	c=0.5
F106					
Fuselage	7.9	7.4	a=11	b=1	c=2
Fuselage using Subgrid (1/4 m)	19	15.9			
Learjet					
Fuselage	11.7	10.5	a=7.5	b=.75	c=.85
Wing	5.6	6.9	a=6	b=1.28	c=.107
Tail	2.3	1.7	a=1.06	b=.854	c=2.03

These results indicate that the use of ellipsoids provides a reasonable estimate of the maximum field enhancement for a particular aircraft part. Here the field enhancement is based on the principal axes of the approximating ellipsoid. The effect of charge can also be included in the calculation. In this case, the potential for a charged ellipsoid is included in the expression for the potential (see Reference [15].)

A plot of the normal electric field along the coordinate axis parallel to the semi-major axis of the ellipsoid as a function of position from the nose of a CV580 is shown in Figure 5.1. Here four different ratios of the semi-minor axes are compared. The maximum field for the semi-minor axes ratio of 1/4 is more than twice the magnitude corresponding to a semi-minor axes ratio of 1. The fields drop off quite rapidly, and within one tenth of a meter, the fields decrease to within a few percent of each other.

5.3 Scaling Laws for a High Impedance Current Source

The maximum values for B-dot, D-dot, and current values will depend on the type of strike (triggered, direct, etc.) channel impedance, and the geometrical characteristics of the aircraft. For a high impedance current source, the maximum source current will not vary significantly for different types of aircraft. From an engineering point of view, it is reasonable to assert that the peak current on the aircraft is bounded by twice the peak value of the source current. The factor of two takes into consideration possible reflections.

The actual distribution of the current will depend primarily on the geometrical characteristics of the aircraft. In order to determine appropriate scaling laws, one must select a set of parameters which are both physically significant and are common to most types of aircraft. As indicated earlier, there are many geometrical differences between aircraft types. Hence, it is difficult to determine which parameters have the greatest significance. The problem is further complicated in that the importance of a particular parameter may be dependent on the configuration of the aircraft. Here it is useful to follow the approach employed in the previous section, and assume that the current distribution for a given aircraft part can be estimated using an ellipsoid which resembles that portion of the aircraft. This type of approximation assumes that the three principal axes of the approximating ellipsoid are the most important parameters.

The current distribution on a metallic body which corresponds to a low frequency high impedance source is roughly proportional to the charge distribution on the same body. Here it is assumed that there are no reflections (i.e., the impedance of the exit channel matches that of the body.) The charge distribution for an ellipsoid is [15]:

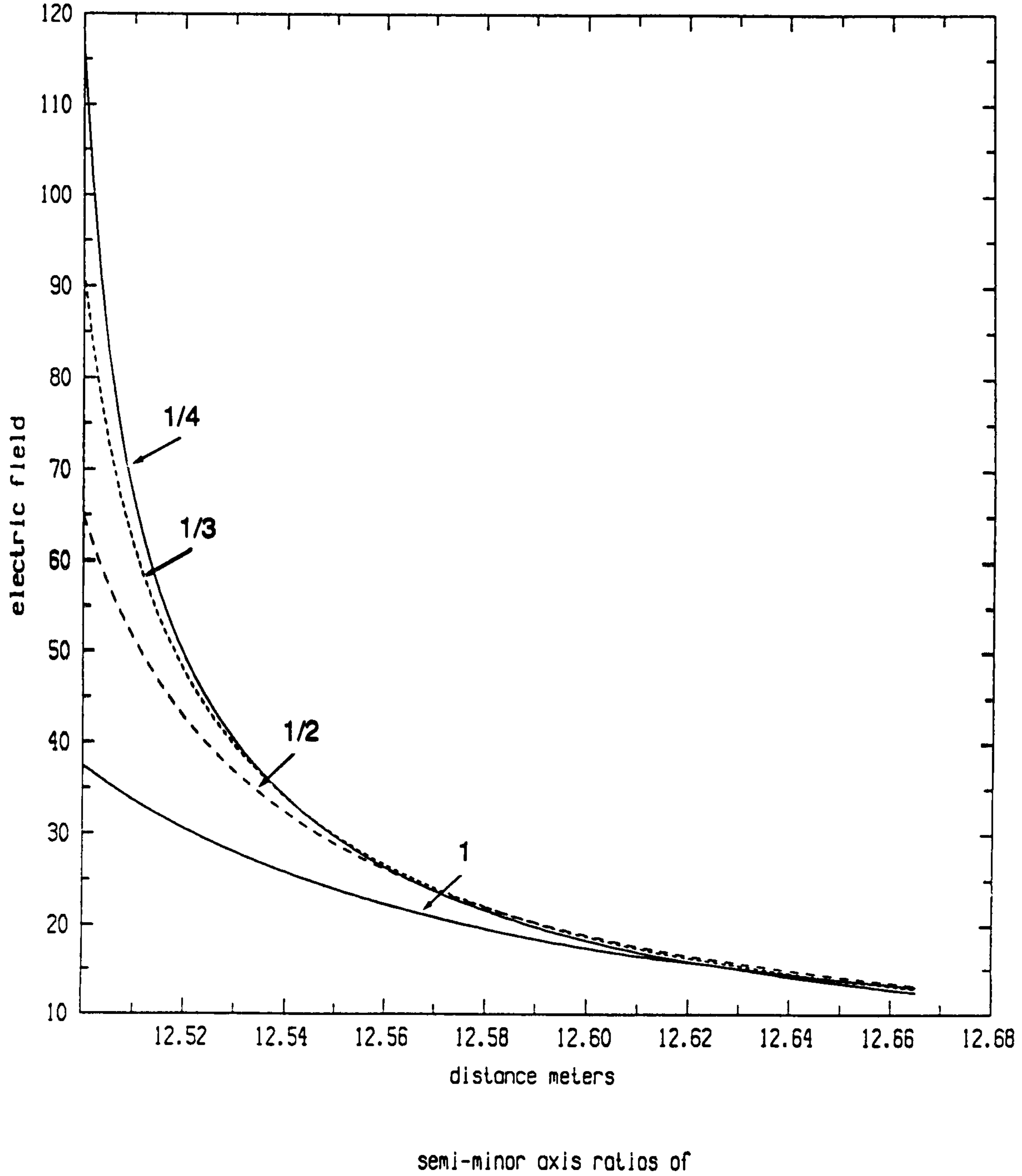

Figure 5.1 Variation in the Normal Electric Field for Different Ratios of the Semi-Minor Axis

$$\sigma = \frac{q}{4\pi abc}\left(\frac{x^2}{a^4} + \frac{y^2}{b^4} + \frac{z^2}{c^4}\right)^{-1/2} \tag{5.4}$$

where the semi-major axis is of length a, and parallel to the x axis. This expression predicts that the current density is a maximum near the end point ($x = a$) and reaches a minimum at the end of the smallest semi-axis ($x = 0$, $z = c$). The current density can be obtained by the use of a suitable proportionality constant. The ratio of the maximum and minimum current density is given by the ratio of the two axes (a/c). D-dot relations follow the current density direction, while B-dot is obtained from its time derivative.

Using this formulation, it is seen that decreasing the dimensions of a given aircraft by a factor of two results in an increase in the current density by a factor of four. In order to determine if this approximation provides reasonable bounds for the measured parameters, numerical models were used to compute B-dot and D-dot for aircraft twice the normal size (all dimensions doubled) and half the normal size (all dimensions halved). Both the F106B and the C130 were used in this analysis. The relative positions of the sensors did not change. For this simulation, an infinite impedance current source was attached to the nose of both types of aircraft. A fifty ohm impedance exit channel was attached to the tail of the aircraft. Comparisons of the current for the three waveforms for D-dot forward and B-dot longitudinal for each aircraft as well as the input current pulse are provided in Figures 5.2 - 5.5. The waveforms have been shifted in time so that the peak values of the currents coincide. The peak values for five different sensors are tabulated in Table 5.2. It is seen that the scale factors for the peak values vary roughly from two to four. The differences between the predicted values and the numerical model values are most likely due to complex behavior such as resonance and radiation. It should also be noted that the numerical models tend to have sharp corners which influence the current pattern. This difference becomes more pronounced for large cell sizes.

It is expected that the dominant frequencies of oscillation will correspond to wavelengths equal to twice the wavelength of the aircraft part. To check this hypothesis a high impedance current source of 5000 amps was injected onto the noses of a CV580 and Learjet. In both cases, an exit channel of fifty ohms was established on the tail of the aircraft. Plots of the total fuselage currents near the wings

(text continued on page 115)

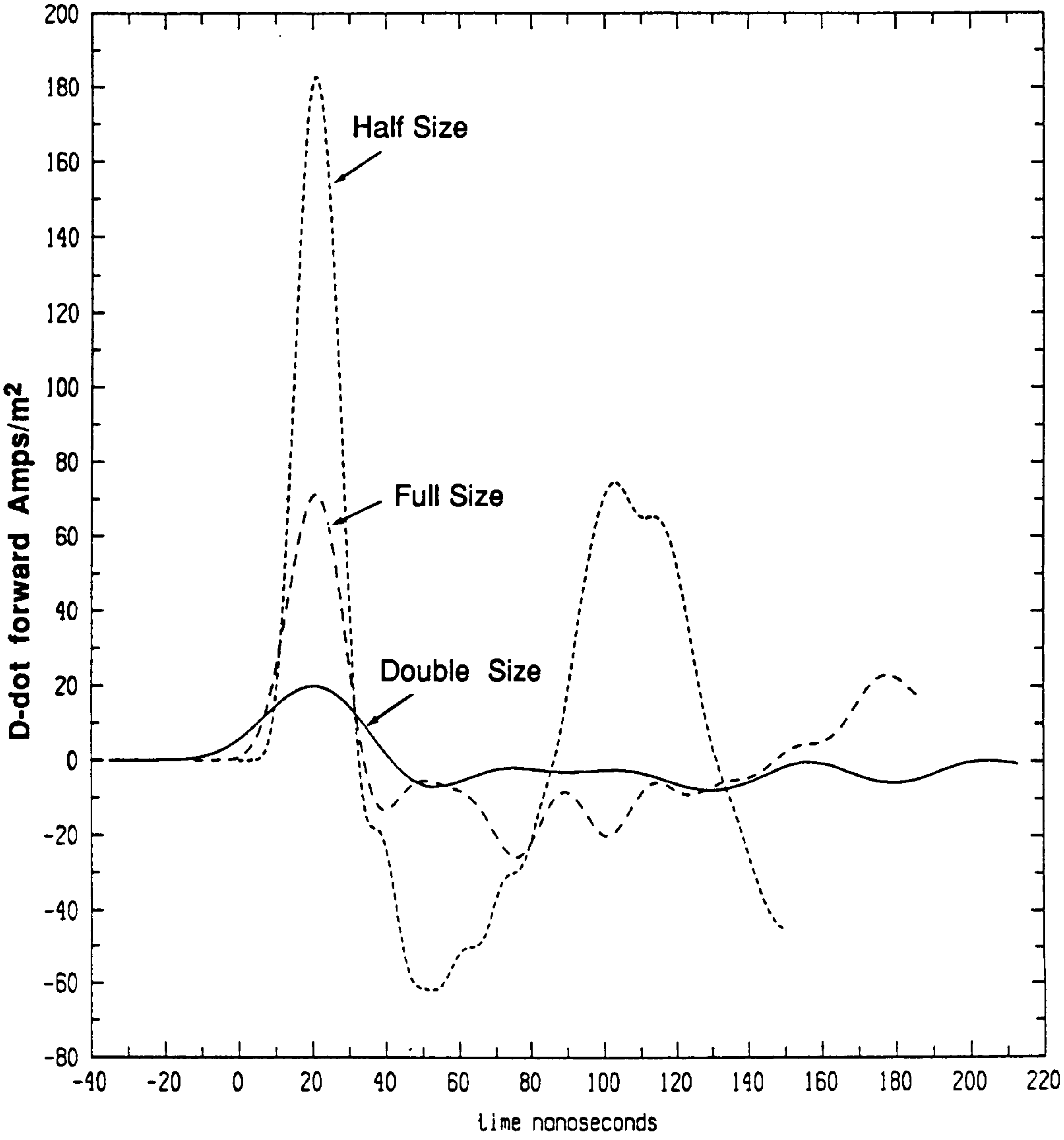

Figure 5.2 Comparison of C130 Response for Half Size, Full Size and Double Size Finite Difference Models

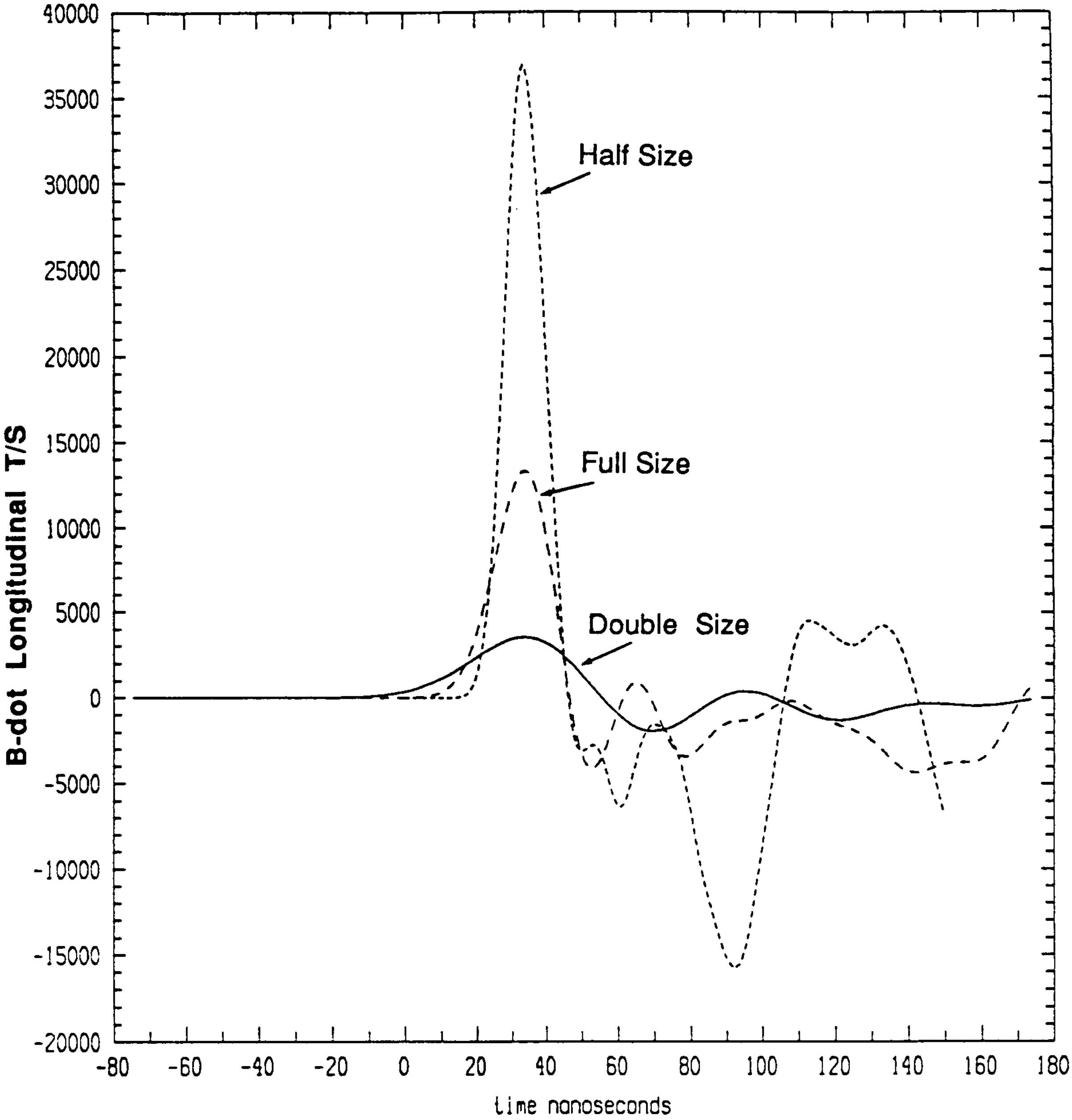

Figure 5.3 Comparison of C130 Response for Half Size, Full Size and Double Size Finite Difference Models

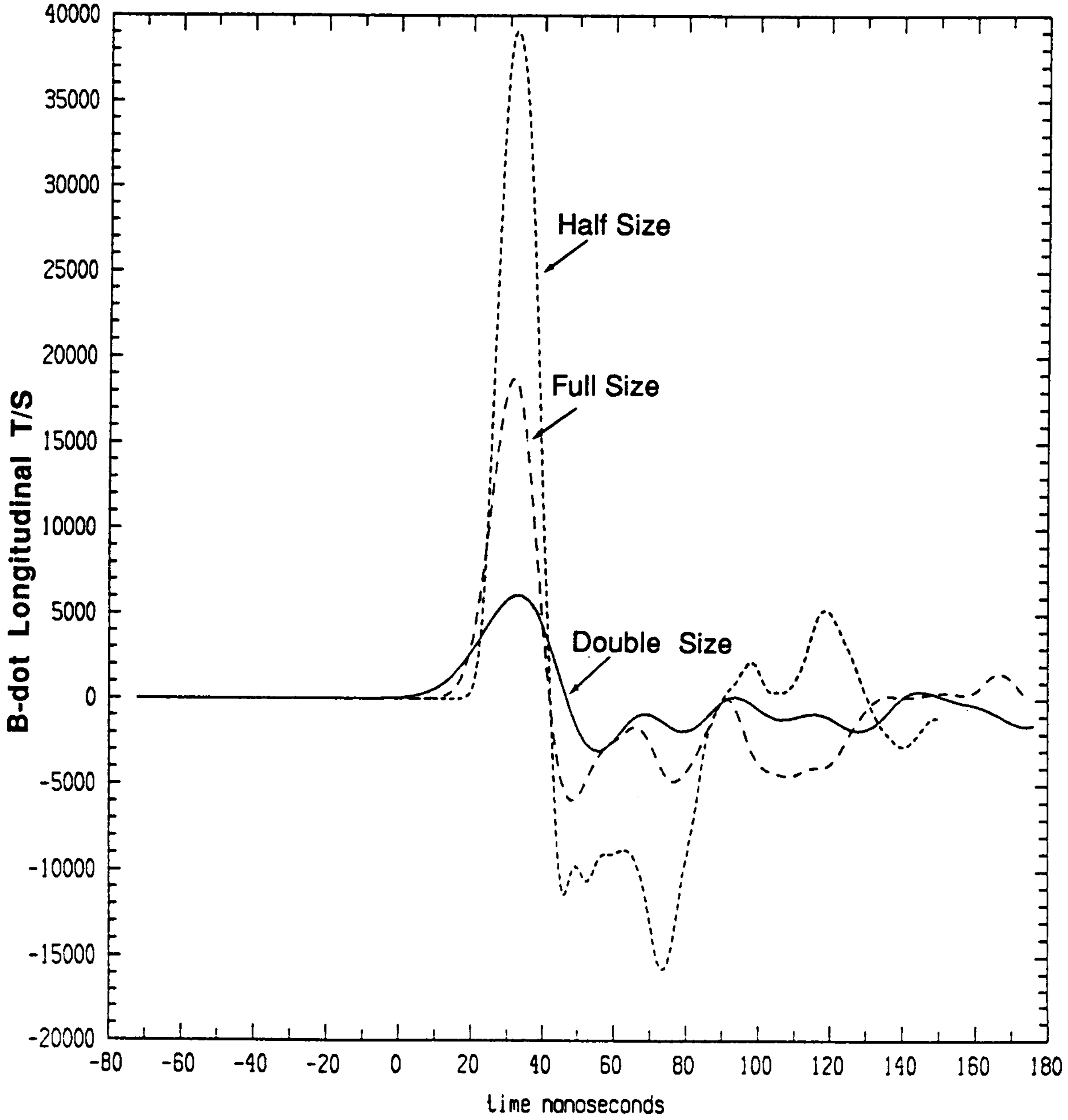

Figure 5.4 Comparison of F106 Response for Half Size, Full Size and Double Size Finite Difference Models

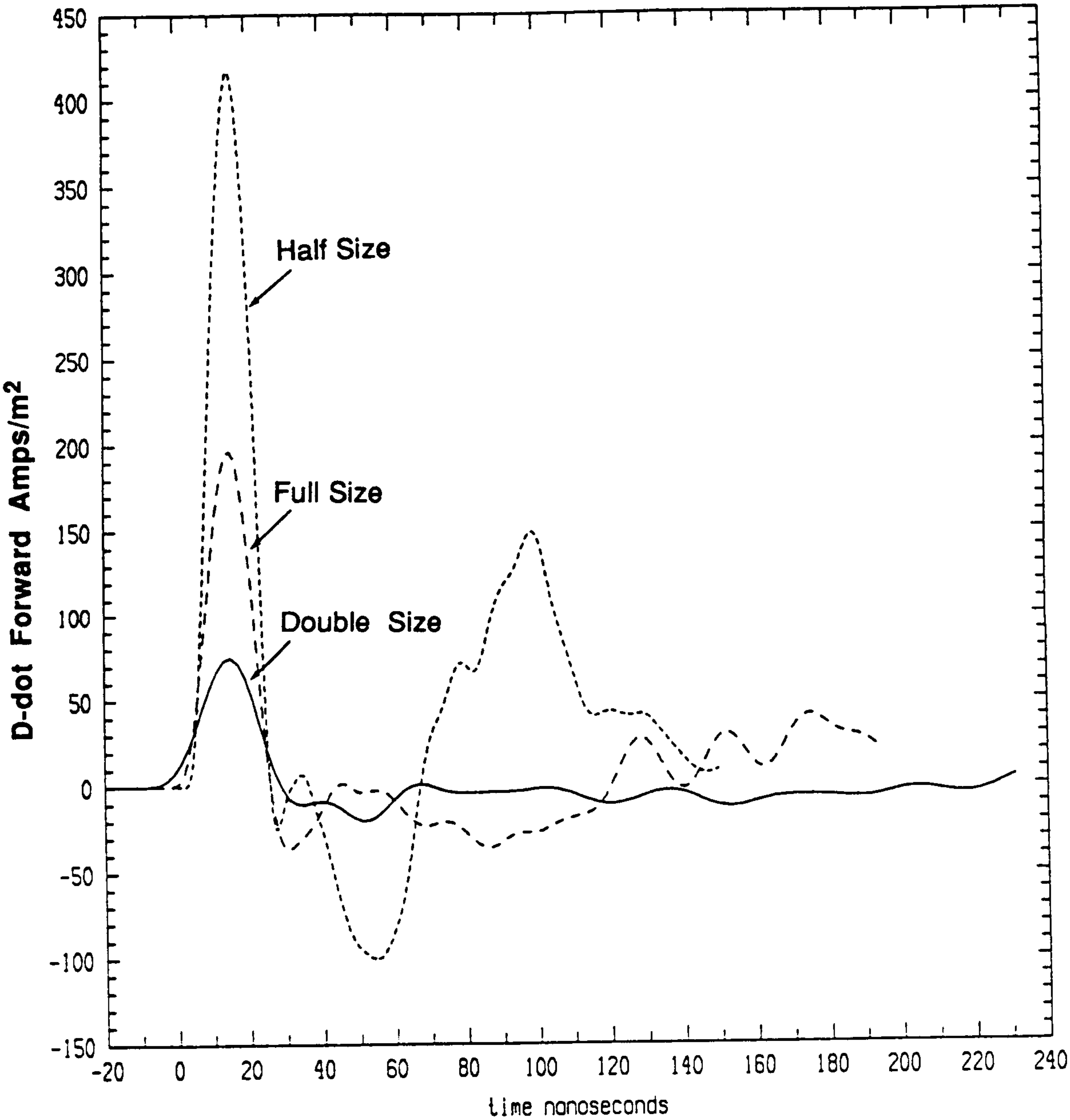

Figure 5.5 **Comparison of F106 Response for Half Size, Full Size and Double Size Finite Difference Models**

TABLE 5.2
Peak Values of Electromagnetic Quantities
(D-dot Values in Amp/m^2, B-dot in Tesla/sec)

	Twice Normal Size	Normal Size	Half Size
C130			
D-dot forward	20	71	182
D-dot left wing	5	23	83
D-dot tail	2	8	25
B-dot longitudinal	3542	13,335	36,847
F106			
D-dot forward	75	196	417
D-dot left wing	17	60	193
D-dot tail	6	27	93
B-dot longitudinal	6092	18,737	39,078

are shown in Figures 5.6 and 5.7. In both cases, the frequency of oscillation is within ten percent of the predicted value.

5.4 Conclusions

The results of this work indicate that triggered lightning can reasonably be predicted by approximating an aircraft part by an ellipsoidal structure. Owing to the fact that the ellipsoid gives a continuous approximation to the actual field at the tip of an aircraft part, it is likely to provide a better picture of the field behavior near the aircraft than a coarse finite difference grid. When the field resulting from the approximating ellipsoid is averaged over a cell length, good agreement is obtained with the results of the finite difference models.

For a direct strike, large currents flow onto the aircraft. Such events are frequently modeled by imposing an infinite impedance current channel on the aircraft. Although the actual response of the aircraft is complicated due to the presence of various structures, one can readily predict worst case bounds for electromagnetic

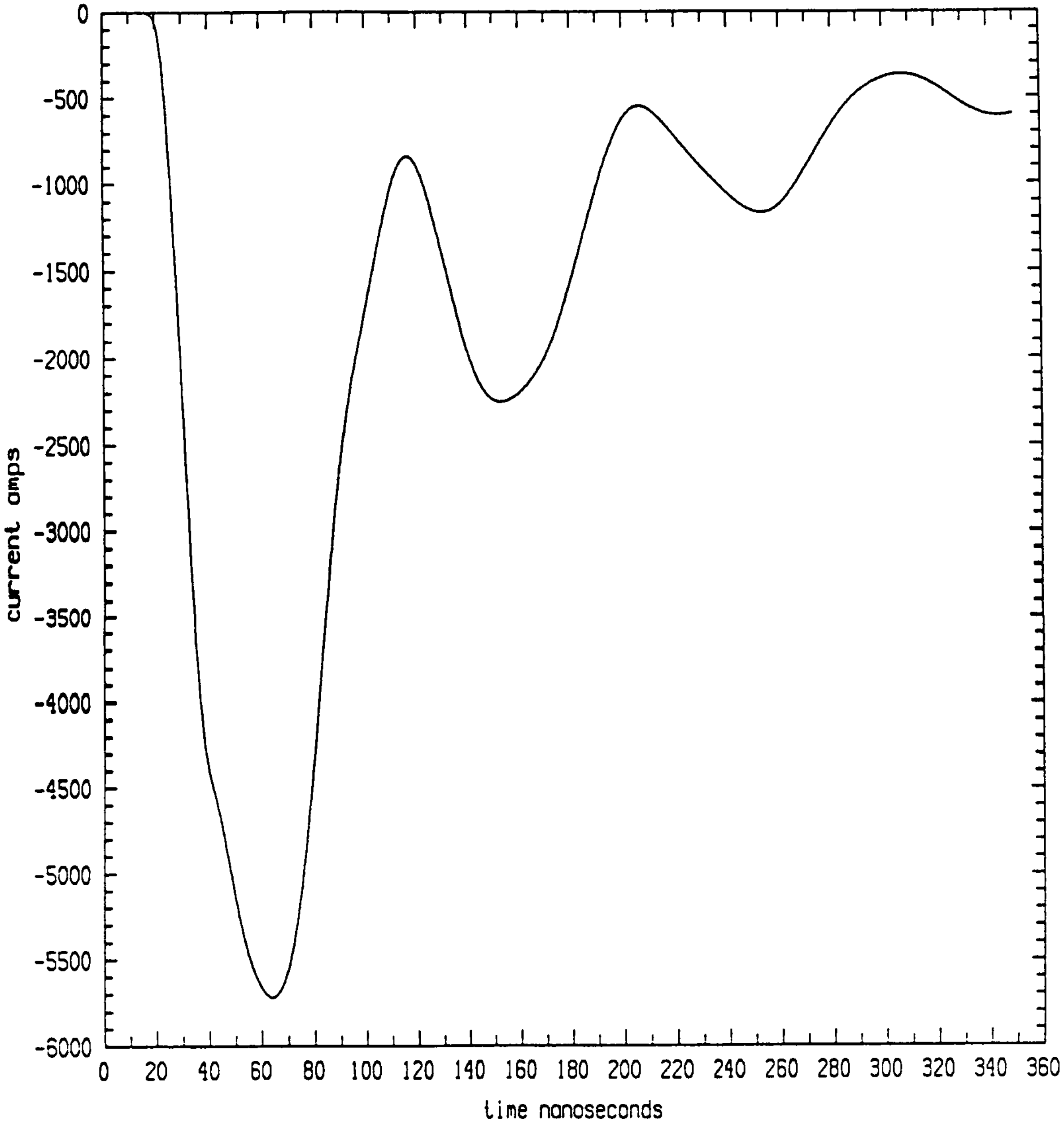

Learjet
Fuselage current

Figure 5.6 Total Fuselage Current in Front of the Wings (Learjet)

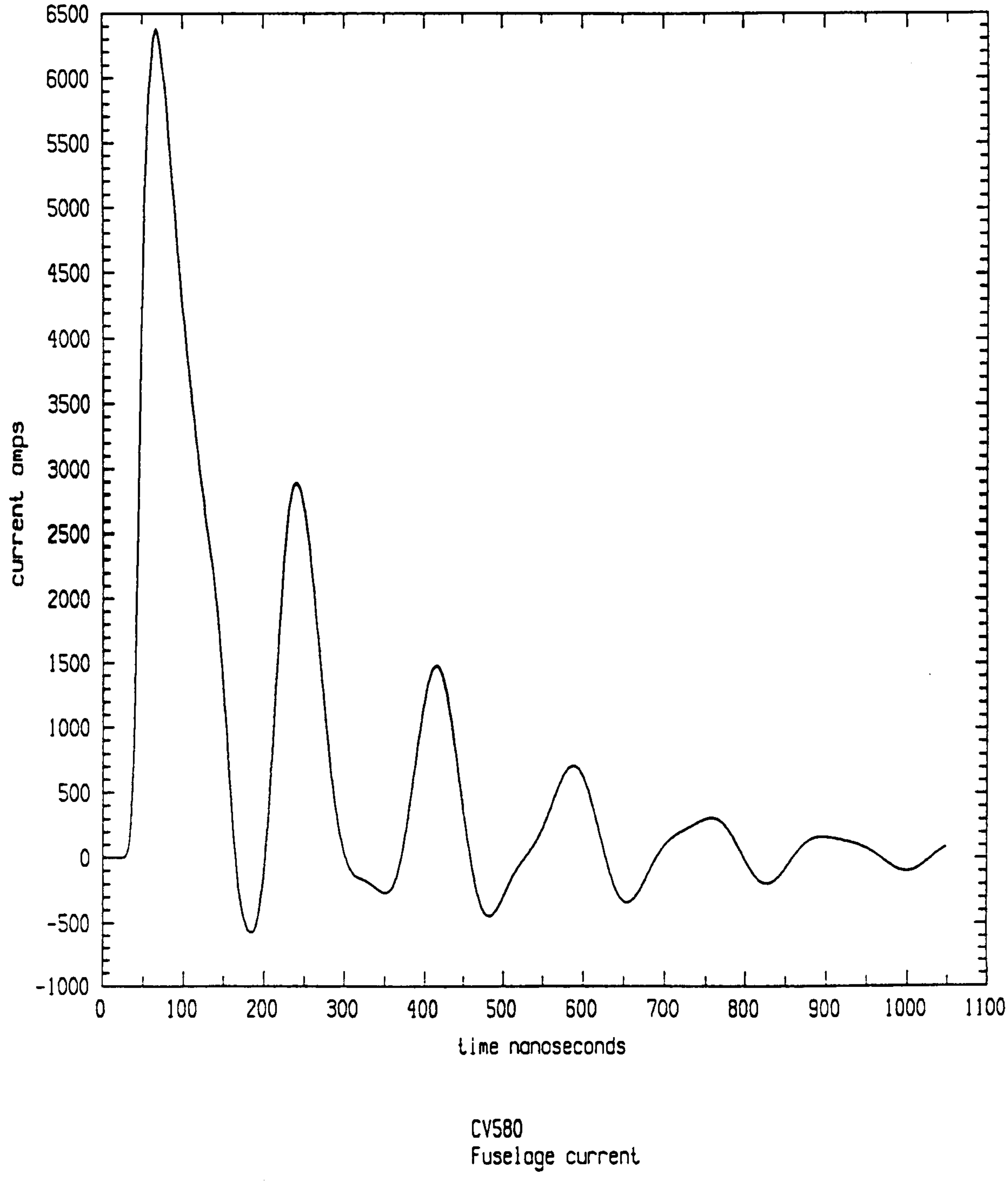

Figure 5.7 Total Fuselage Current In Front of the Wings (CV580)

quantities. Here the expected bounds of twice the peak, and resonant frequencies governed by the length of a given aircraft are supported by the finite difference models. Determination of rules to predict the actual current distribution, and quantities such as B-dot and D-dot for different aircraft is somewhat more difficult. In this analysis, it is asserted that the current distribution can be estimated from the expected low frequency distribution of current on an ellipsoid. Here reflections are not considered. It was found that, on the whole and as expected, the current density should increase by a factor of four when the dimensions are reduced by one half. Comparison with the models indicates that factors ranging from two to four are obtained depending on the sensor location. In this case, the ellipsoidal model yields reasonable bounds on the factor governing the increase in current density, B-dot and D-dot, when the size of the aircraft part is reduced.

In conclusion, the important parameters governing the response of an aircraft to a lightning threat have been reduced to the three semi-axes of an approximating ellipsoid. Although this leaves out many of the structural features of a given aircraft, it appears to be well-suited to the prediction of maximum field enhancement for a given structure. It is clear that the techniques described here are most effective for aircraft that are ellipsoidal in their major features. This includes most large commercial aircraft, because of their large fuselages. Predicted responses on the fuselage for this type of aircraft should be reasonably accurate. Structures such as a vertical tail are completely ignored by the technique, and responses on these structures, and the perturbations they cause to fuselage responses, cannot be determined using the technique.

CHAPTER 6
INTERACTION OF F106 WITH A LIGHTNING RETURN STROKE

6.1 Introduction

The nonlinear corona model has been extensively applied to the study of lightning strikes to the F106B aircraft [4]. This corona model couples the process of air breakdown with its electromagnetic environment through the conductivity term in Maxwell's equations. The breakdown of air is strongly dependent on the local electric field near the aircraft. The ionized air in turn modifies the local and nearby electromagnetic field. The corona model is especially suited to the study of triggered lightning in which the initial breakdown of air and the formation of corona occurs near an extremity of an aircraft. Since most of the lightning strikes that attached to the F106B were triggered by the aircraft, predictions of the model have been in reasonably good agreement with the measured transient data when the appropriate initial conditions defining the lightning environment were used. Previous studies have shown that the corona formed in the initial discharge is rather limited in extent (a few meters, at most) for an electric field which is not much higher than the theoretical value required for breakdown. Therefore it may be speculated that the good agreement between the model results and the measured data indicates that the measured transient data were the responses of the aircraft to corona discharge with minimal contribution from the subsequent leader channel. Two previous studies [2,4] have exploited this characteristic to examine the interaction of the aircraft with a lightning strike. In these studies it was implicitly assumed that the measured data came from the early time of a strike (less than a few microseconds) so that simulations only needed to cover that time period. In one study, the effect of an approaching leader was studied by terminating a leader current one meter away from the aircraft. The resulting charge generated a field which was large enough to break down the air between the leader channel and the aircraft. The responses on the aircraft to this breakdown were presented. In another study, the interaction of the F106B with a large current return stroke was studied by depositing the current directly onto the aircraft [4]. The resulting charge built up on the aircraft eventually caused corona formation all over the immediate neighborhood of the aircraft.

This chapter reports results from a reexamination of the interaction of the F106B aircraft with a return stroke current. The present calculation assumes that the partially ionized channel produced by a leader persists and that the return stroke current follows that path. Though the path of the return stroke current is predetermined as in the previous study, the flow and attachment of the current to the aircraft is not forced but is calculated by the model. The return stroke current is forced to flow only at the boundary of the problem space. At all other locations the air conductivity determines the current flow.

6.2 Return Stroke Model

There are limitations in applying the standard corona model [2] to the study of the interaction of a lightning return stroke with an aircraft. The rates for the various processes were obtained experimentally under swarm conditions [17]. Therefore the model is strictly only suitable for the study of weakly ionized air. A leader channel ahead of a return stroke current is likely to be weakly ionized, so the model should still be applicable. This is not the case in the return stroke channel where the air is highly ionized with high conductivity. Therefore the corona model needs to be modified for the channel calculation.

The main contribution to the conductivity of the channel comes from free electrons. In the standard corona model, free electrons are lost through electron-ion recombination and attachment to neutrals, and the heavy ions are lost through ion-ion neutralization. Because the coefficients for the electron-ion recombination and ion-ion neutralization used in the standard corona model are not applicable for highly ionized air, they were arbitrarily removed from the rate equations in the channel calculation but were retained in the region away from the channel. Therefore, in the return stroke channel, free electrons can be lost only through attachment to neutrals to form negative ions. It should be noted that attachment to neutrals is in any case the dominant process for the depletion of free electrons. Hence the exclusion of electron-ion recombination of the existing leader channel before the arrival of the return stroke is not as drastic a change as it may appear to be. Because of the rapid attachment of electrons to neutrals, most of the charges in the leader channel are carried by heavy ions. Detachment of electrons from the negative ions should be very important in increasing the conductivity of the existing leader channel to form the return stroke channel. Therefore detachment of electrons from negative ions was included in the rate equations. The coefficient of detachment was obtained from the work of Parkes [18].

The proper specification of the initial lightning environmental parameters is crucial in the successful application of the nonlinear corona model. For example, the most important factor in the calculation of aircraft response to triggered lightning is the specification of the magnitude and orientation of the ambient field before the initiation of the discharge. In the cases studied here, the important features were the location and conductivity of the existing leader channel and the corona that existed around various portions of the aircraft. Therefore, for simplicity, the ambient field was ignored and initial charge densities were specified throughout the problem space, with higher densities for those cells in the chosen path of the channel. For a given channel orientation and the input current, the response of the aircraft was then determined by the initial charge densities assigned to the leader channel and the corona around the aircraft. For the case presented here, the relative air density was set to 0.5 with zero percent water vapor, the ion densities were initialized to 1×10^{17} m^{-3}. The leader channel extended from the problem space boundary to the nose of the aircraft along the fuselage direction. For the single cells at the core of the channel, the ion densities were initialized to 1×10^{19} m^{-3}, and for the cells adjacent to the core to 1×10^{18} m^{-3}. The electron density at a given location was initialized to a value three orders of magnitude down from the corresponding ion densities to reflect the rapid attachment to neutrals in an old leader channel. The return stroke current was injected into one end of the channel located next to the problem space boundary. The injected current waveform had a sine squared leading edge of 250 nanoseconds rise time to a constant amplitude of 50 kiloamperes.

6.3 Results

The calculated electromagnetic sensor responses for the case described in Section 6.1 are shown in Figures 6.1 - 6.3. The locations of the sensors were shown in Figure 3.2. Figure 6.4 shows the channel current in the cells along the core of the original leader channel between the forced current and the nose of the aircraft. Curve 1 in that figure gives the current at the location just inside the problem space from the forced current at the problem space boundary, curve 2 one meter farther away, etc. Curve 6 shows the current located farthest away from the forced current and is adjacent to the nose of the aircraft. It can be seen that for the first 100 nanoseconds,

(text continued on page 126)

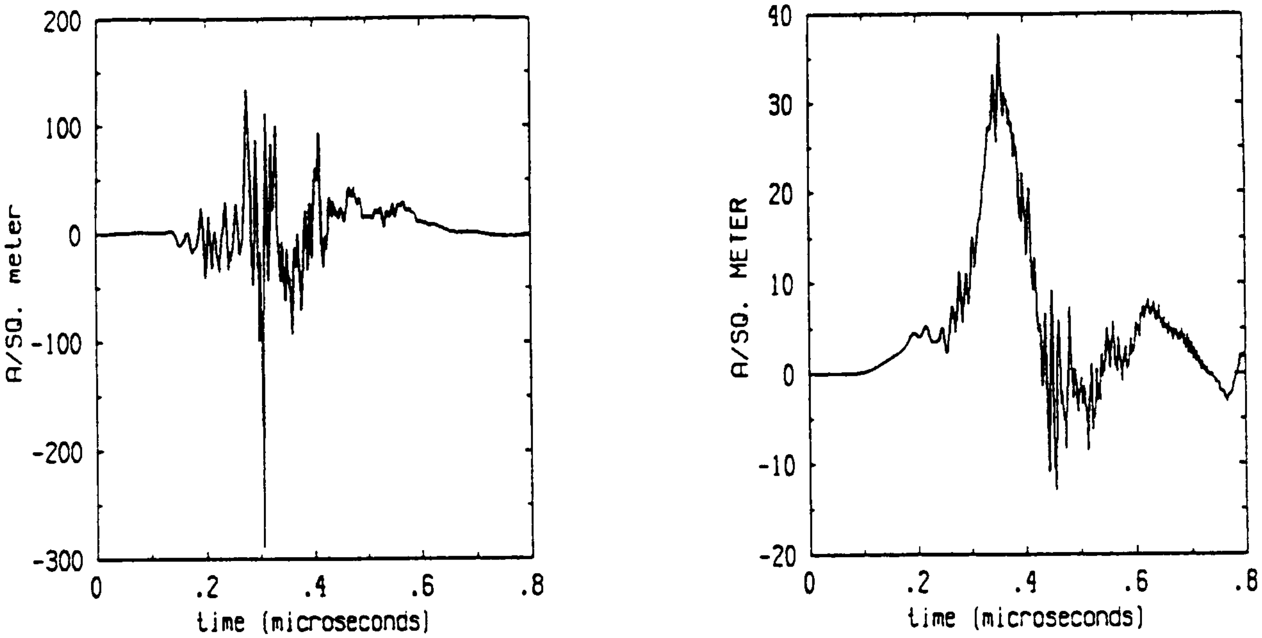

D-DOT FWD

D-DOT TAIL

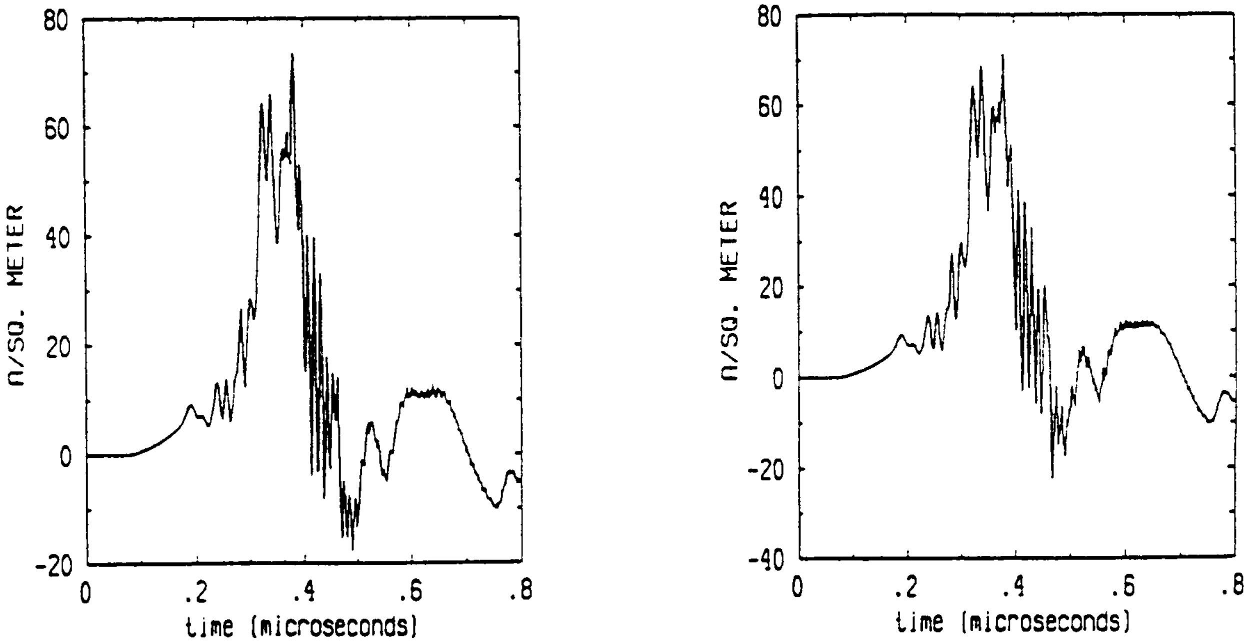

D-DOT LW

D-DOT RW

Figure 6.1 F106B Electromagnetic Sensor Responses for Return Stroke Attachment

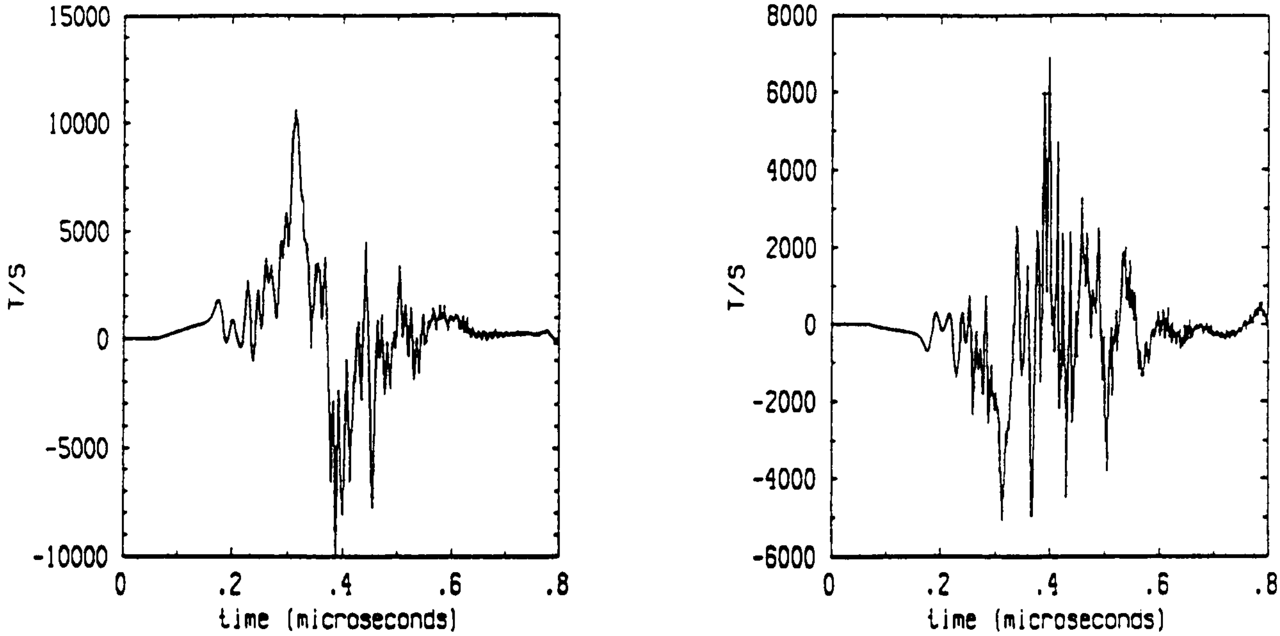

B-DOT LONG

B-DOT TRANS

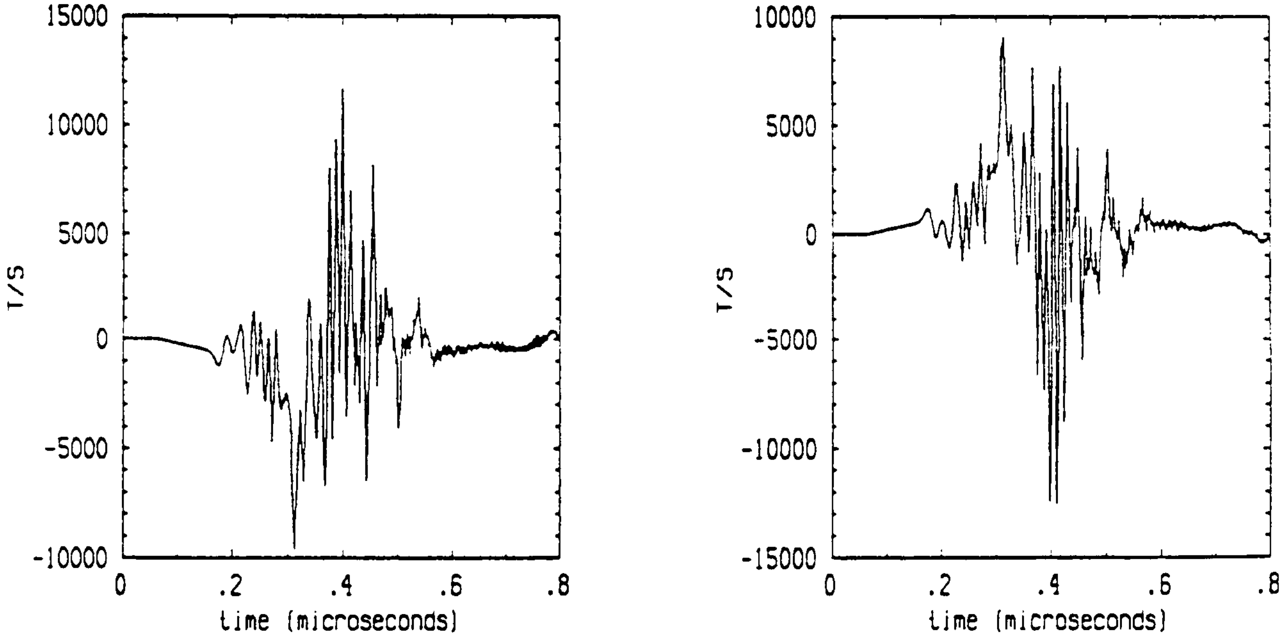

B-DOT RW

B-DOT LW

Figure 6.2 **F106B Electromagnetic Sensor Responses for Return Stroke Attachment**

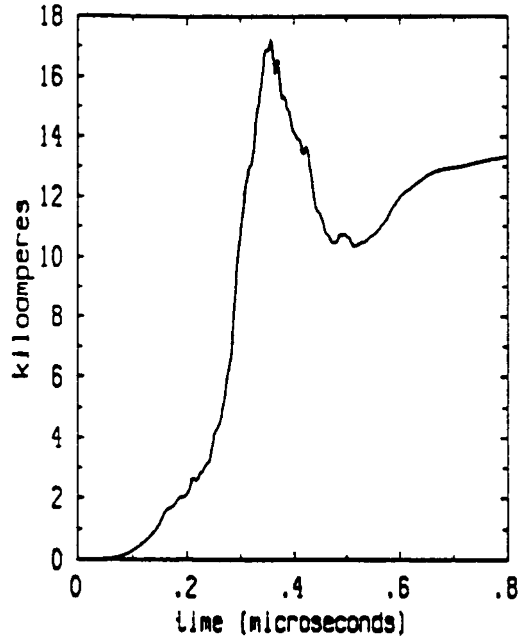

nose current

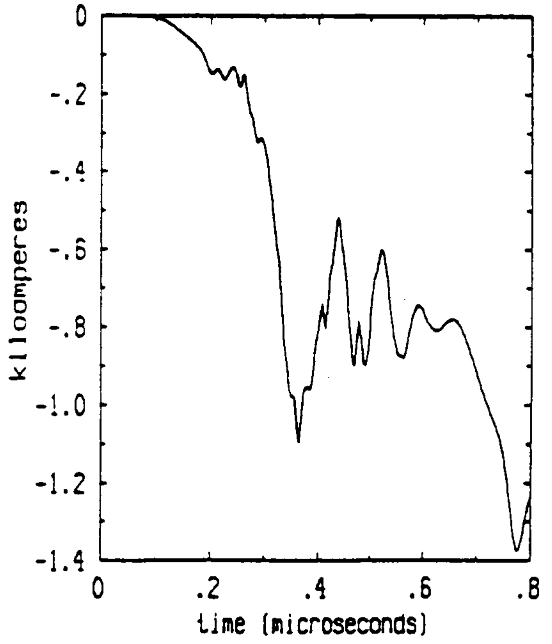

tail current

Figure 6.3 **Return Stroke Current Waveforms at Locations of Current Sensors on the F106B**

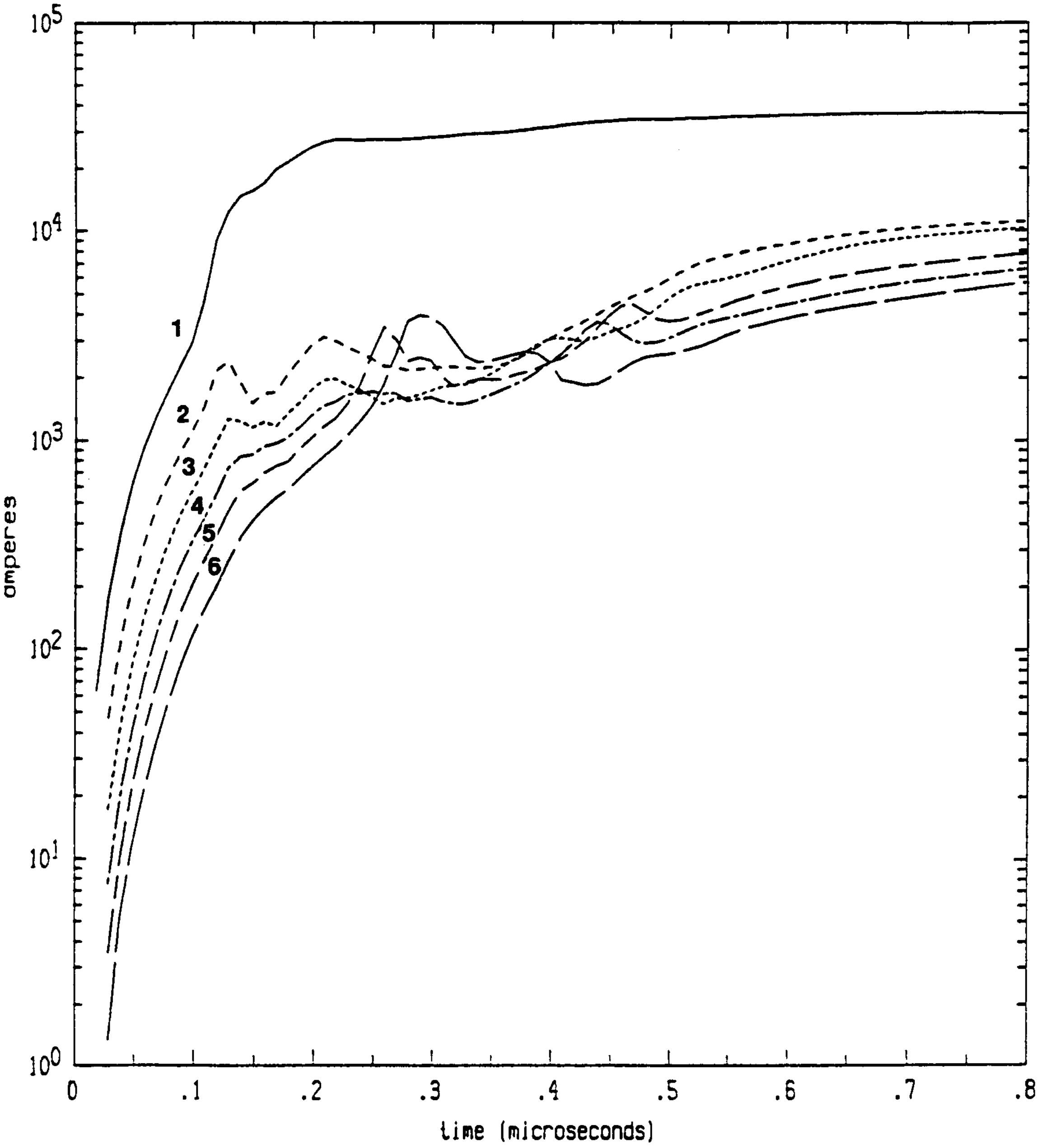

Curve 1 = 5.5 meters from the nose of aircraft
2 = 4.5 meters from the nose of aircraft
3 = 3.5 meters from the nose of aircraft
4 = 2.5 meters from the nose of aircraft
5 = 1.5 meters from the nose of aircraft
6 = .5 meters from the nose of aircraft

Figure 6.4 **Currents in the Lightning Channel at Varying Distances from the Nose of the F106B**

the current patterns are those expected for a fairly conductive path, showing time-delayed growth along the channel. The current waveform shown in curve 1 is quite similar to the forced current waveform. The amplitude is smaller because the injected current was allowed to flow transverse to the original leader channel as well as along it. After the first hundred nanoseconds, the charge deposited by the injected current is large enough to cause further ionization of the air with an accompanying increase in the conductivity. The competing process of attachment, however, tends to lower the conductivity. Consequently, the conductivity along the channel fluctuates both in time and space as shown in Figure 6.5. That figure shows the conductivity associated with cells along the core of the channel. The labeling of the curves is the same as in Figure 6.4, i.e., curve 1 is the conductivity of the cell just ahead of the injected current, curve 2 is one meter further along the channel, etc. The decrease of the conductivity in the first 100 nanoseconds occurs because of the attachment of the electrons that were initially assigned to the channel. For the next 500 nanoseconds, the interplay of the processes of electron avalanche and attachment produces a period of rapid change in the conductivity along the channel. This is also reflected in the calculated sensor responses as shown in Figures 6.1 and 6.2. Subsequent to this active period, the conductivity and current in the channel increase gradually and smoothly. Because the sensor measured the time rate of change of the field, their responses were reduced to comparatively low level. Corona formation around the aircraft also tended to shield the sensors from transients produced elsewhere.

The total current flowing onto the aircraft, represented by the nose current, is shown in Figure 6.3. It is less than the injected current of 50 kA because of corona shielding, which tends to divert current away from the aircraft. The tail current is negative which indicates that current is exiting the aircraft at the vertical fin into the air. Currents flowing on other parts of the aircraft were not monitored. However, because charge densities were assigned initially throughout the problem space and there was probable corona discharge at various locations on the aircraft due to charge accumulation, it is reasonable to assume that current was also exiting at other locations, notably at the wing tips.

6.4 Conclusions

In conclusion, the response of the F106B aircraft to a return stroke current has been calculated using a nonlinear model. The calculated responses for the rate of

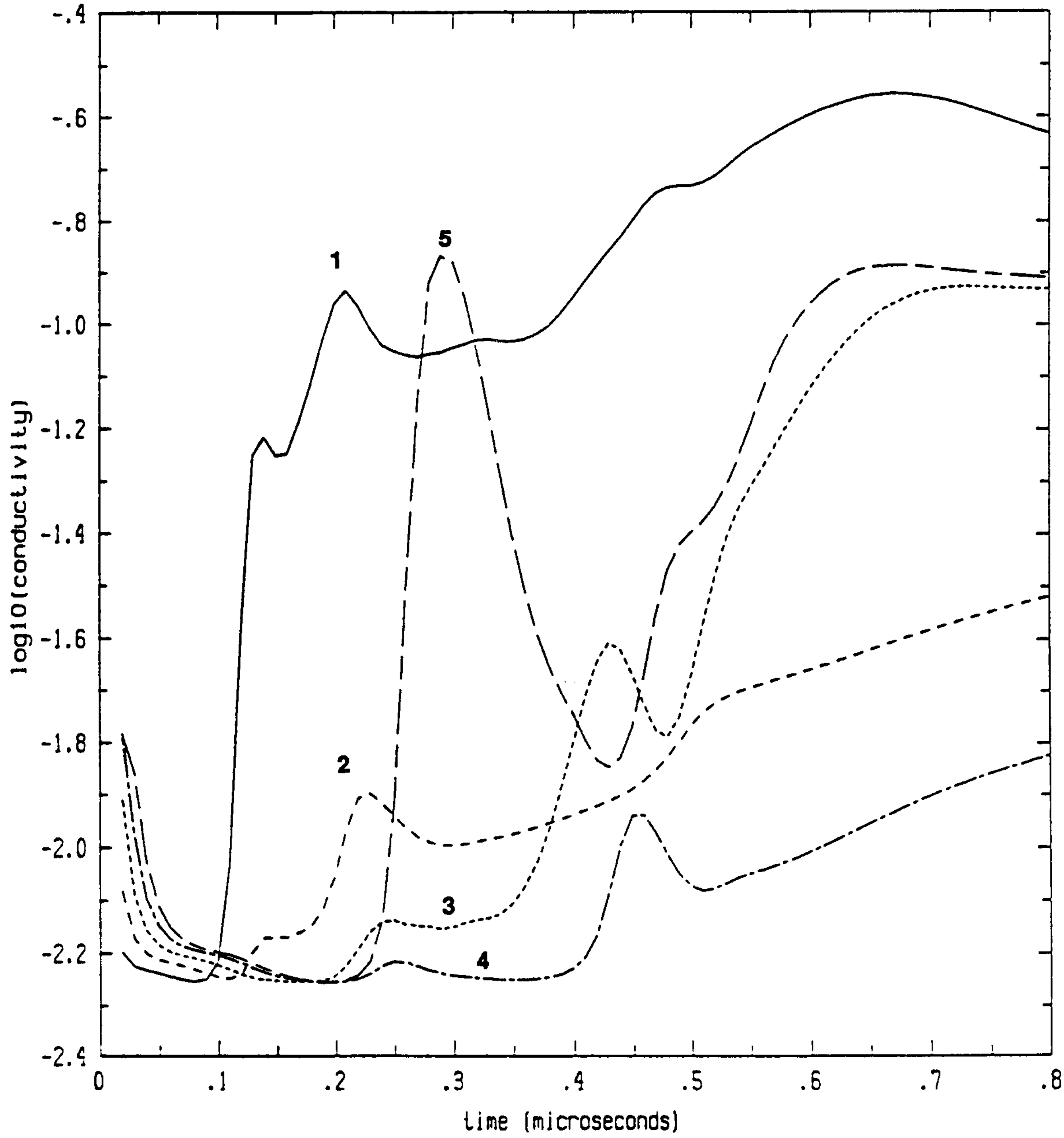

Curve 1 = 5.5 meters from the nose of aircraft
2 = 4.5 meters from the nose of aircraft
3 = 3.5 meters from the nose of aircraft
4 = 2.5 meters from the nose of aircraft
5 = 1.5 meters from the nose of aircraft

Figure 6.5 Air Conductivity as a Function of Time and Space Along the Lightning Channel

change sensors were pulse-like in character in response to the rapid variation of the conductivity of the channel during the few hundred nanoseconds immediately after the arrival of the lightning current. Once the channel was established, as indicated by high conductivity, the sensor responses were reduced to a relatively low level. It should be noted that in general the calculated responses are significantly larger than measured responses.

CHAPTER 7
SUMMARY

The work reported here has concentrated on the application of existing numerical models to measured F106B data, and the extension of that work to aircraft other than the F106B. The correlations developed from the extended application of the linear triggered lightning model to the 1984 F106B data set are useful in inferring triggered lightning currents and rise rates for strikes in which these quantities were not measured. The analysis shows reasonably good linear correlations between the peak responses of selected sensors.

Field mill data from three selected flights have been analyzed to predict ambient electric field and aircraft charge just before the occurrence of a triggered strike. Although there are uncertainties in the accuracy of the field mill system, the analysis predicts field and charge levels which are adequate to cause a triggered strike to the F106B. Comparison of calculated sensor responses with measured responses was not done, as digitized observational data was not available at the time of this report.

Application of subgrid techniques have been applied to the situation of a triggered strike to the nose of the F106B. This has produced refined estimates for the electric field level necessary to cause air breakdown at that location. More precise definition of triggering conditions needs to take into account the presence of atmospheric particles and field gradients, in addition to absolute field levels. Waveforms of nonlinear predicted transient responses have been compared with measured responses and with non-subgrid nonlinear responses. The subgrid responses appear to match the measured responses slightly better than the non-subgrid responses.

Extension of the triggered lightning models developed under this program to other aircraft (CV-580, C-130, LearJet) has been accomplished. Scaling laws have been developed for triggering field levels for aircraft of varying sizes and shapes, and principles for scaling transient responses between different aircraft have been investigated.

The response of the F106B to a leader-return stroke combination of events has been documented. In this model, the leader is assumed to have formed a channel of which the aircraft is a part. This partly ionized channel then carries a return stroke current which passes through the F106B . Transient responses and channel parameters have been calculated, allowing comparison with responses from flight data of triggered lightning events.

REFERENCES

1. Rudolph, T., and R.A. Perala, "Interpretation Methodology and Analysis of In-Flight Lightning Data," NASA CR-3590, October 1982.

2. Rudolph, T.H., and R.A. Perala, "Linear and Nonlinear Interpretation of the Direct Strike Lightning Response of the NASA F106B Thunderstorm Research Aircraft," NASA CR-3746, March 1983.

3. Rudolph, T.H., R.A. Perala, P.M. McKenna, and S.L. Parker, "Investigations Into the Triggered Lightning Response of the F106B Thunderstorm Research Aircraft," NASA CR-3902, June 1985.

4. Rudolph, T.H., R.A. Perala, C.C. Easterbrook, and S.L. Parker, "Development and Application of Linear and Nonlinear Methods for the Interpretation of Lightning Strikes to In-Flight Aircraft," NASA CR-3974, September 1986.

5. Rudolph, T., C.C. Easterbrook, P.H. Ng, R.W. Haupt, and R.A. Perala, "Experimental and Analytic Studies of the Triggered Lightning Environment of the F106B," NASA CR-4104, December 1987.

6. Pitts, Felix L., and Mitchel E. Thomas, "1980 Direct Strike Lightning Data," NASA TM-81946, February 1981.

7. Pitts, Felix L., and Mitchel E. Thomas, "1981 Direct Strike Lightning Data," NASA TM-83273, March 1982.

8. Thomas, Mitchel E., and Felix L. Pitts, "1982 Direct Strike Lightning Data," NASA TM-84626, March 1983.

9. Thomas, Mitchel E., "1983 Direct Strike Lightning Data," NASA TM-86426, August 1985.

10. Thomas, Mitchel E., and Harold K. Carney, "1984 Direct Strike Lightning Data NASA TM-87690, September 1986.

11. Zaepfel, Klaus, P., and Harold K. Carney, "1985 and 1986 Direct Strike Lightning Data," NASA TM-100533, March 1988.

12. Golub, Gene H., C.F. Van Loon, "Matrix Computations," The Johns Hopkins University Press, 1983.

13. Mazur, V., L.H. Ruhnke, and T. Rudolph, "Effect of E-Field Mill Location on Accuracy of Electric Field Measurements with Instrumented Airplane," Journal of Geophysical Research, 92, No. D10, October 20, 1987, pp. 12,013-12,019.

14. Merewether, D.E., and R. Fisher, "Finite Difference Solution of Maxwell's Equations for EMP Applications," Defense Nuclear Agency 5301F, (Contract Number DNA001-78-C-0231), Electro Magnetic Applications, Inc., April 1980.

15. Stratton, J.A., "Electromagnetic Theory," McGraw-Hill, New York, 1941.

16. Abramowitz, M., I.A. Stegun, "Handbook of Mathematical Functions," Dover, New York, 1965.

17. Radasky, William A., "An Examination of the Adequacy of the Three Species Air Chemistry Treatment for the Prediction of Surface Burst EMP," Defense Nuclear Agency 3880T, (Contract Number DNA001-75-C-0094), Mission Research Corp., December 1975.

18. Parkes, D.A., "Negative-ion/Molecule Reactions Under Swarm Conditions," Vacuum 24, 1976, pp. 561-571.

APPENDIX A

Overlays of Measured Sensor Responses and Predicted Waveforms Calculated from Linear Triggered Lightning Model

For I-dot Comparisons see Section 2.2.3

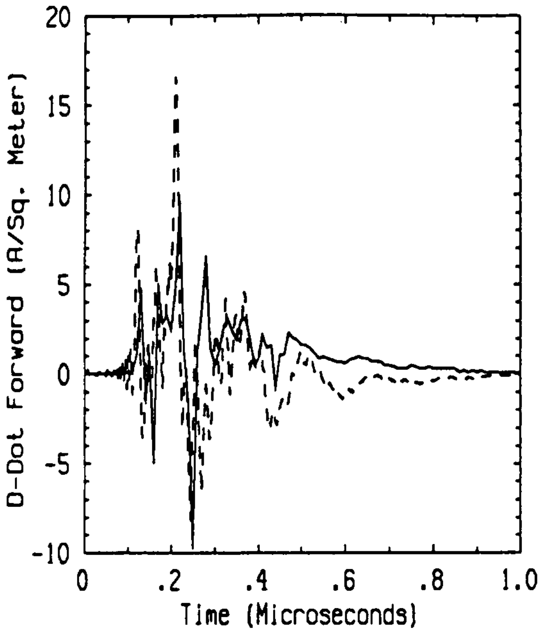

Flight 84.017 Run 001 Strike 002
- Measured -- Predicted

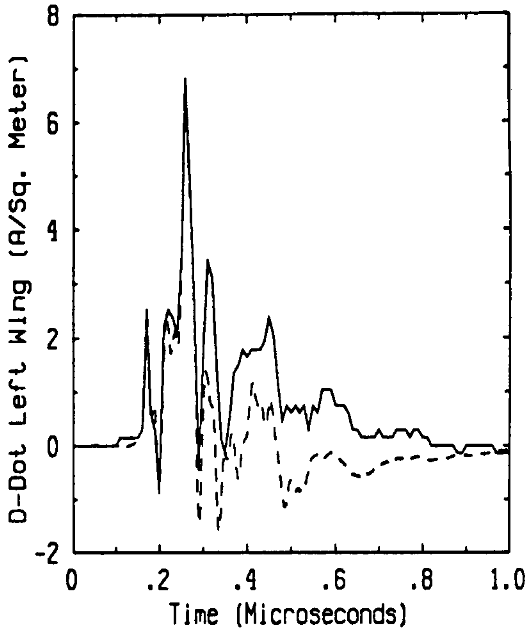

Flight 84.017 Run 001 Strike 002
- Measured -- Predicted

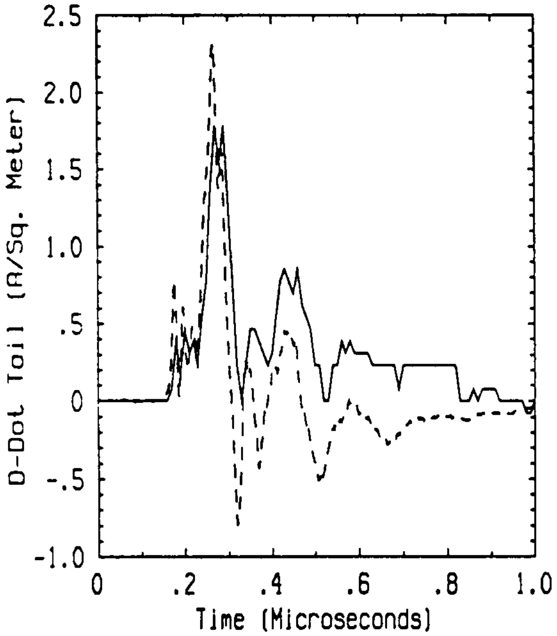

Flight 84.017 Run 001 Strike 002
- Measured -- Predicted

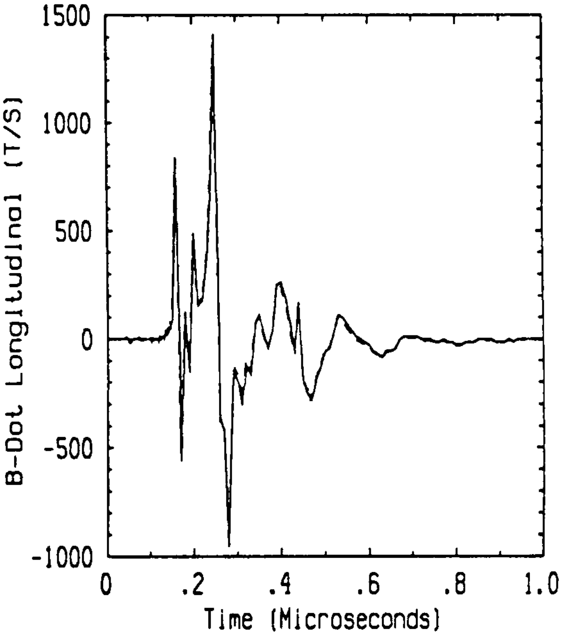

Flight 84.017 Run 001 Strike 002
- Measured -- Predicted

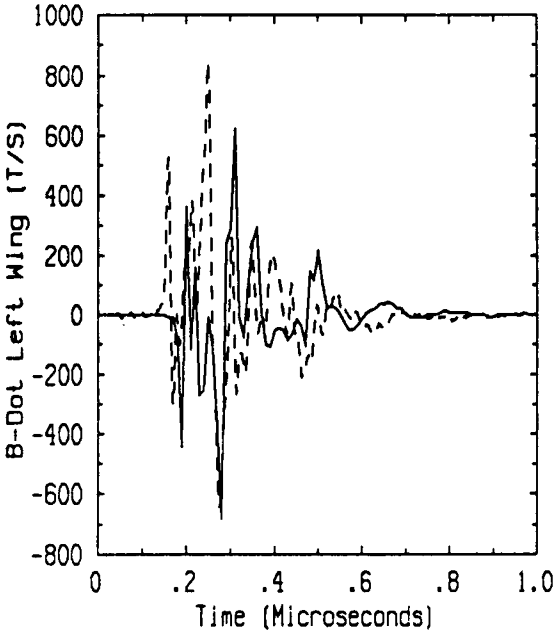

Flight 84.017 Run 001 Strike 002
- Measured -- Predicted

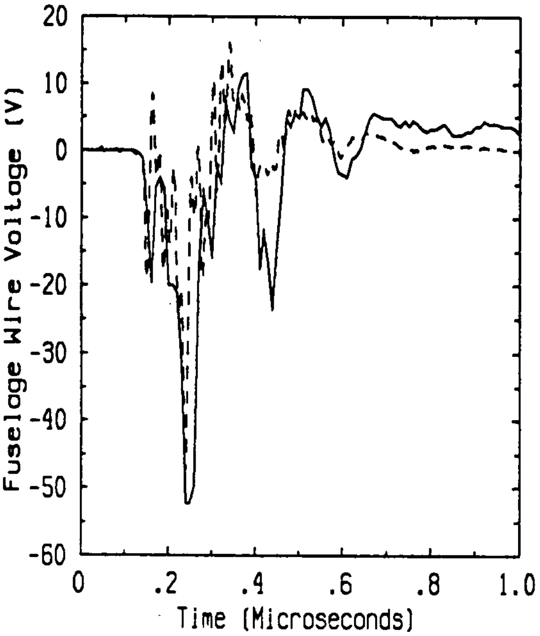

Flight 84.017 Run 001 Strike 002
- Measured -- Predicted

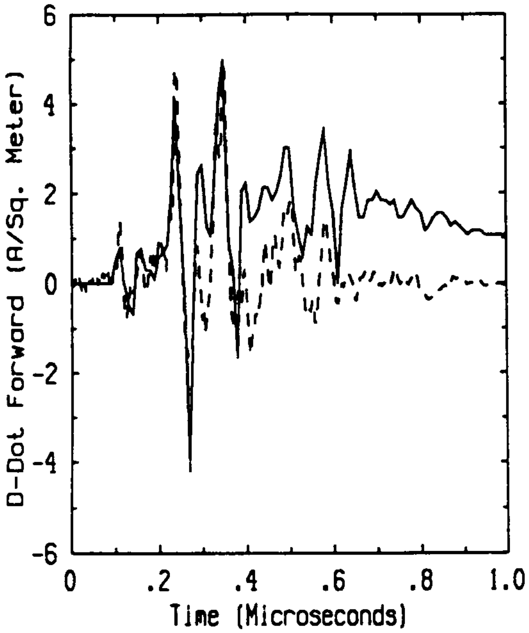

Flight 84.021 Run 001 Strike 001
- Measured -- Predicted

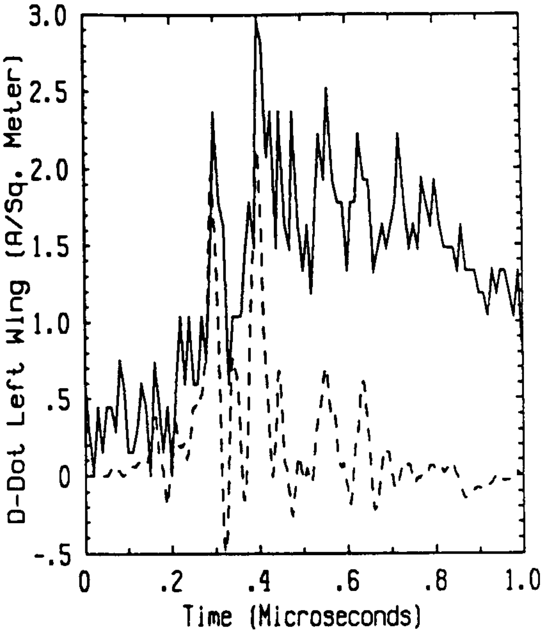

Flight 84.021 Run 001 Strike 001
- Measured -- Predicted

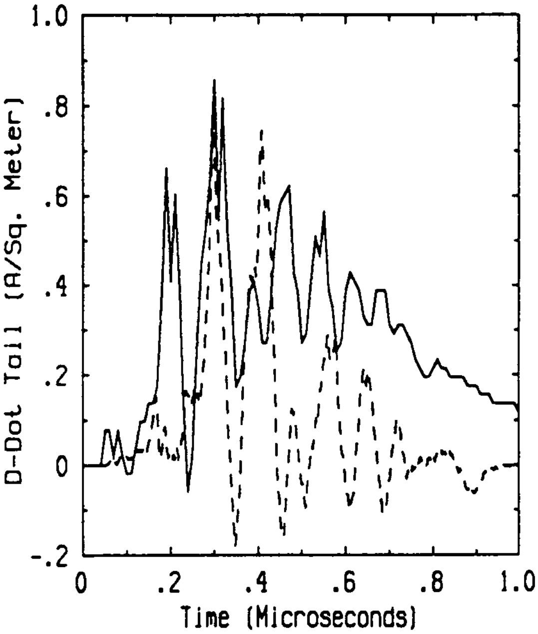

Flight 84.021 Run 001 Strike 001
- Measured -- Predicted

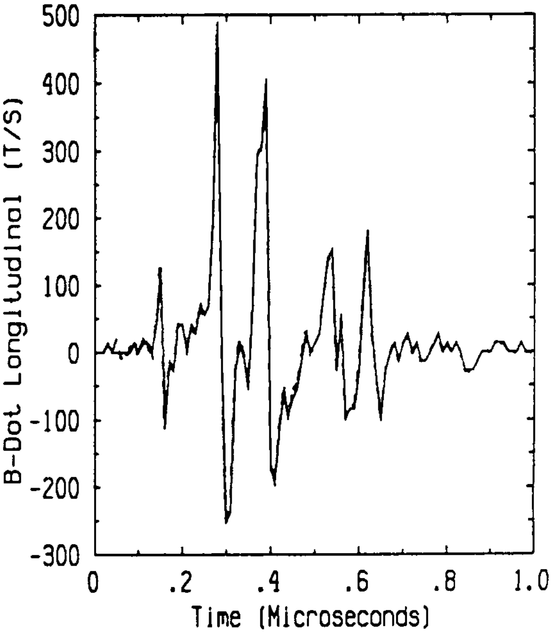

Flight 84.021 Run 001 Strike 001
- Measured -- Predicted

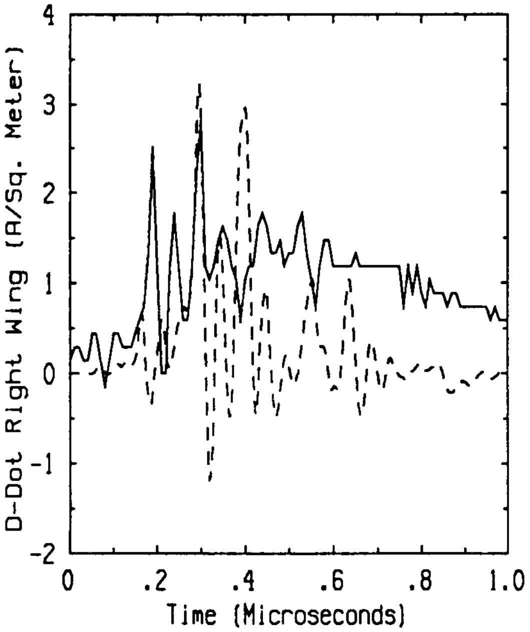

Flight 84.021 Run 001 Strike 001
- Measured -- Predicted

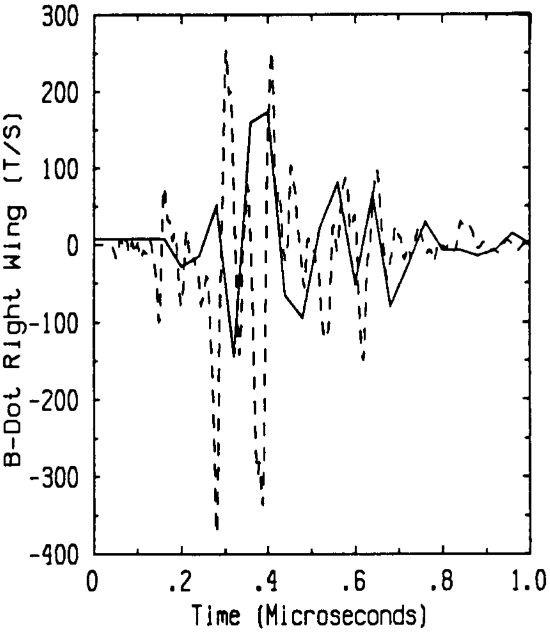

Flight 84.021 Run 001 Strike 001
- Measured -- Predicted

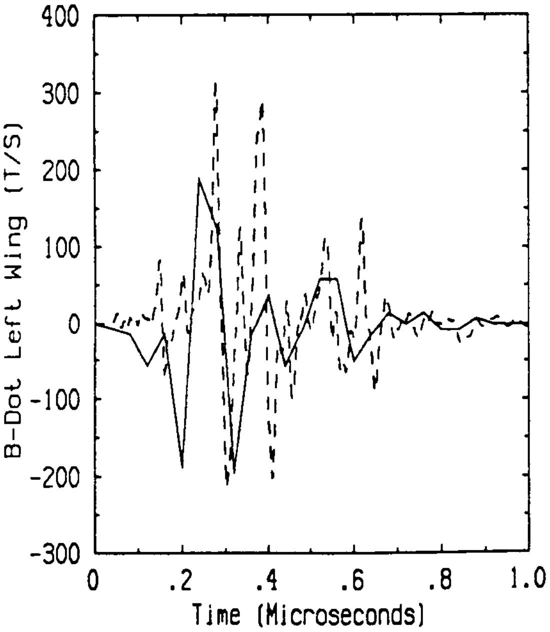

Flight 84.021 Run 001 Strike 001
- Measured -- Predicted

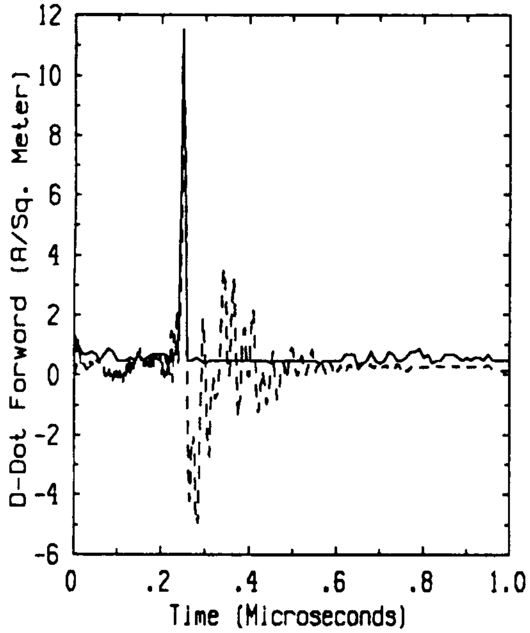

Flight 84.021 Run 003 Strike 001
- Measured -- Predicted

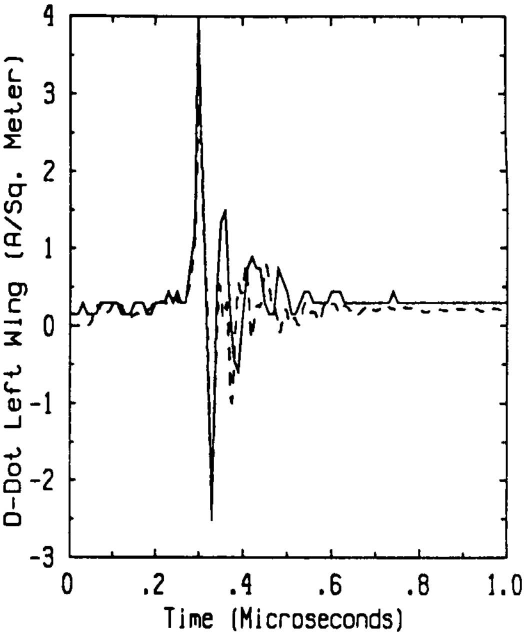

Flight 84.021 Run 003 Strike 001
- Measured -- Predicted

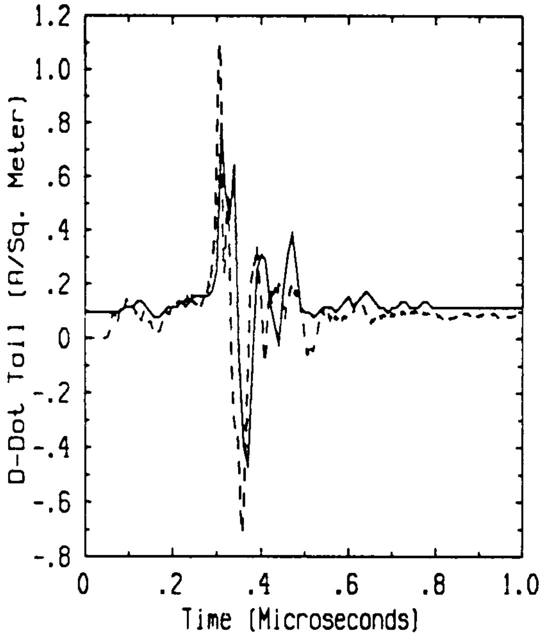

Flight 84.021 Run 003 Strike 001
- Measured -- Predicted

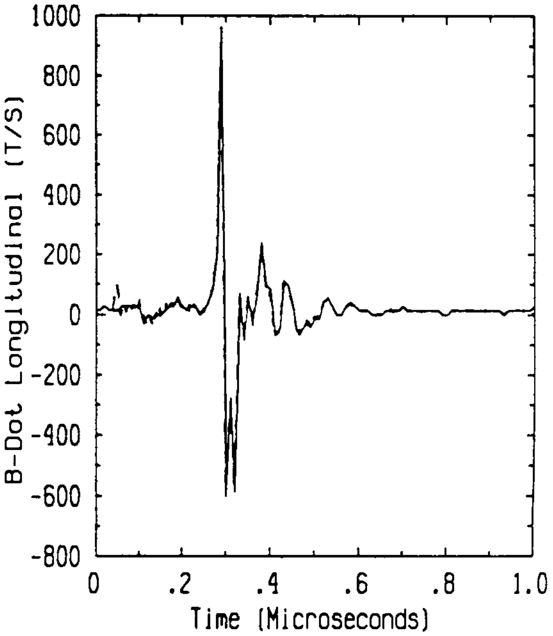

Flight 84.021 Run 003 Strike 001
- Measured -- Predicted

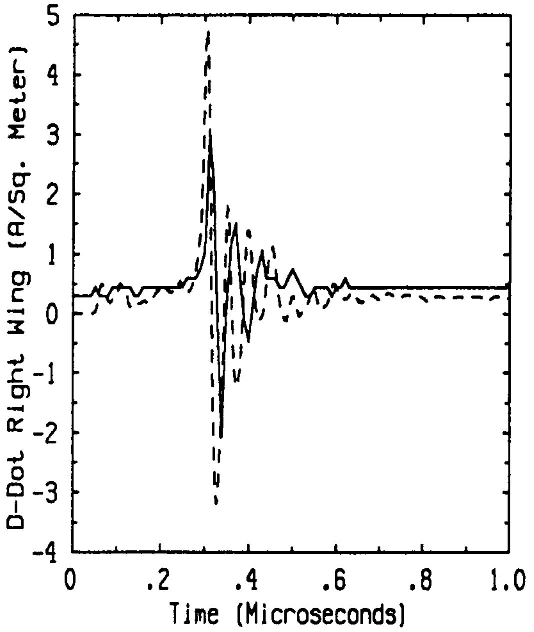

Flight 84.021 Run 003 Strike 001
- Measured -- Predicted

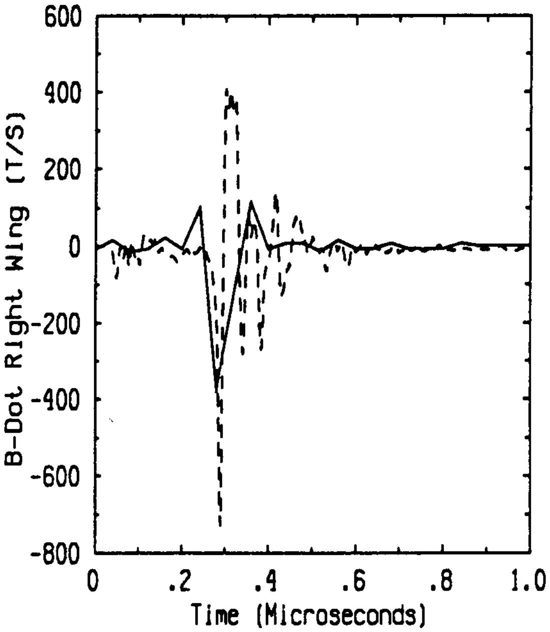

Flight 84.021 Run 003 Strike 001
- Measured -- Predicted

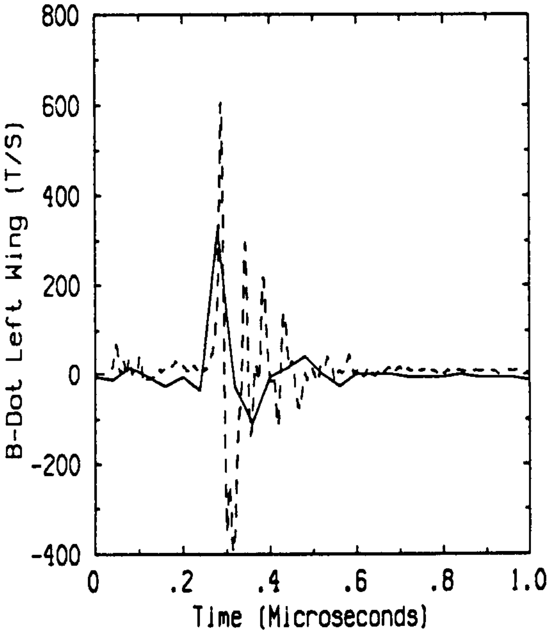

Flight 84.021 Run 003 Strike 001
- Measured -- Predicted

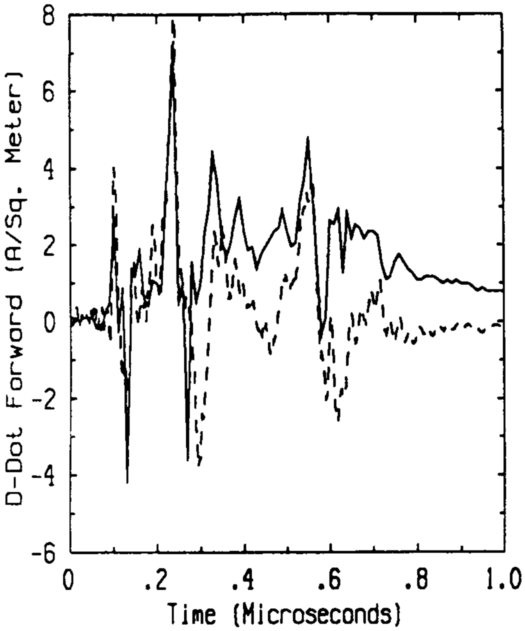

Flight 84.023 Run 002 Strike 002
- Measured -- Predicted

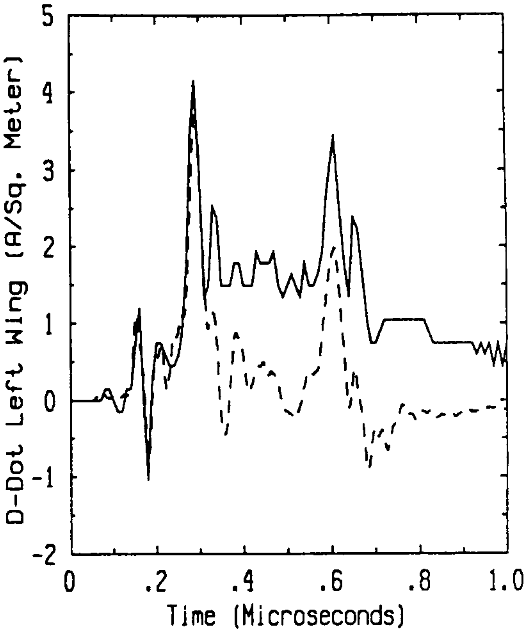

Flight 84.023 Run 002 Strike 002
- Measured -- Predicted

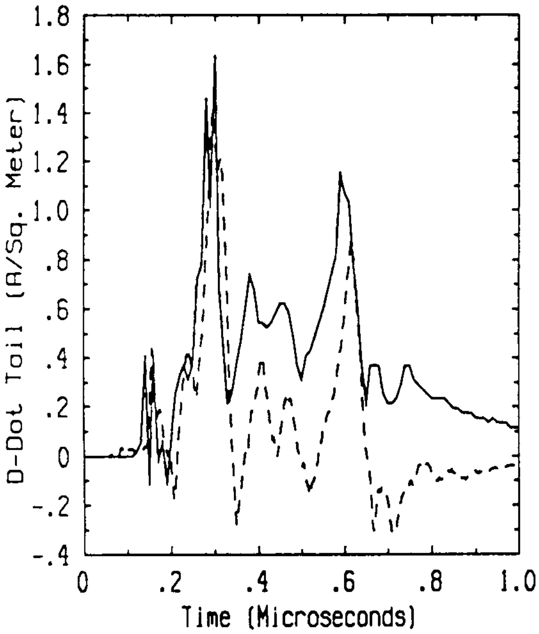

Flight 84.023 Run 002 Strike 002
- Measured -- Predicted

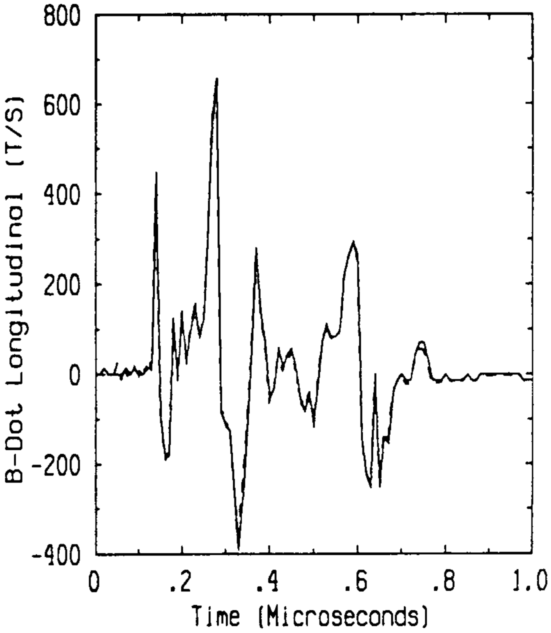

Flight 84.023 Run 002 Strike 002
- Measured -- Predicted

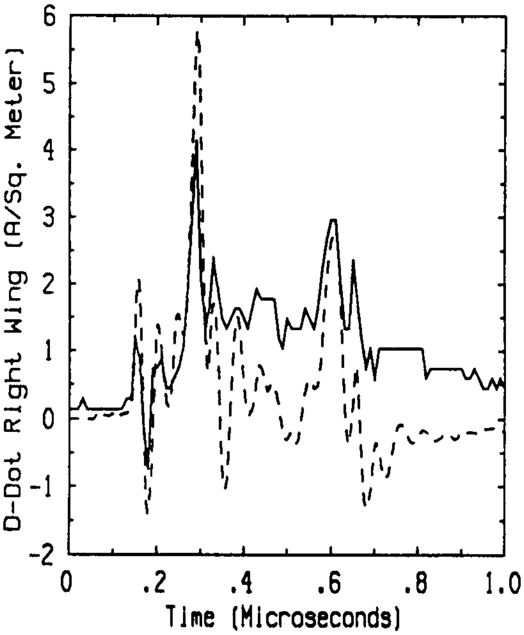

Flight 84.023 Run 002 Strike 002
- Measured -- Predicted

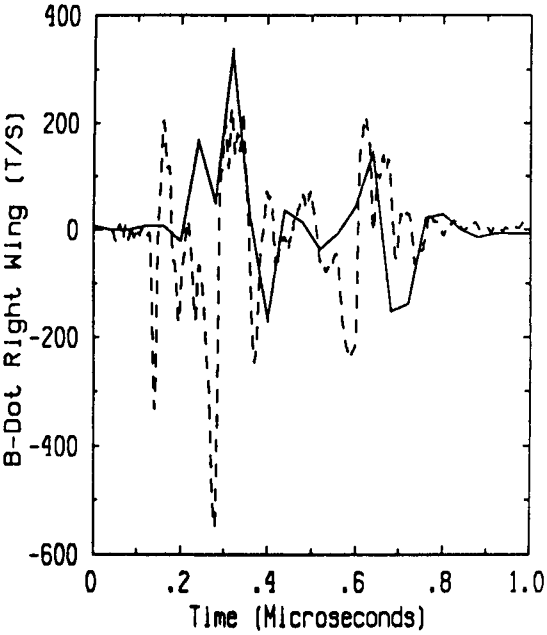

Flight 84.023 Run 002 Strike 002
- Measured -- Predicted

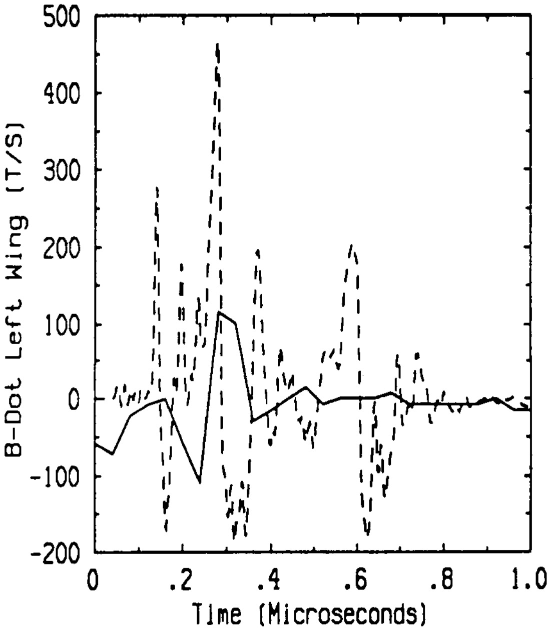

Flight 84.023 Run 002 Strike 002
- Measured -- Predicted

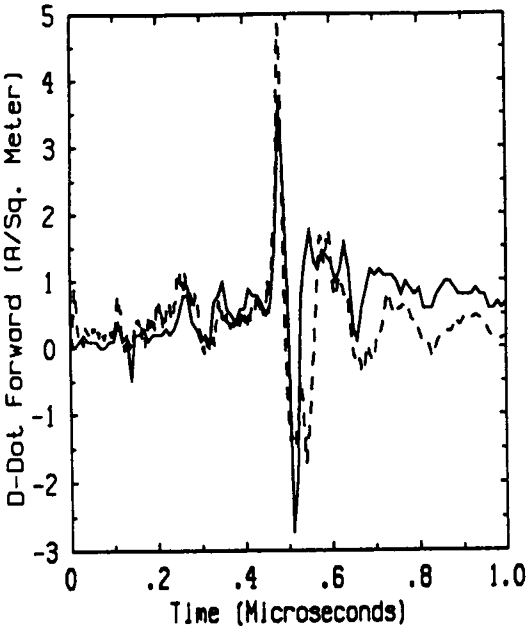

Flight 84.024 Run 001 Strike 001
- Measured -- Predicted

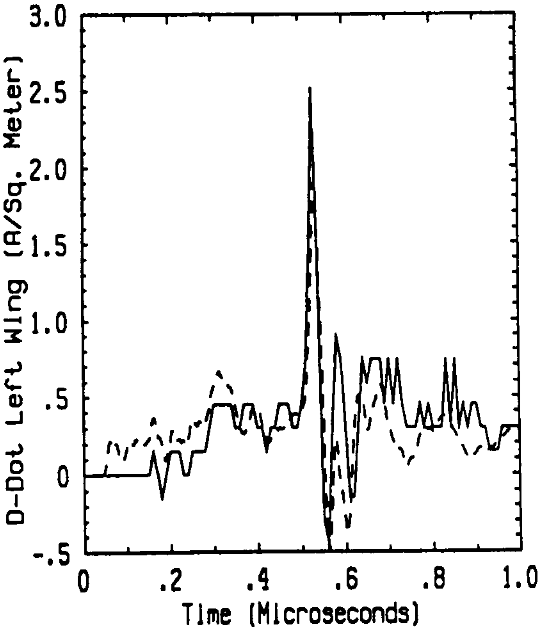

Flight 84.024 Run 001 Strike 001
- Measured -- Predicted

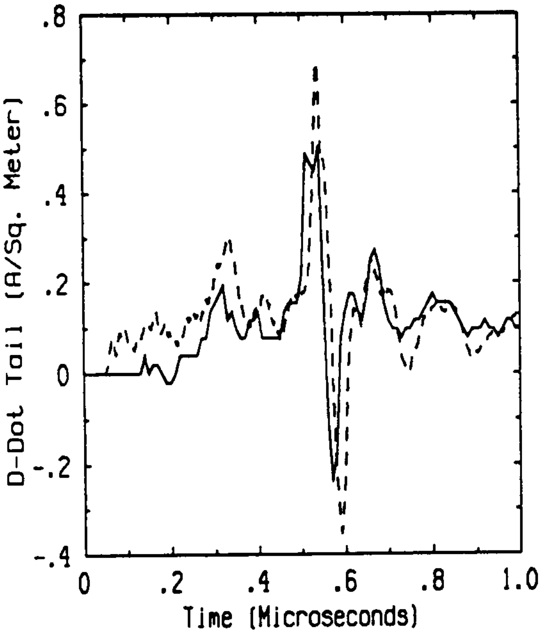

Flight 84.024 Run 001 Strike 001
- Measured -- Predicted

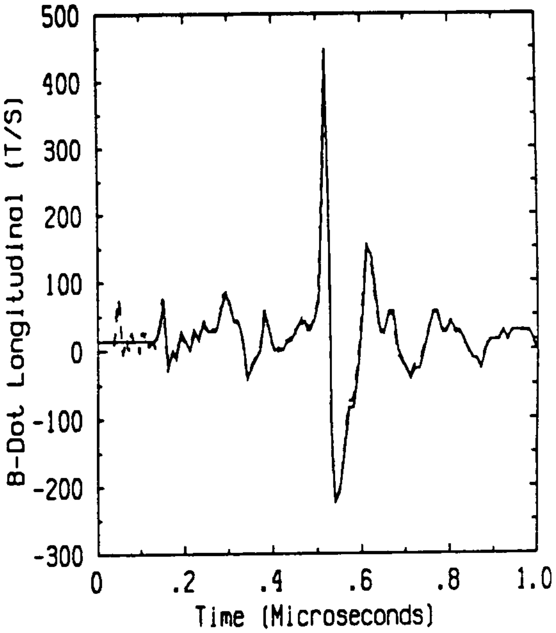

Flight 84.024 Run 001 Strike 001
- Measured -- Predicted

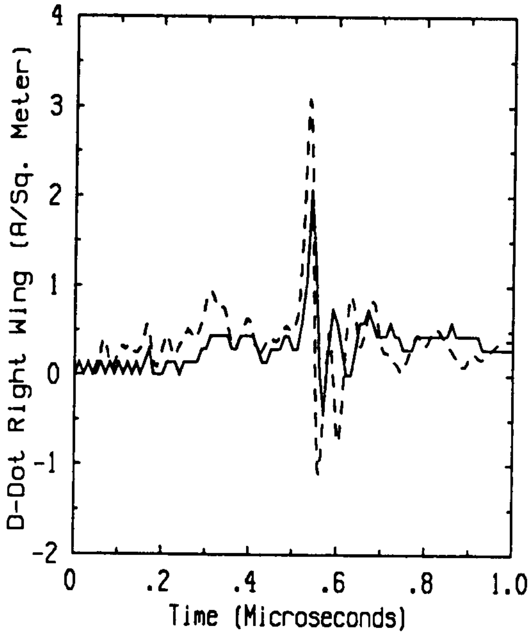

Flight 84.024 Run 001 Strike 001
- Measured -- Predicted

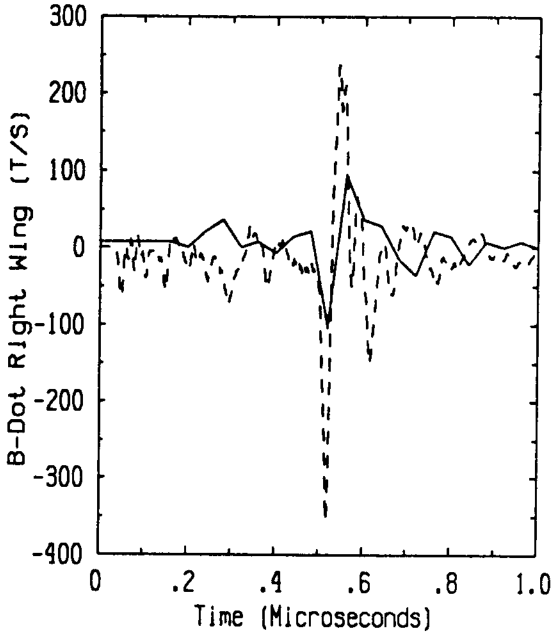

Flight 84.024 Run 001 Strike 001
- Measured -- Predicted

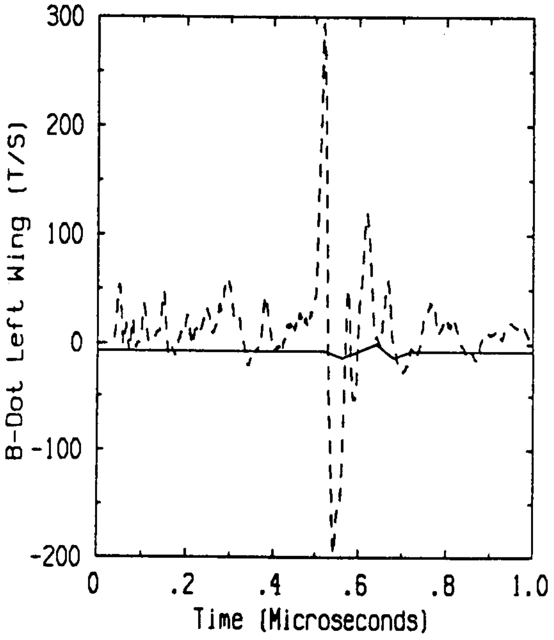

Flight 84.024 Run 001 Strike 001
- Measured -- Predicted

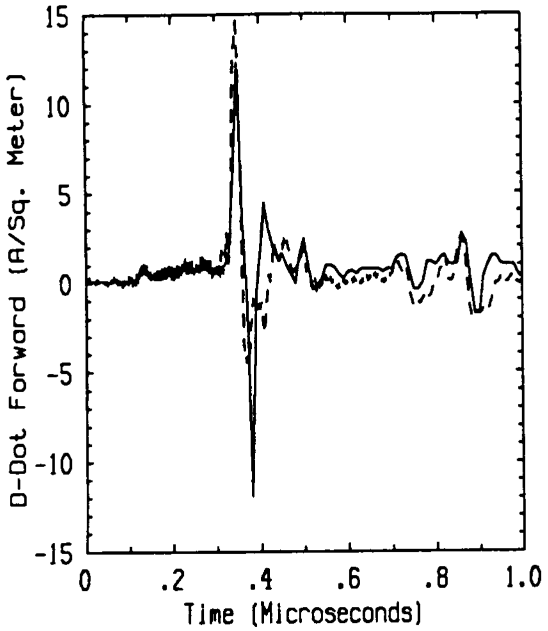

Flight 84.024 Run 003 Strike 003
- Measured -- Predicted

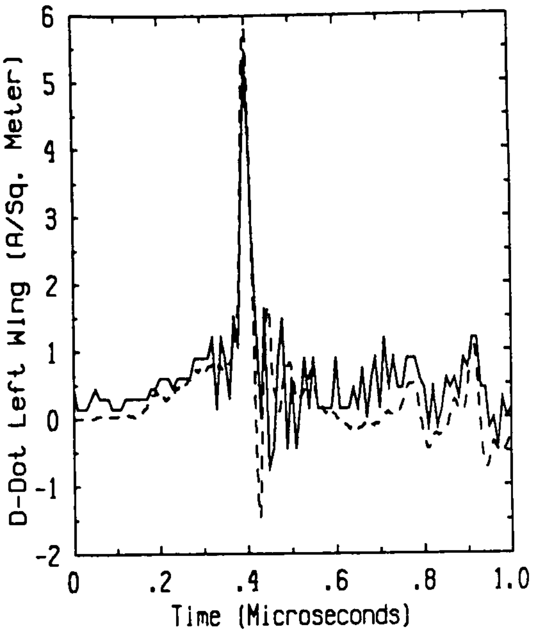

Flight 84.024 Run 003 Strike 003
- Measured -- Predicted

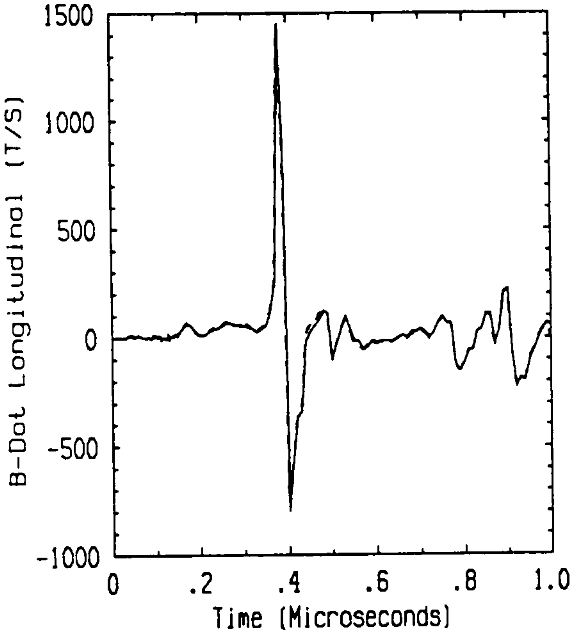

Flight 84.024 Run 003 Strike 003
- Measured -- Predicted

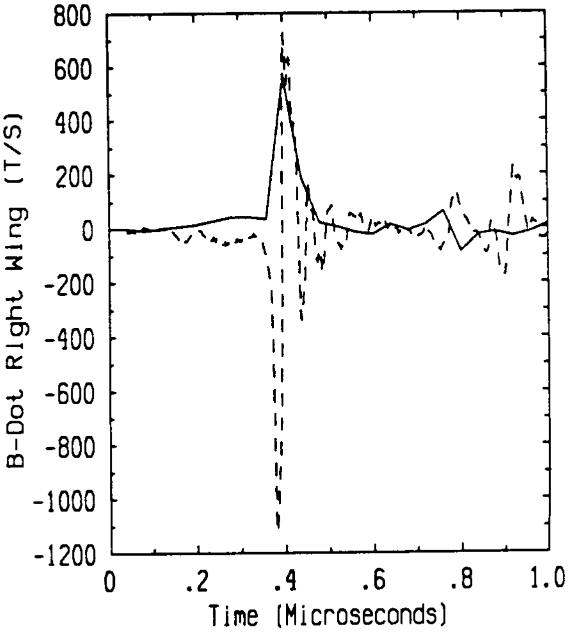

Flight 84.024 Run 003 Strike 003
- Measured -- Predicted

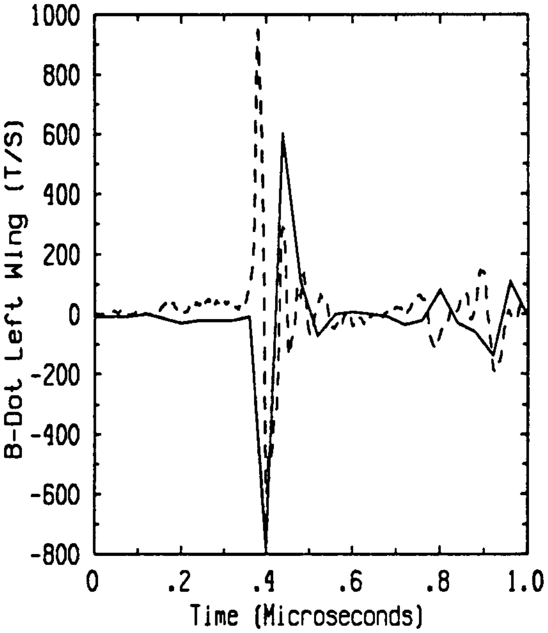

Flight 84.024 Run 003 Strike 003
- Measured -- Predicted

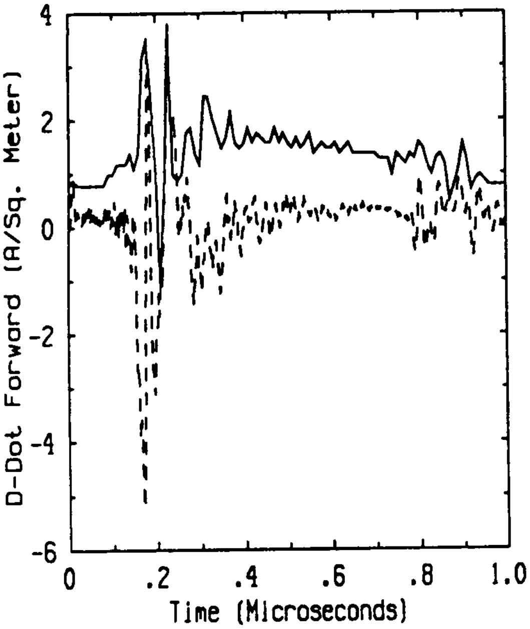

Flight 84.025 Run 001 Strike 001
- Measured -- Predicted

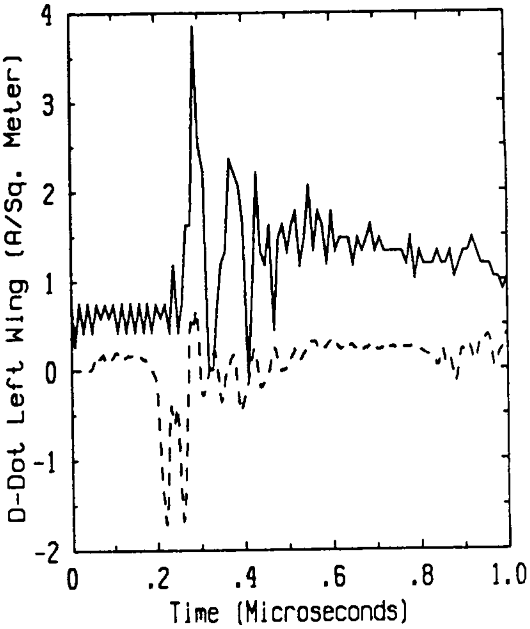

Flight 84.025 Run 001 Strike 001
- Measured -- Predicted

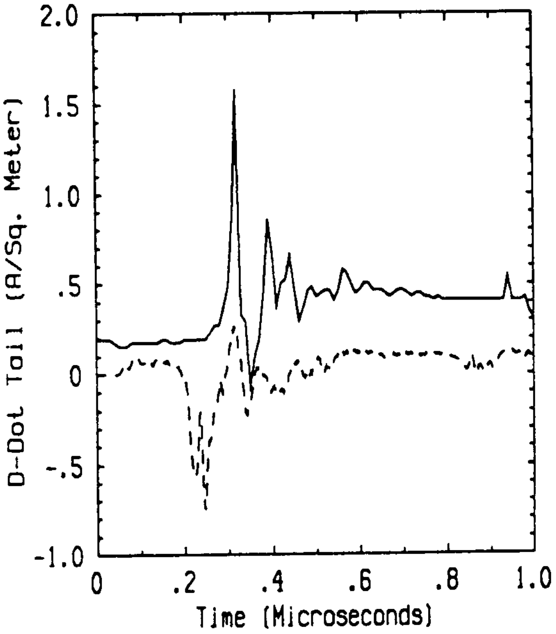

Flight 84.025 Run 001 Strike 001
- Measured -- Predicted

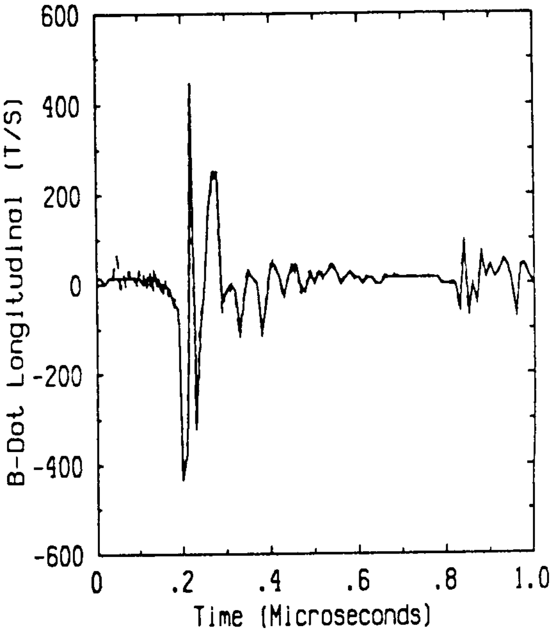

Flight 84.025 Run 001 Strike 001
- Measured -- Predicted

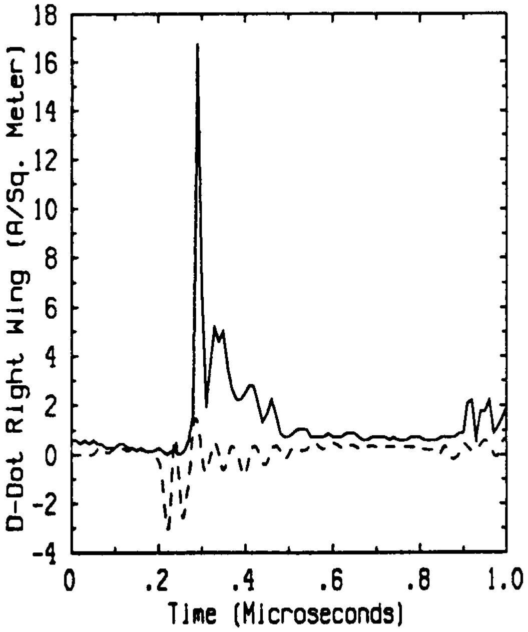

Flight 84.025 Run 001 Strike 001
- Measured -- Predicted

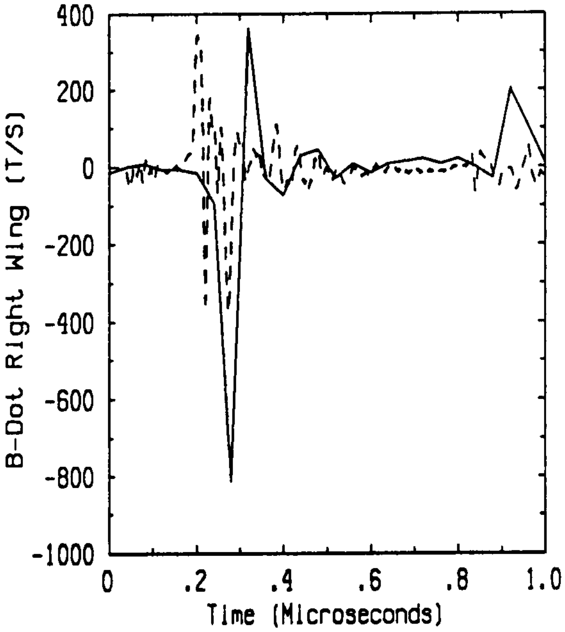

Flight 84.025 Run 001 Strike 001
- Measured -- Predicted

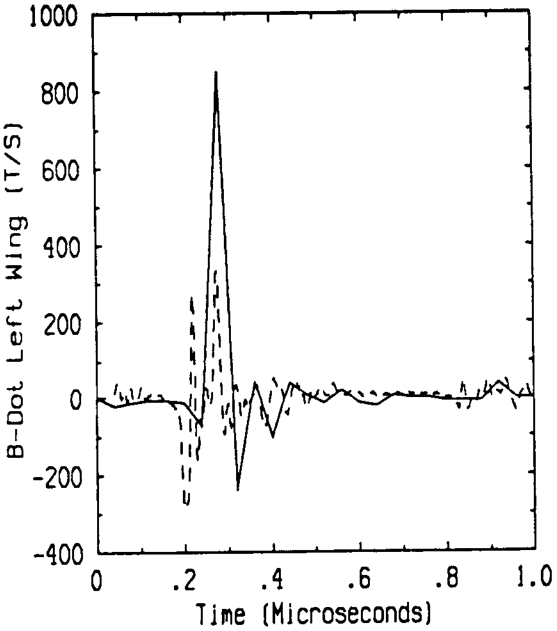

Flight 84.025 Run 001 Strike 001
- Measured -- Predicted

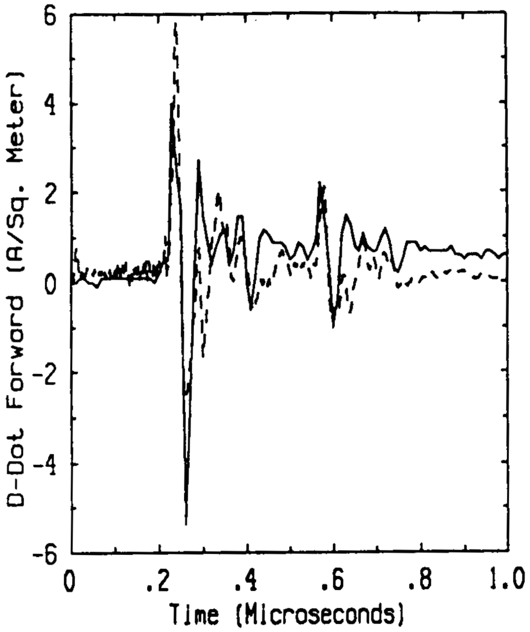

Flight 84.025 Run 002 Strike 003
- Measured -- Predicted

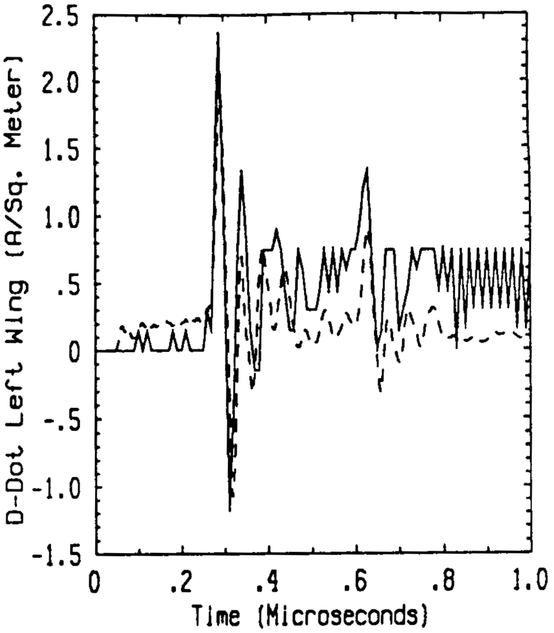

Flight 84.025 Run 002 Strike 003
- Measured -- Predicted

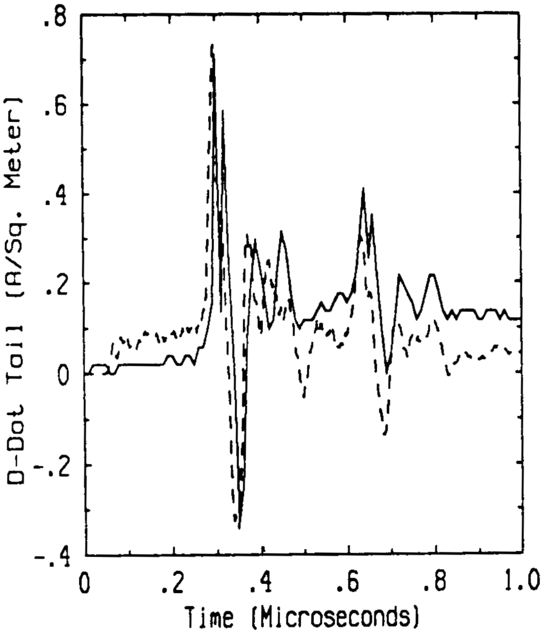

Flight 84.025 Run 002 Strike 003
- Measured -- Predicted

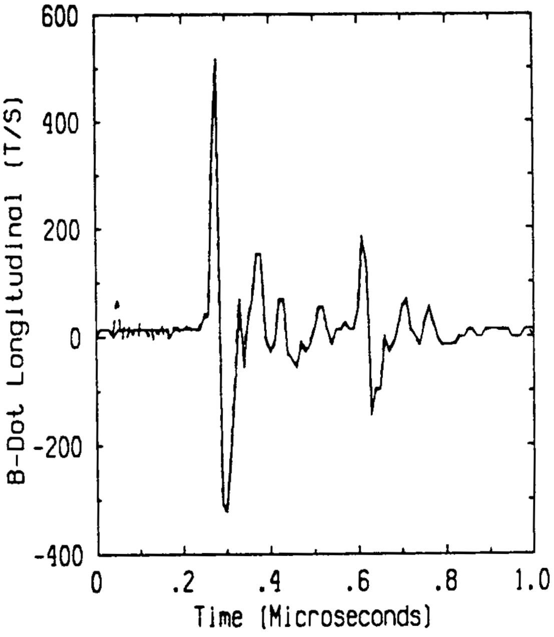

Flight 84.025 Run 002 Strike 003
- Measured -- Predicted

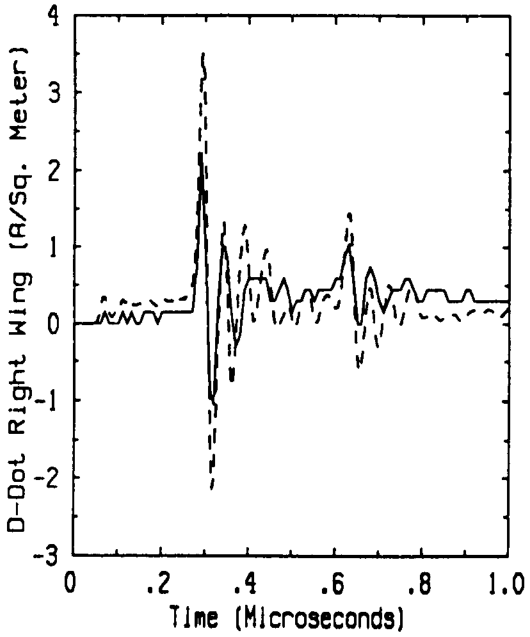

Flight 84.025 Run 002 Strike 003
- Measured -- Predicted

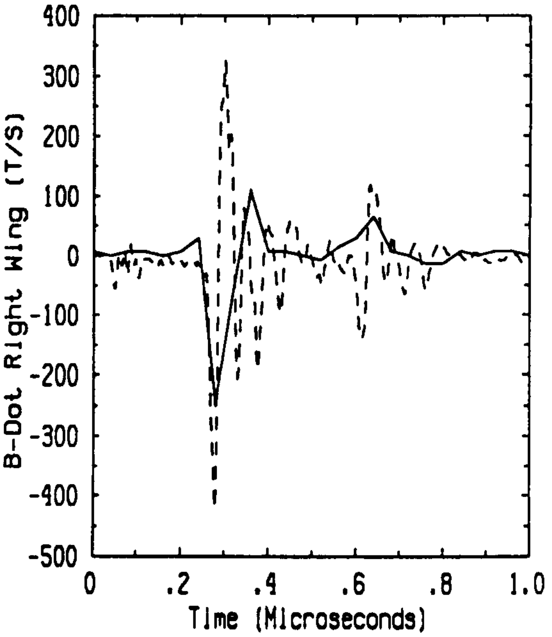

Flight 84.025 Run 002 Strike 003
- Measured -- Predicted

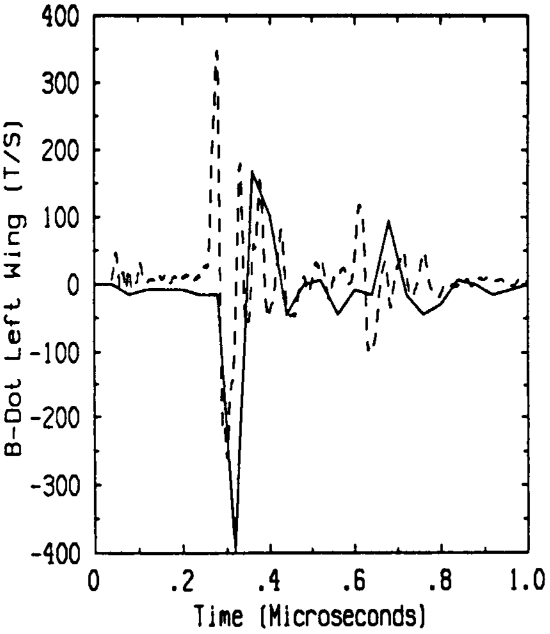

Flight 84.025 Run 002 Strike 003
- Measured -- Predicted

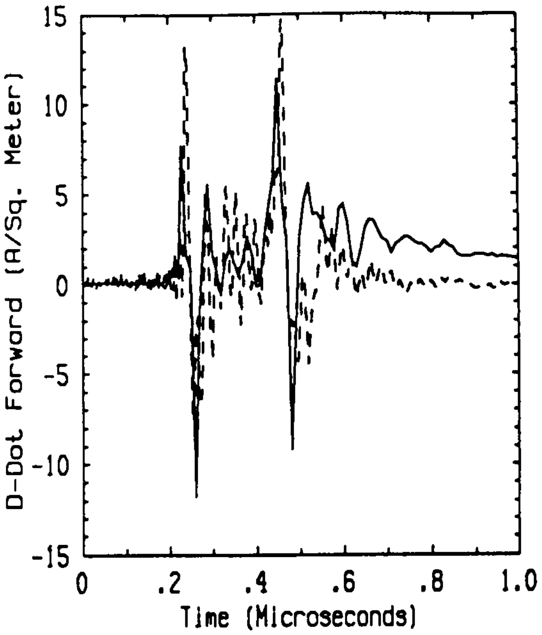

Flight 84.025 Run 003 Strike 004
- Measured -- Predicted

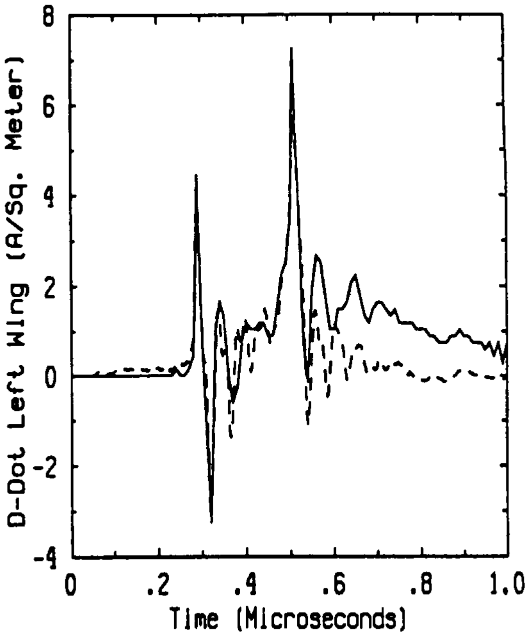

Flight 84.025 Run 003 Strike 004
- Measured -- Predicted

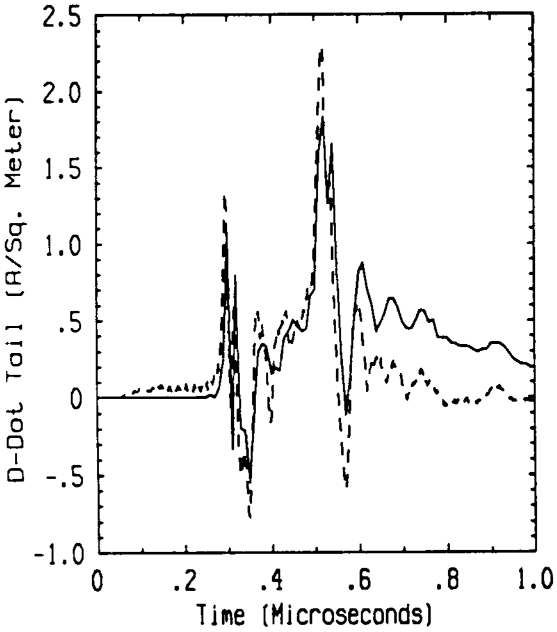

Flight 84.025 Run 003 Strike 004
- Measured -- Predicted

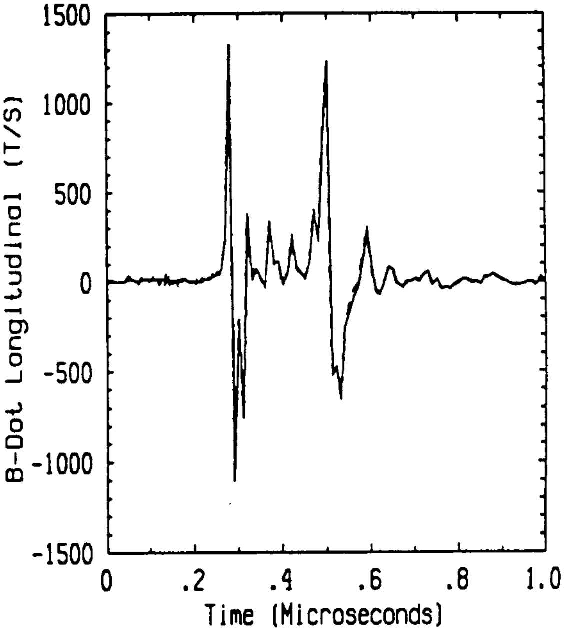

Flight 84.025 Run 003 Strike 004
- Measured -- Predicted

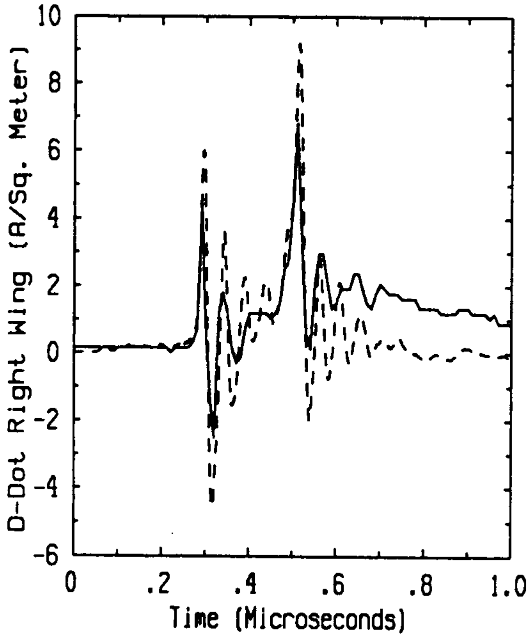

Flight 84.025 Run 003 Strike 004
- Measured -- Predicted

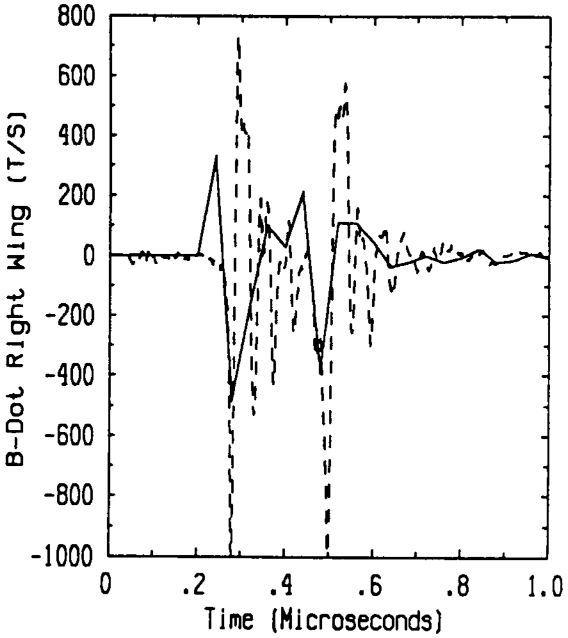

Flight 84.025 Run 003 Strike 004
- Measured -- Predicted

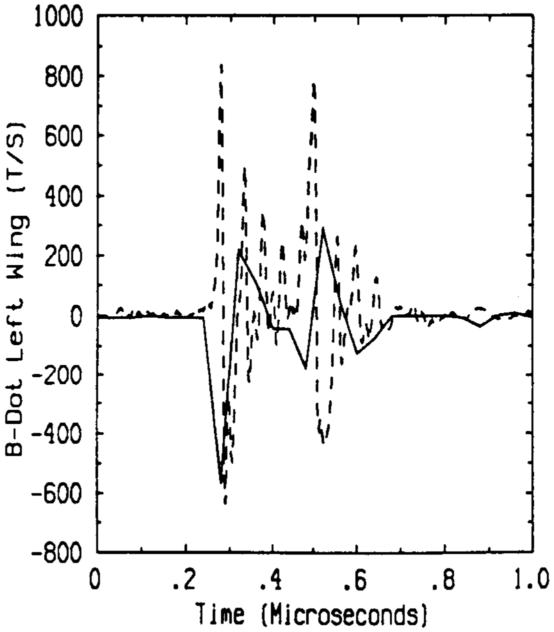

Flight 84.025 Run 003 Strike 004
- Measured -- Predicted

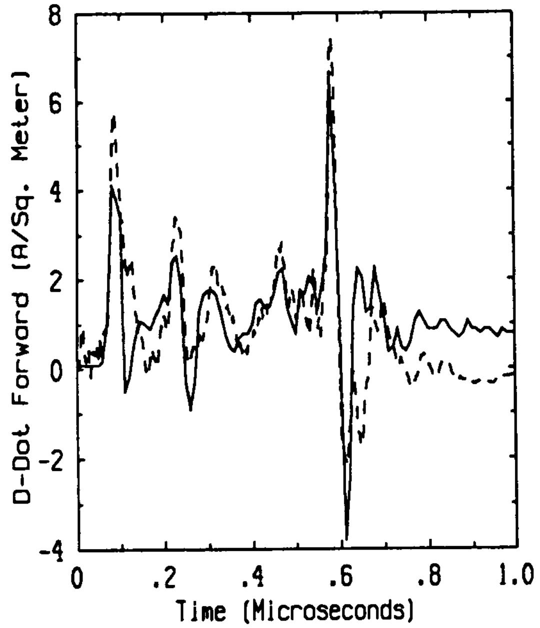

Flight 84.025 Run 004 Strike 005
- Measured -- Predicted

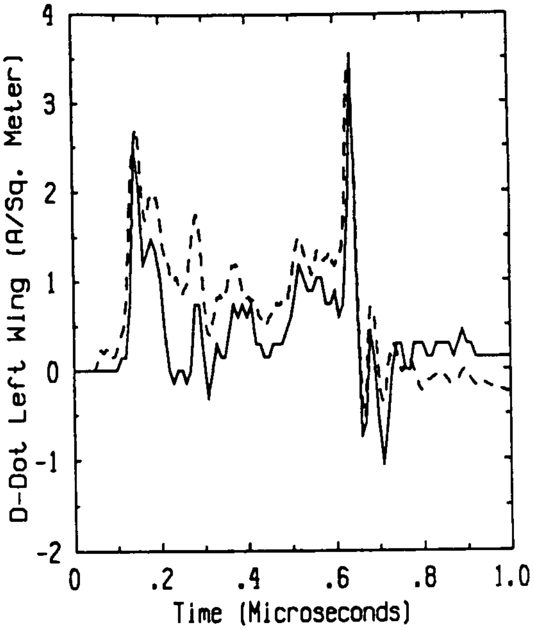

Flight 84.025 Run 004 Strike 005
- Measured -- Predicted

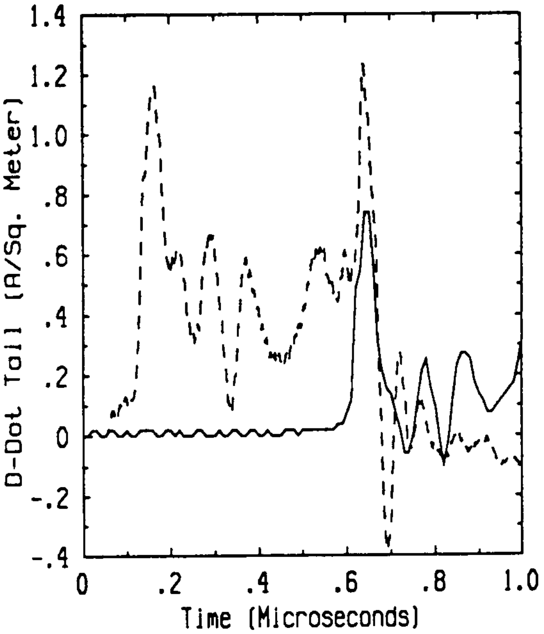

Flight 84.025 Run 004 Strike 005
- Measured -- Predicted

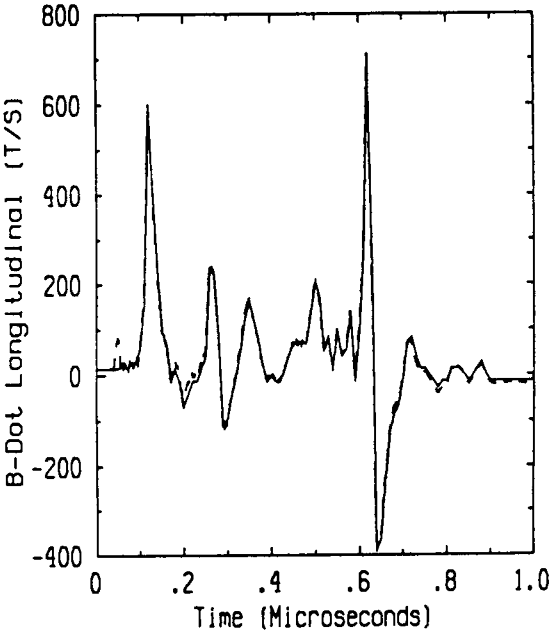

Flight 84.025 Run 004 Strike 005
- Measured -- Predicted

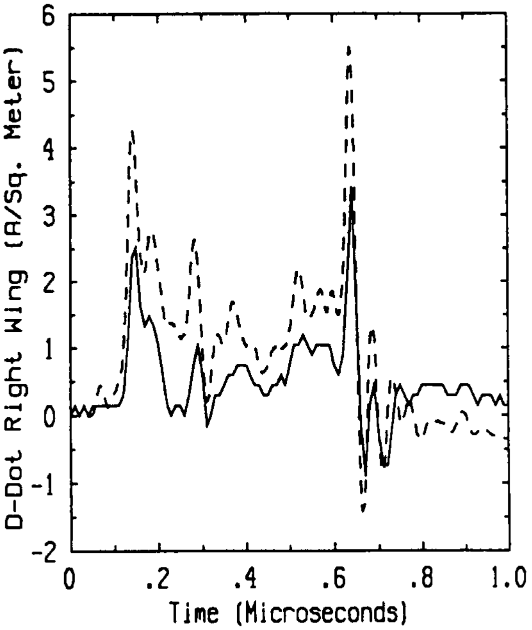

Flight 84.025 Run 004 Strike 005
- Measured -- Predicted

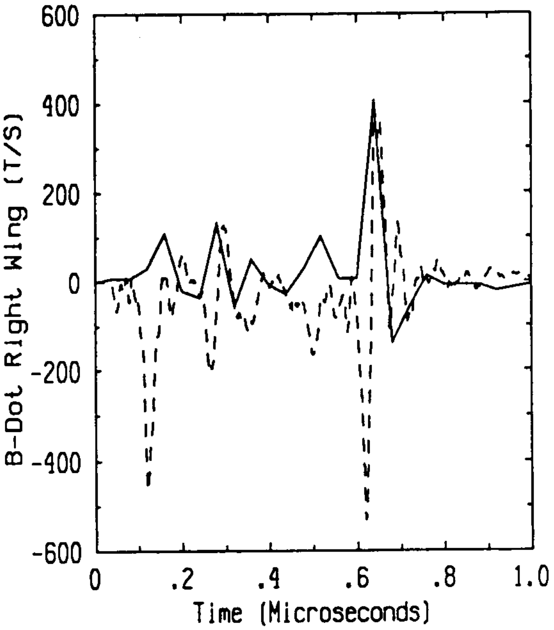

Flight 84.025 Run 004 Strike 005
- Measured -- Predicted

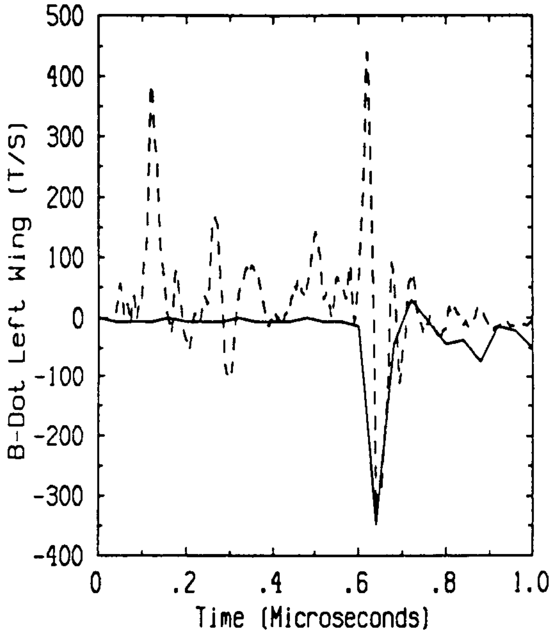

Flight 84.025 Run 004 Strike 005
- Measured -- Predicted

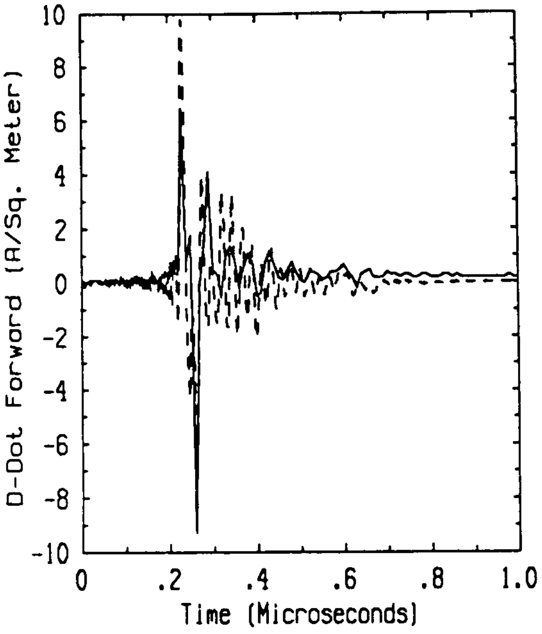

Flight 84.025 Run 007 Strike 010
- Measured -- Predicted

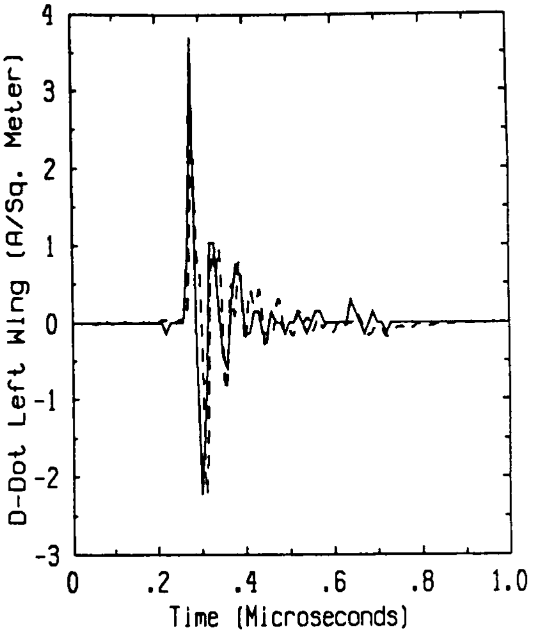

Flight 84.025 Run 007 Strike 010
- Measured -- Predicted

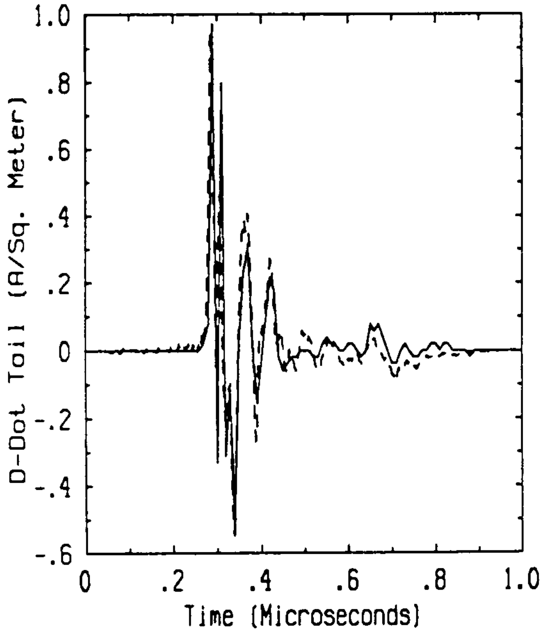

Flight 84.025 Run 007 Strike 010
- Measured -- Predicted

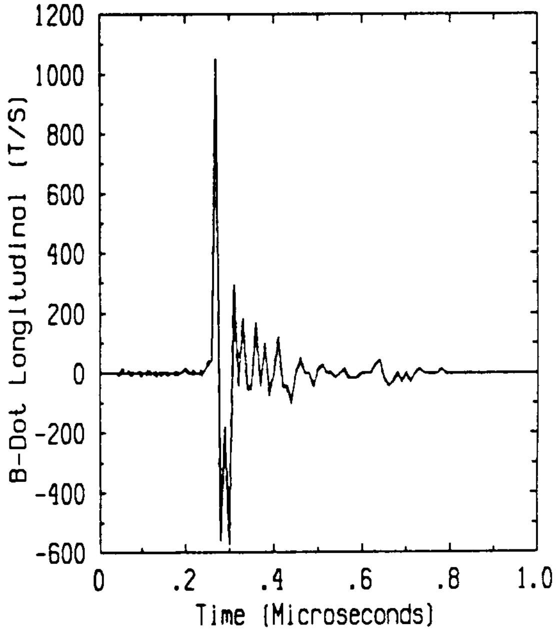

Flight 84.025 Run 007 Strike 010
- Measured -- Predicted

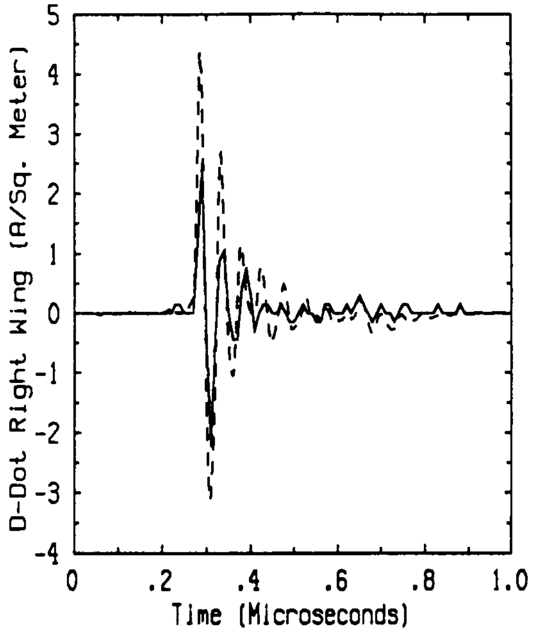

Flight 84.025 Run 007 Strike 010
- Measured -- Predicted

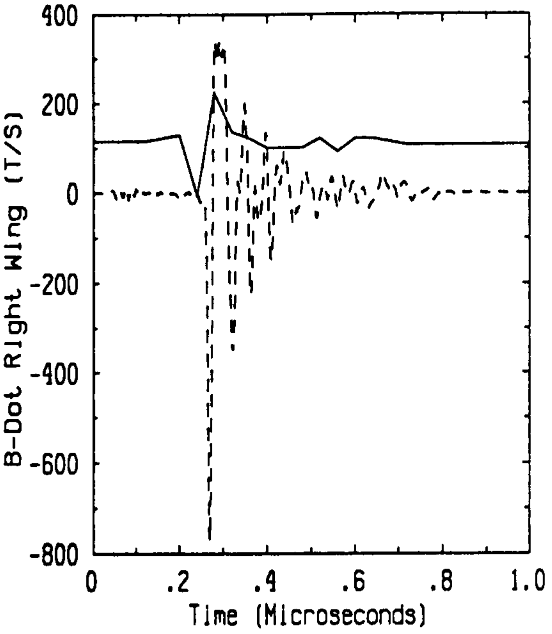

Flight 84.025 Run 007 Strike 010
- Measured -- Predicted

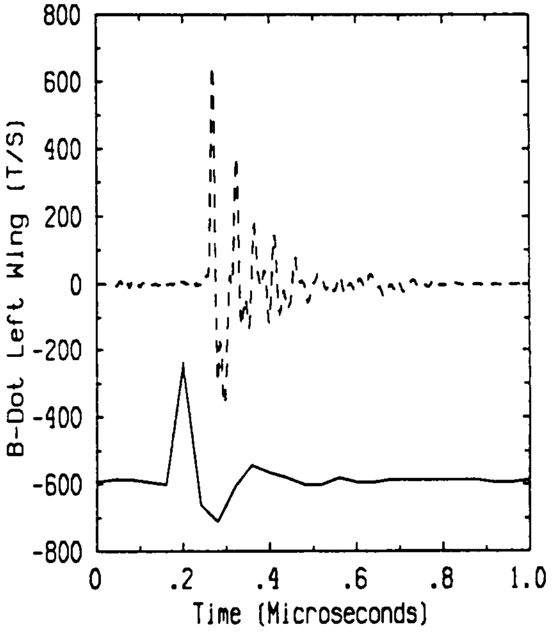

Flight 84.025 Run 007 Strike 010
- Measured -- Predicted

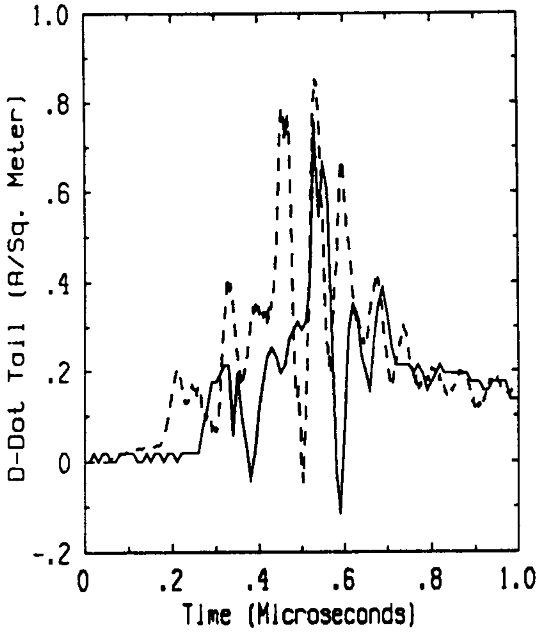

Flight 84.025 Run 008 Strike 011
- Measured -- Predicted

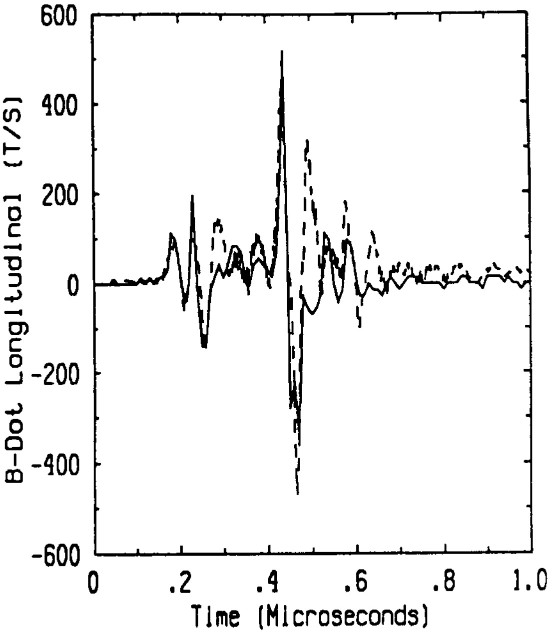

Flight 84.025 Run 008 Strike 011
- Measured -- Predicted

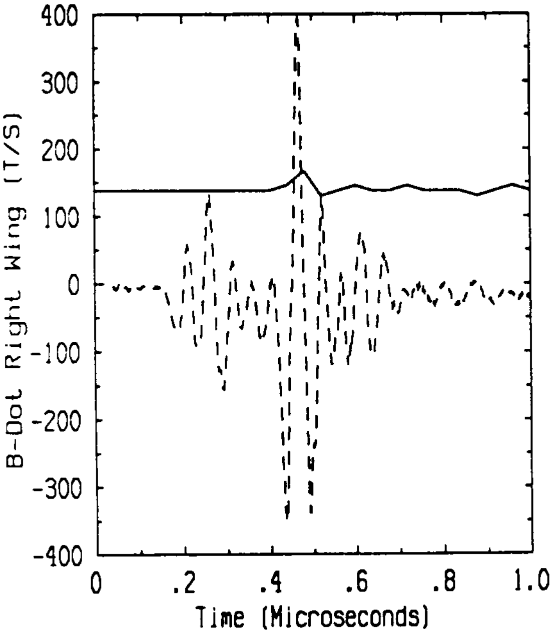

Flight 84.025 Run 008 Strike 011
- Measured -- Predicted

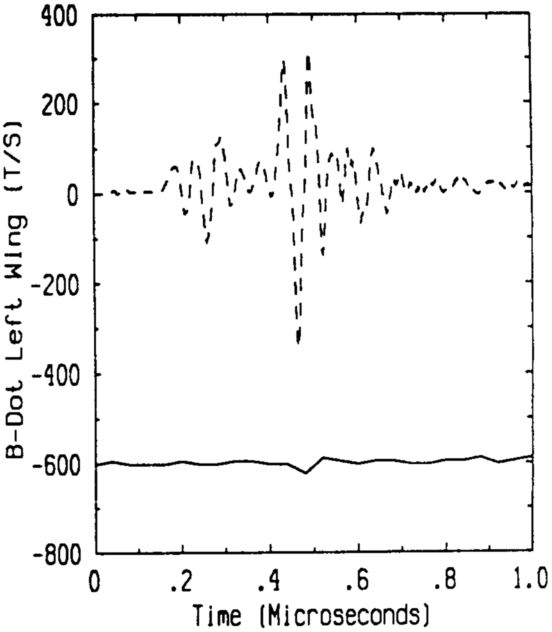

Flight 84.025 Run 008 Strike 011
- Measured -- Predicted

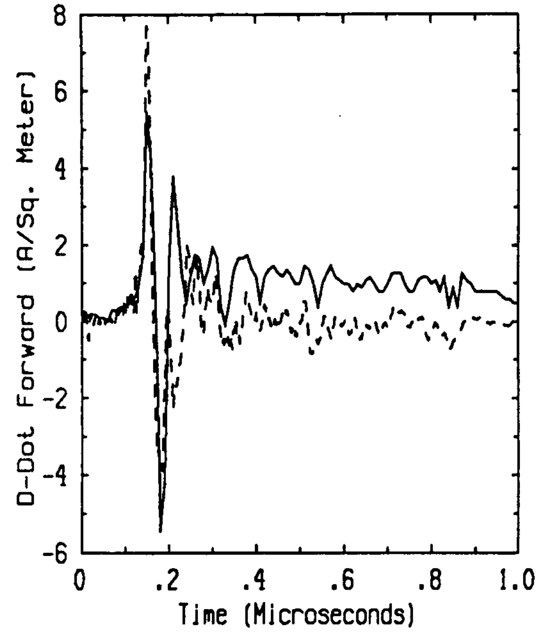

Flight 84.025 Run 011 Strike 014
- Measured -- Predicted

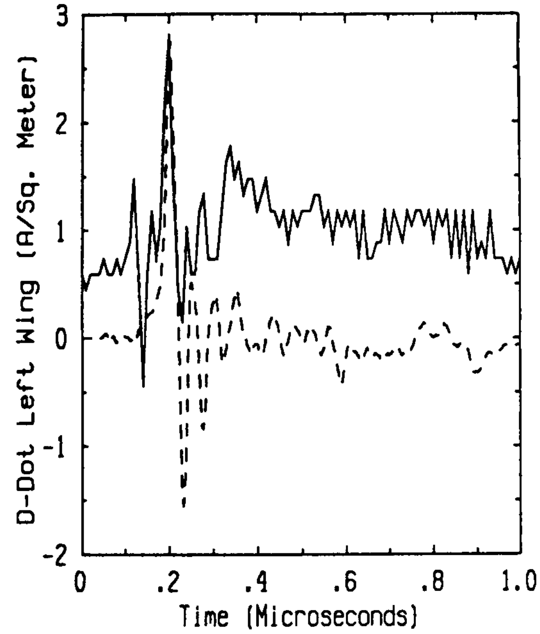

Flight 84.025 Run 011 Strike 014
- Measured -- Predicted

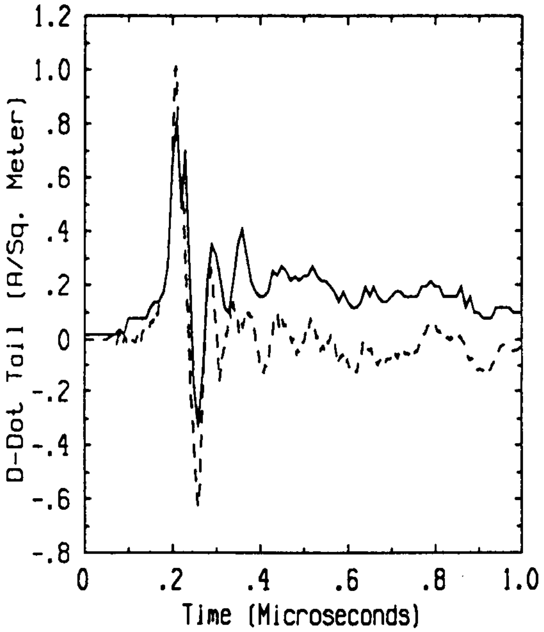

Flight 84.025 Run 011 Strike 014
- Measured -- Predicted

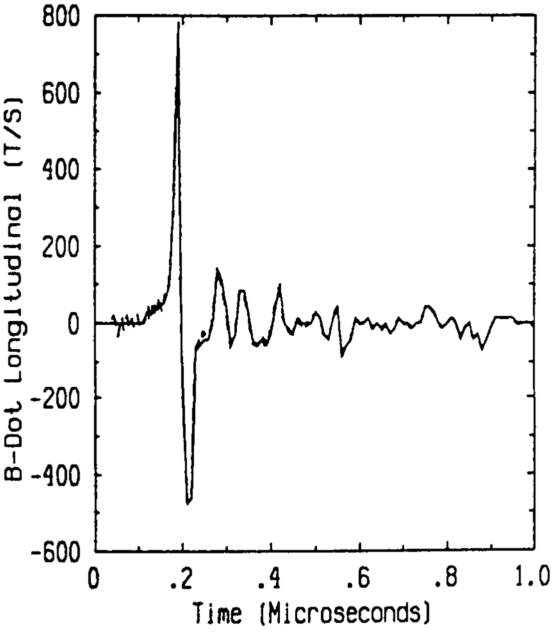

Flight 84.025 Run 011 Strike 014
- Measured -- Predicted

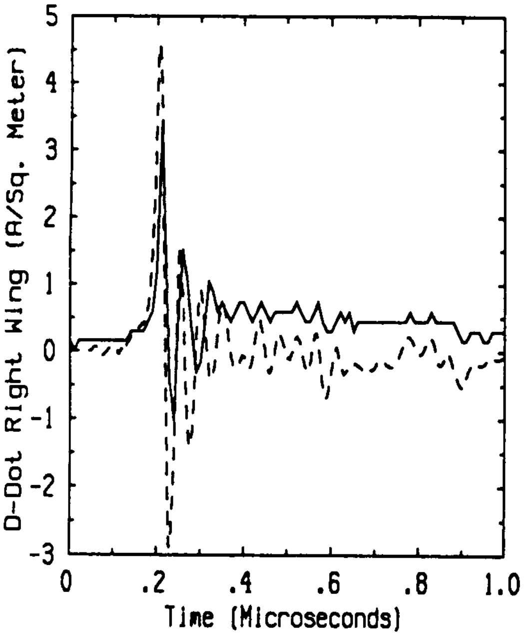

Flight 84.025 Run 011 Strike 014
- Measured -- Predicted

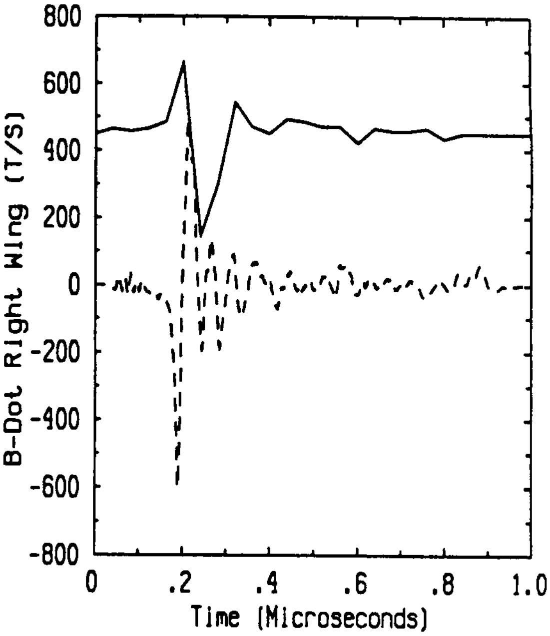

Flight 84.025 Run 011 Strike 014
- Measured -- Predicted

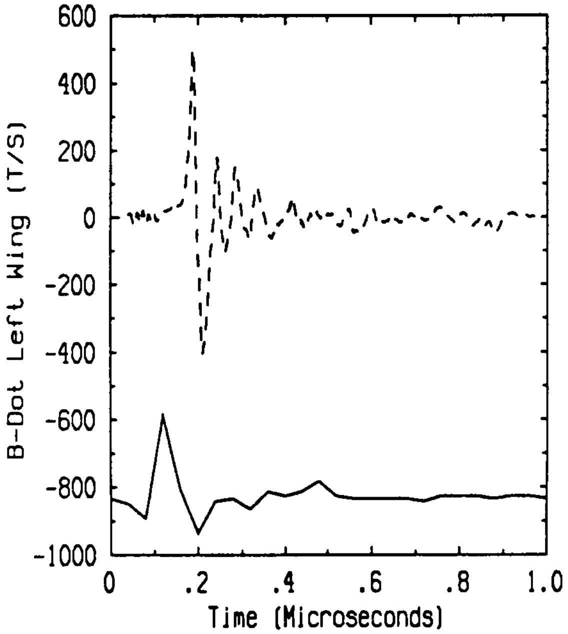

Flight 84.025 Run 011 Strike 014
- Measured -- Predicted

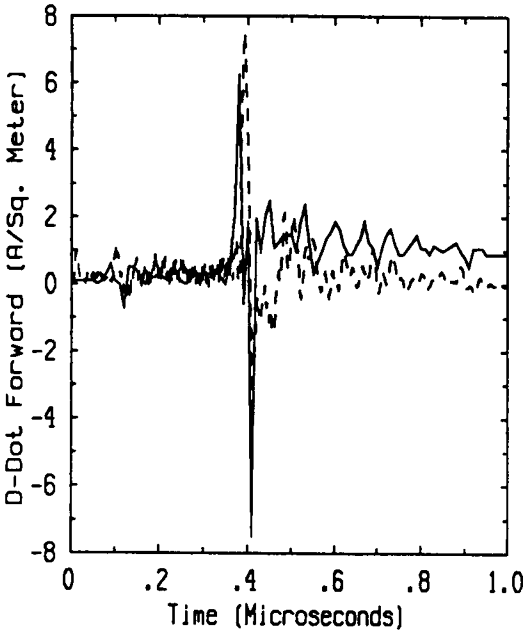

Flight 84.025 Run 013 Strike 017
- Measured -- Predicted

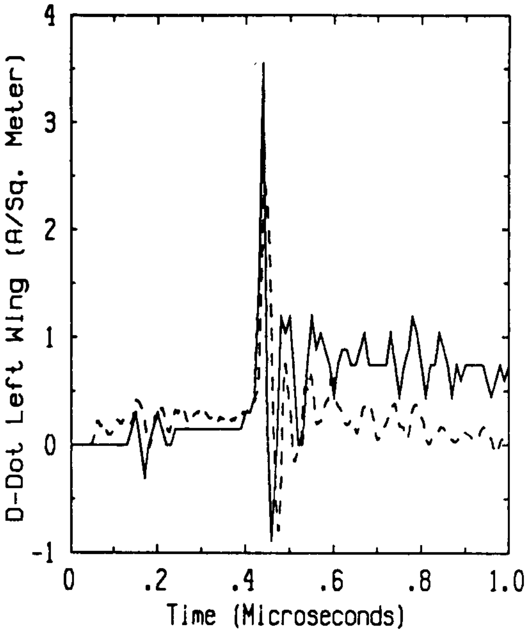

Flight 84.025 Run 013 Strike 017
- Measured -- Predicted

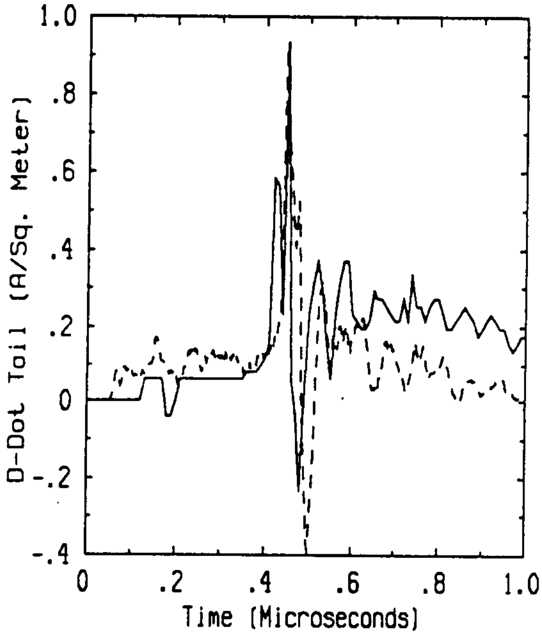

Flight 84.025 Run 013 Strike 017
- Measured -- Predicted

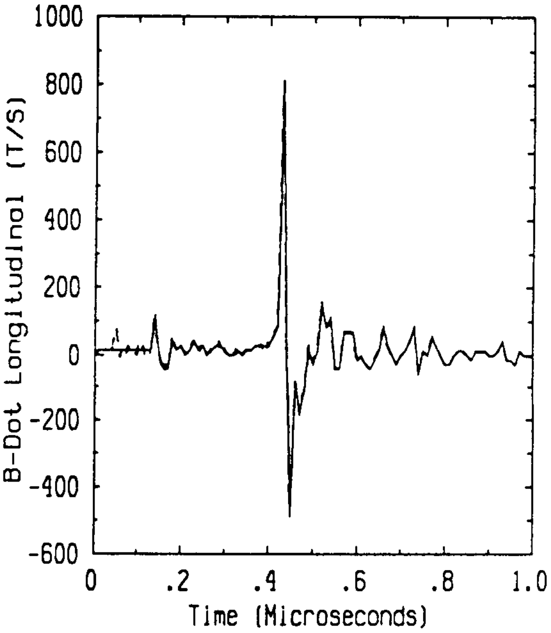

Flight 84.025 Run 013 Strike 017
- Measured -- Predicted

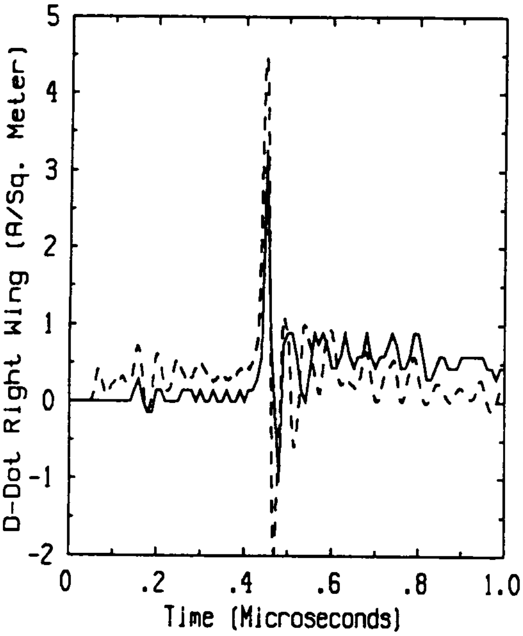

Flight 84.025 Run 013 Strike 017
- Measured -- Predicted

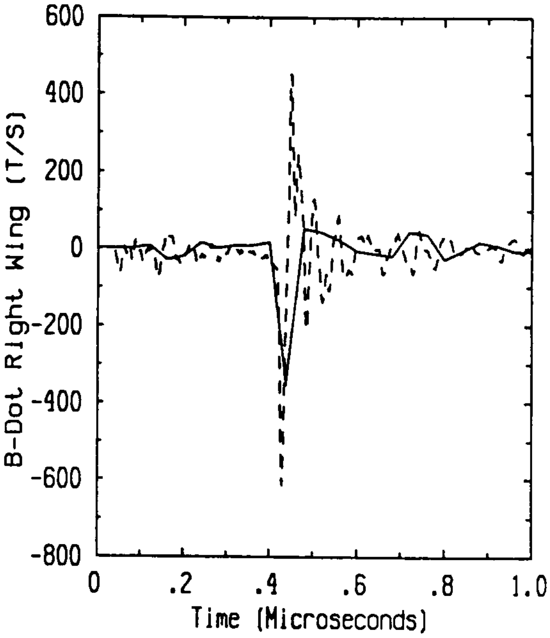

Flight 84.025 Run 013 Strike 017
- Measured -- Predicted

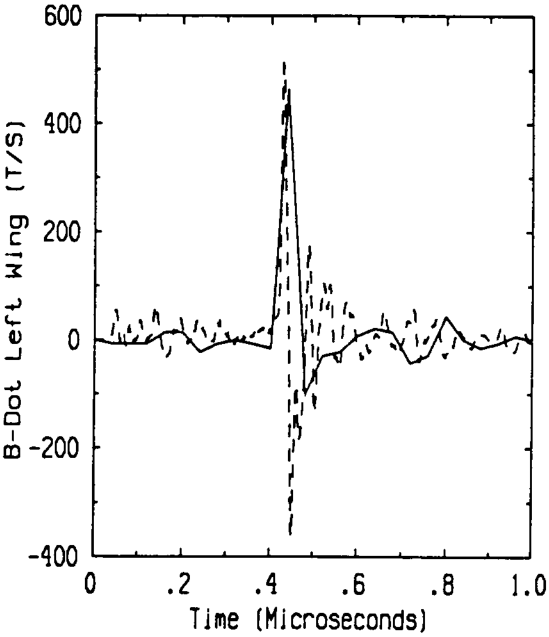

Flight 84.025 Run 013 Strike 017
- Measured -- Predicted

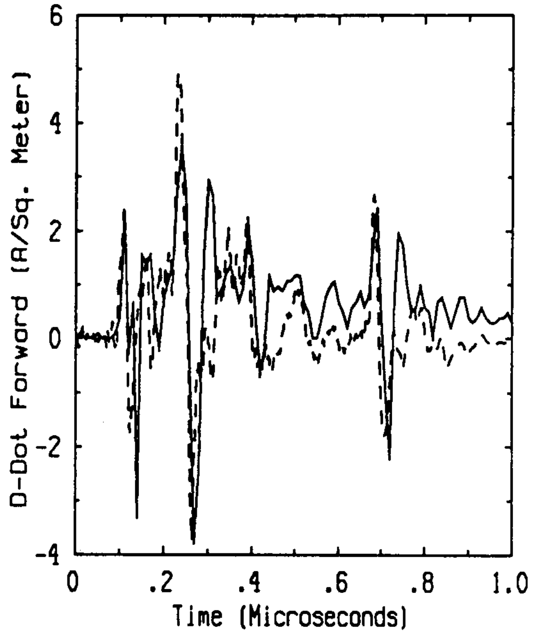

Flight 84.025 Run 015 Strike 019
- Measured -- Predicted

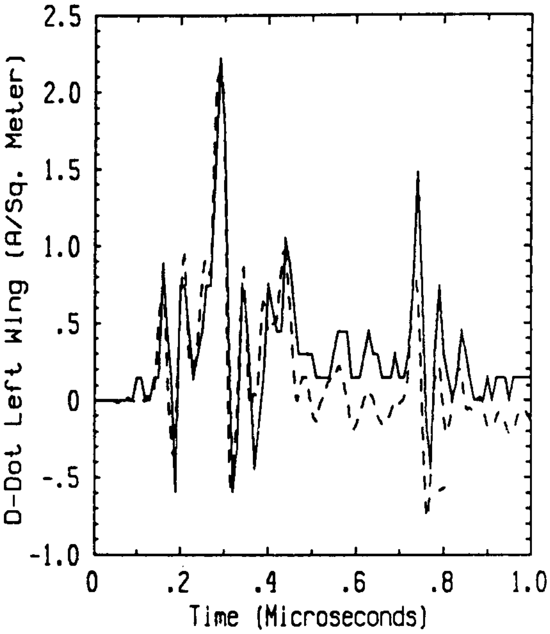

Flight 84.025 Run 015 Strike 019
- Measured -- Predicted

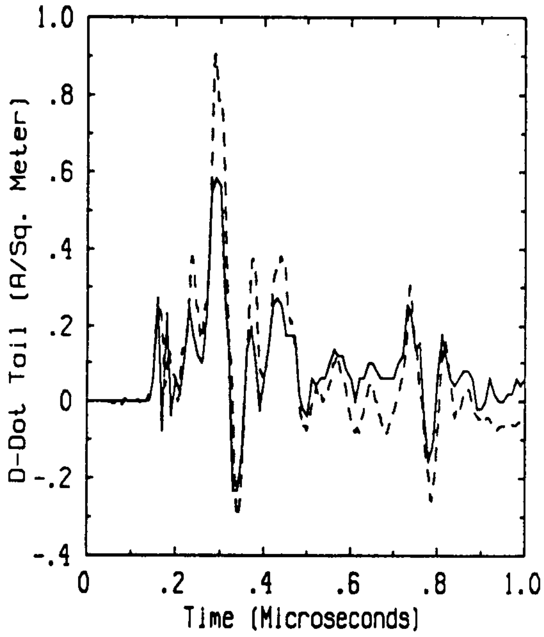

Flight 84.025 Run 015 Strike 019
- Measured -- Predicted

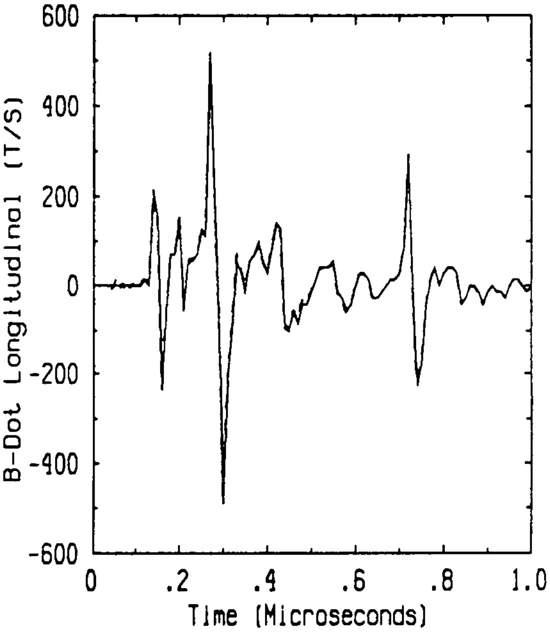

Flight 84.025 Run 015 Strike 019
- Measured -- Predicted

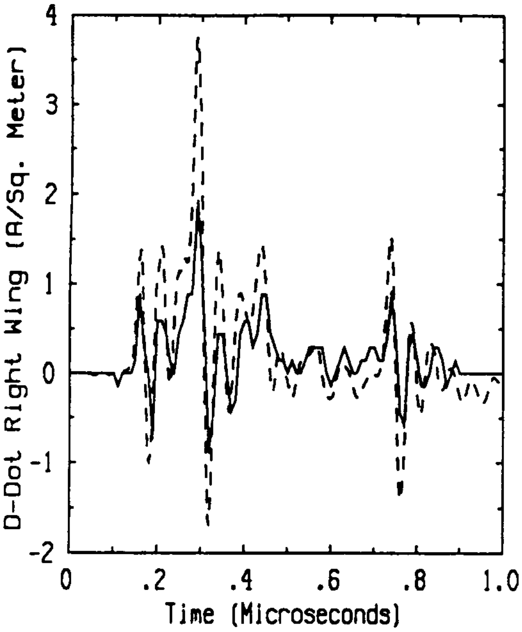

Flight 84.025 Run 015 Strike 019
- Measured -- Predicted

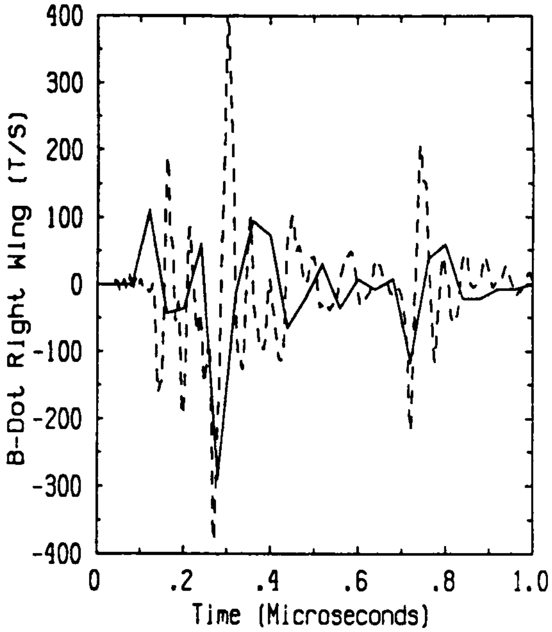

Flight 84.025 Run 015 Strike 019
- Measured -- Predicted

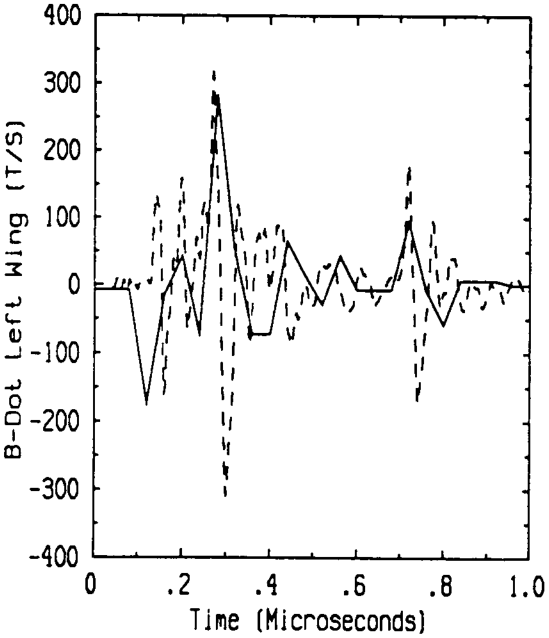

Flight 84.025 Run 015 Strike 019
- Measured -- Predicted

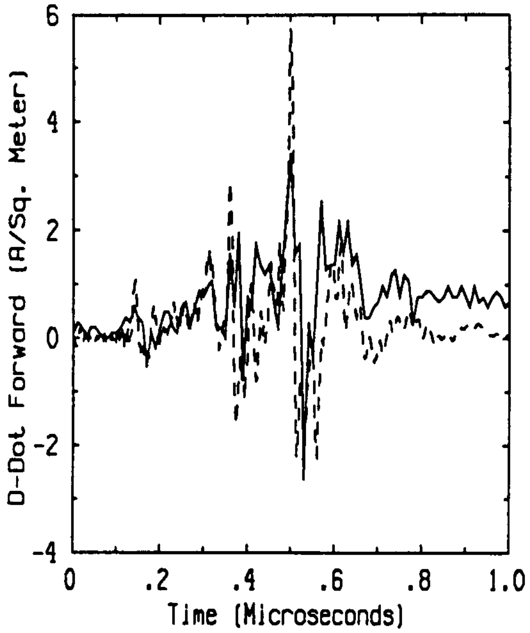

Flight 84.027 Run 001 Strike 001
- Measured -- Predicted

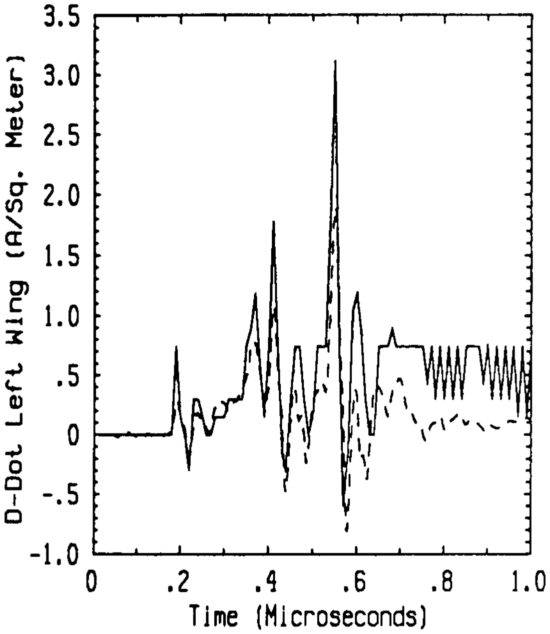

Flight 84.027 Run 001 Strike 001
- Measured -- Predicted

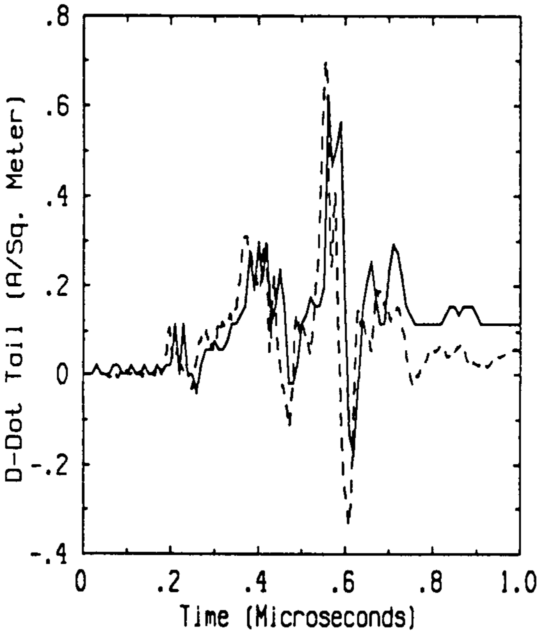

Flight 84.027 Run 001 Strike 001
- Measured -- Predicted

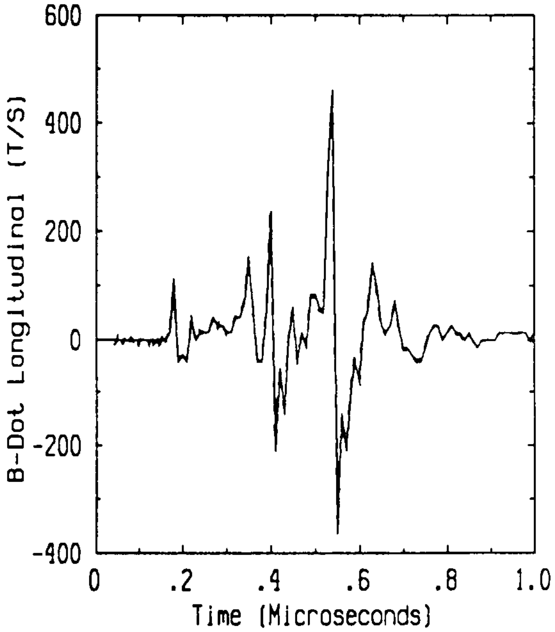

Flight 84.027 Run 001 Strike 001
- Measured -- Predicted

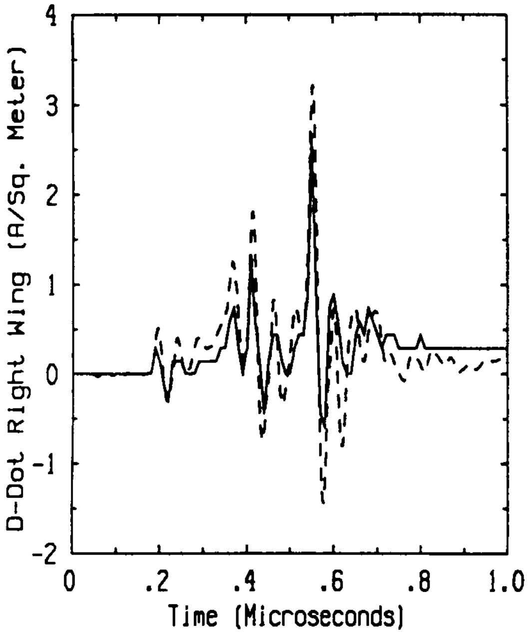

Flight 84.027 Run 001 Strike 001
- Measured -- Predicted

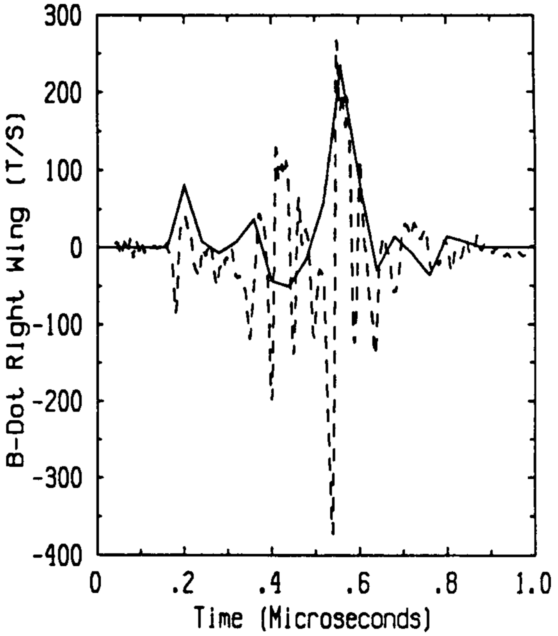

Flight 84.027 Run 001 Strike 001
- Measured -- Predicted

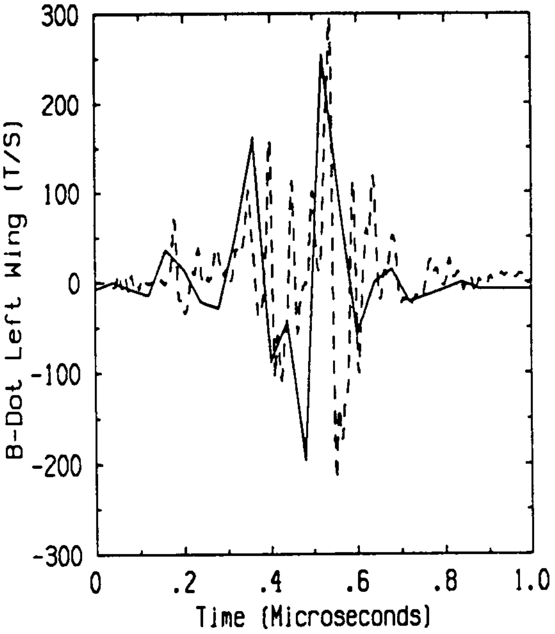

Flight 84.027 Run 001 Strike 001
- Measured -- Predicted

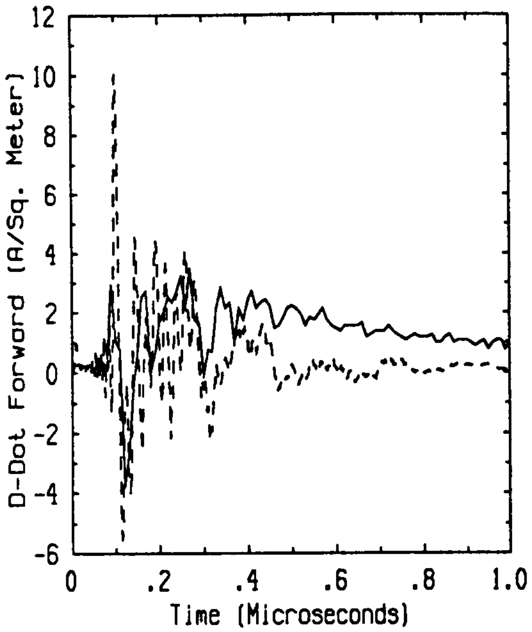

Flight 84.027 Run 002 Strike 002
- Measured -- Predicted

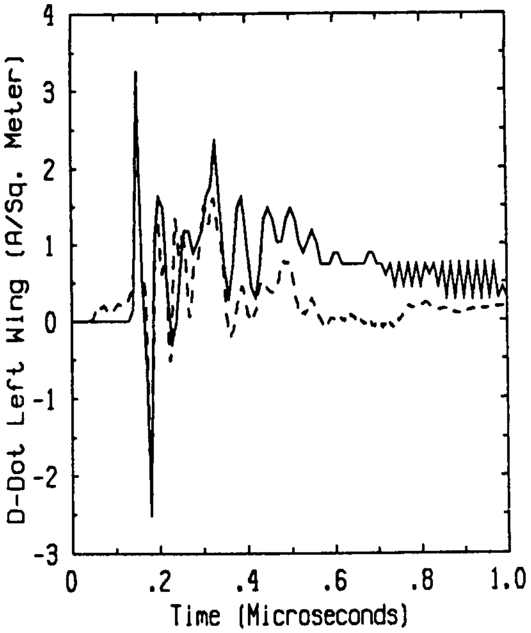

Flight 84.027 Run 002 Strike 002
- Measured -- Predicted

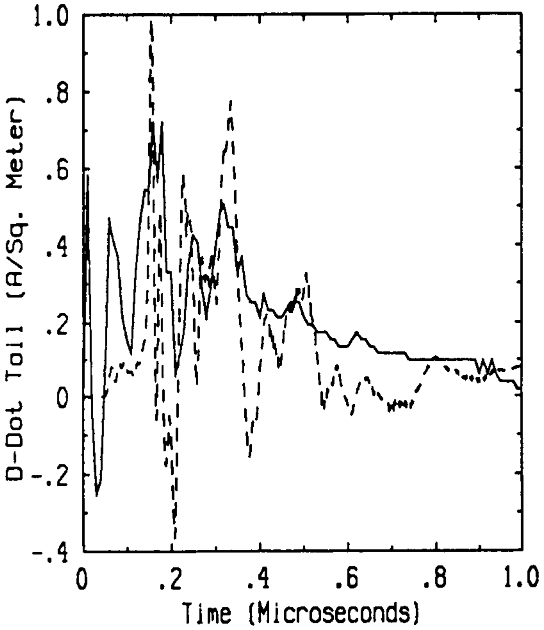

Flight 84.027 Run 002 Strike 002
- Measured -- Predicted

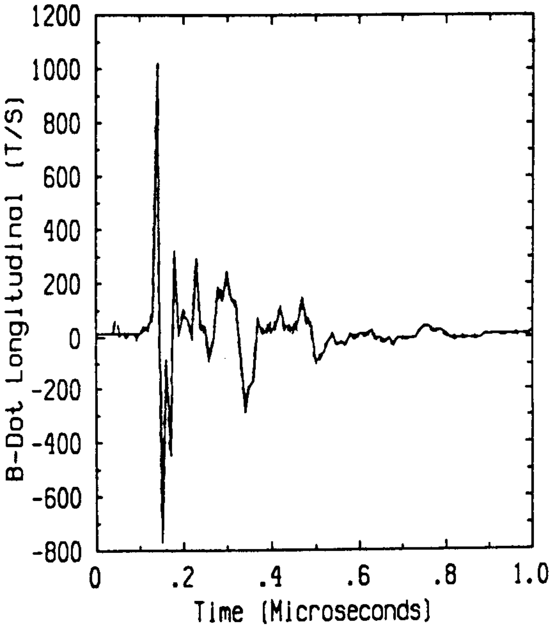

Flight 84.027 Run 002 Strike 002
- Measured -- Predicted

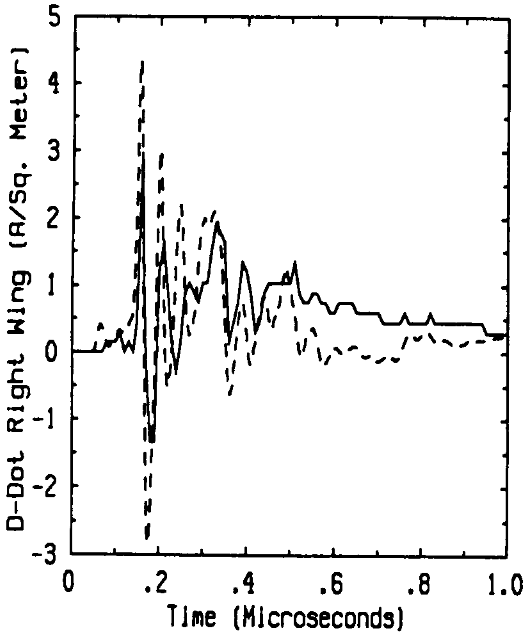

Flight 84.027 Run 002 Strike 002
- Measured -- Predicted

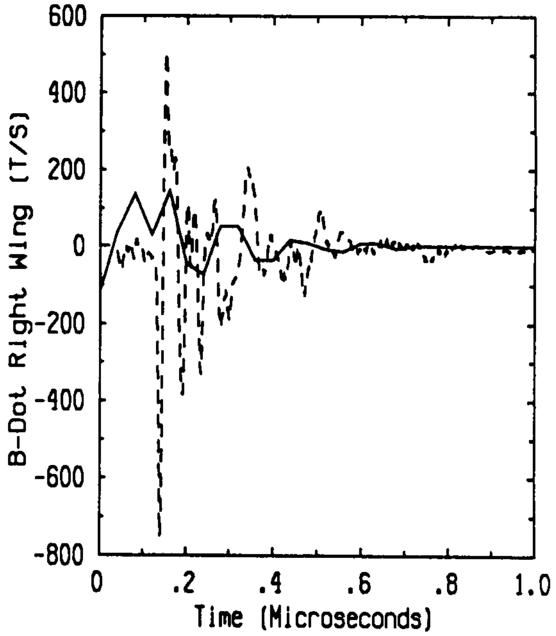

Flight 84.027 Run 002 Strike 002
- Measured -- Predicted

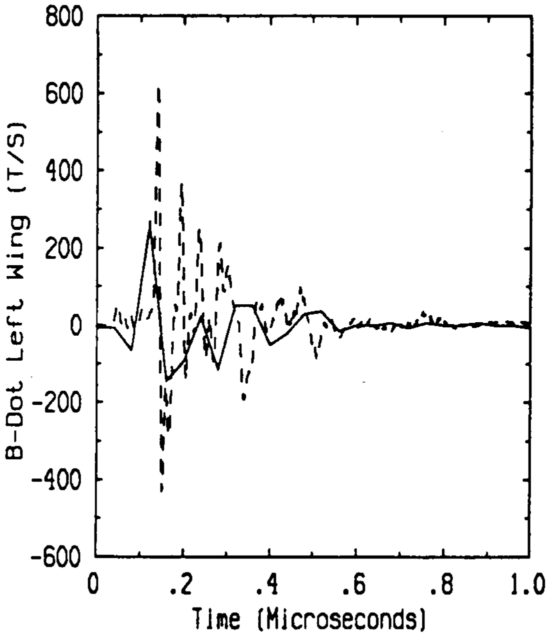

Flight 84.027 Run 002 Strike 002
- Measured -- Predicted

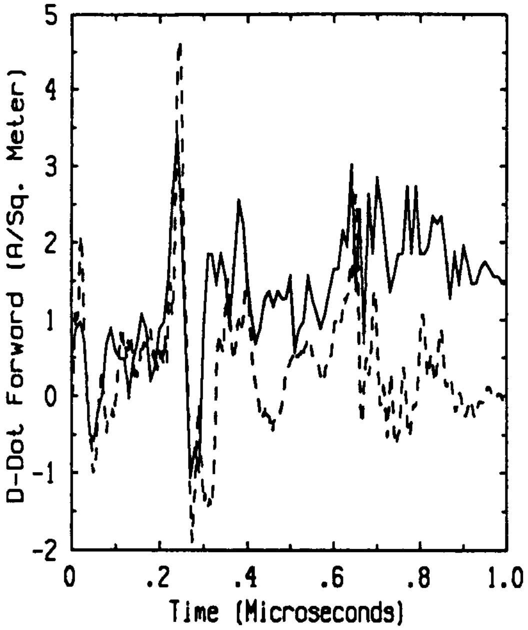

Flight 84.028 Run 001 Strike 001
- Measured -- Predicted

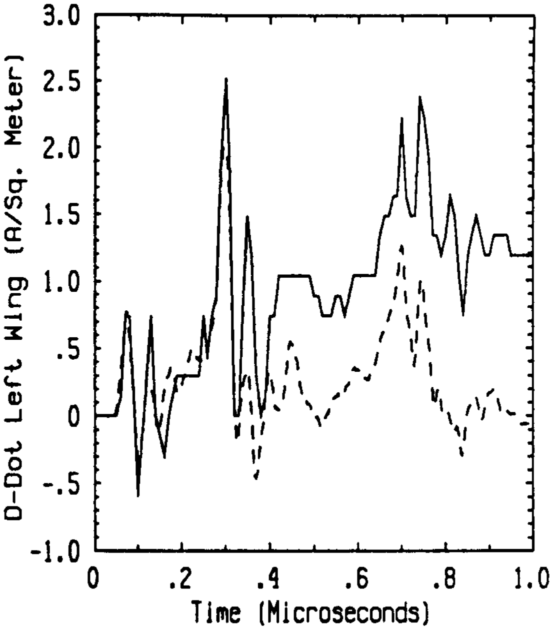

Flight 84.028 Run 001 Strike 001
- Measured -- Predicted

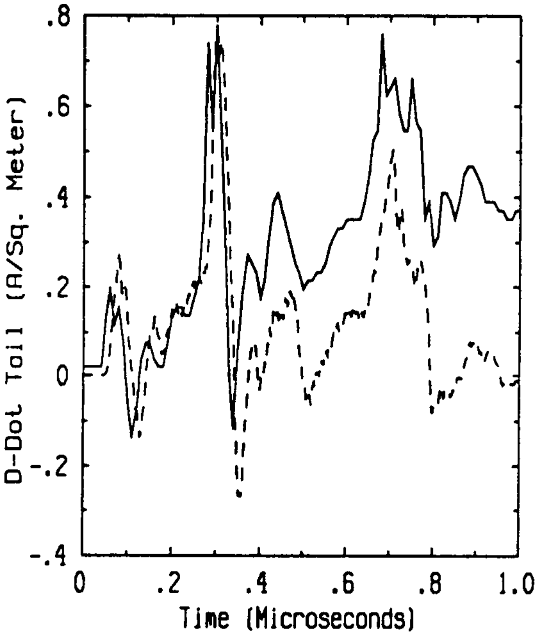

Flight 84.028 Run 001 Strike 001
- Measured -- Predicted

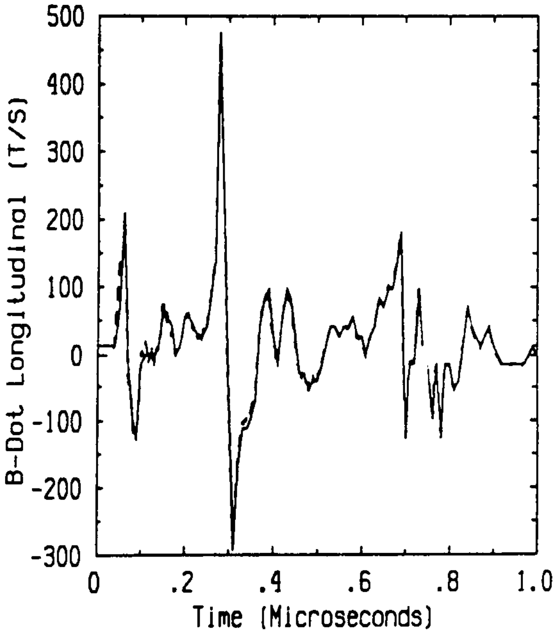

Flight 84.028 Run 001 Strike 001
- Measured -- Predicted

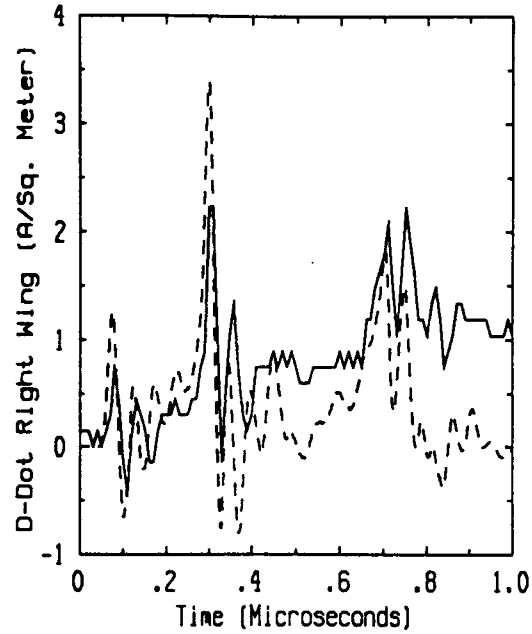

Flight 84.028 Run 001 Strike 001
- Measured -- Predicted

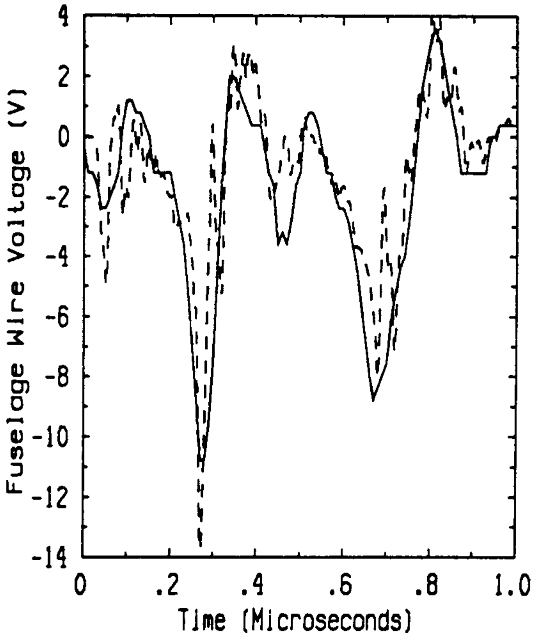

Flight 84.028 Run 001 Strike 001
- Measured -- Predicted

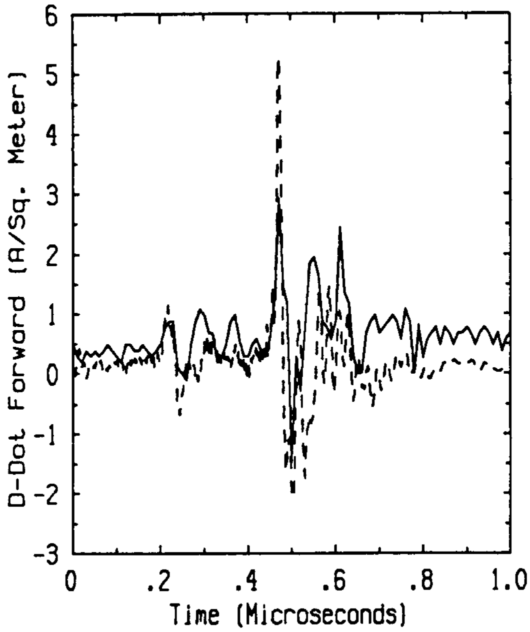

Flight 84.028 Run 002 Strike 002
- Measured -- Predicted

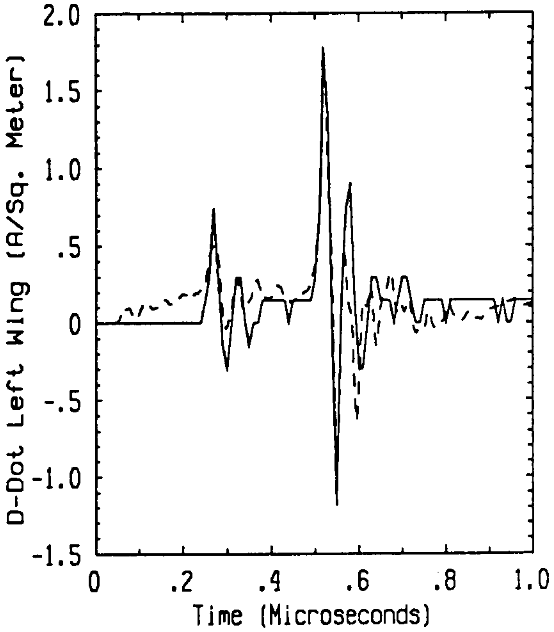

Flight 84.028 Run 002 Strike 002
- Measured -- Predicted

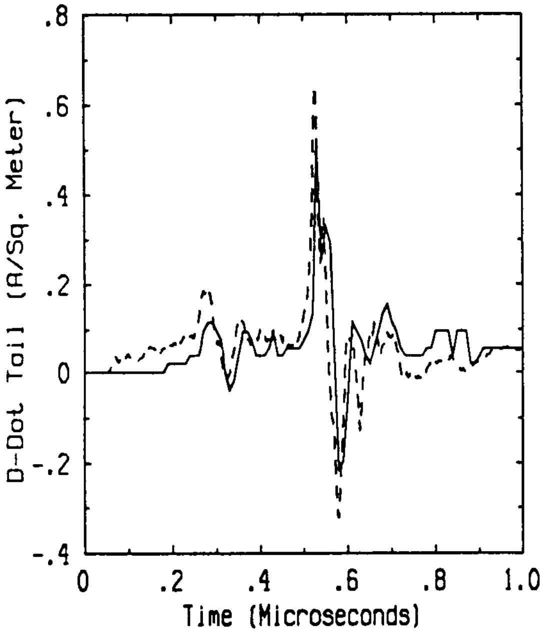

Flight 84.028 Run 002 Strike 002
- Measured -- Predicted

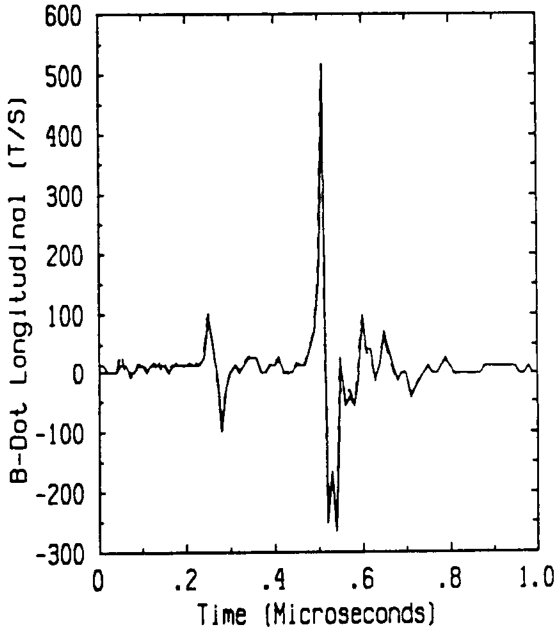

Flight 84.028 Run 002 Strike 002
- Measured -- Predicted

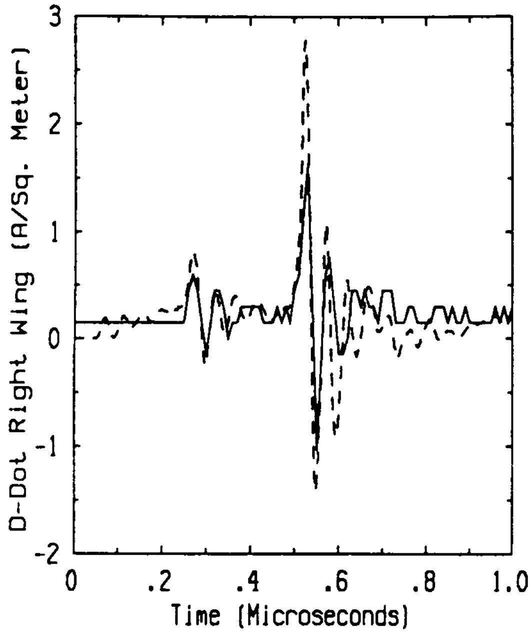

Flight 84.028 Run 002 Strike 002
- Measured -- Predicted

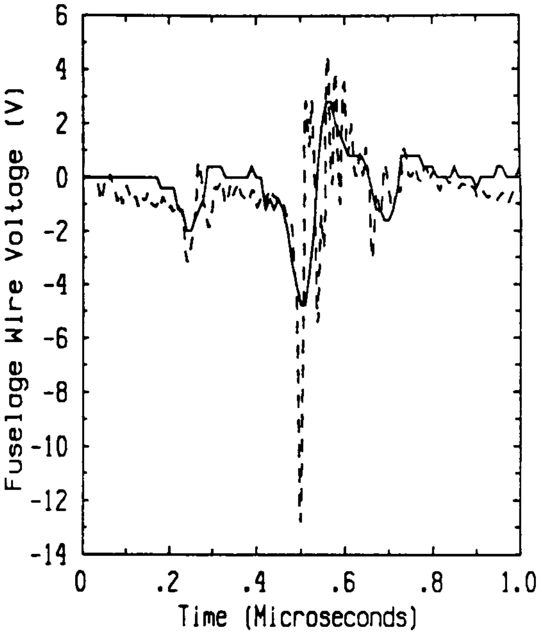

Flight 84.028 Run 002 Strike 002
- Measured -- Predicted

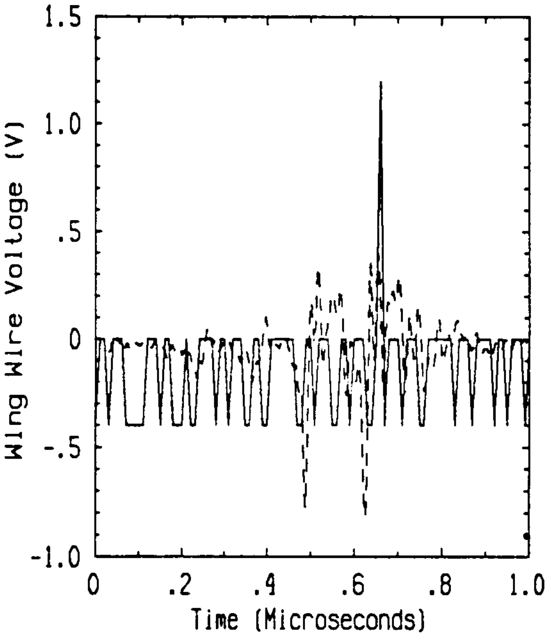

Flight 84.028 Run 002 Strike 002
- Measured -- Predicted

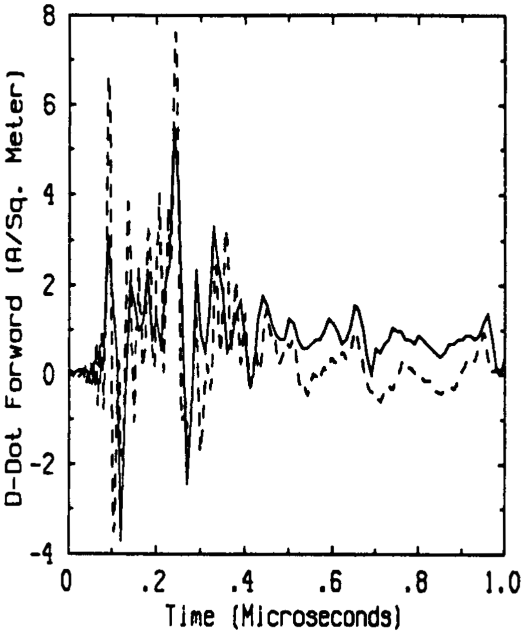

Flight 84.028 Run 004 Strike 005
- Measured -- Predicted

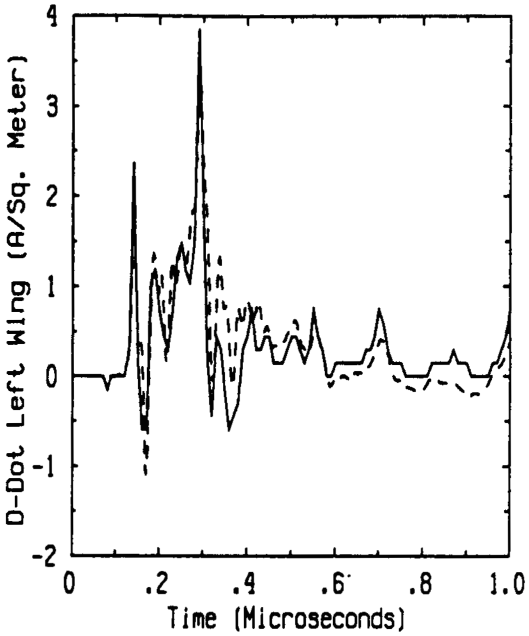

Flight 84.028 Run 004 Strike 005
- Measured -- Predicted

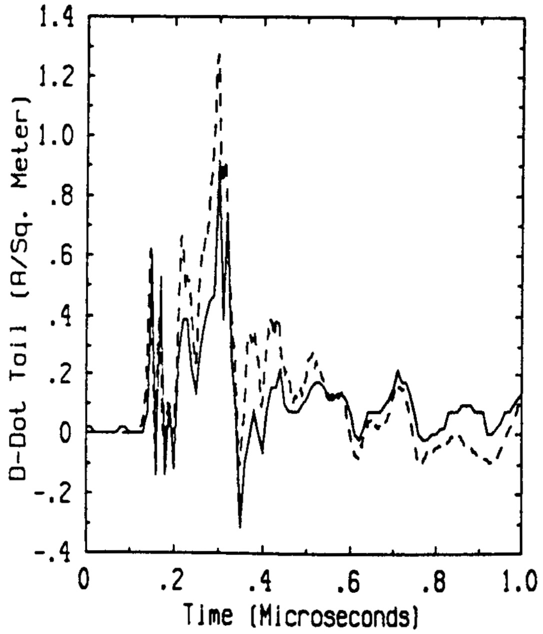

Flight 84.028 Run 004 Strike 005
- Measured -- Predicted

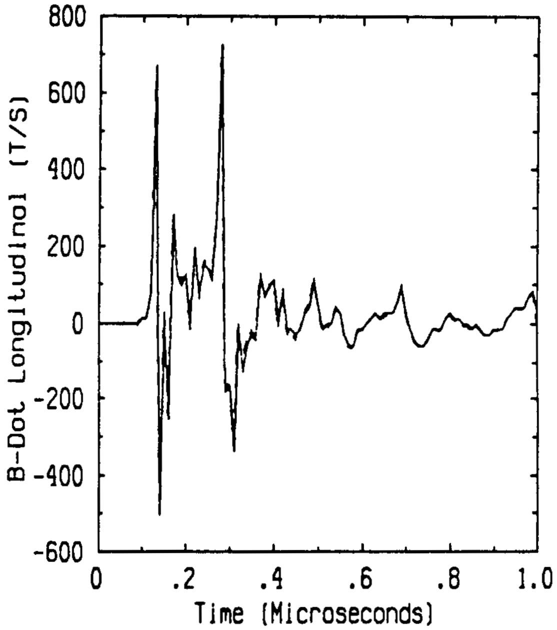

Flight 84.028 Run 004 Strike 005
- Measured -- Predicted

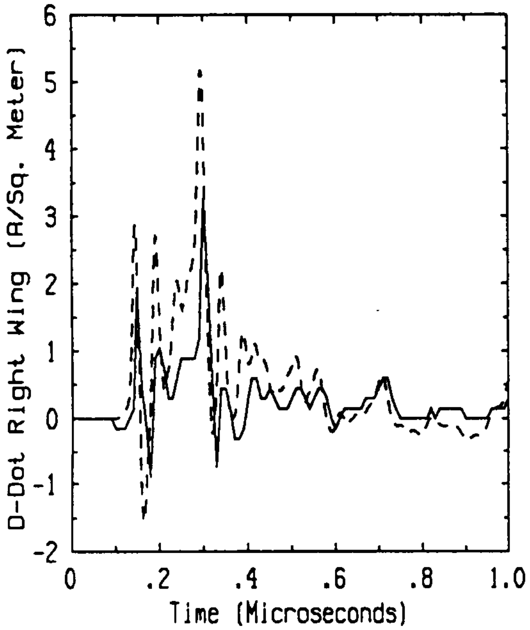

Flight 84.028 Run 004 Strike 005
- Measured -- Predicted

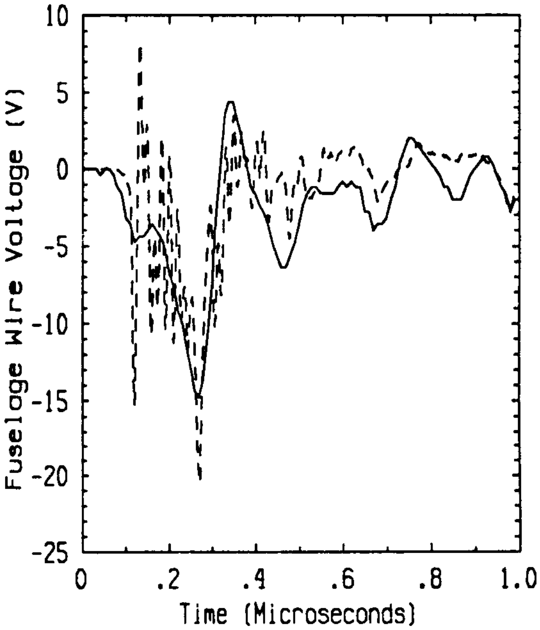

Flight 84.028 Run 004 Strike 005
- Measured -- Predicted

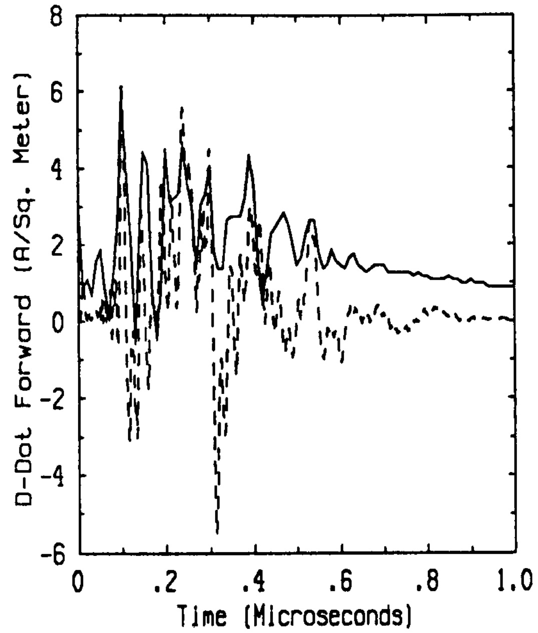

Flight 84.028 Run 005 Strike 006
- Measured -- Predicted

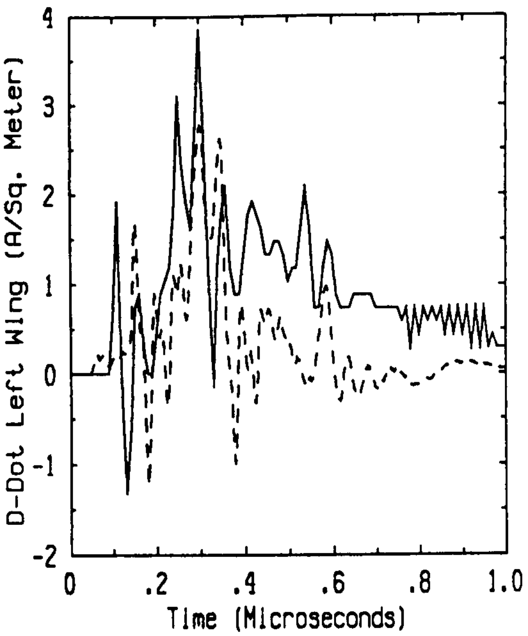

Flight 84.028 Run 005 Strike 006
- Measured -- Predicted

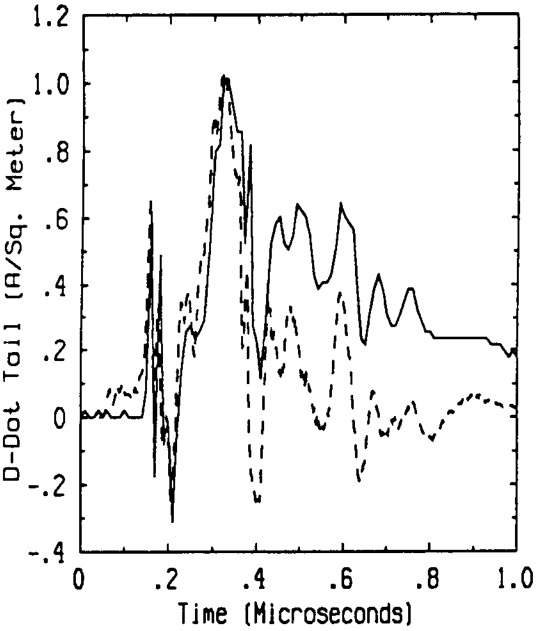

Flight 84.028 Run 005 Strike 006
- Measured -- Predicted

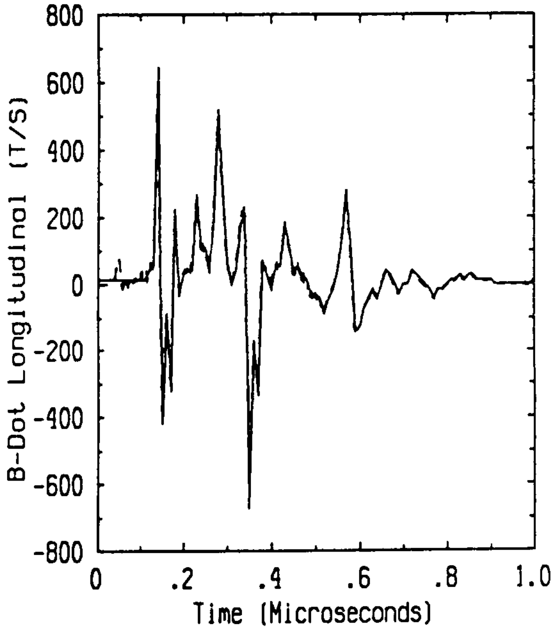

Flight 84.028 Run 005 Strike 006
- Measured -- Predicted

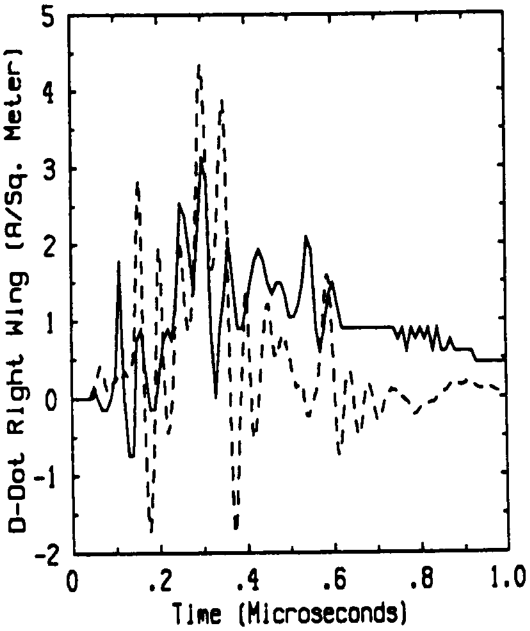

Flight 84.028 Run 005 Strike 006
- Measured -- Predicted

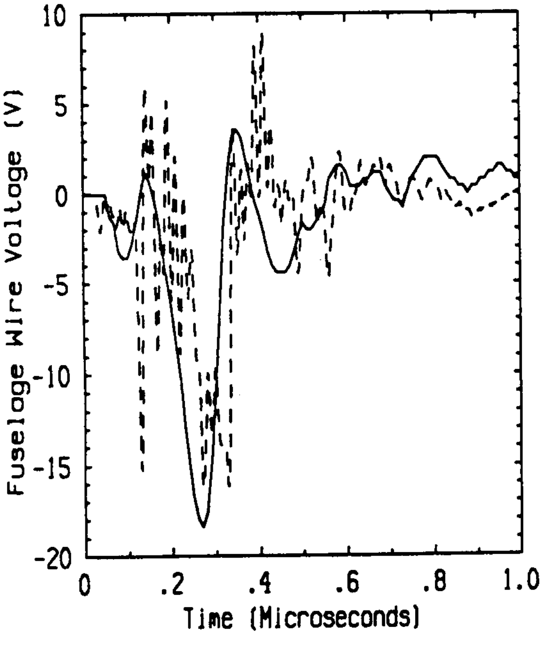

Flight 84.028 Run 005 Strike 006
- Measured -- Predicted

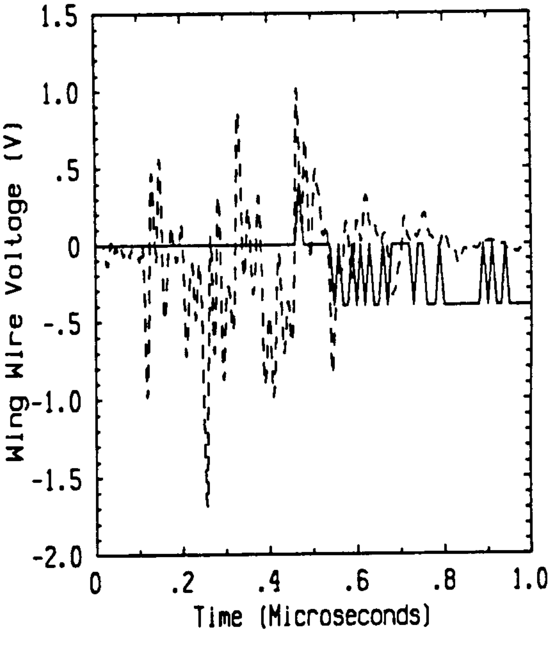

Flight 84.028 Run 005 Strike 006
- Measured -- Predicted

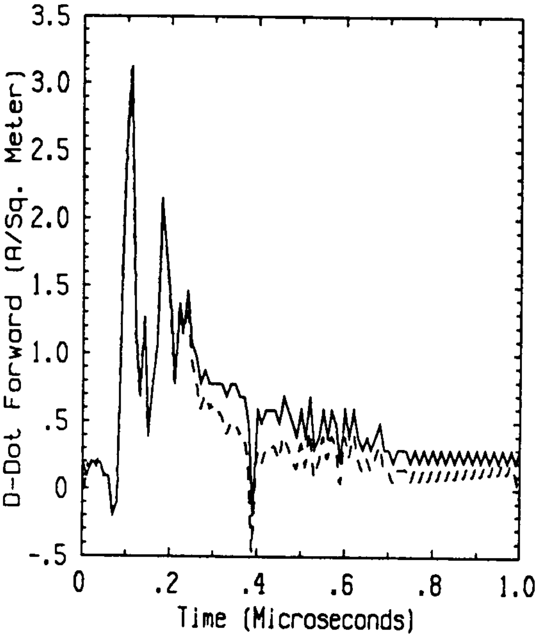

Flight 84.032 Run 001 Strike 002
- Measured -- Predicted

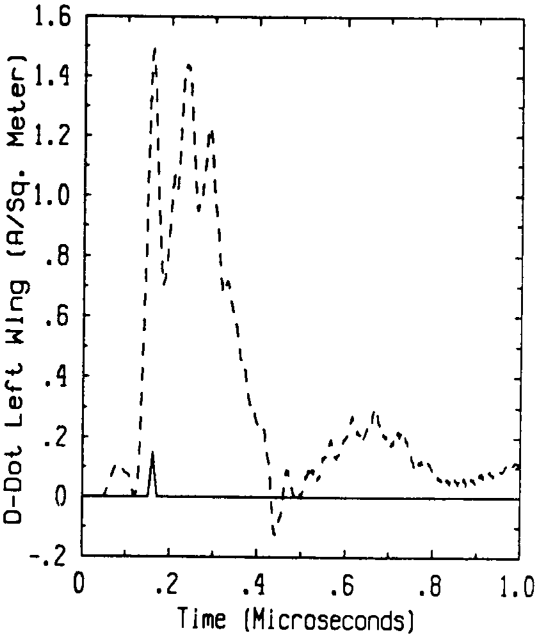

Flight 84.032 Run 001 Strike 002
- Measured -- Predicted

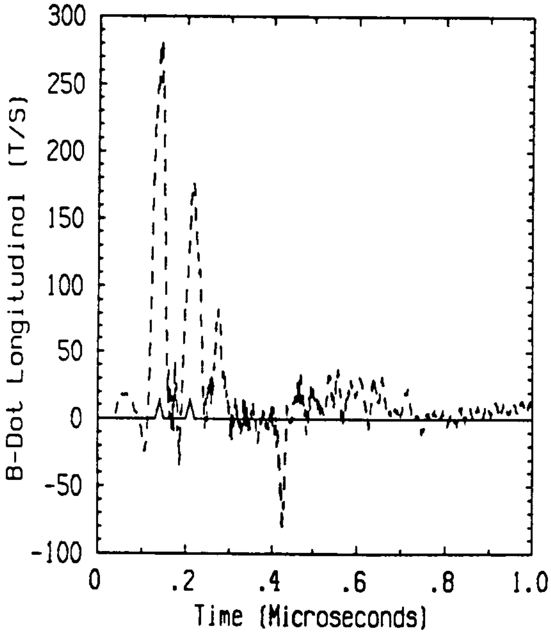

Flight 84.032 Run 001 Strike 002
- Measured -- Predicted

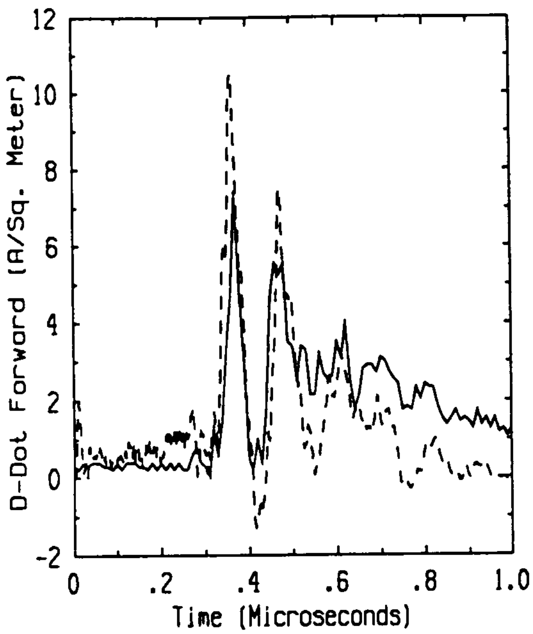

Flight 84.032 Run 002 Strike 003
- Measured -- Predicted

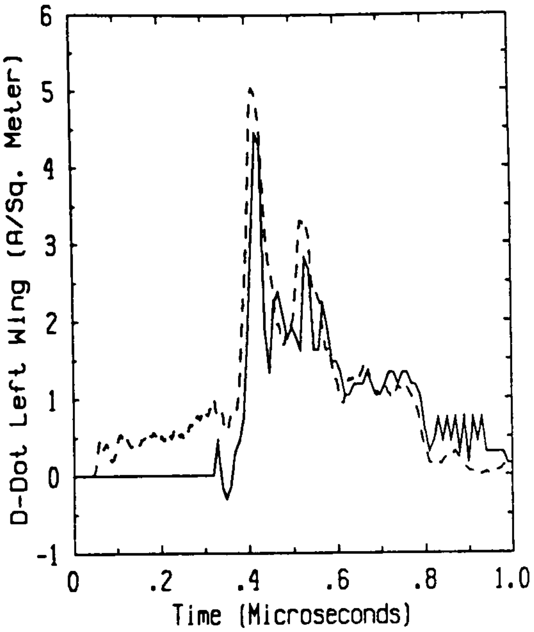

Flight 84.032 Run 002 Strike 003
- Measured -- Predicted

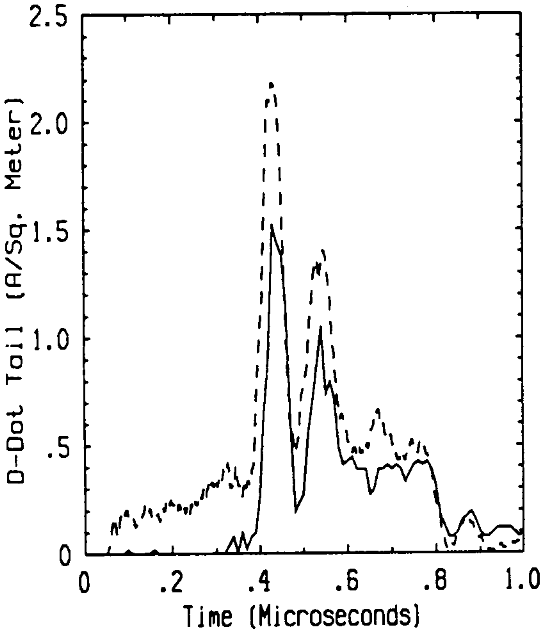

Flight 84.032 Run 002 Strike 003
- Measured -- Predicted

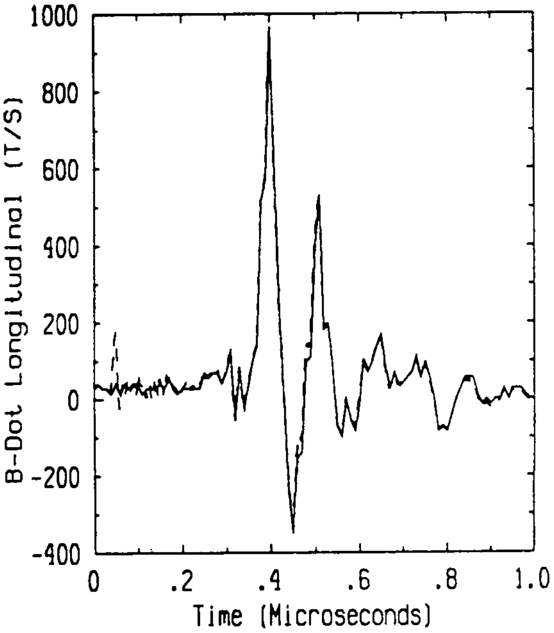

Flight 84.032 Run 002 Strike 003
- Measured -- Predicted

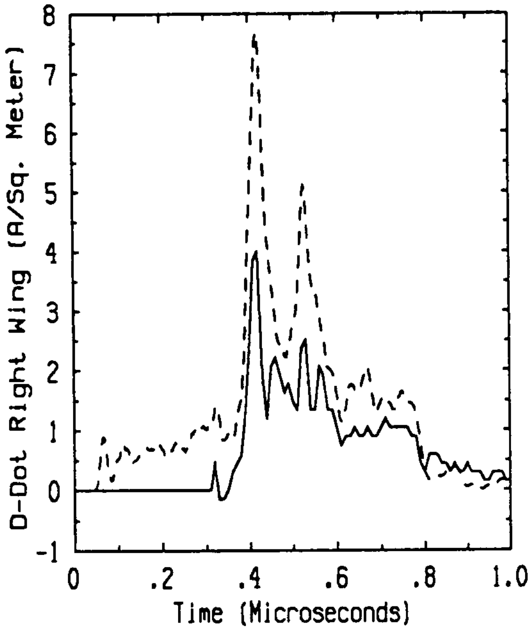

Flight 84.032 Run 002 Strike 003
- Measured -- Predicted

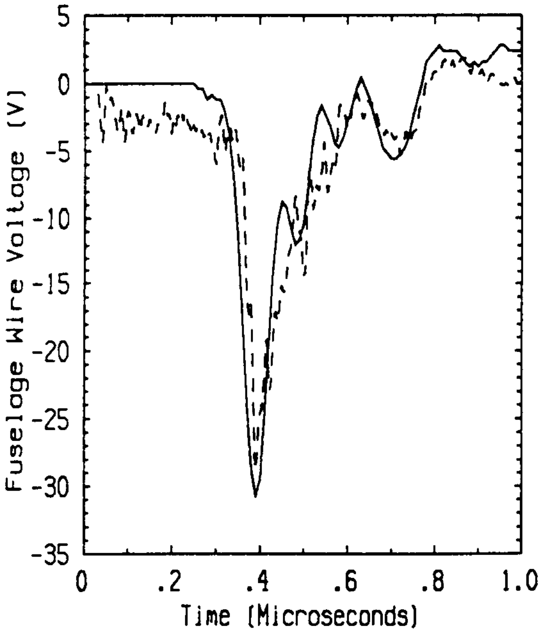

Flight 84.032 Run 002 Strike 003
- Measured -- Predicted

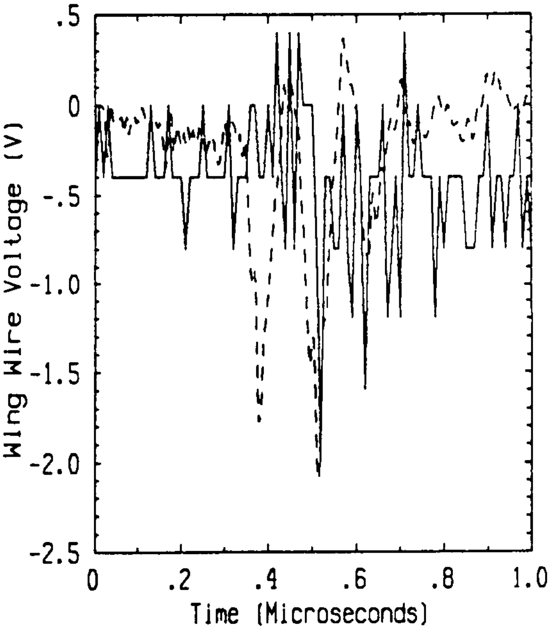

Flight 84.032 Run 002 Strike 003
- Measured -- Predicted

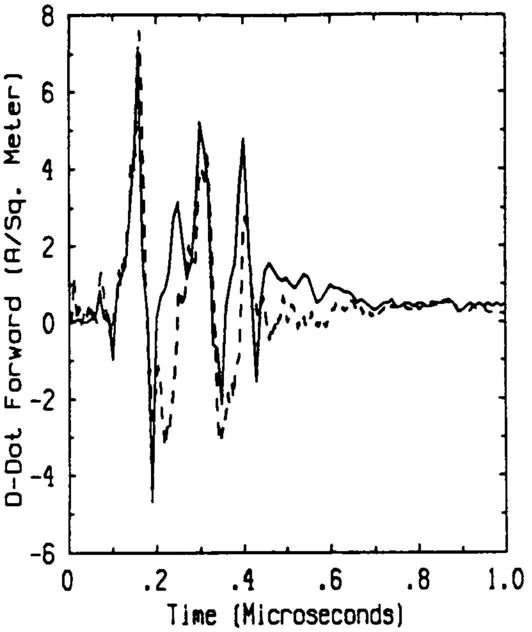

Flight 84.032 Run 003 Strike 005
- Measured -- Predicted

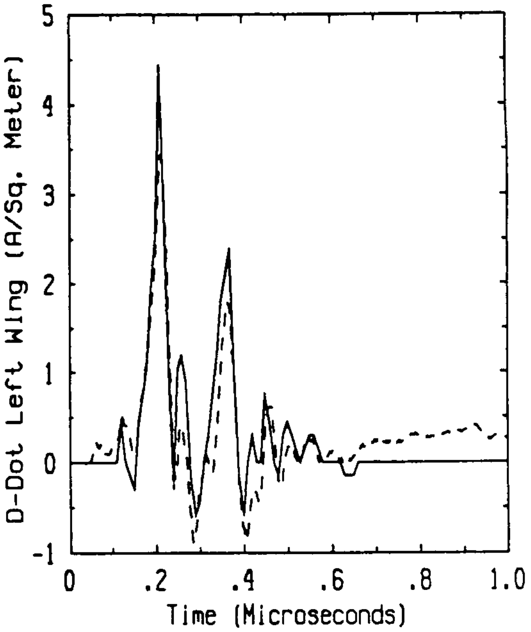

Flight 84.032 Run 003 Strike 005
- Measured -- Predicted

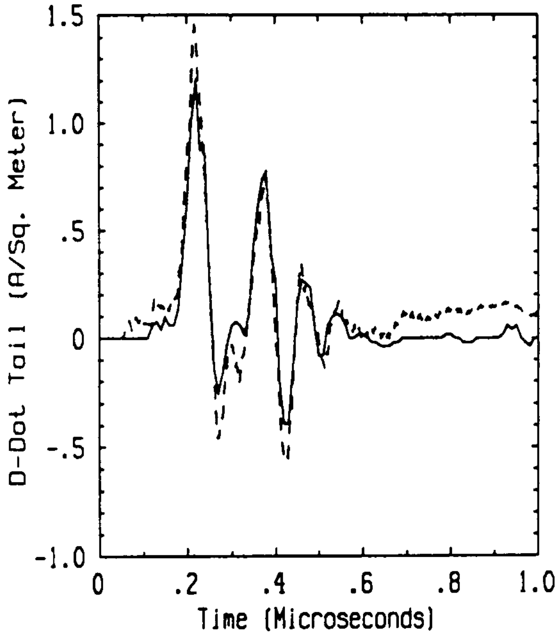

Flight 84.032 Run 003 Strike 005
- Measured -- Predicted

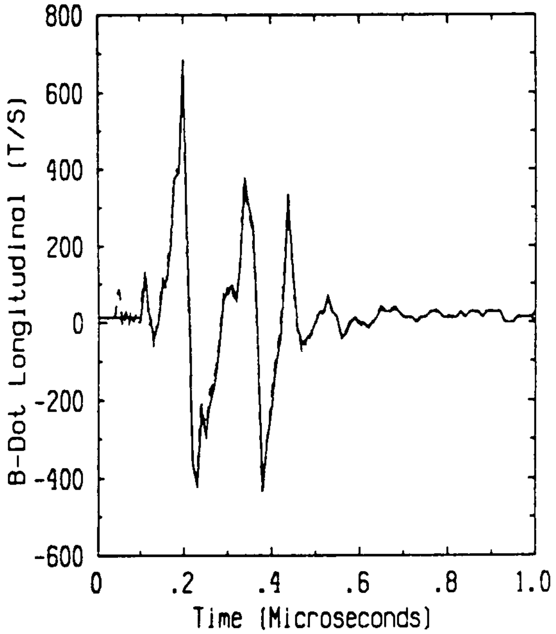

Flight 84.032 Run 003 Strike 005
- Measured -- Predicted

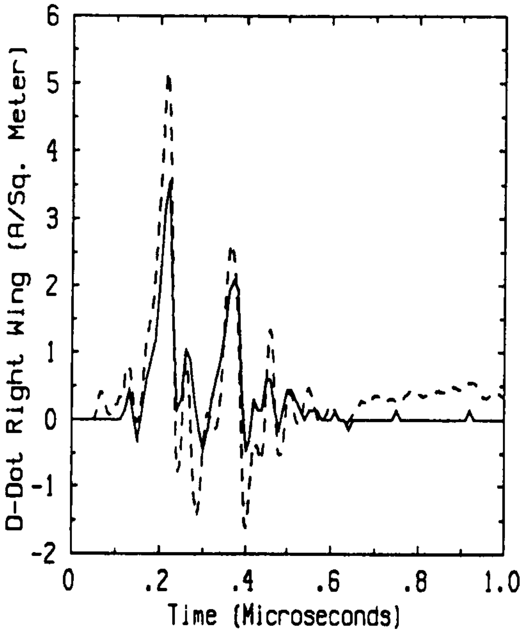

Flight 84.032 Run 003 Strike 005
- Measured -- Predicted

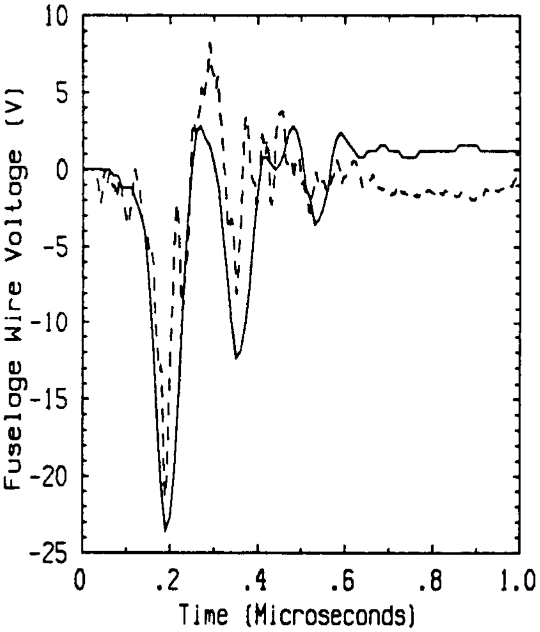

Flight 84.032 Run 003 Strike 005
- Measured -- Predicted

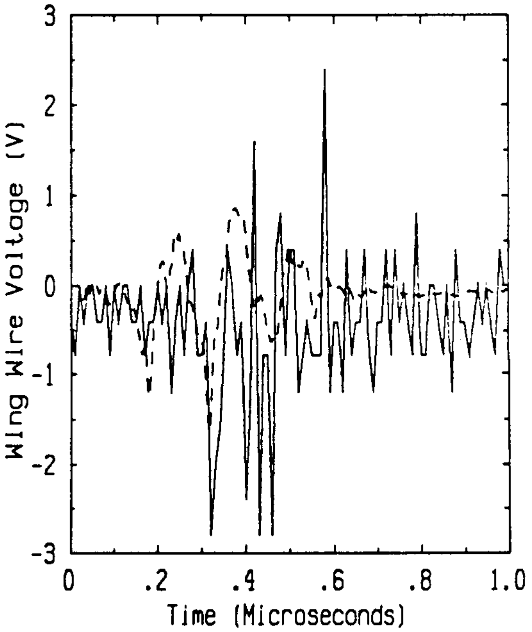

Flight 84.032 Run 003 Strike 005
- Measured -- Predicted

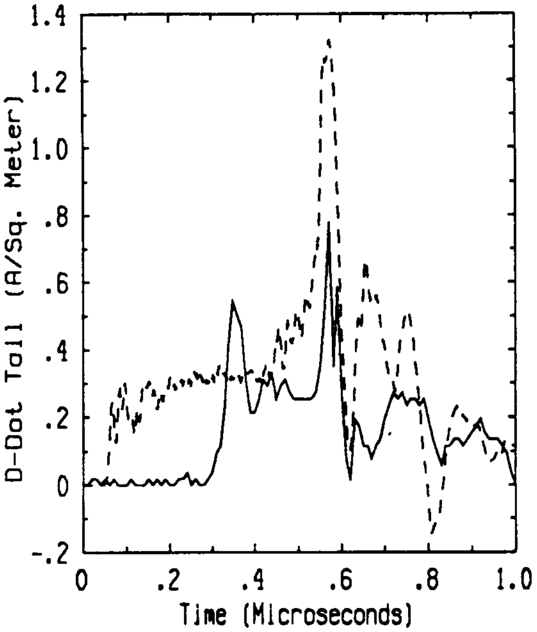

Flight 84.033 Run 001 Strike 001
- Measured -- Predicted

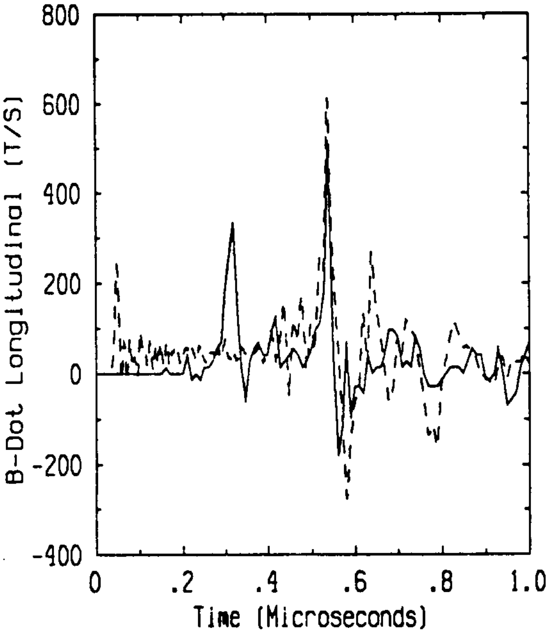

Flight 84.033 Run 001 Strike 001
- Measured -- Predicted

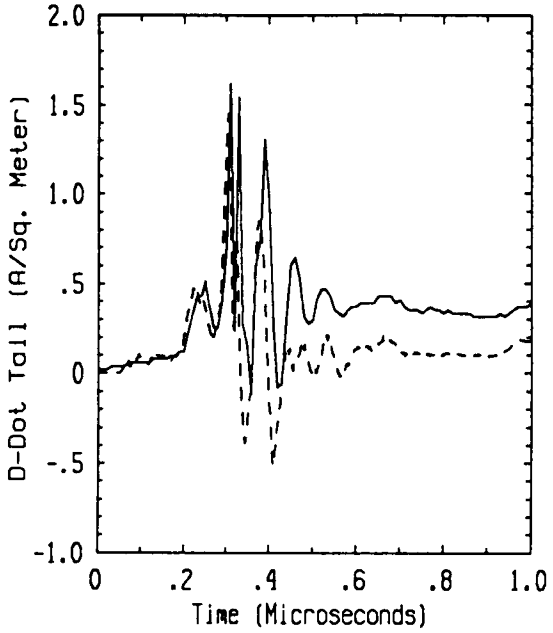

Flight 84.033 Run 002 Strike 004
- Measured -- Predicted

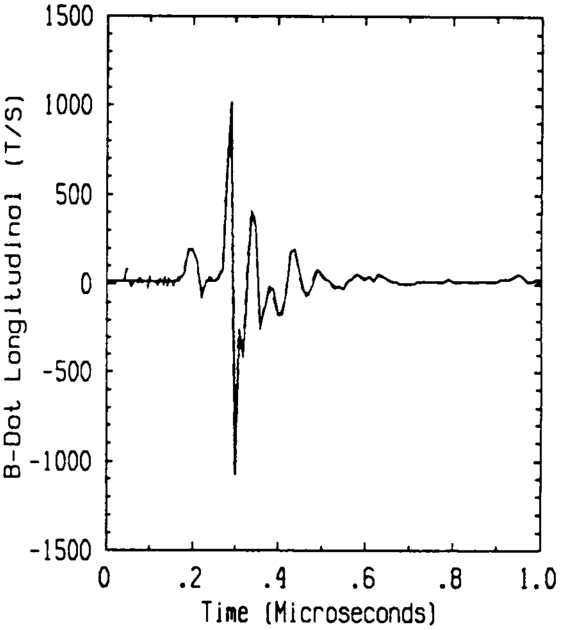

Flight 84.033 Run 002 Strike 004
- Measured -- Predicted

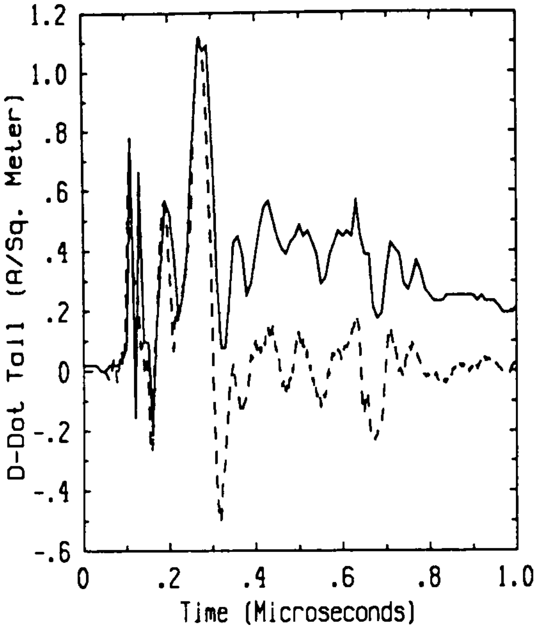

Flight 84.033 Run 004 Strike 013
- Measured -- Predicted

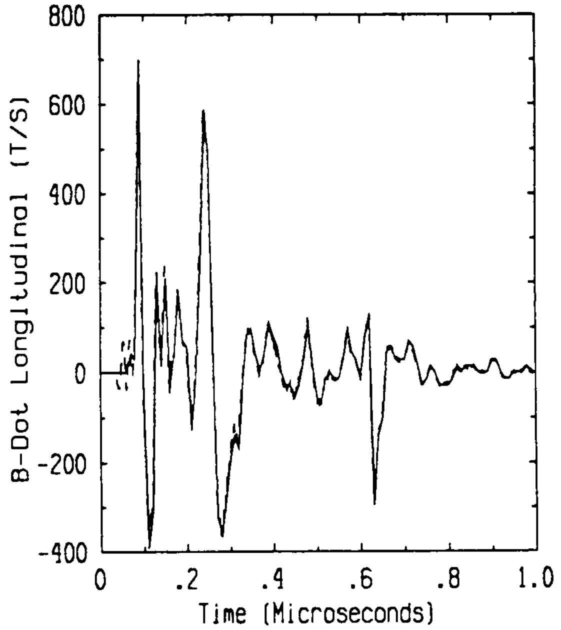

Flight 84.033 Run 004 Strike 013
- Measured -- Predicted

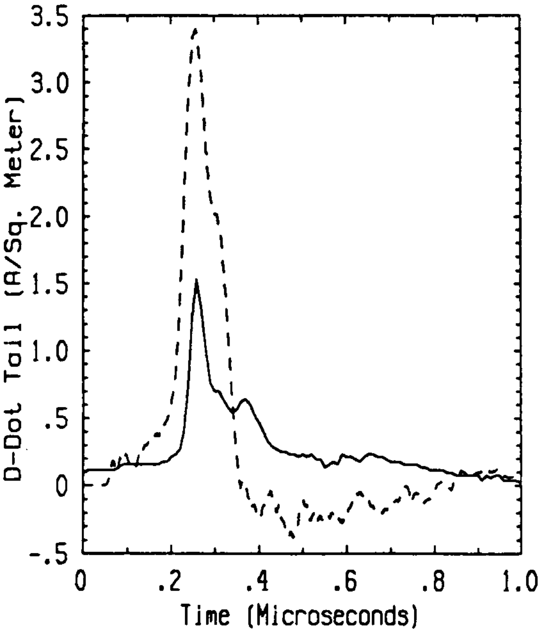

Flight 84.035 Run 003 Strike 004
- Measured -- Predicted

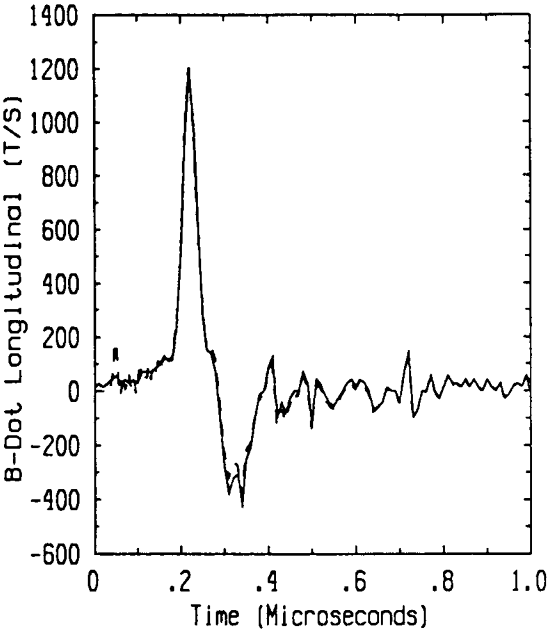

Flight 84.035 Run 003 Strike 004
- Measured -- Predicted

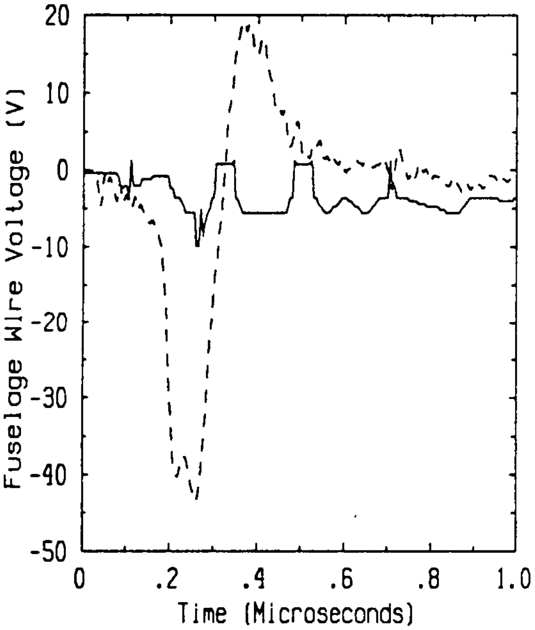

Flight 84.035 Run 003 Strike 004
- Measured -- Predicted

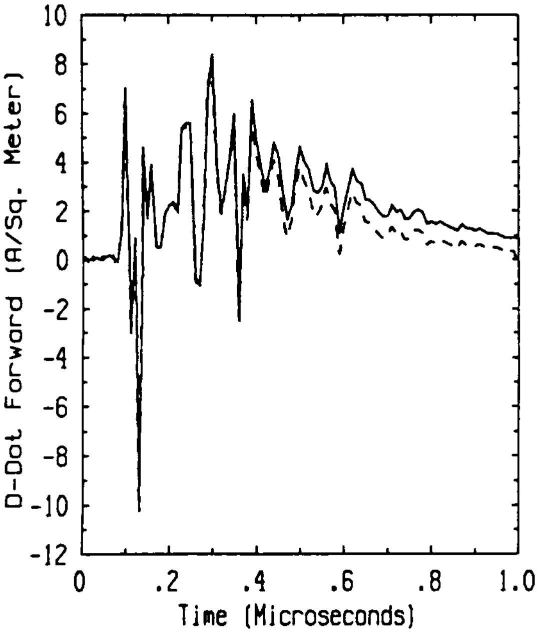

Flight 84.036 Run 001 Strike 001
- Measured -- Predicted

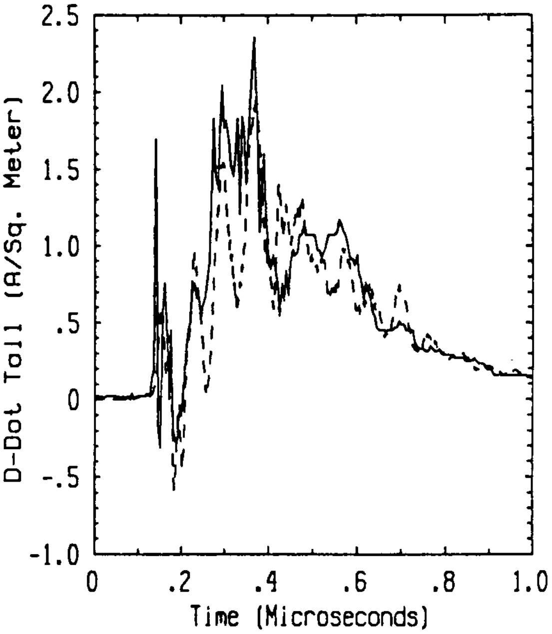

Flight 84.036 Run 001 Strike 001
- Measured -- Predicted

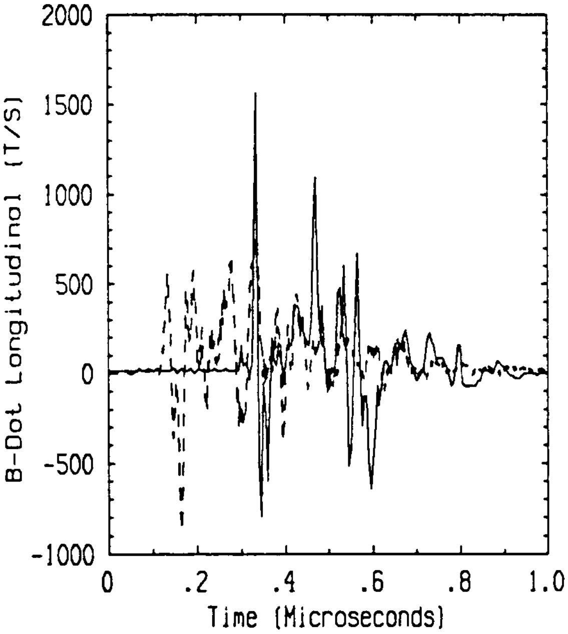

Flight 84.036 Run 001 Strike 001
- Measured -- Predicted

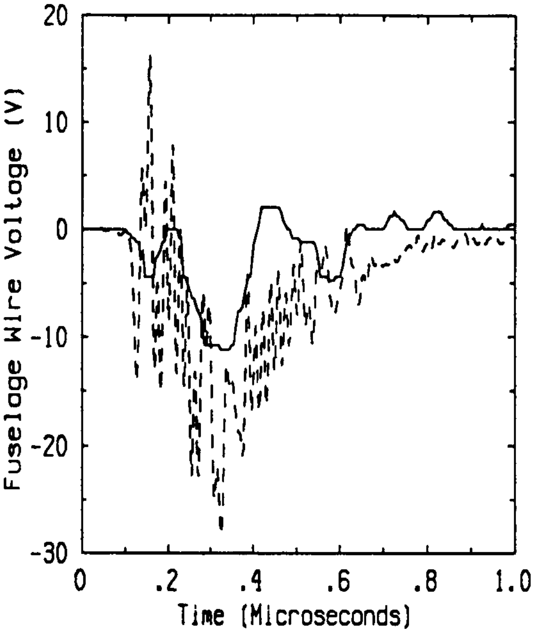

Flight 84.036 Run 001 Strike 001
- Measured -- Predicted

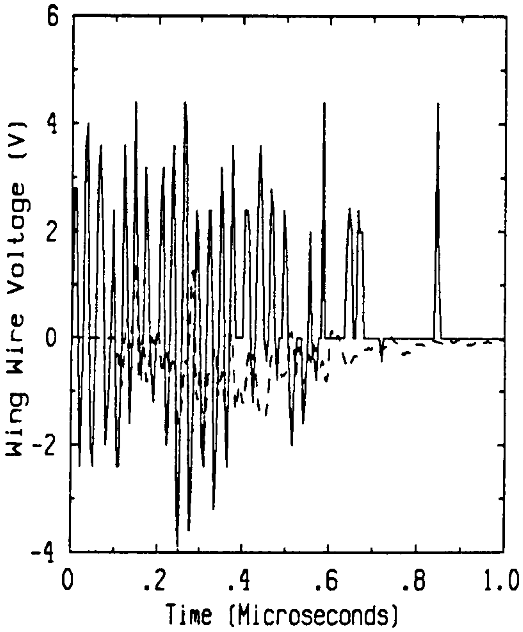

Flight 84.036 Run 001 Strike 001
- Measured -- Predicted

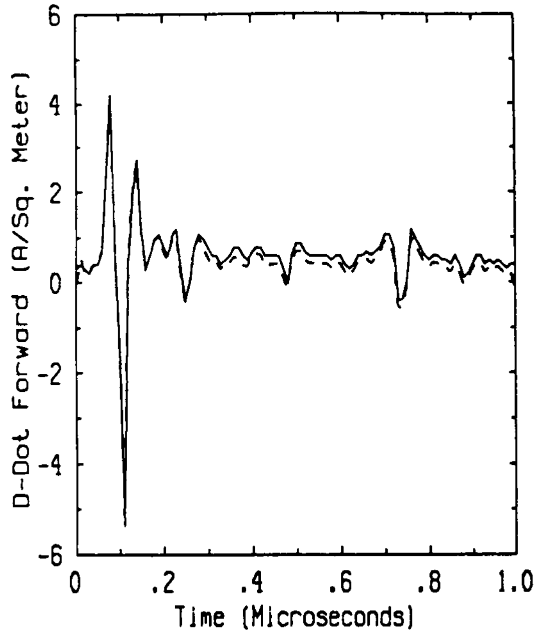

Flight 84.036 Run 002 Strike 002
- Measured -- Predicted

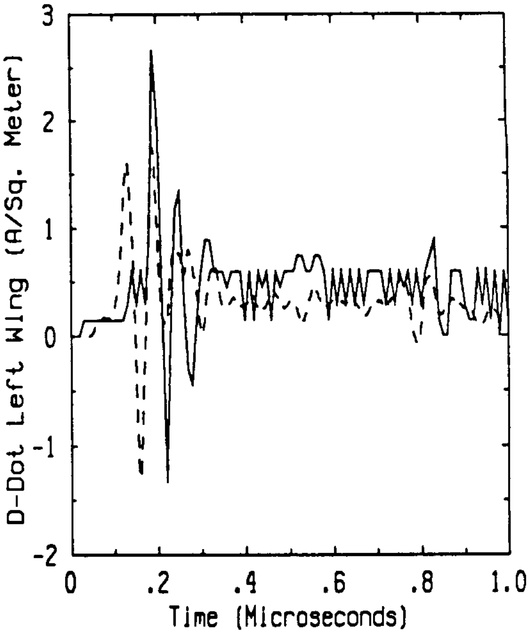

Flight 84.036 Run 002 Strike 002
- Measured -- Predicted

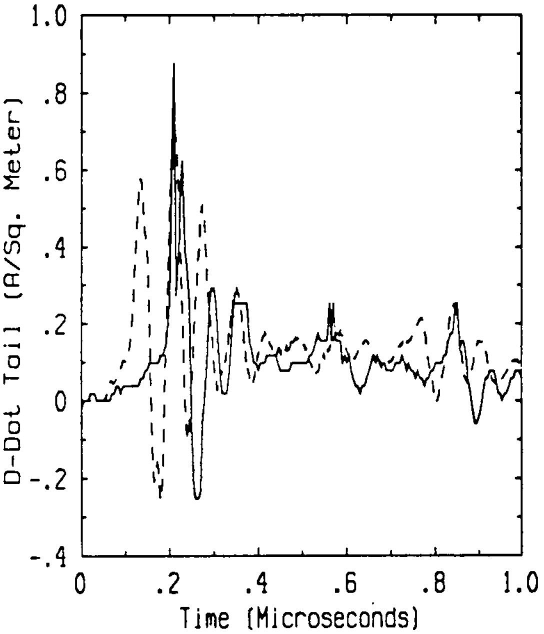

Flight 84.036 Run 002 Strike 002
- Measured -- Predicted

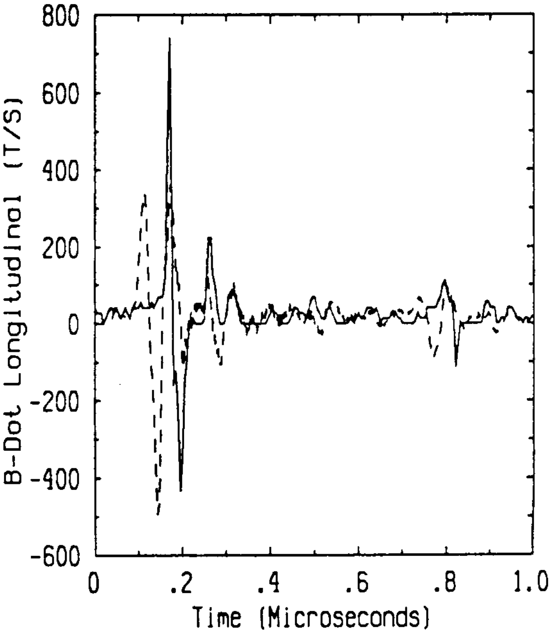

Flight 84.036 Run 002 Strike 002
- Measured -- Predicted

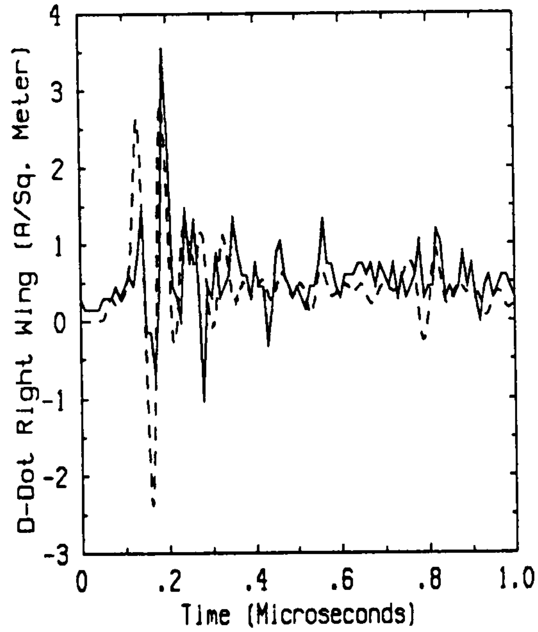

Flight 84.036 Run 002 Strike 002
- Measured -- Predicted

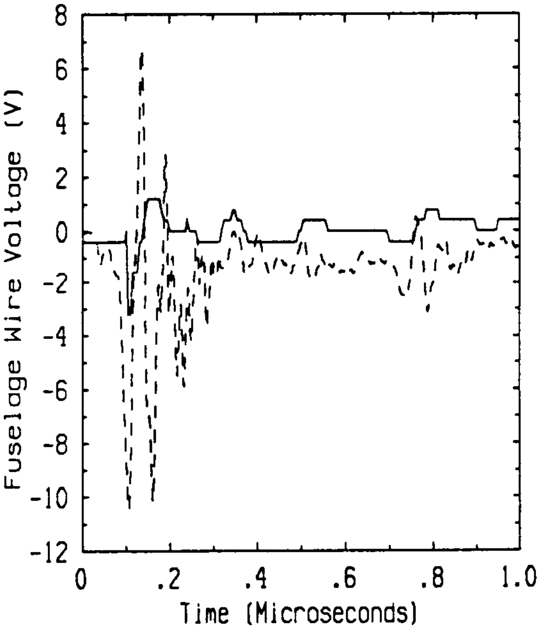

Flight 84.036 Run 002 Strike 002
- Measured -- Predicted

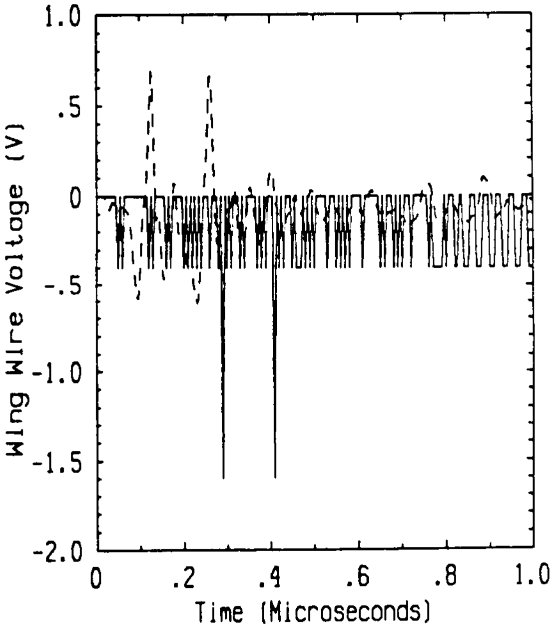

Flight 84.036 Run 002 Strike 002
- Measured -- Predicted

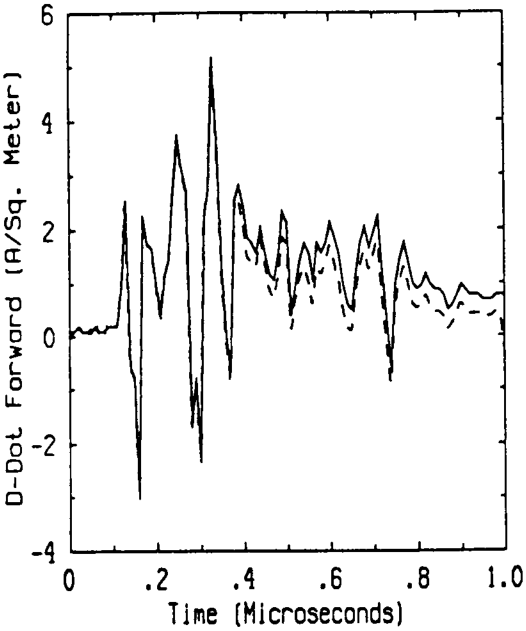

Flight 84.036 Run 006 Strike 009
- Measured -- Predicted

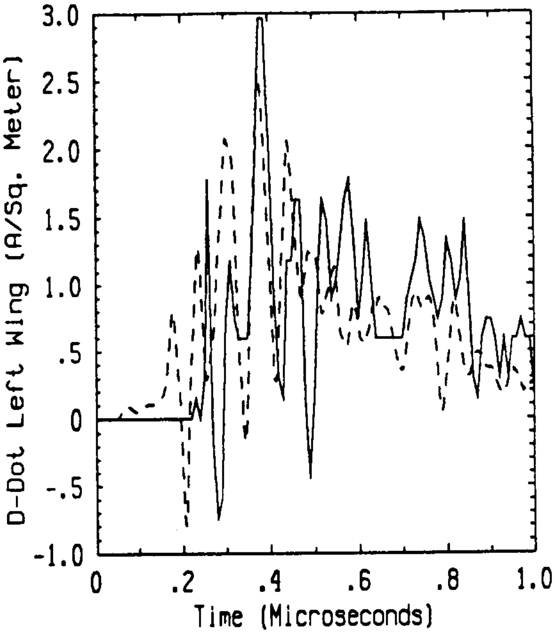

Flight 84.036 Run 006 Strike 009
- Measured -- Predicted

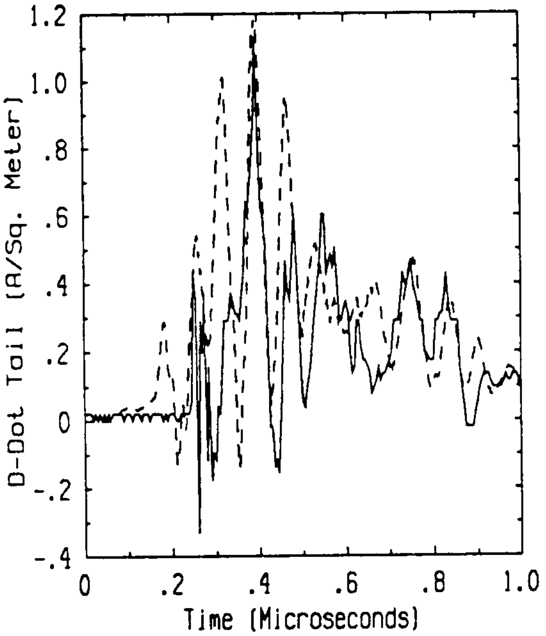

Flight 84.036 Run 006 Strike 009
- Measured -- Predicted

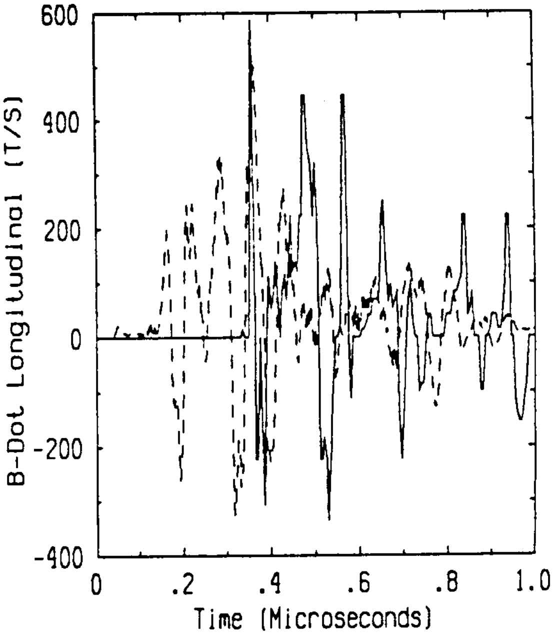

Flight 84.036 Run 006 Strike 009
- Measured -- Predicted

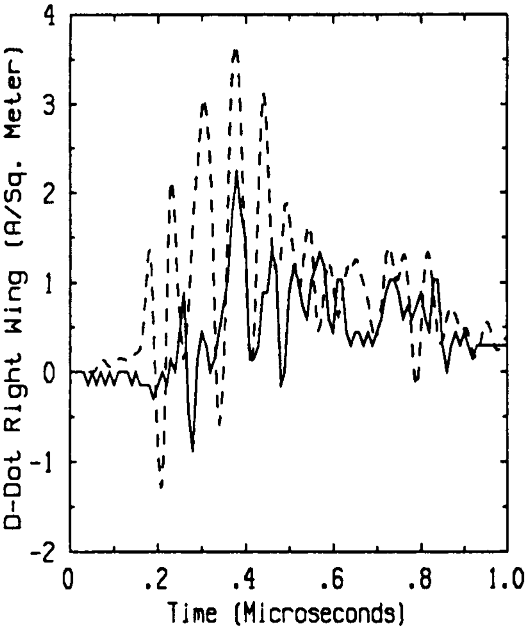

Flight 84.036 Run 006 Strike 009
- Measured -- Predicted

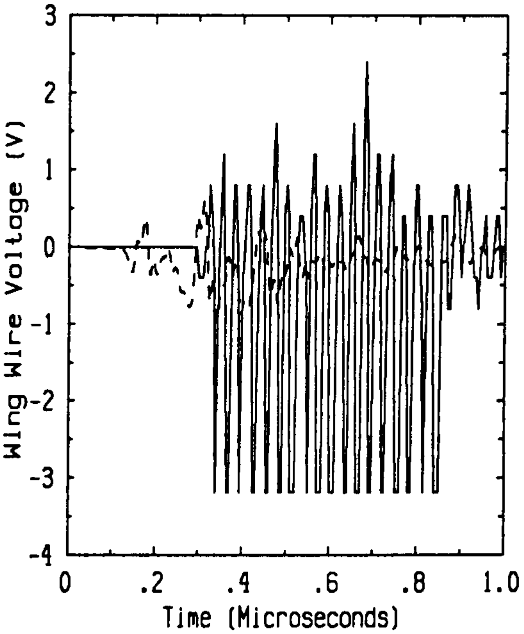

Flight 84.036 Run 006 Strike 009
- Measured -- Predicted

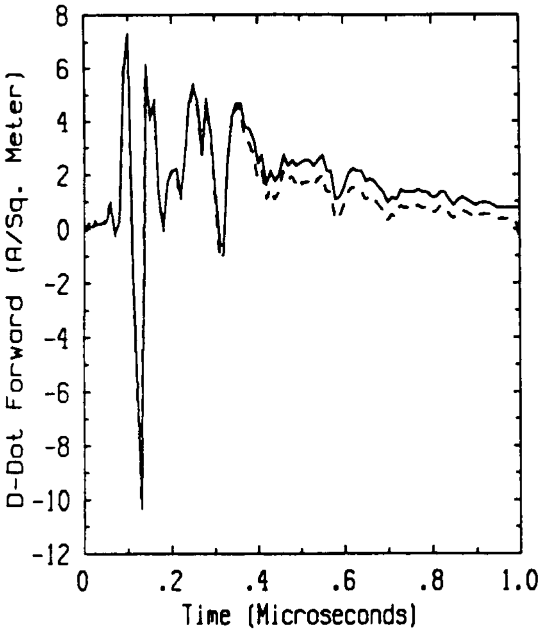

Flight 84.037 Run 002 Strike 018
- Measured -- Predicted

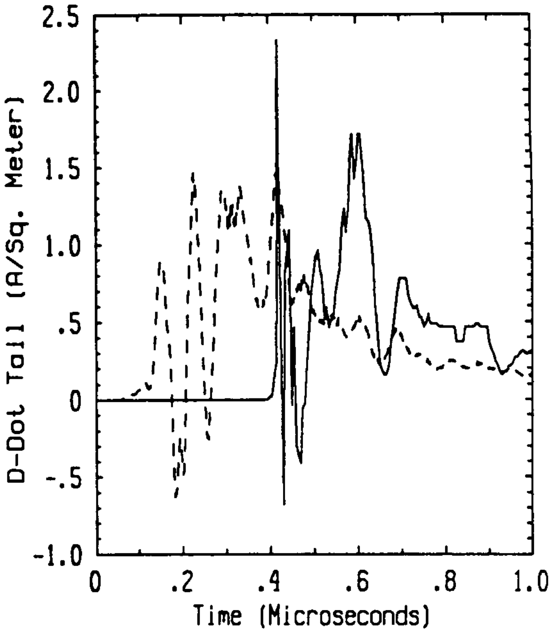

Flight 84.037 Run 002 Strike 018
- Measured -- Predicted

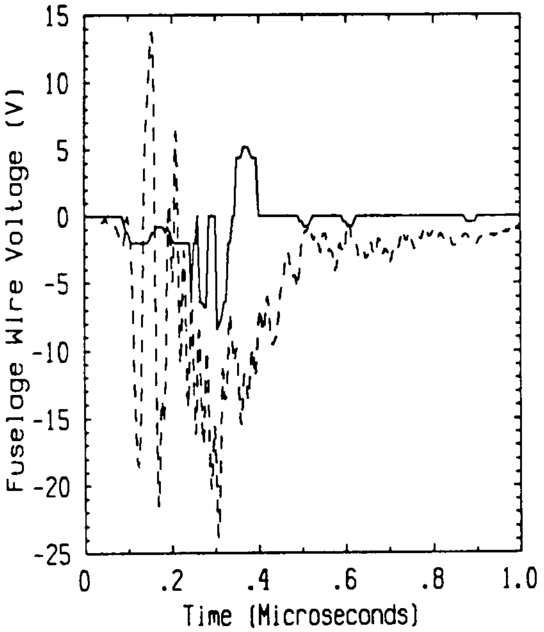

Flight 84.037 Run 002 Strike 018
- Measured -- Predicted

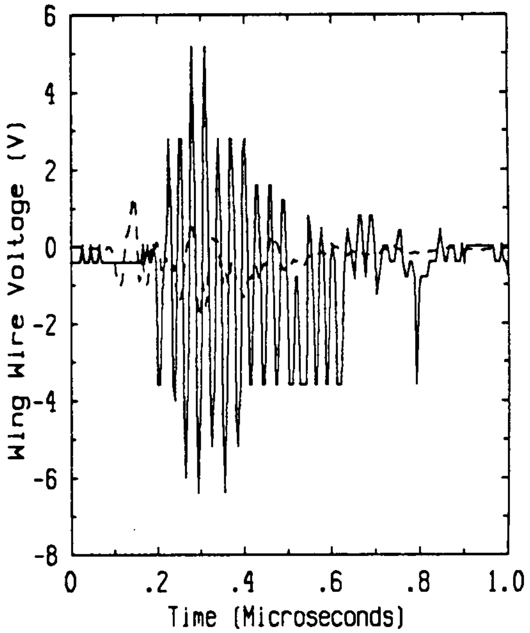

Flight 84.037 Run 002 Strike 018
- Measured -- Predicted

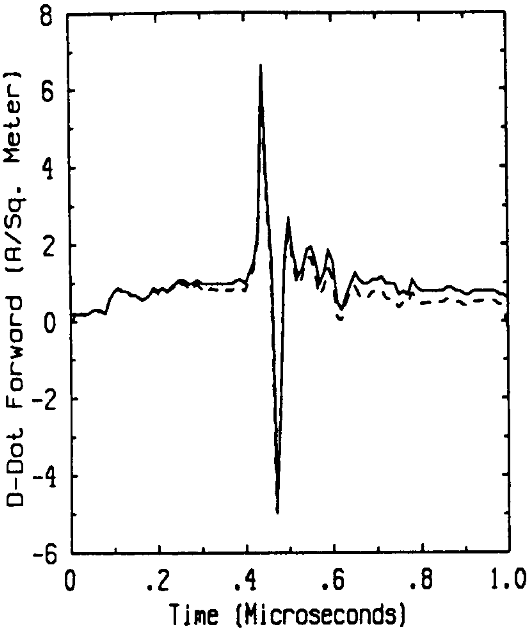

Flight 84.037 Run 003 Strike 022
- Measured -- Predicted

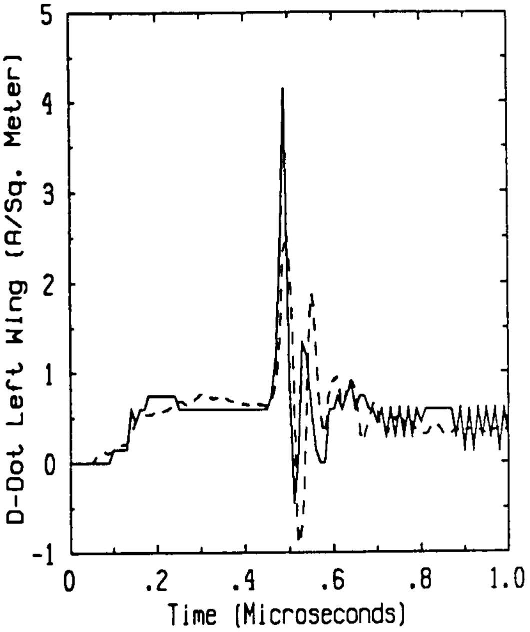

Flight 84.037 Run 003 Strike 022
- Measured -- Predicted

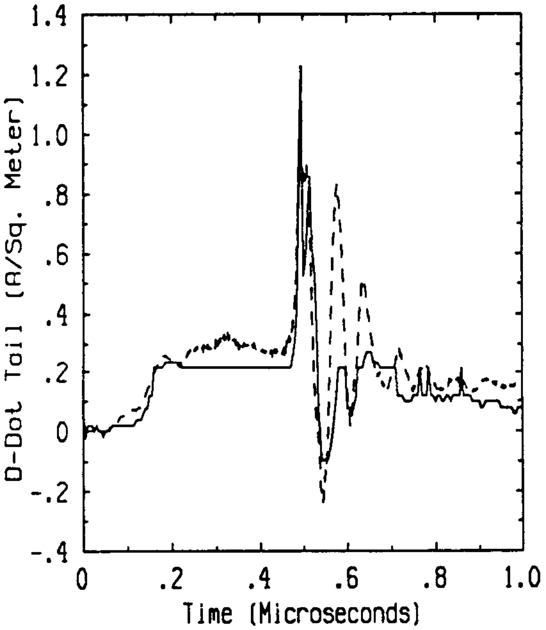

Flight 84.037 Run 003 Strike 022
- Measured -- Predicted

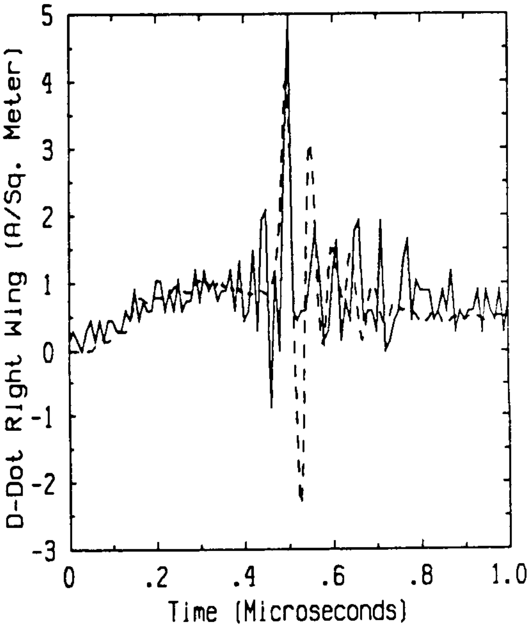

Flight 84.037 Run 003 Strike 022
- Measured -- Predicted

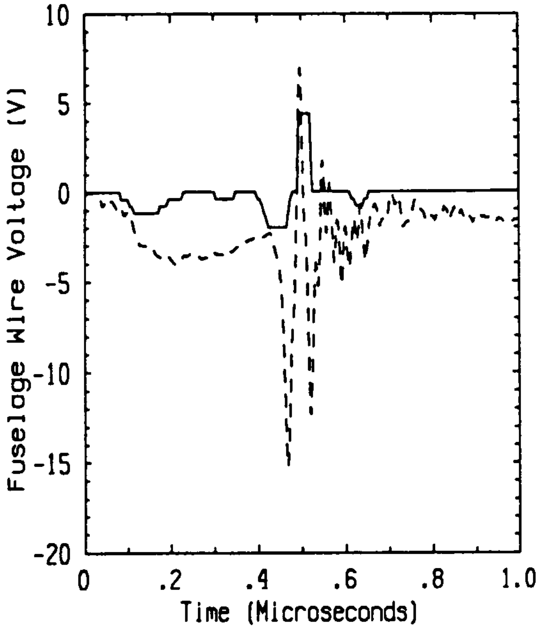

Flight 84.037 Run 003 Strike 022
- Measured -- Predicted

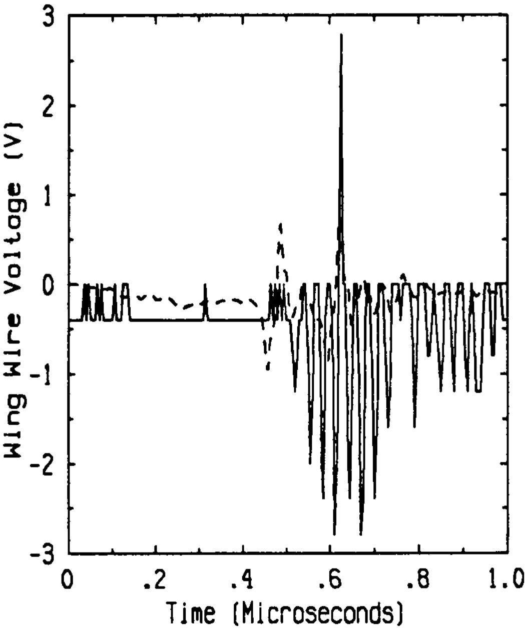

Flight 84.037 Run 003 Strike 022
- Measured -- Predicted

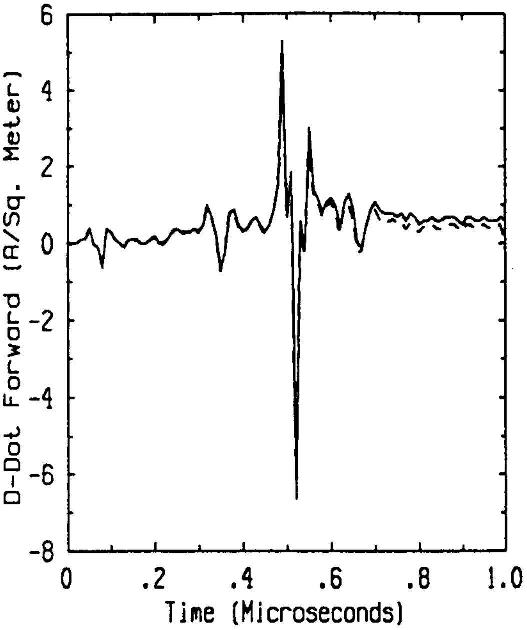

Flight 84.037 Run 004 Strike 024
- Measured -- Predicted

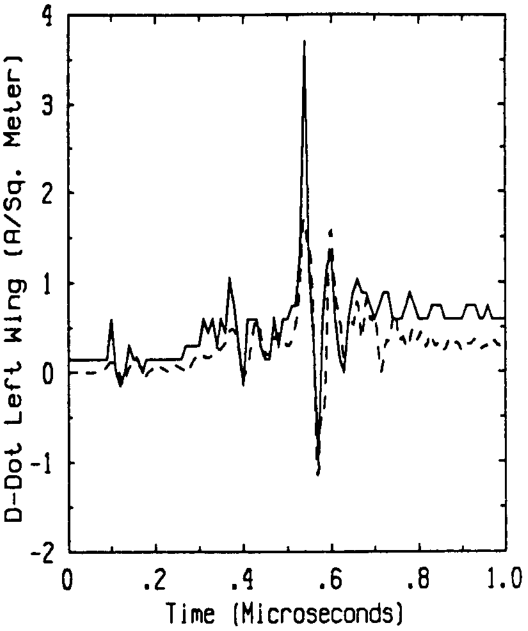

Flight 84.037 Run 004 Strike 024
- Measured -- Predicted

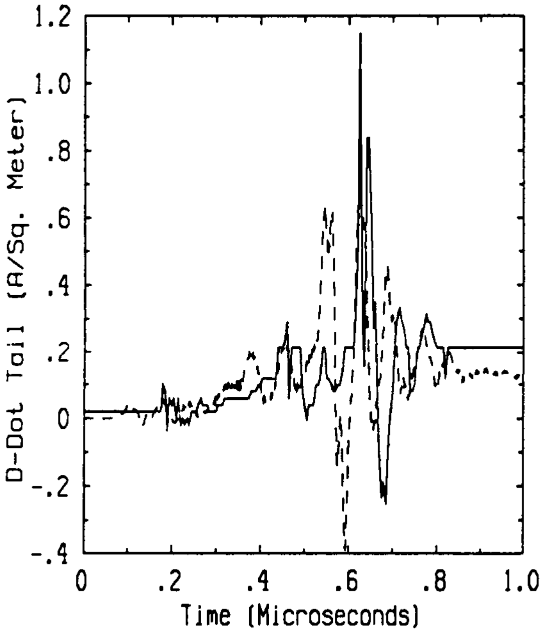

Flight 84.037 Run 004 Strike 024
- Measured -- Predicted

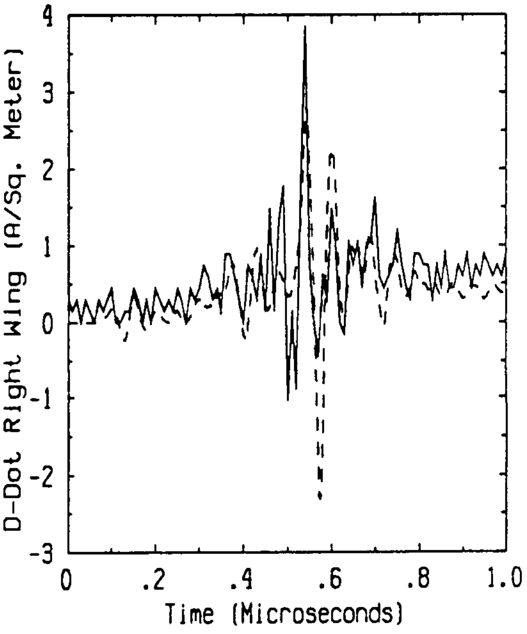

Flight 84.037 Run 004 Strike 024
- Measured -- Predicted

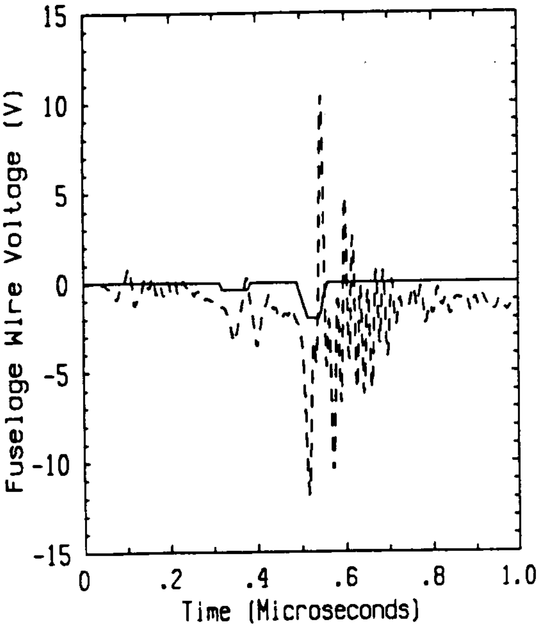

Flight 84.037 Run 004 Strike 024
- Measured -- Predicted

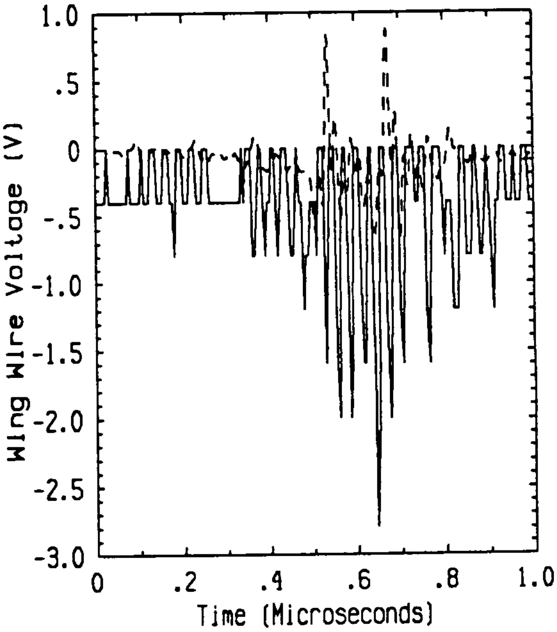

Flight 84.037 Run 004 Strike 024
- Measured -- Predicted

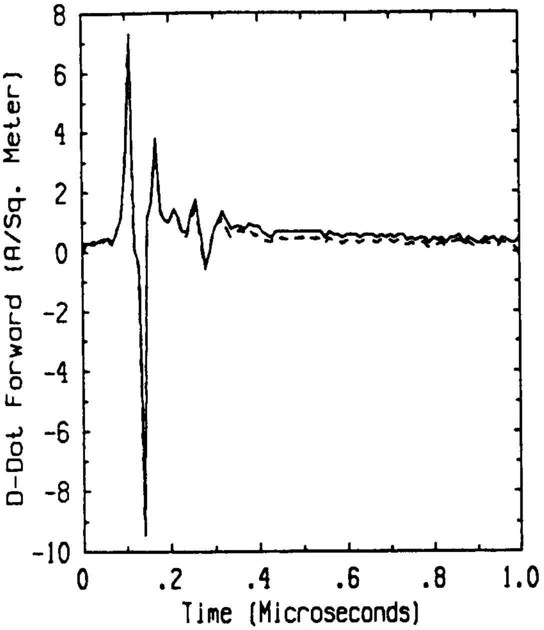

Flight 84.037 Run 005 Strike 029
- Measured -- Predicted

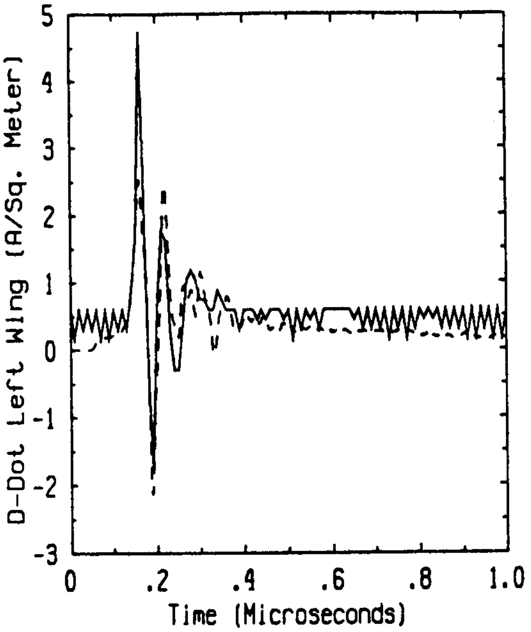

Flight 84.037 Run 005 Strike 029
- Measured -- Predicted

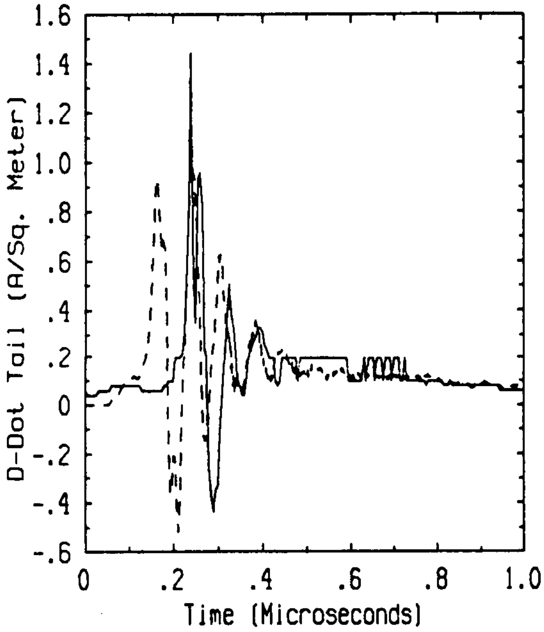

Flight 84.037 Run 005 Strike 029
- Measured -- Predicted

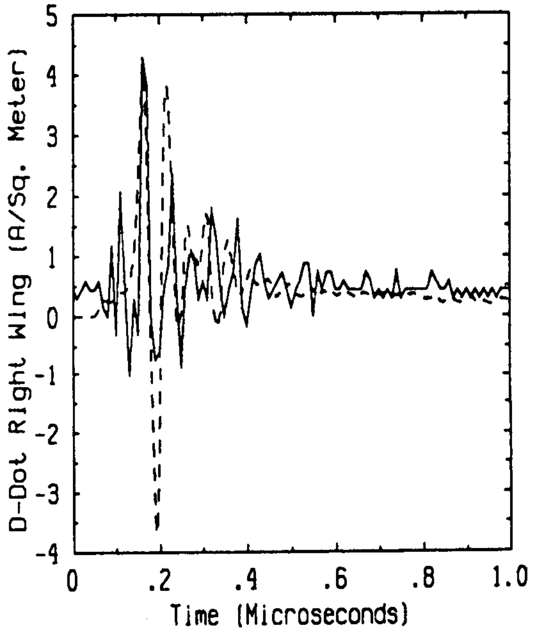

Flight 84.037 Run 005 Strike 029
- Measured -- Predicted

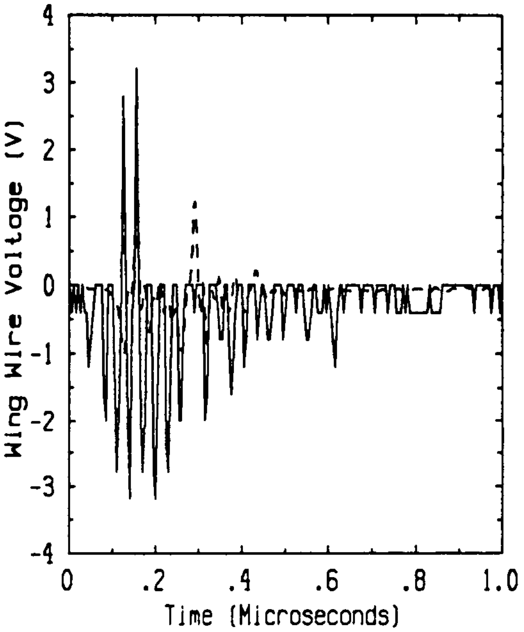

Flight 84.037 Run 005 Strike 029
- Measured -- Predicted

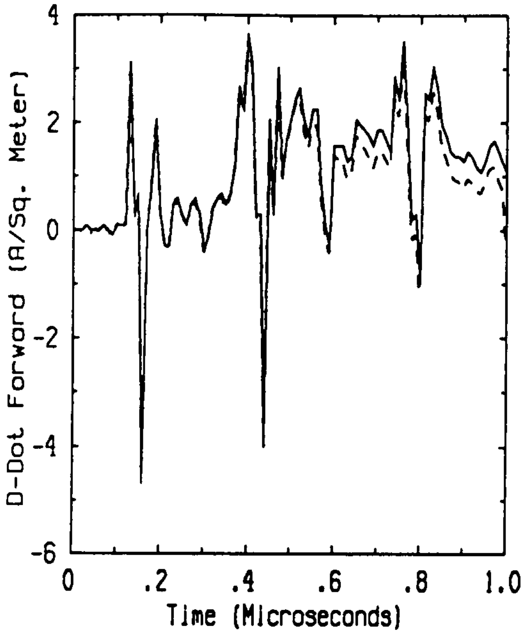

Flight 84.037 Run 006 Strike 034
- Measured -- Predicted

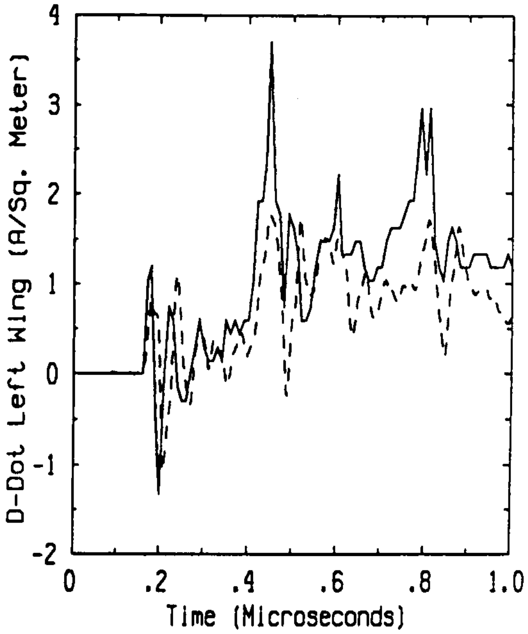

Flight 84.037 Run 006 Strike 034
- Measured -- Predicted

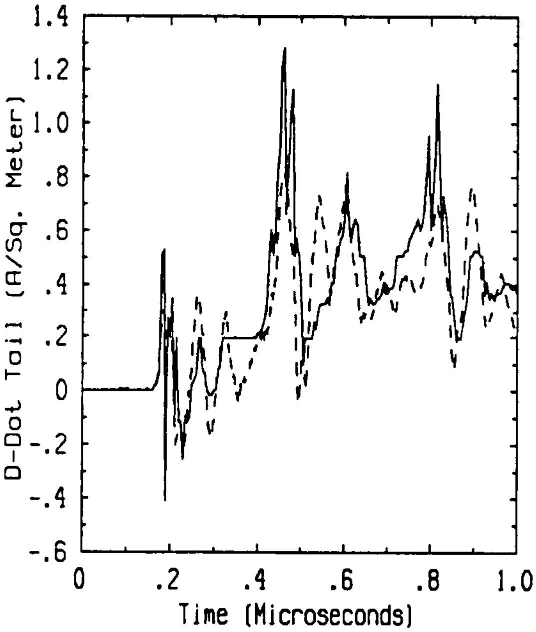

Flight 84.037 Run 006 Strike 034
- Measured -- Predicted

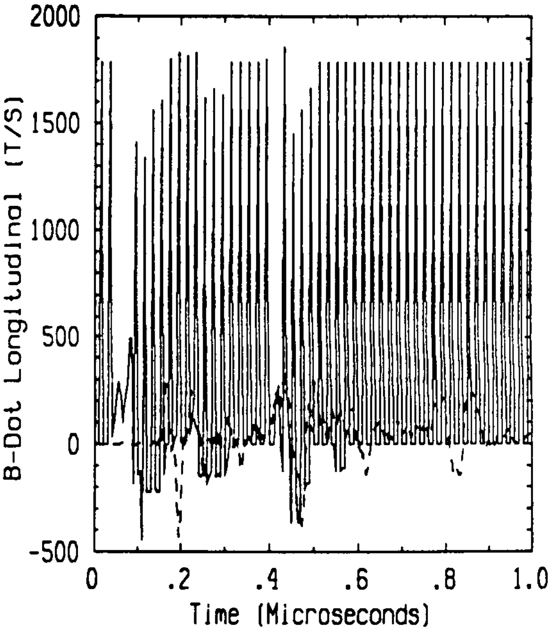

Flight 84.037 Run 006 Strike 034
- Measured -- Predicted

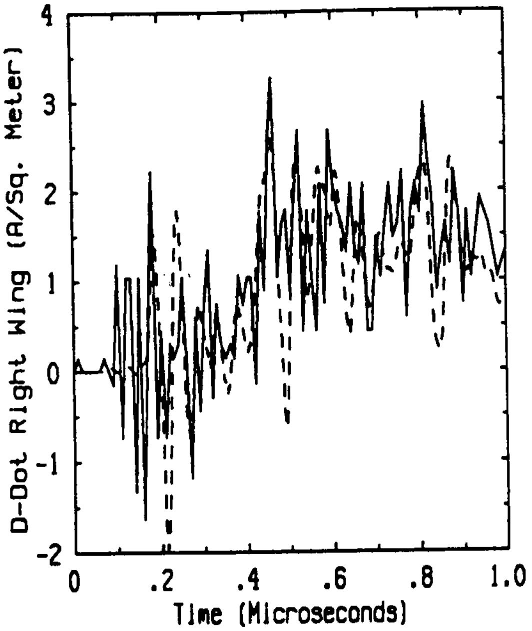

Flight 84.037 Run 006 Strike 034
- Measured -- Predicted

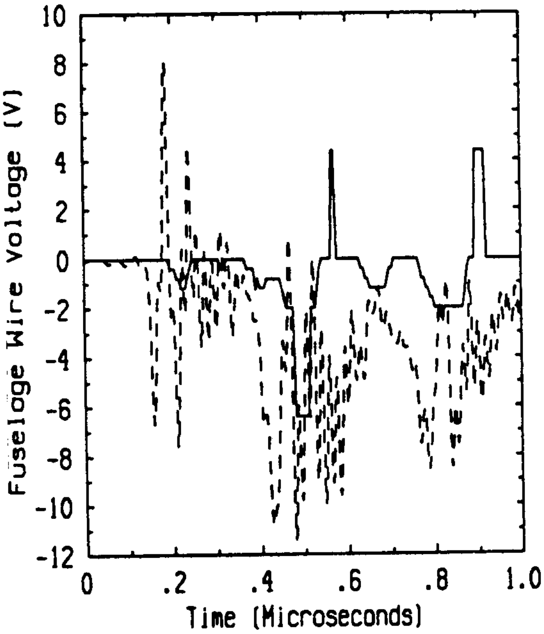

Flight 84.037 Run 006 Strike 034
- Measured -- Predicted

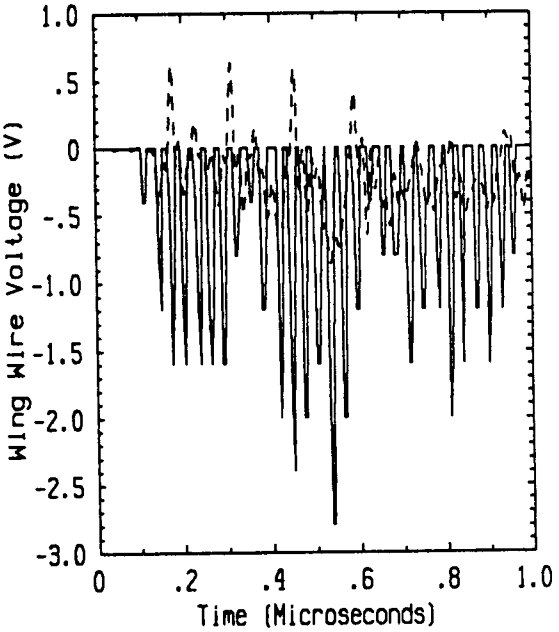

Flight 84.037 Run 006 Strike 034
- Measured -- Predicted

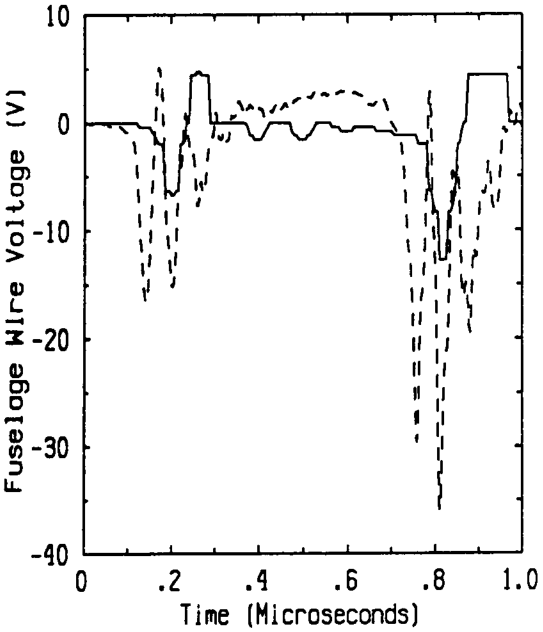

Flight 84.037 Run 008 Strike 041
- Measured -- Predicted

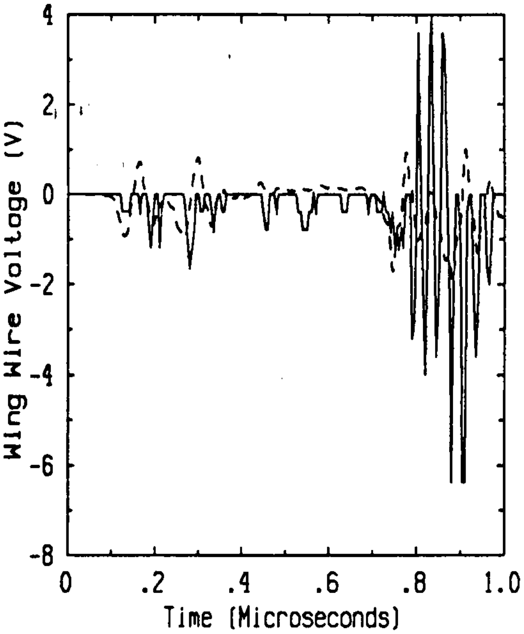

Flight 84.037 Run 008 Strike 041
- Measured -- Predicted

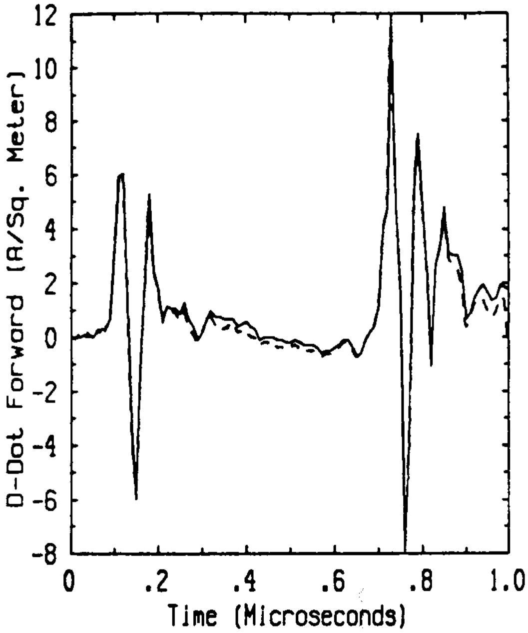

Flight 84.037 Run 008 Strike 041
- Measured -- Predicted

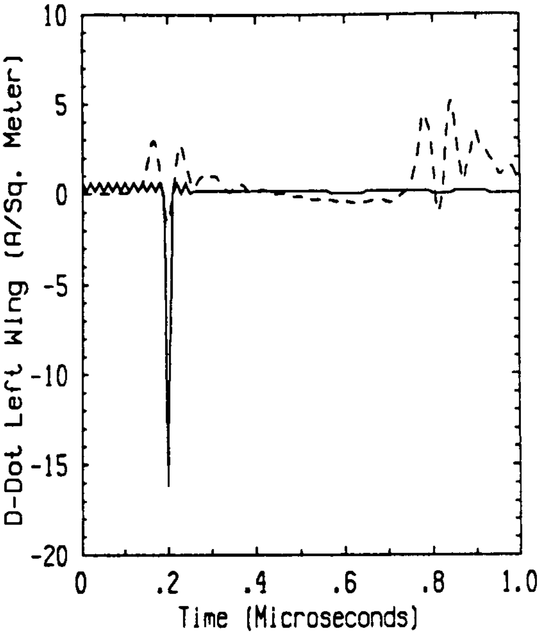

Flight 84.037 Run 008 Strike 041
- Measured -- Predicted

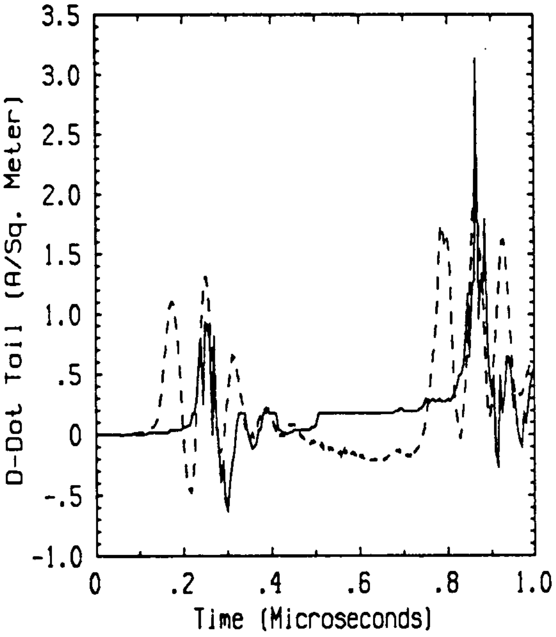

Flight 84.037 Run 008 Strike 041
- Measured -- Predicted

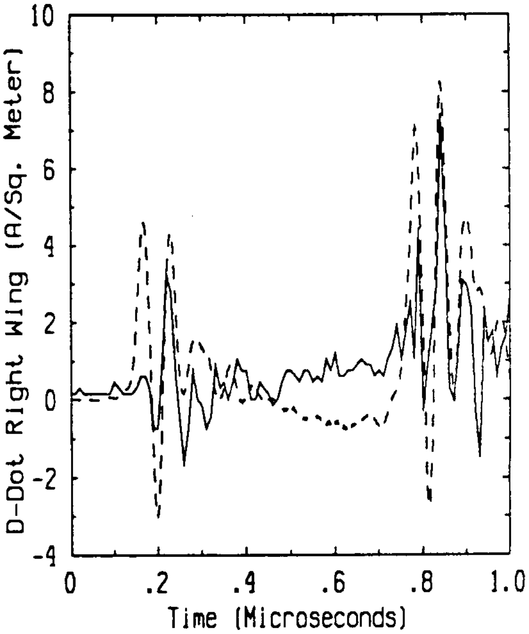

Flight 84.037 Run 008 Strike 041
- Measured -- Predicted

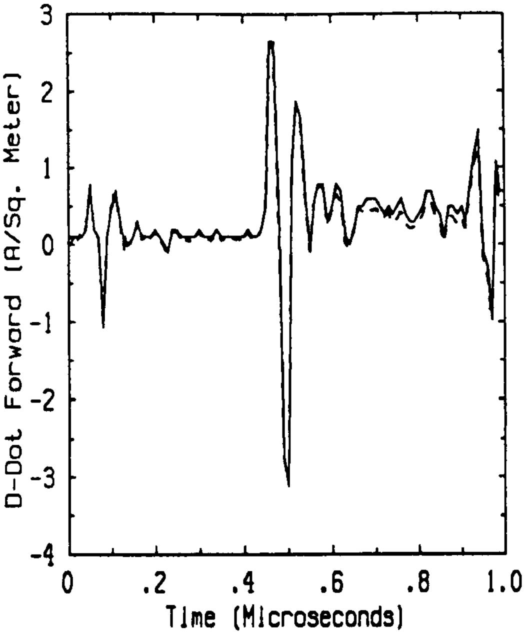

Flight 84.037 Run 009 Strike 044
- Measured -- Predicted

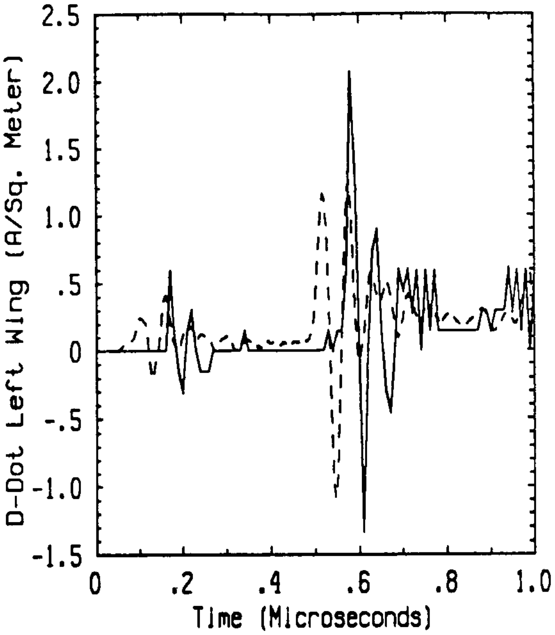

Flight 84.037 Run 009 Strike 044
- Measured -- Predicted

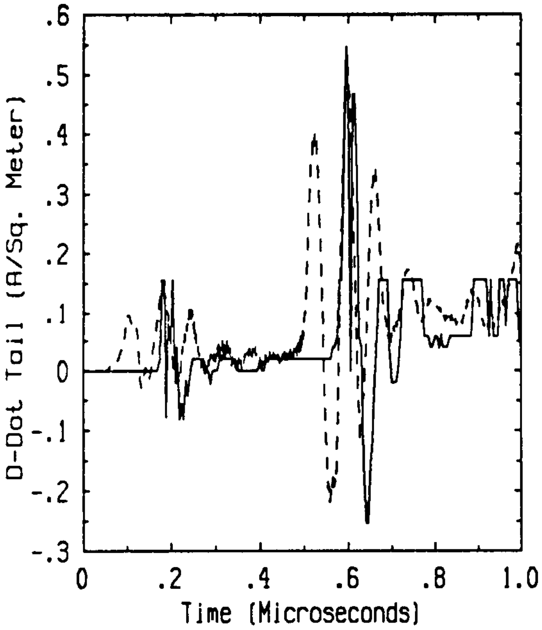

Flight 84.037 Run 009 Strike 044
- Measured -- Predicted

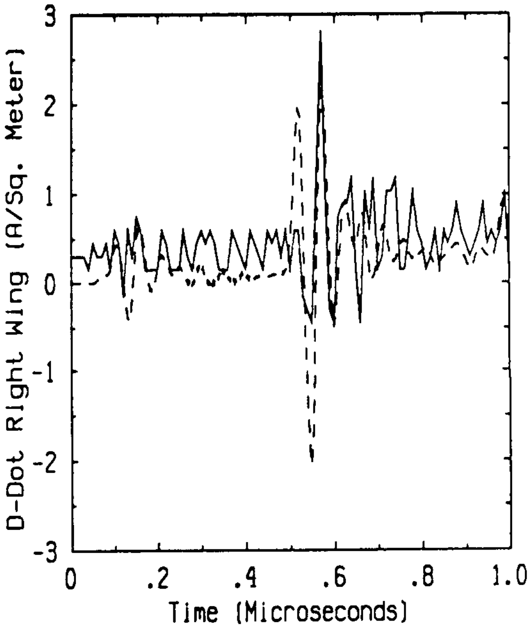

Flight 84.037 Run 009 Strike 044
- Measured -- Predicted

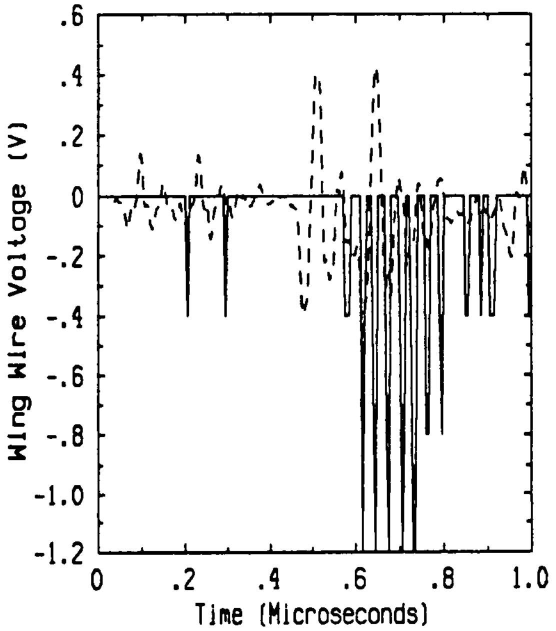

Flight 84.037 Run 009 Strike 044
- Measured -- Predicted

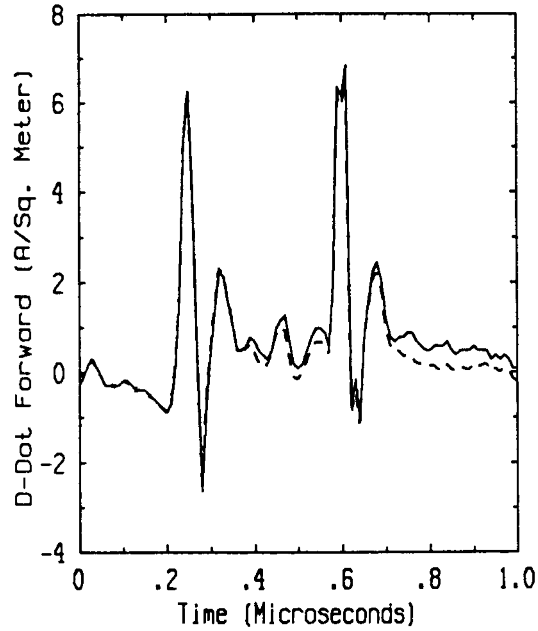

Flight 84.037 Run 010 Strike 052
- Measured -- Predicted

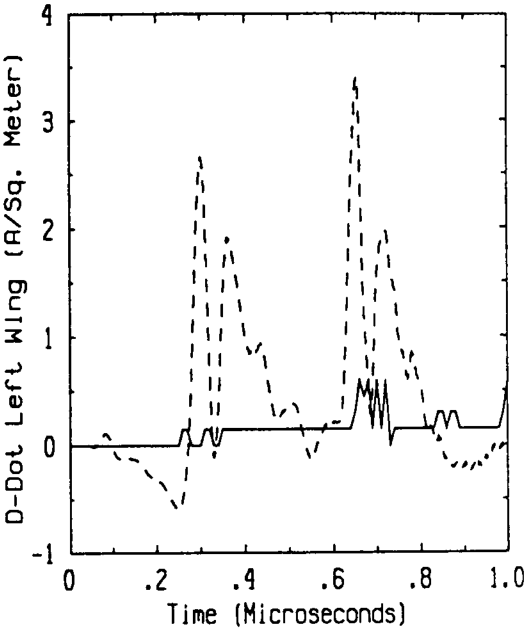

Flight 84.037 Run 010 Strike 052
- Measured -- Predicted

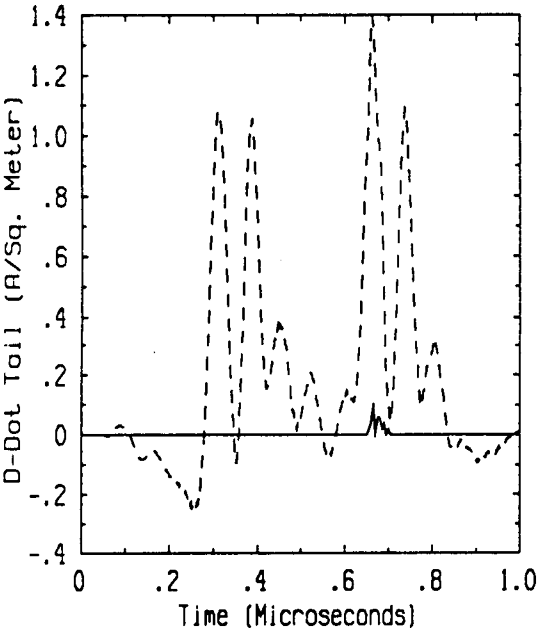

Flight 84.037 Run 010 Strike 052
- Measured -- Predicted

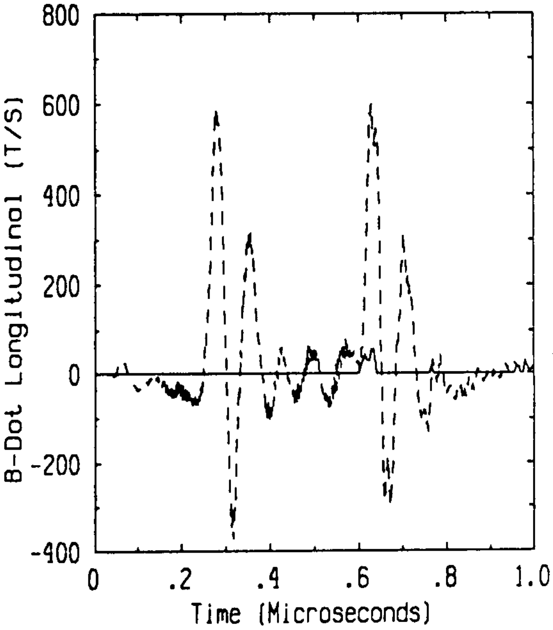

Flight 84.037 Run 010 Strike 052
- Measured -- Predicted

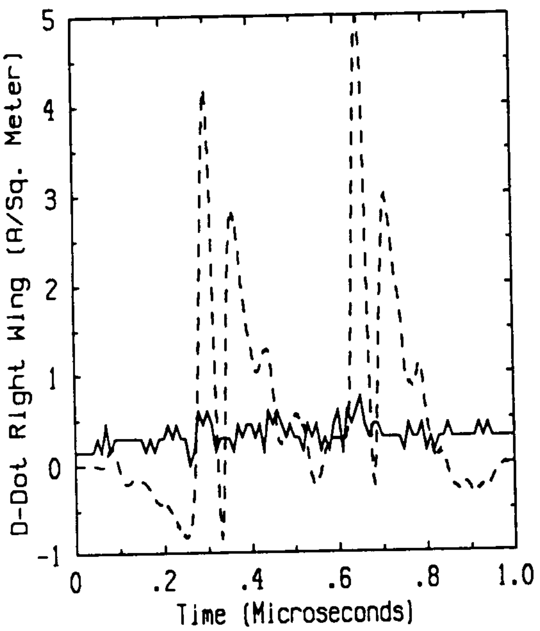

Flight 84.037 Run 010 Strike 052
- Measured -- Predicted

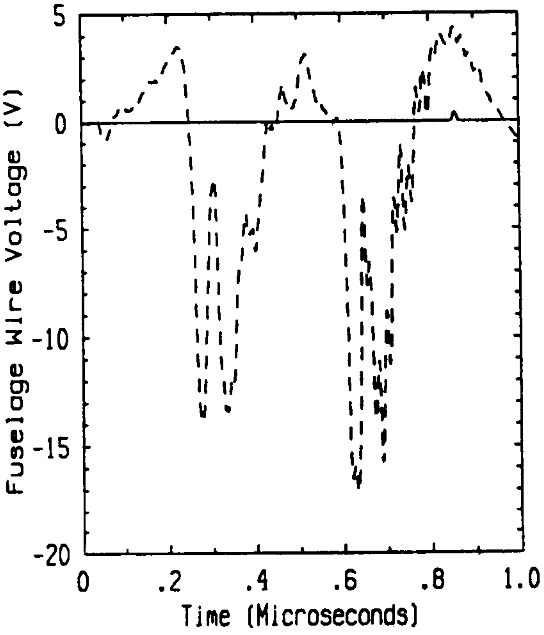

Flight 84.037 Run 010 Strike 052
- Measured -- Predicted

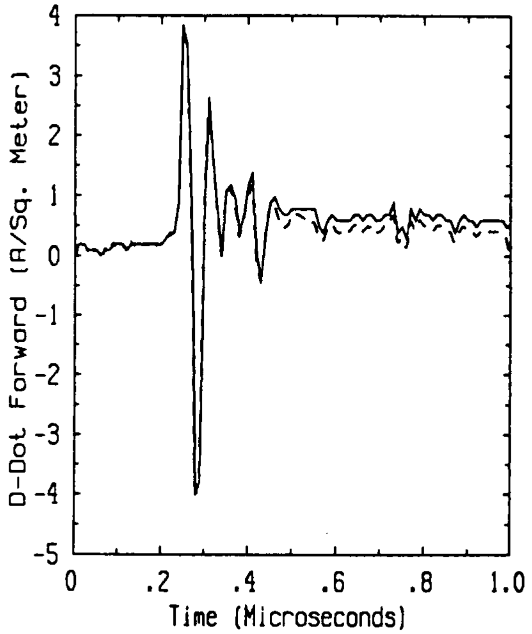

Flight 84.037 Run 014 Strike 058
- Measured -- Predicted

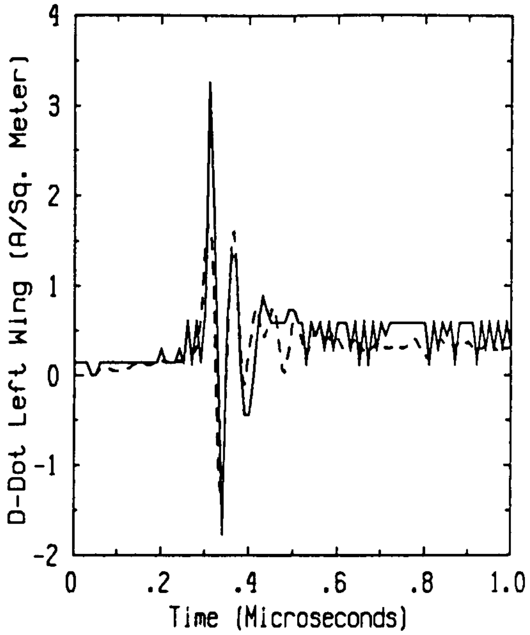

Flight 84.037 Run 014 Strike 058
- Measured -- Predicted

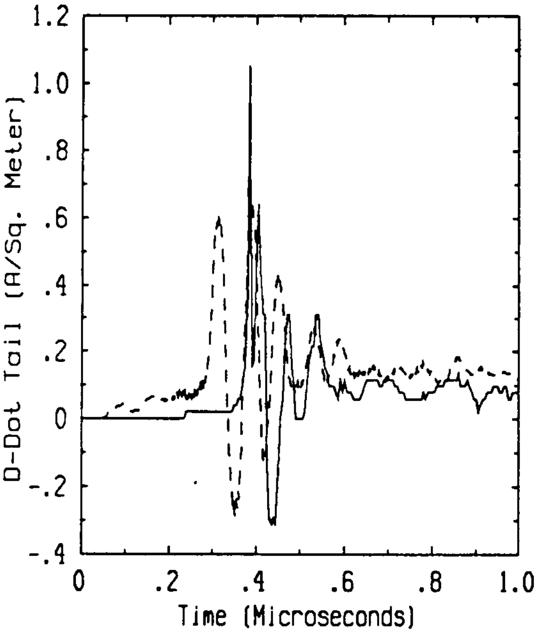

Flight 84.037 Run 014 Strike 058
- Measured -- Predicted

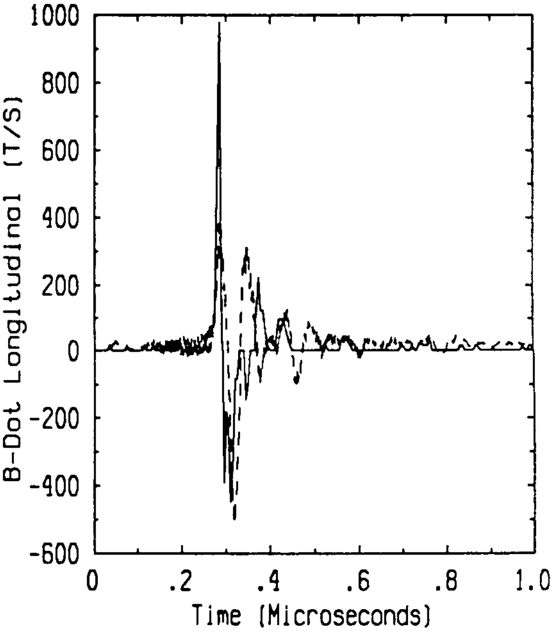

Flight 84.037 Run 014 Strike 058
- Measured -- Predicted

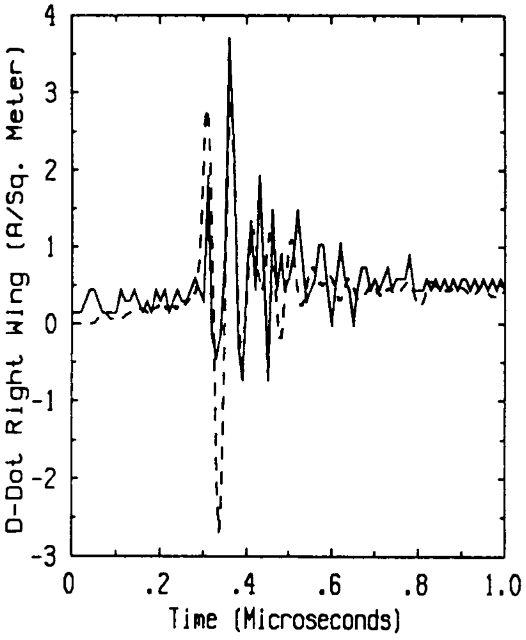

Flight 84.037 Run 014 Strike 058
- Measured -- Predicted

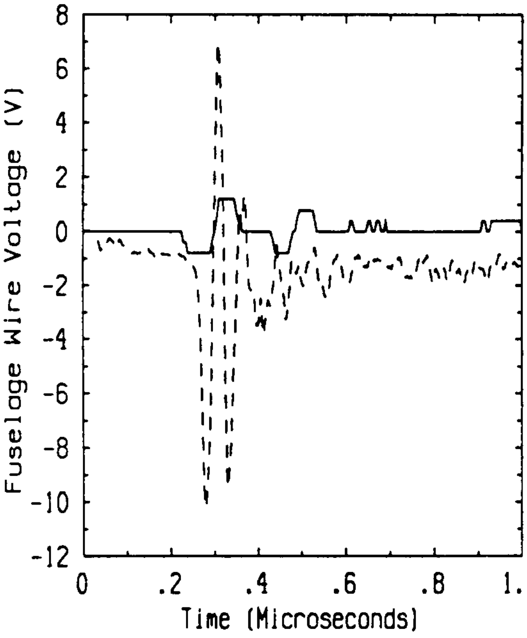

Flight 84.037 Run 014 Strike 058
- Measured -- Predicted

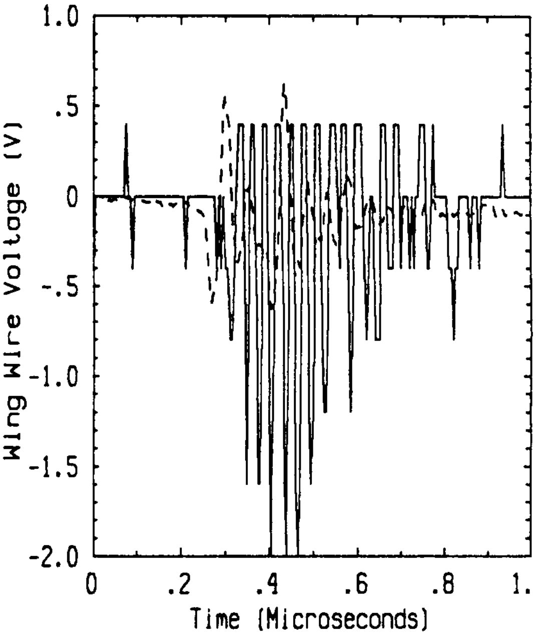

Flight 84.037 Run 014 Strike 058
- Measured -- Predicted

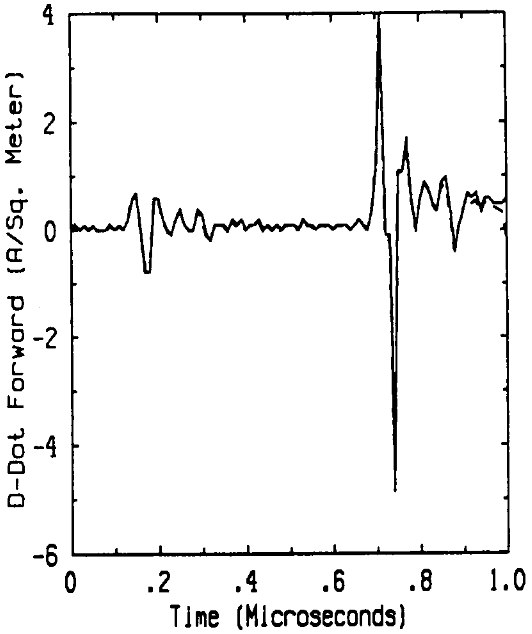

Flight 84.037 Run 015 Strike 062
- Measured -- Predicted

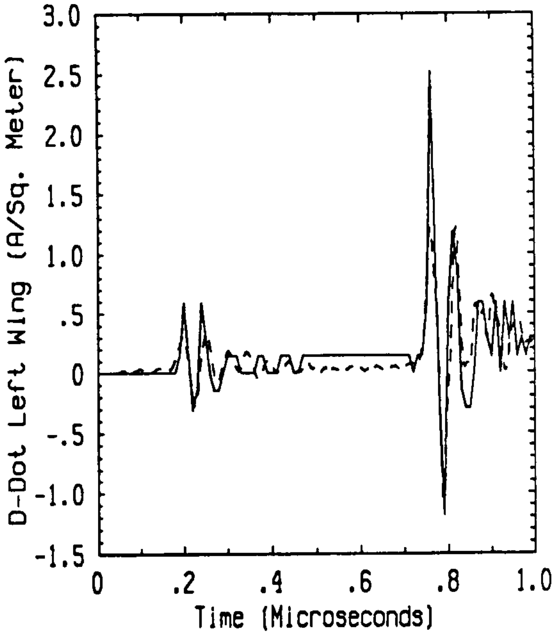

Flight 84.037 Run 015 Strike 062
- Measured -- Predicted

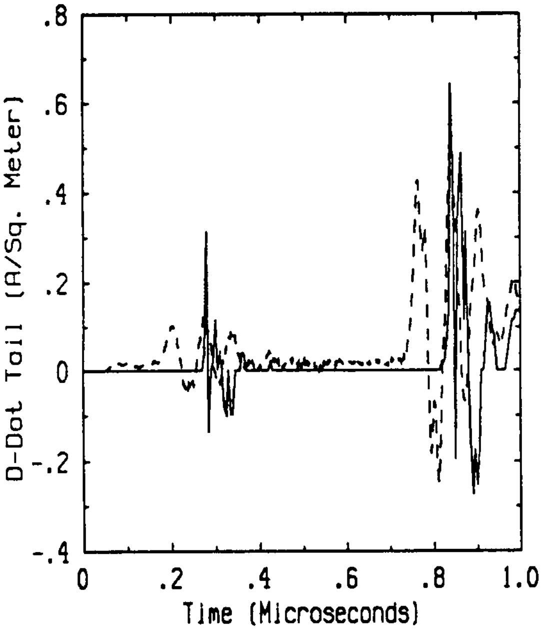

Flight 84.037 Run 015 Strike 062
- Measured -- Predicted

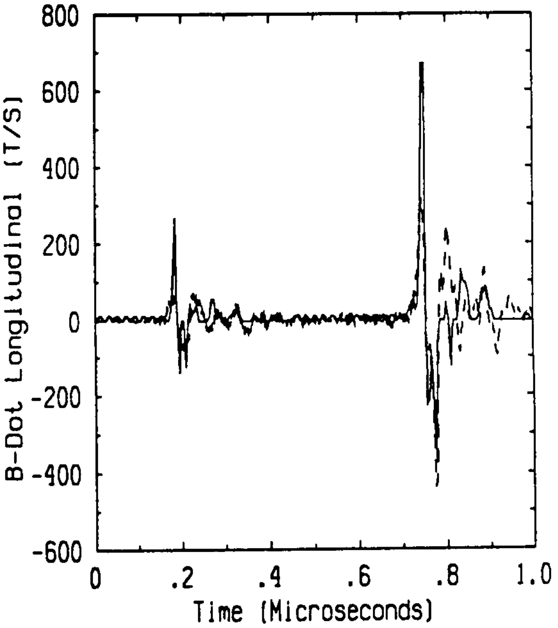

Flight 84.037 Run 015 Strike 062
- Measured -- Predicted

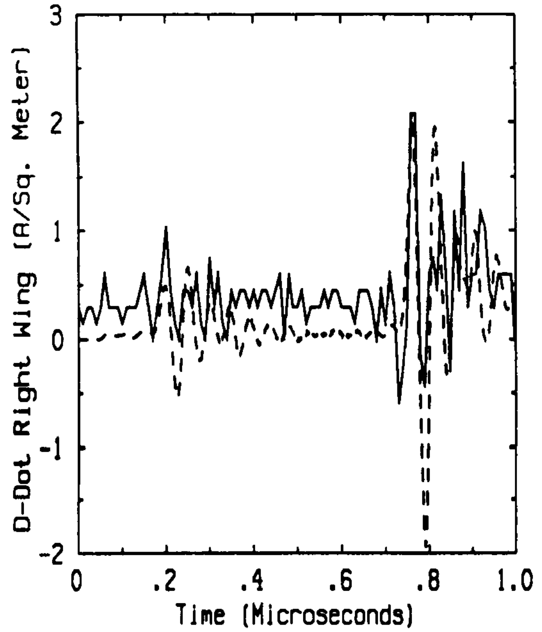

Flight 84.037 Run 015 Strike 062
- Measured -- Predicted

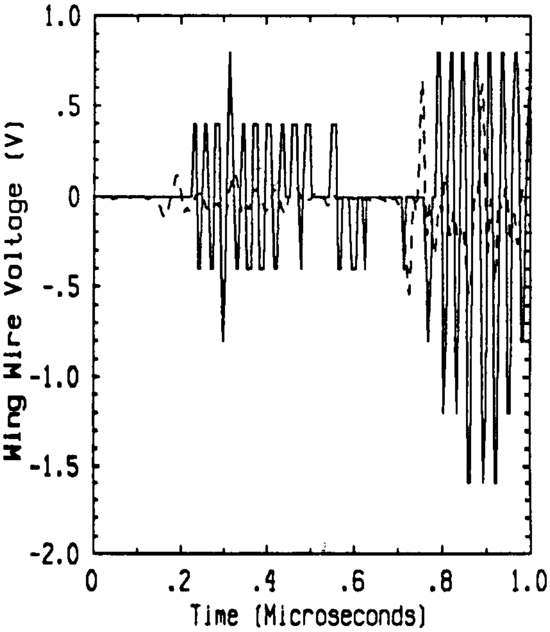

Flight 84.037 Run 015 Strike 062
- Measured -- Predicted

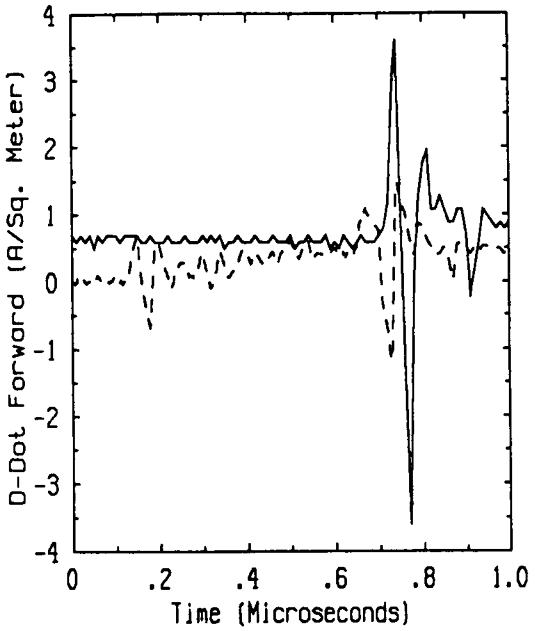

Flight 84.037 Run 016 Strike 063
- Measured -- Predicted

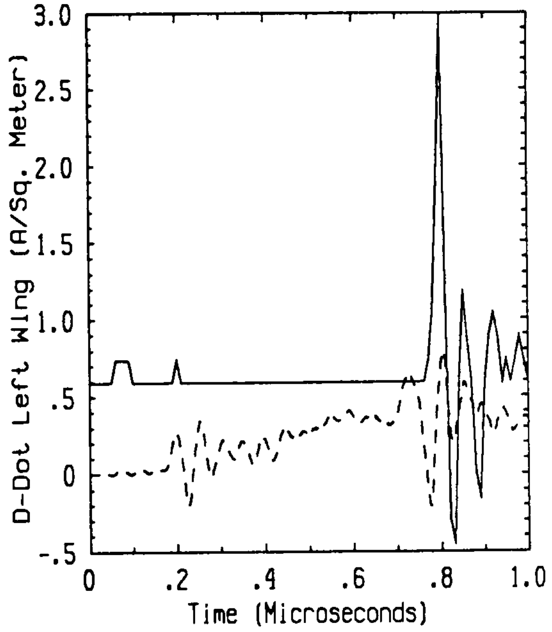

Flight 84.037 Run 016 Strike 063
- Measured -- Predicted

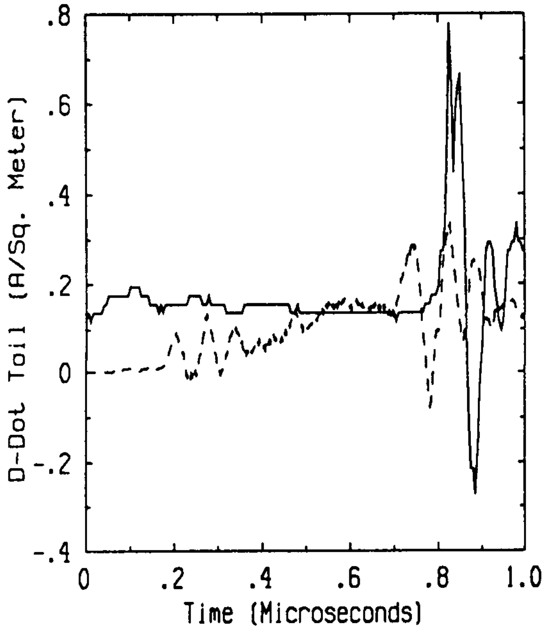

Flight 84.037 Run 016 Strike 063
- Measured -- Predicted

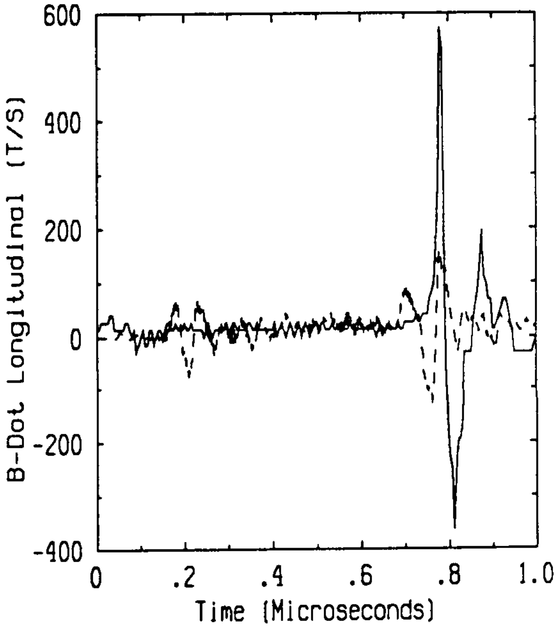

Flight 84.037 Run 016 Strike 063
- Measured -- Predicted

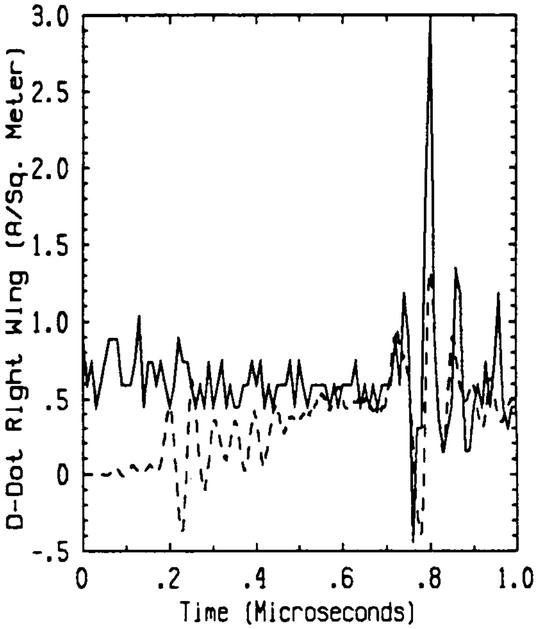

Flight 84.037 Run 016 Strike 063
- Measured -- Predicted

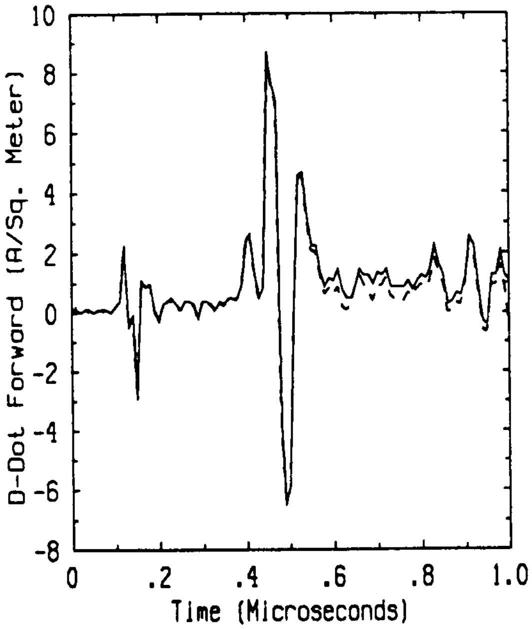

Flight 84.037 Run 017 Strike 066
- Measured -- Predicted

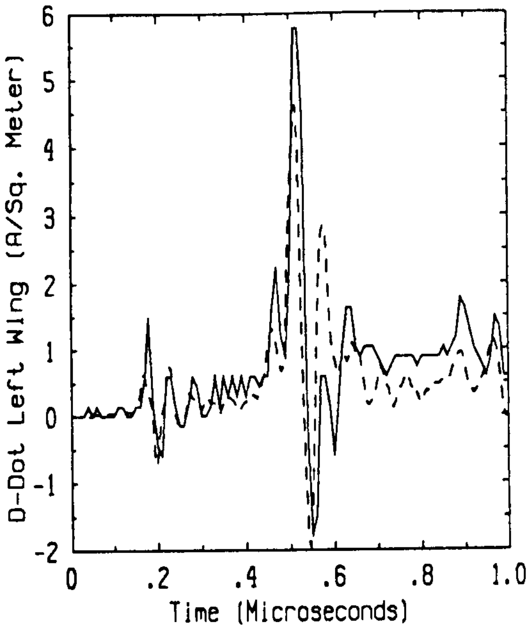

Flight 84.037 Run 017 Strike 066
- Measured -- Predicted

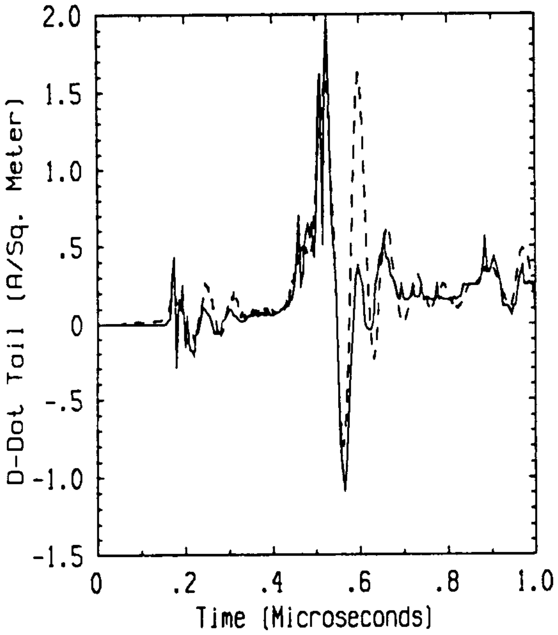

Flight 84.037 Run 017 Strike 066
- Measured -- Predicted

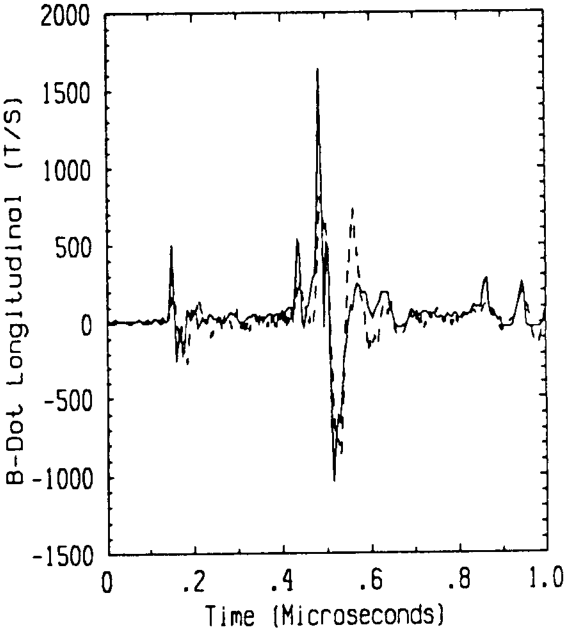

Flight 84.037 Run 017 Strike 066
- Measured -- Predicted

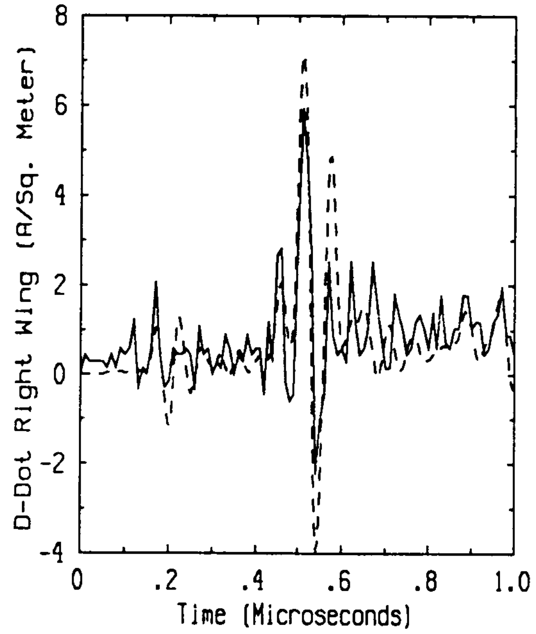

Flight 84.037 Run 017 Strike 066
- Measured -- Predicted

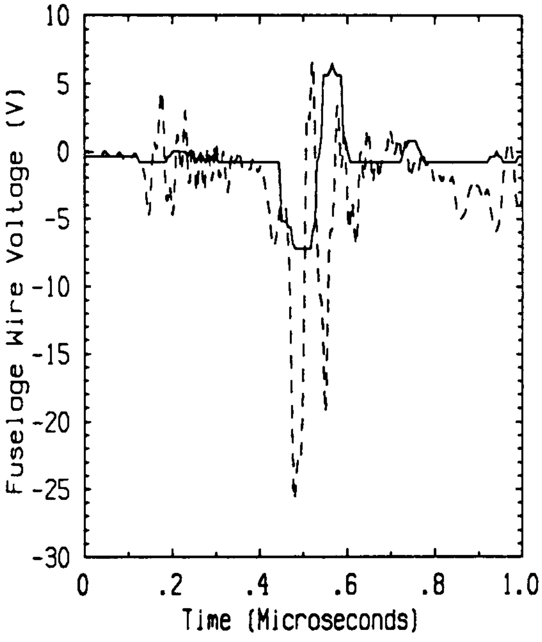

Flight 84.037 Run 017 Strike 066
- Measured -- Predicted

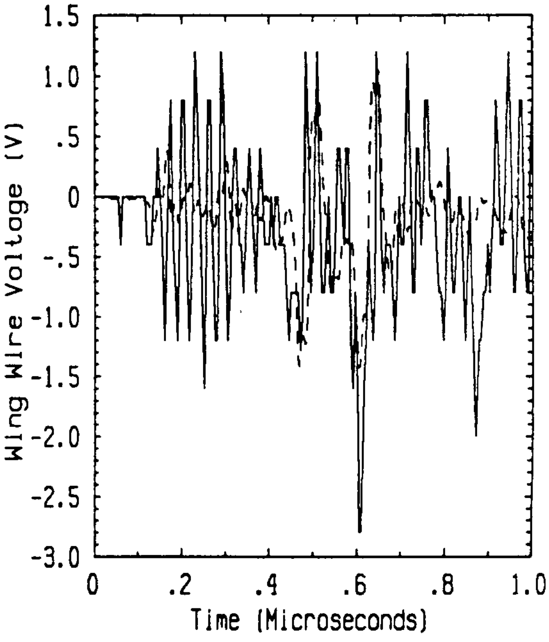

Flight 84.037 Run 017 Strike 066
- Measured -- Predicted

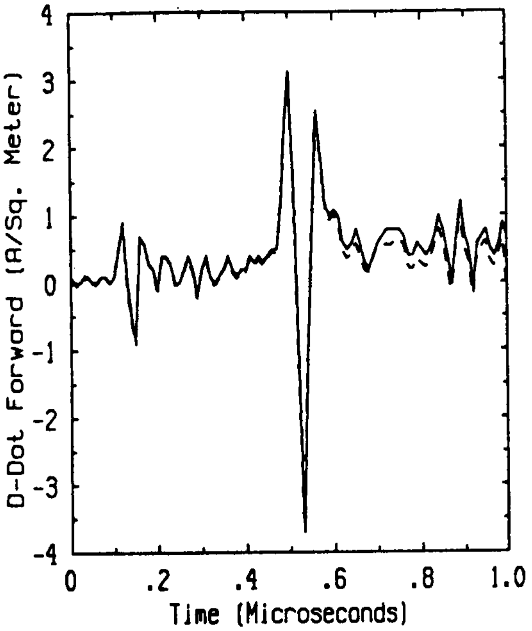

Flight 84.037 Run 019 Strike 071
- Measured -- Predicted

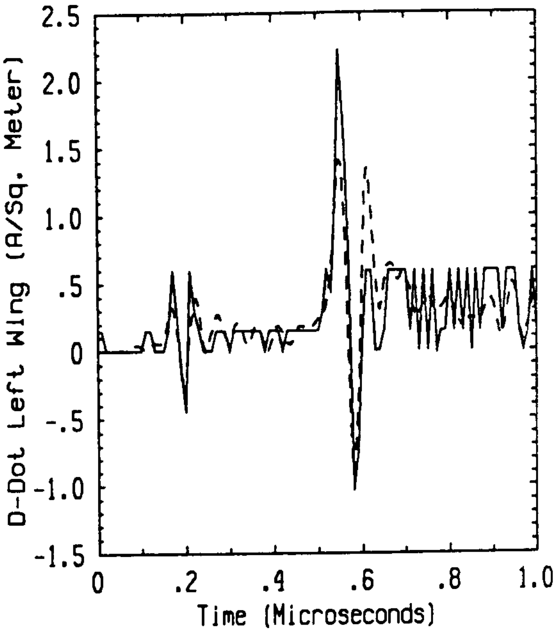

Flight 84.037 Run 019 Strike 071
- Measured -- Predicted

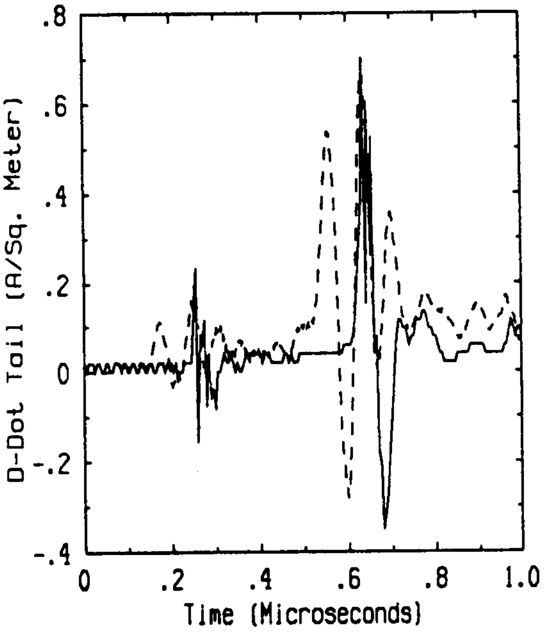

Flight 84.037 Run 019 Strike 071
- Measured -- Predicted

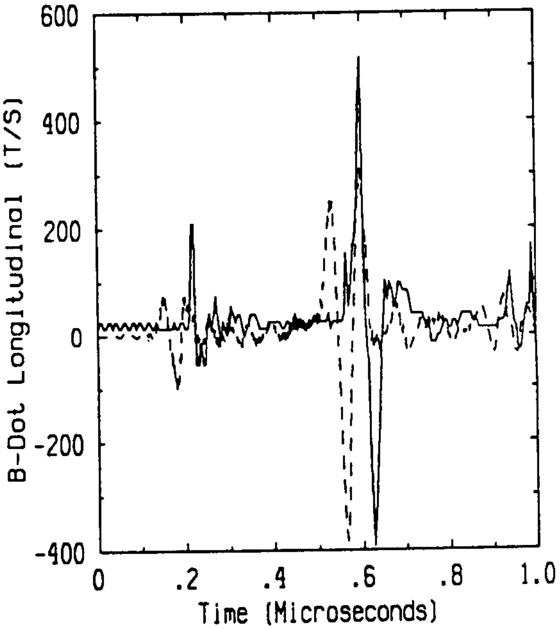

Flight 84.037 Run 019 Strike 071
- Measured -- Predicted

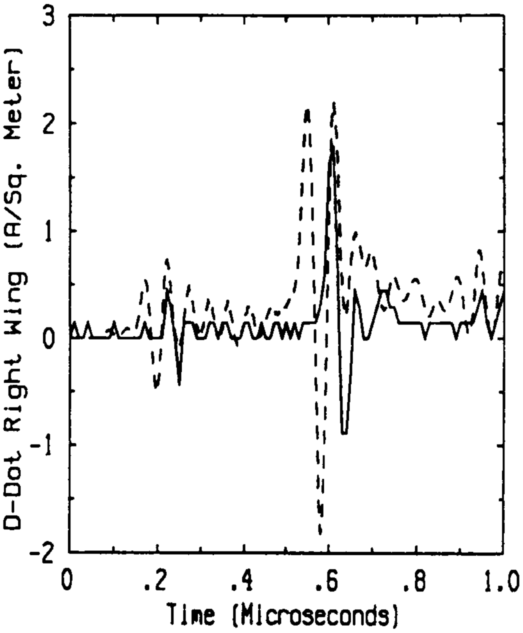

Flight 84.037 Run 019 Strike 071
- Measured -- Predicted

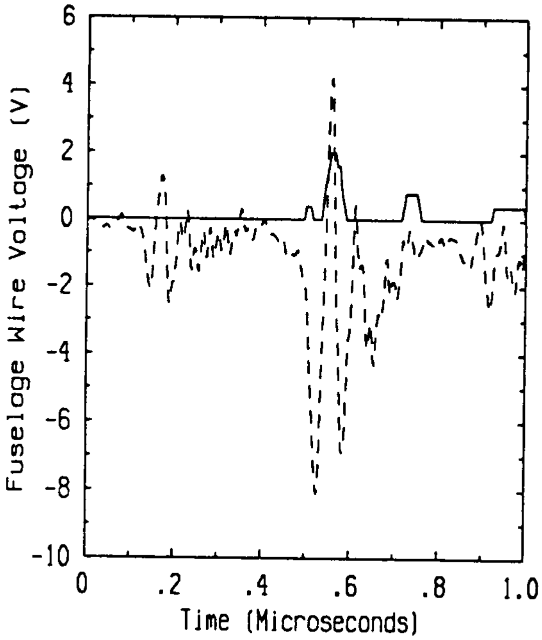

Flight 84.037 Run 019 Strike 071
- Measured -- Predicted

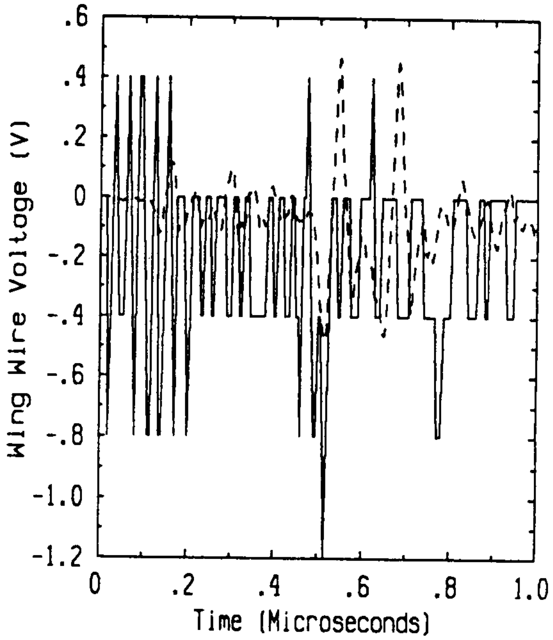

Flight 84.037 Run 019 Strike 071
- Measured -- Predicted

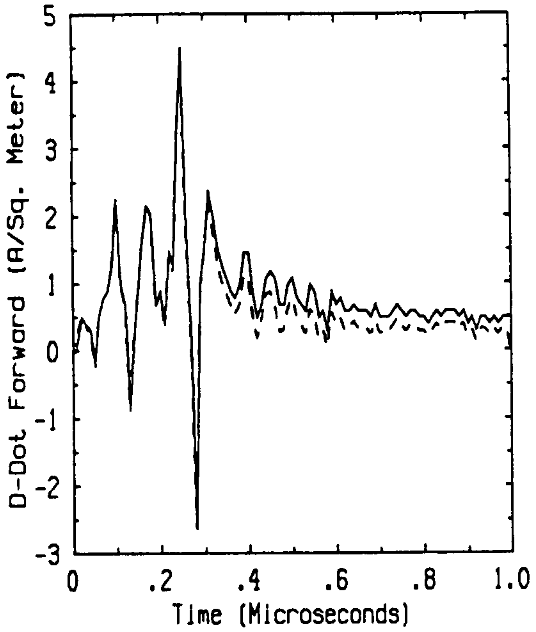

Flight 84.038 Run 001 Strike 002
- Measured -- Predicted

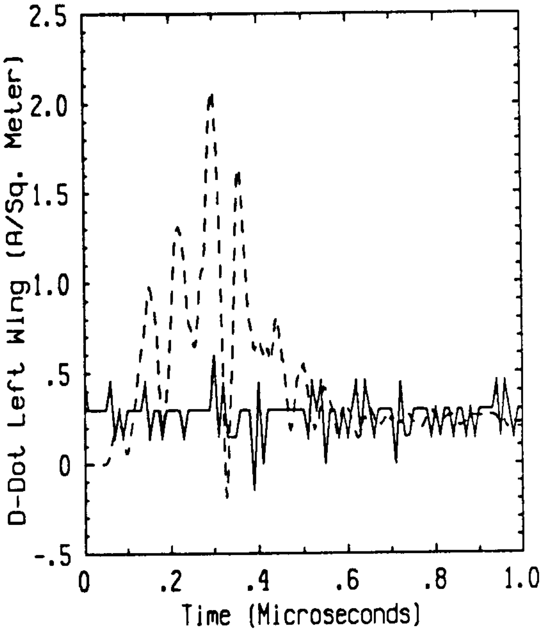

Flight 84.038 Run 001 Strike 002
- Measured -- Predicted

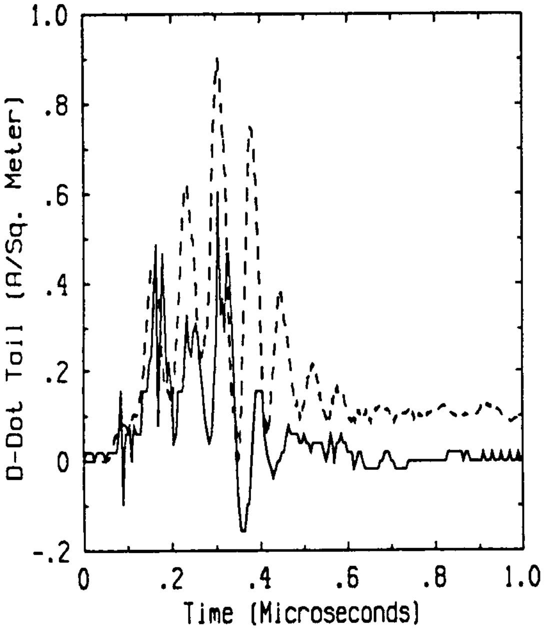

Flight 84.038 Run 001 Strike 002
- Measured -- Predicted

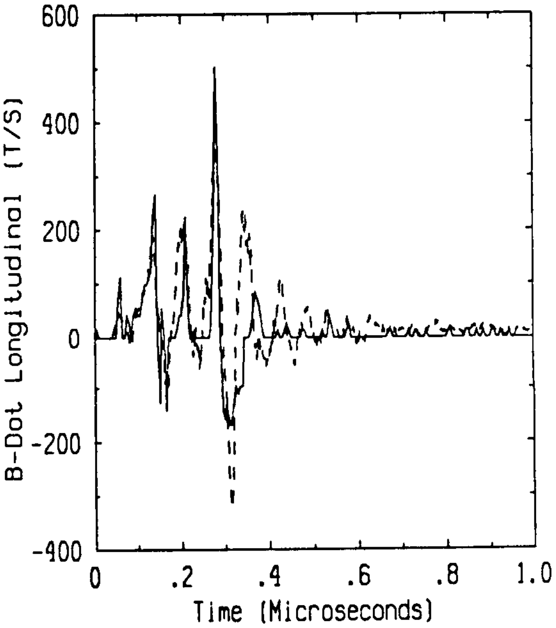

Flight 84.038 Run 001 Strike 002
- Measured -- Predicted

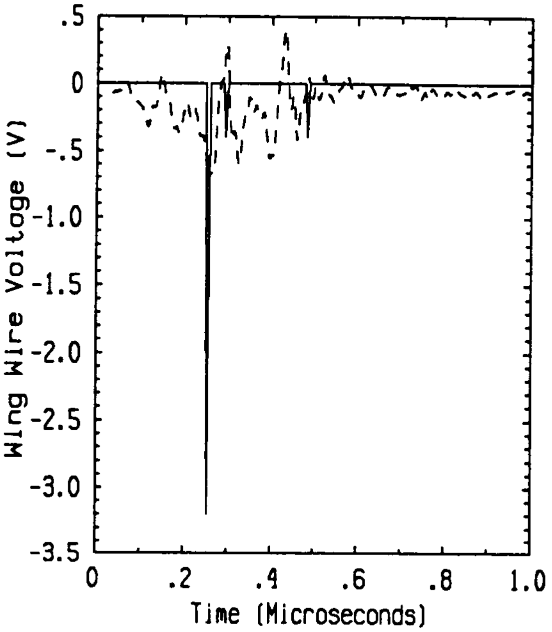

Flight 84.038 Run 001 Strike 002
- Measured -- Predicted

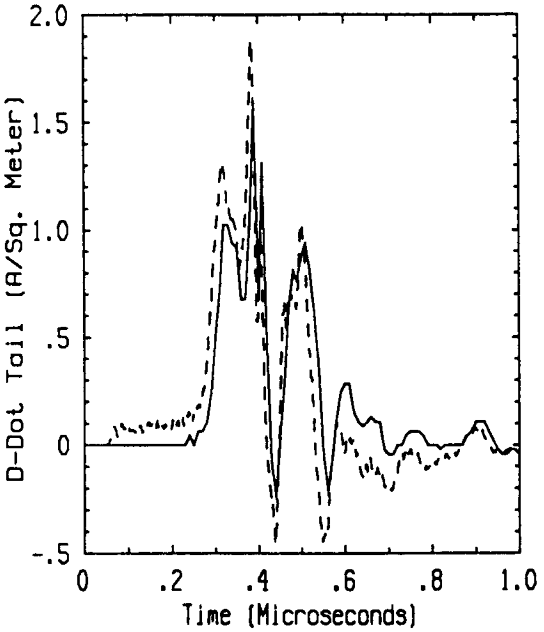

Flight 84.043 Run 001 Strike 001
- Measured -- Predicted

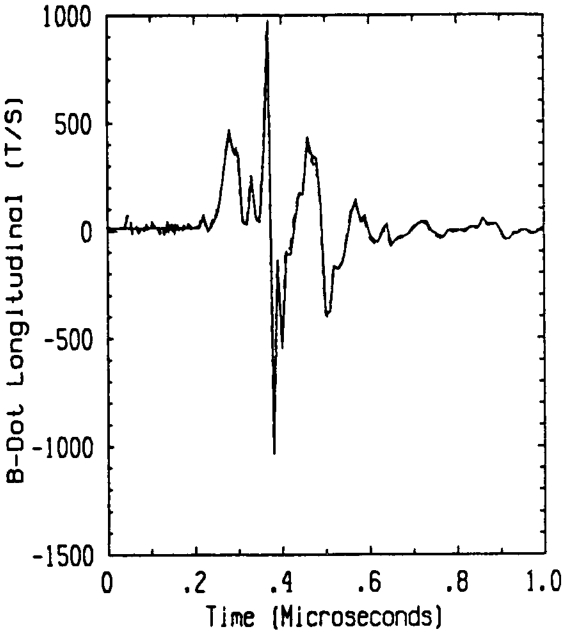

Flight 84.043 Run 001 Strike 001
- Measured -- Predicted

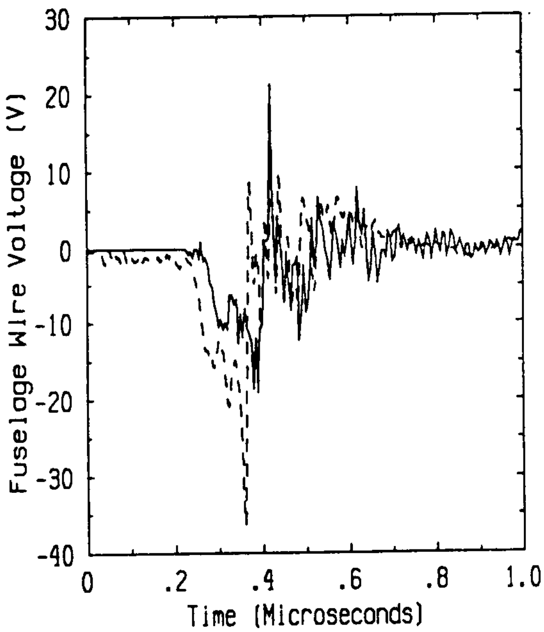

Flight 84.043 Run 001 Strike 001
- Measured -- Predicted

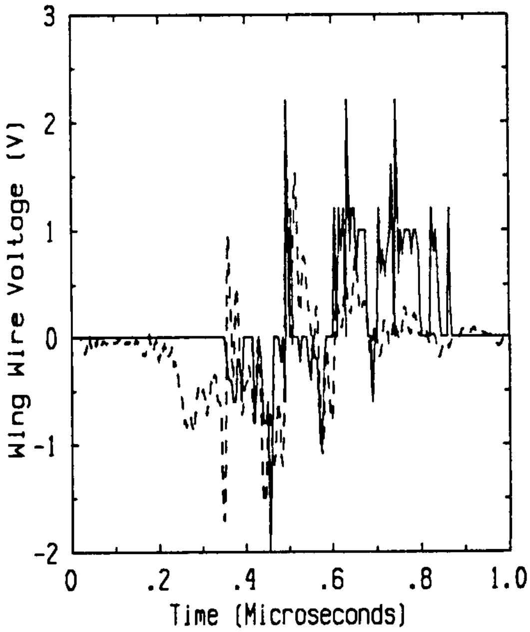

Flight 84.043 Run 001 Strike 001
- Measured -- Predicted

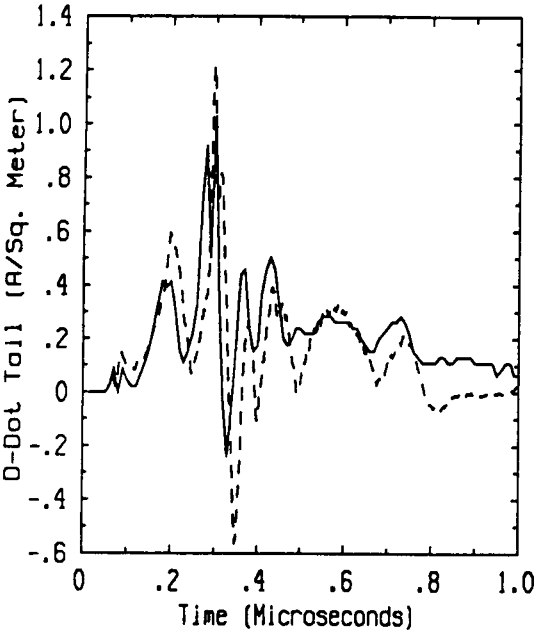

Flight 84.043 Run 005 Strike 005
- Measured -- Predicted

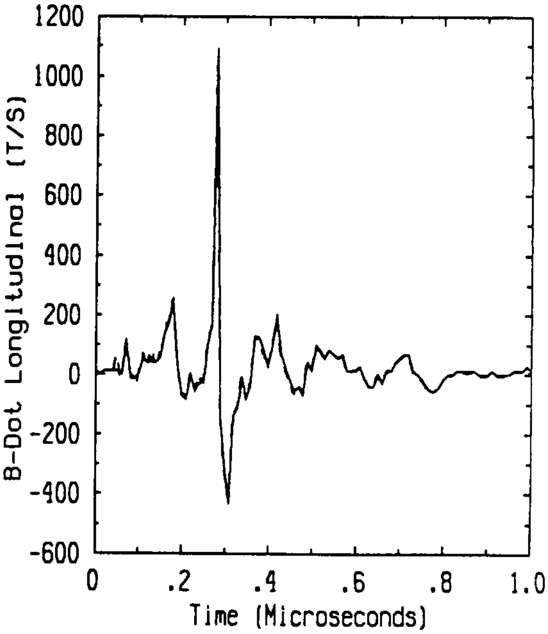

Flight 84.043 Run 005 Strike 005
- Measured -- Predicted

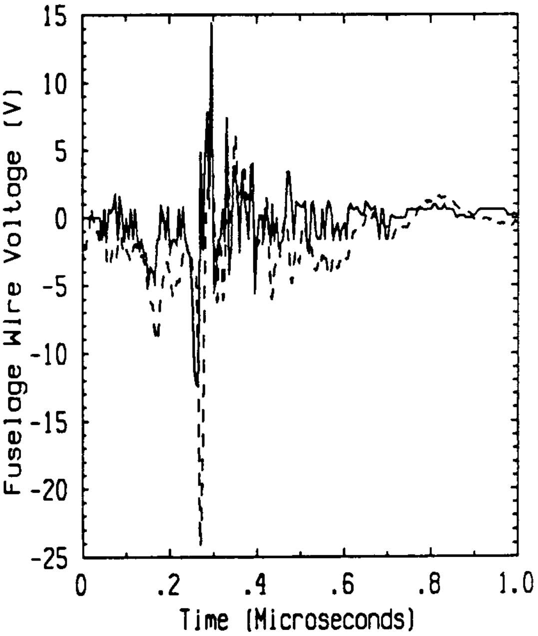

Flight 84.043 Run 005 Strike 005
- Measured -- Predicted

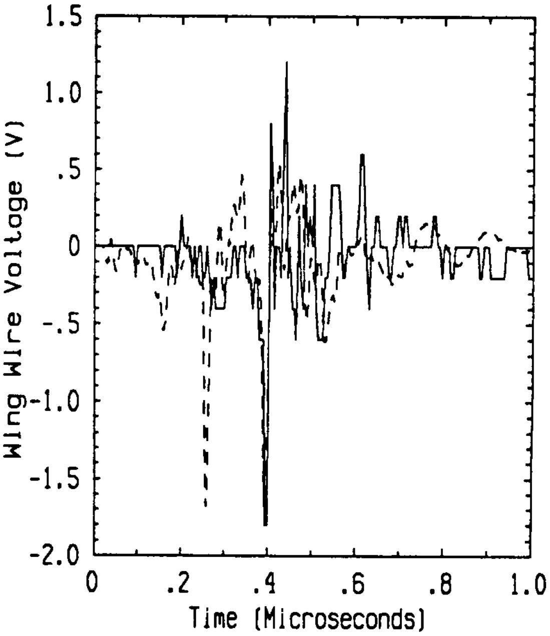

Flight 84.043 Run 005 Strike 005
- Measured -- Predicted

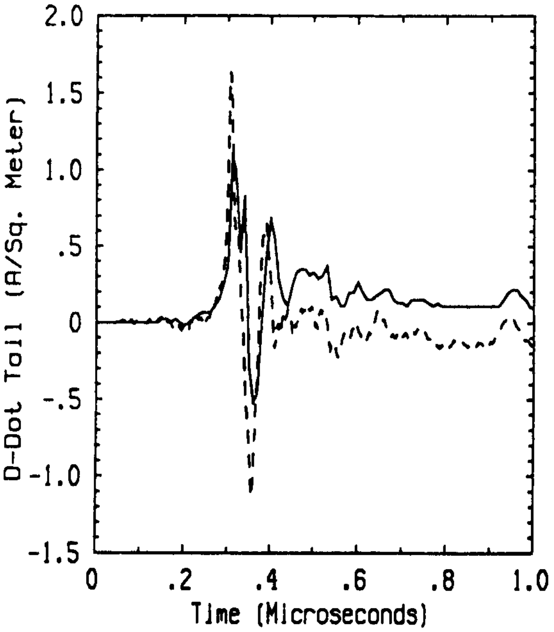

Flight 84.044 Run 002 Strike 003
- Measured -- Predicted

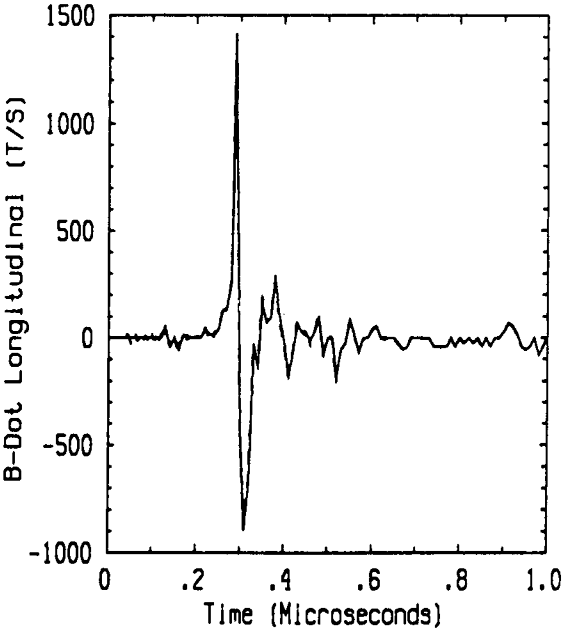

Flight 84.044 Run 002 Strike 003
- Measured -- Predicted

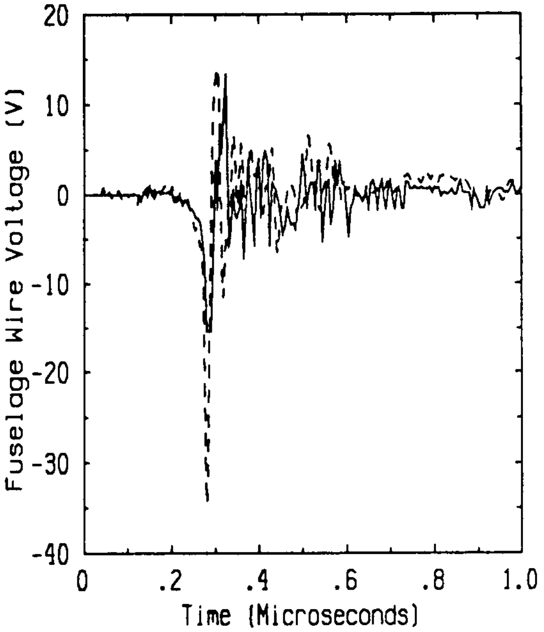

Flight 84.044 Run 002 Strike 003
- Measured -- Predicted

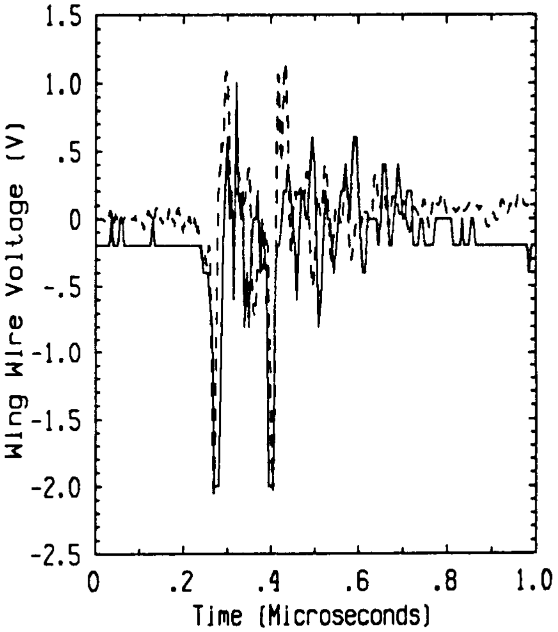

Flight 84.044 Run 002 Strike 003
- Measured -- Predicted

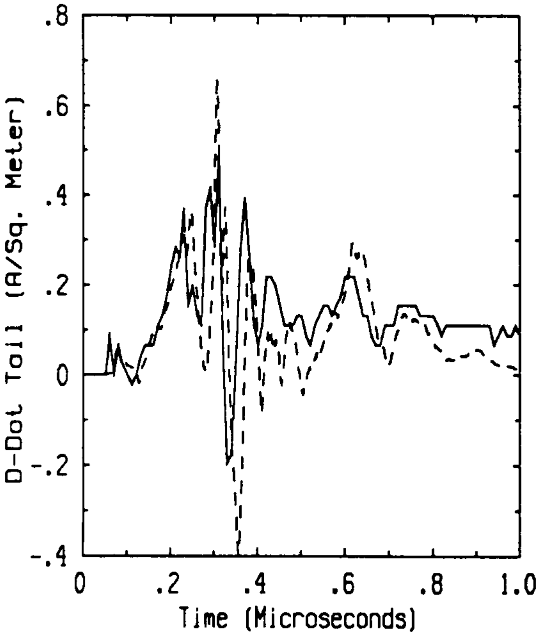

Flight 84.044 Run 003 Strike 004
- Measured -- Predicted

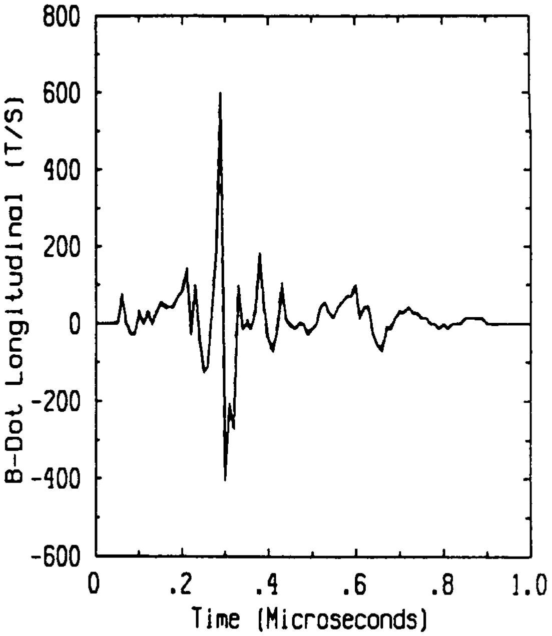

Flight 84.044 Run 003 Strike 004
- Measured -- Predicted

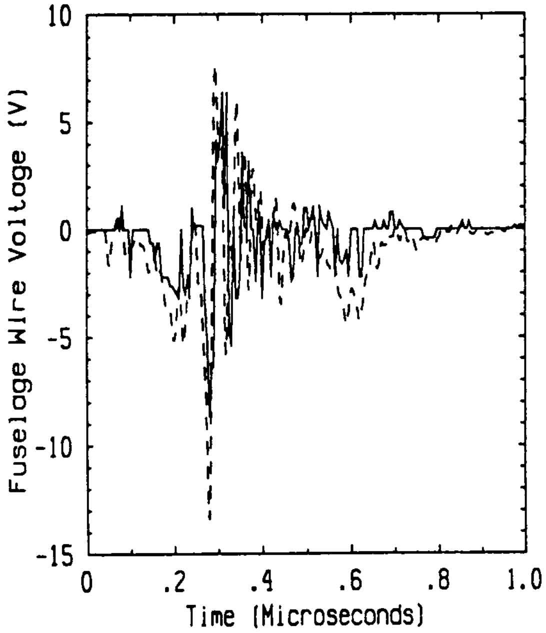

Flight 84.044 Run 003 Strike 004
- Measured -- Predicted

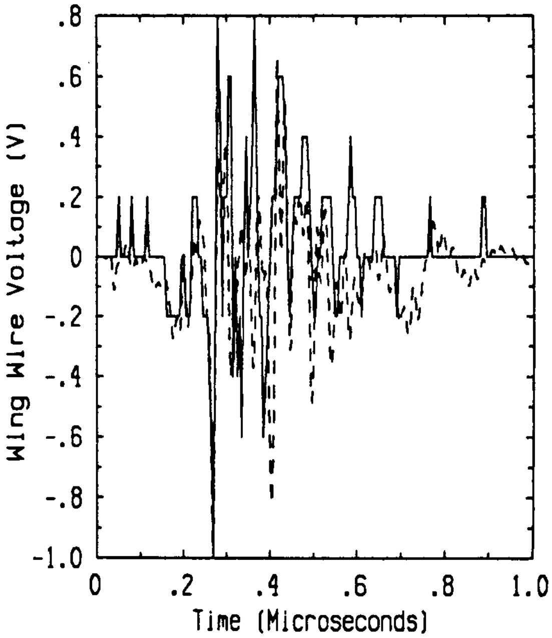

Flight 84.044 Run 003 Strike 004
- Measured -- Predicted

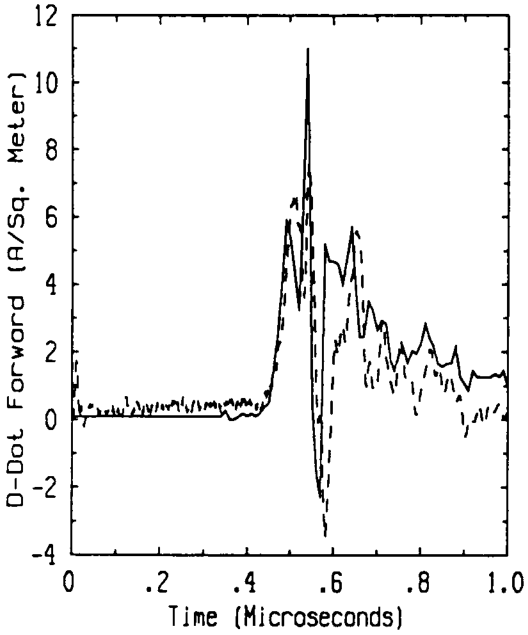

Flight 84.050 Run 002 Strike 002
- Measured -- Predicted

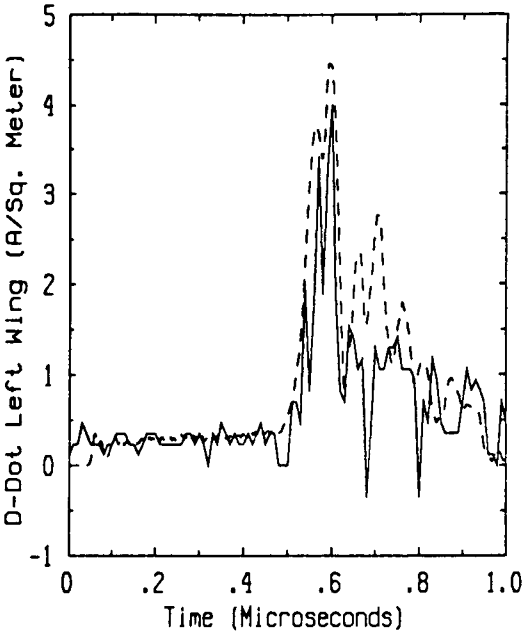

Flight 84.050 Run 002 Strike 002
- Measured -- Predicted

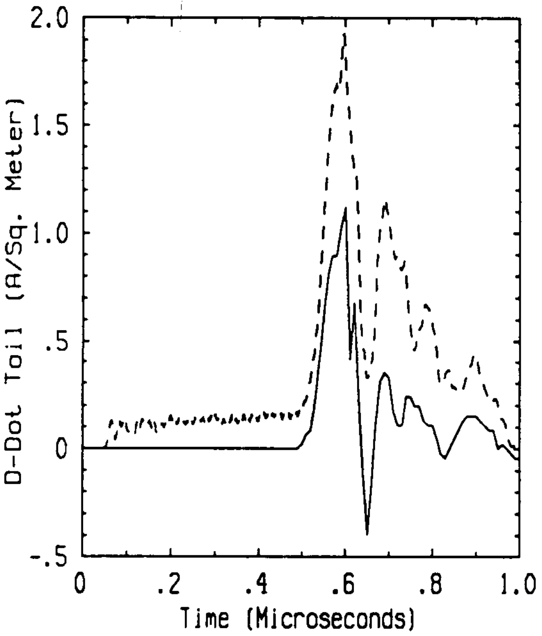

Flight 84.050 Run 002 Strike 002
- Measured -- Predicted

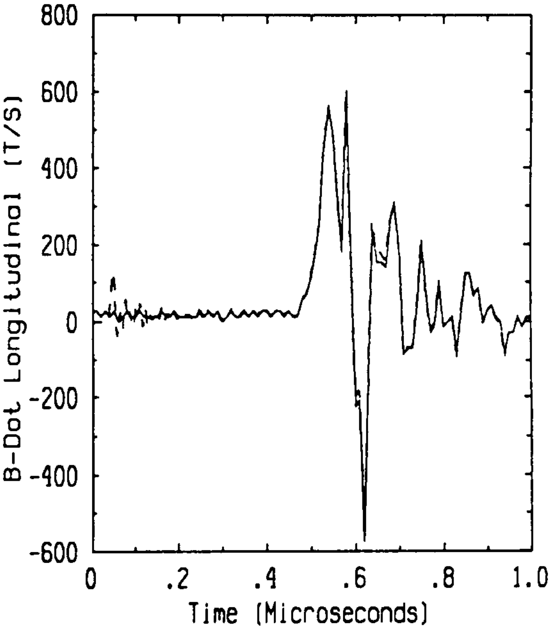

Flight 84.050 Run 002 Strike 002
- Measured -- Predicted

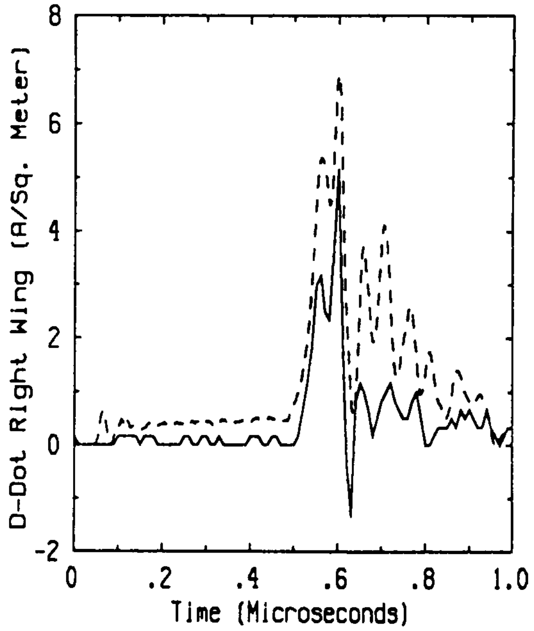

Flight 84.050 Run 002 Strike 002
- Measured -- Predicted

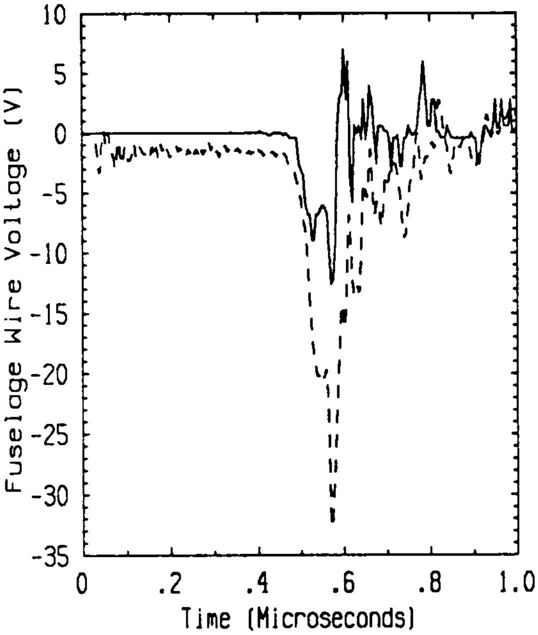

Flight 84.050 Run 002 Strike 002
- Measured -- Predicted

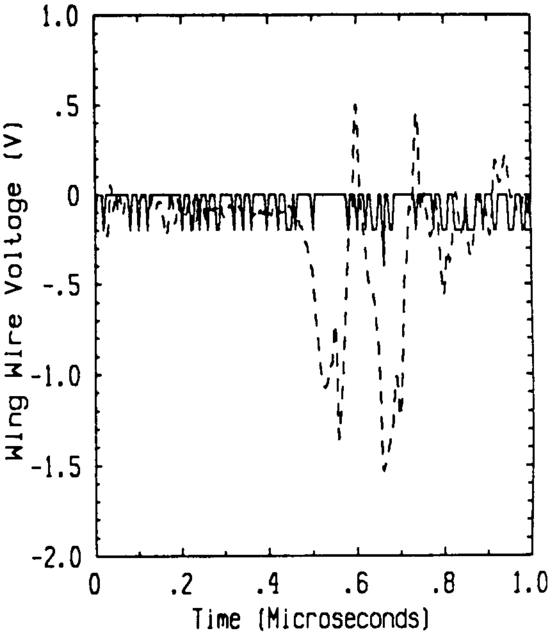

Flight 84.050 Run 002 Strike 002
- Measured -- Predicted

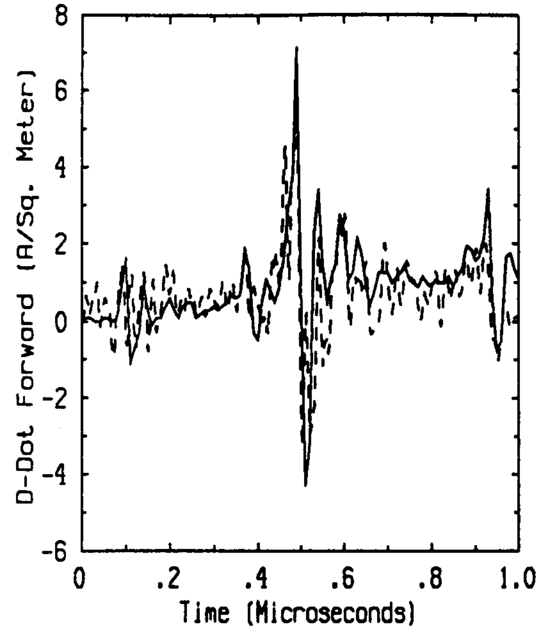

Flight 84.050 Run 004 Strike 007
- Measured -- Predicted

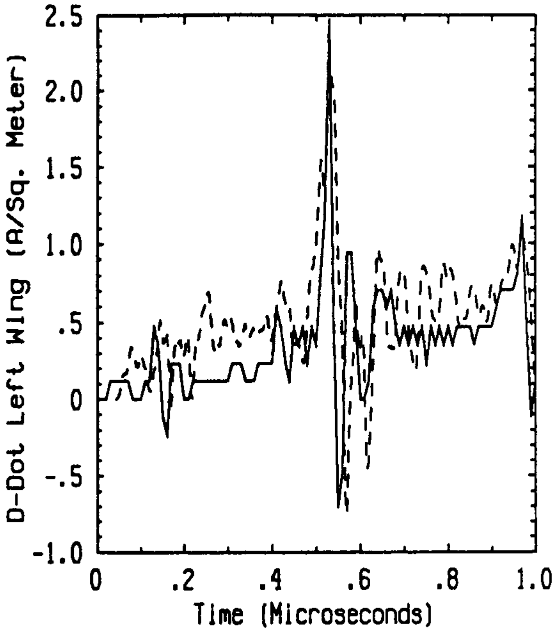

Flight 84.050 Run 004 Strike 007
- Measured -- Predicted

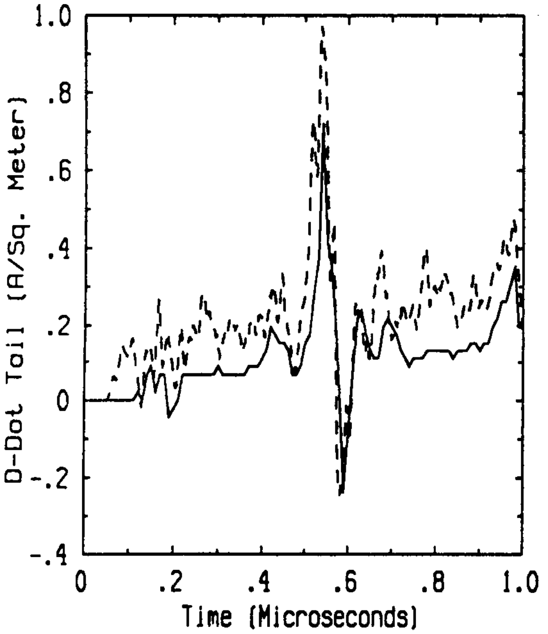

Flight 84.050 Run 004 Strike 007
- Measured -- Predicted

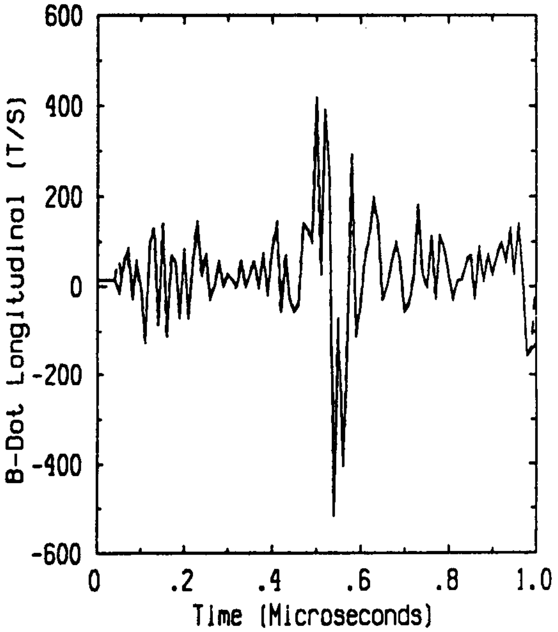

Flight 84.050 Run 004 Strike 007
- Measured -- Predicted

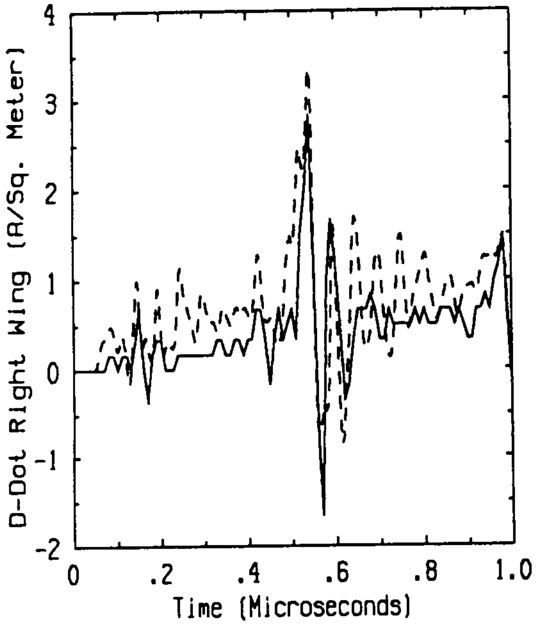

Flight 84.050 Run 004 Strike 007
- Measured -- Predicted

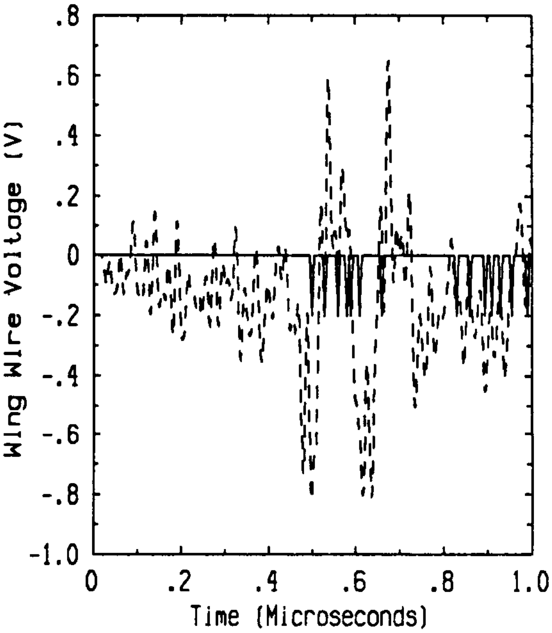

Flight 84.050 Run 004 Strike 007
- Measured -- Predicted

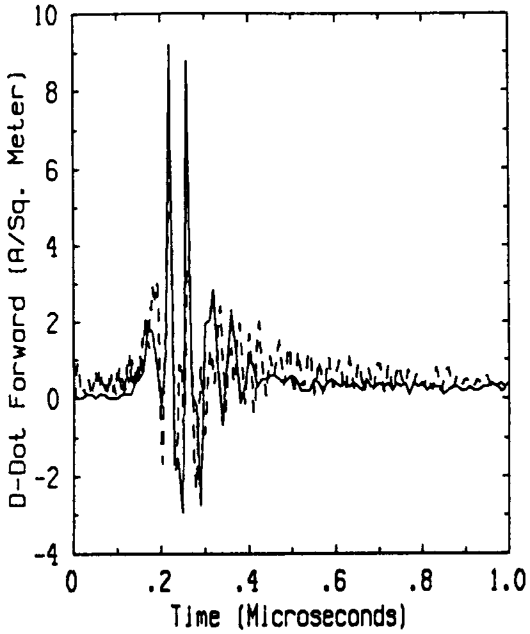

Flight 84.050 Run 008 Strike 020
- Measured -- Predicted

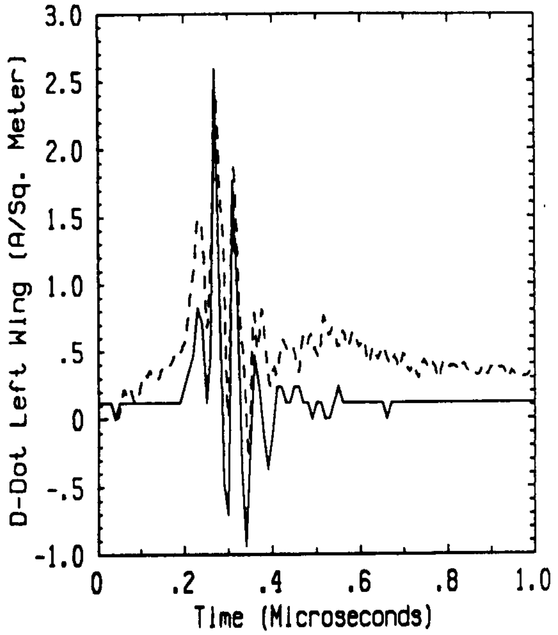

Flight 84.050 Run 008 Strike 020
- Measured -- Predicted

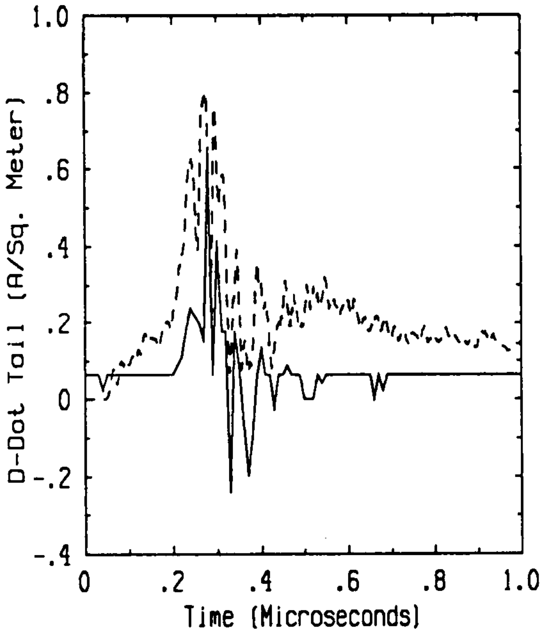

Flight 84.050 Run 008 Strike 020
- Measured -- Predicted

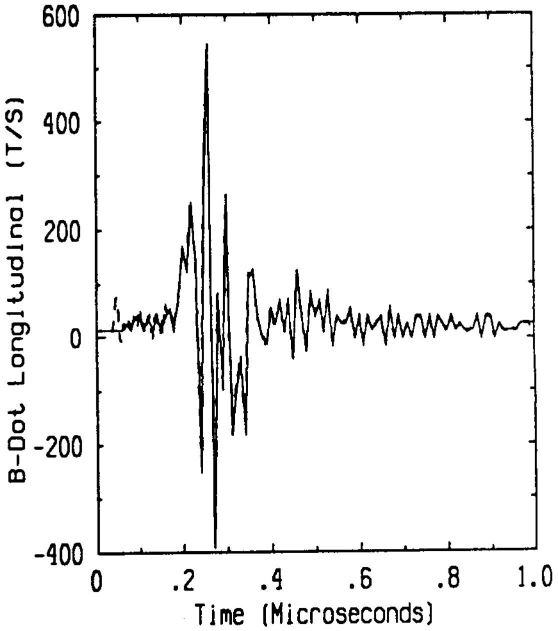

Flight 84.050 Run 008 Strike 020
- Measured -- Predicted

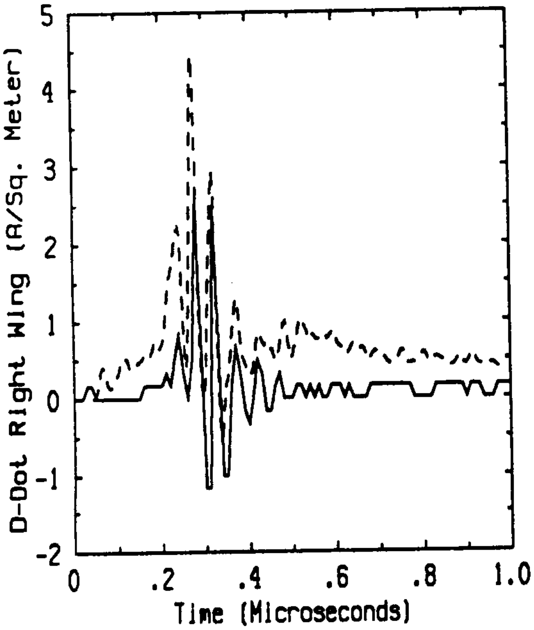

Flight 84.050 Run 008 Strike 020
- Measured -- Predicted

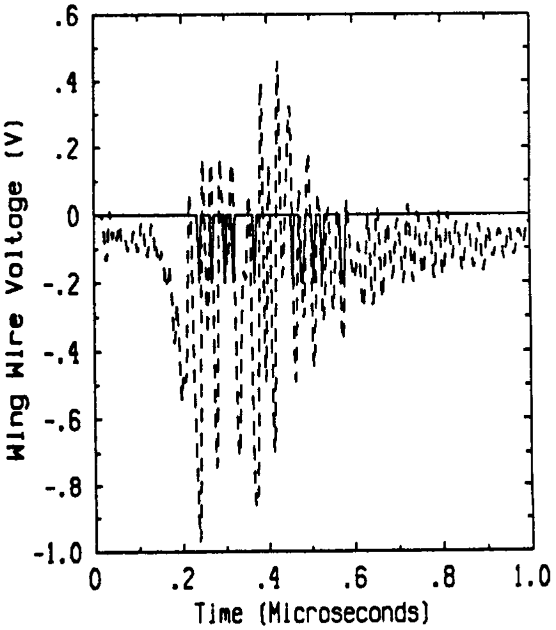

Flight 84.050 Run 008 Strike 020
- Measured -- Predicted

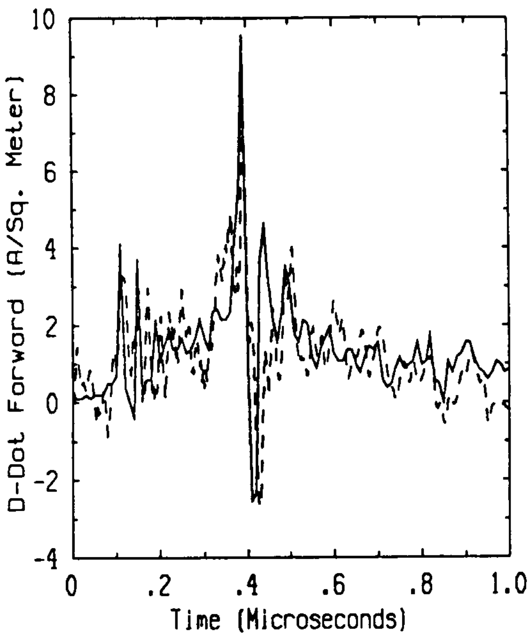

Flight 84.050 Run 010 Strike 025
- Measured -- Predicted

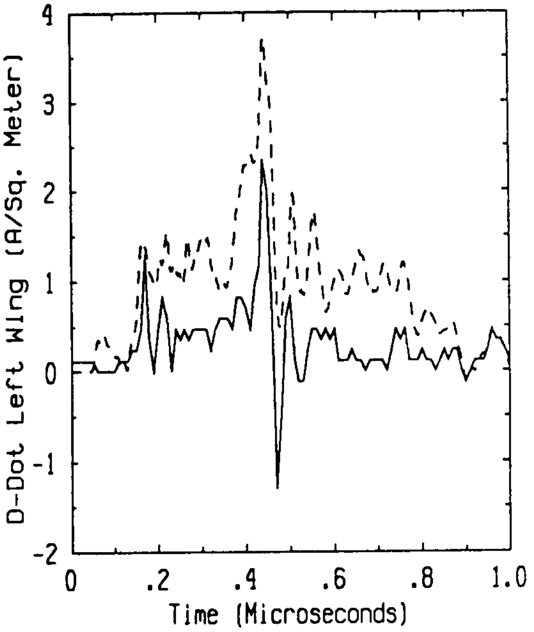

Flight 84.050 Run 010 Strike 025
- Measured -- Predicted

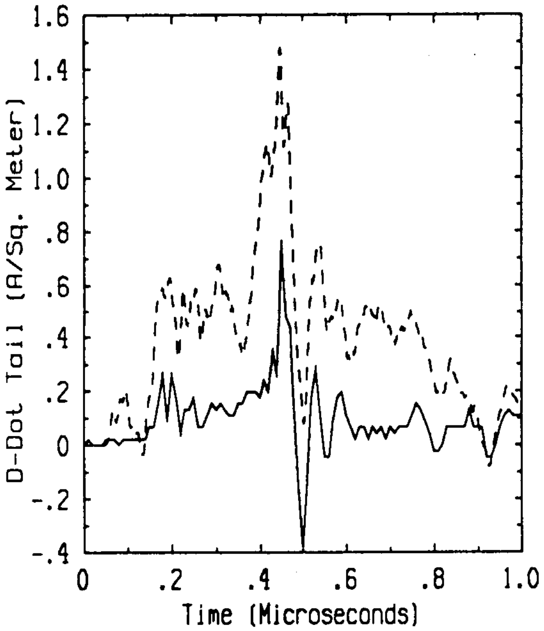

Flight 84.050 Run 010 Strike 025
- Measured -- Predicted

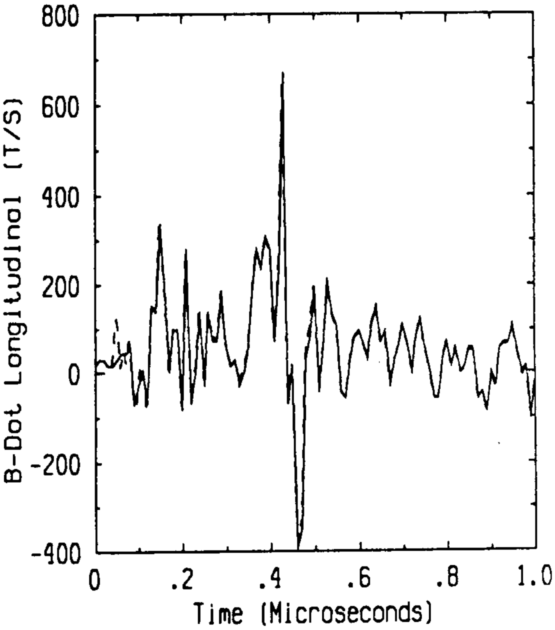

Flight 84.050 Run 010 Strike 025
- Measured -- Predicted

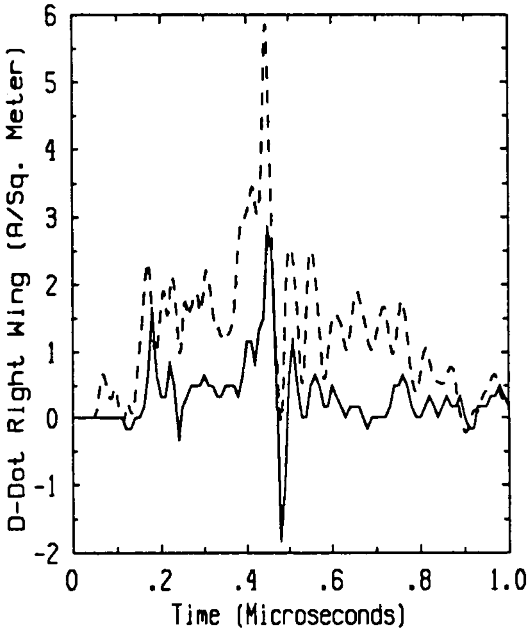

Flight 84.050 Run 010 Strike 025
- Measured -- Predicted

NASA

Report Documentation Page

1. Report No.
NASA CR-4207

2. Government Accession No.

3. Recipient's Catalog No.

4. Title and Subtitle
Application of Triggered Lightning Numerical Models to the F106B and Extension to Other Aircraft

5. Report Date
December 1988

6. Performing Organization Code

7. Author(s)
Poh H. Ng, Roger A. Dalke, Jim Horembala, Terence Rudolph, and Rodney A. Perala

8. Performing Organization Report No.
EMA-88-R-1

10. Work Unit No.
505-66-21-04

9. Performing Organization Name and Address
Electro Magnetic Applications, Inc.
12567 West Cedar Drive, Suite 250
Lakewood, CO 80228

11. Contract or Grant No.
NAS1-17748

13. Type of Report and Period Covered
Contractor Report

12. Sponsoring Agency Name and Address
National Aeronautics and Space Administration
Langley Research Center
Hampton, VA 23665-5225

14. Sponsoring Agency Code

15. Supplementary Notes
Langley Technical Monitor: Felix L. Pitts

16. Abstract

The goal of the F106B Thunderstorm Research Program is to characterize the lightning environment for aircraft in-flight. This report documents the application of numerical electromagnetic models to this problem. Topics include:

1. Extensive application of linear triggered lightning to F106B data
2. Electrostatic analysis of F106B field mill data
3. Application of subgrid modeling to F106B nose region, including both static and nonlinear models
4. Extension of F106B results to other aircraft of varying sizes and shapes
5. Application of nonlinear model to interaction of F106B with lightning leader-return stroke event.

17. Key Words (Suggested by Author(s))
F106B
Triggered Lightning
Finite Difference Modeling
Nonlinear Modeling

18. Distribution Statement
Unclassified - Unlimited

Subject Category 47

19. Security Classif. (of this report)
Unclassified

20. Security Classif. (of this page)
Unclassified

21. No. of pages
244

22. Price
A11

NASA FORM 1626 OCT 86

NASA-Langley, 1988

For sale by the National Technical Information Service, Springfield, Virginia 22161-2171

★U.S. GOVERNMENT PRINTING OFFICE:1989 -627 -064/ 86013